SYNTHESIS AND CHARACTERIZATION OF RUTHENIUM BASED COMPOSITE MATERIALS FOR SUPERCAPACITORS

XIAORONG LIU


CENTRE FOR NFLD. STUDIES
MEMORIAL UNIVERSITY
OF NEWFOUNDLAND

Synthesis and Characterization of Ruthenium Based Composite Materials for Supercapacitors

by

Xiaorong Liu

A thesis submitted to the
School of Graduate Studies
in partial fulfillment of the
requirements for the degree of
Doctor of Philosophy

Department of Chemistry
Memorial University of Newfoundland
September, 2010
St. John's, Newfoundland

Abstract

Ruthenium-based materials, including pure hydrous Ru oxide and composites of Ru oxide/carbon fabric (CF), nanostructured Ru oxide/multiwall carbon nanotube (MWCNT), thin film Ru oxide/CF and binary Mn-Ru oxide/CF have been synthesized using various methods. Their properties were characterized by scanning electron microscopy (SEM), transmission electron microscopy (TEM), X-ray diffraction (XRD), thermogravimetric analysis (TGA), cyclic voltammetry, impedance spectroscopy and constant current discharging. The purpose of the work was to improve the performances of Ru oxide supercapacitors and enhance the utilization of Ru in the composites.

Hydrous Ru oxide was prepared by a modified sol-gel method. The factors influencing the performances of Ru oxide supercapacitors, such as annealing temperature, electrode preparation method, electrode loading, separator, and stability, have been investigated in detail. XRD patterns show that the hydrous Ru oxide had an amorphous structure, while a crystalline structure was formed at annealing temperatures over 200 °C. The best specific capacitance for hydrous Ru oxide was 716±24 F/g at an annealing temperature of 110 °C. Hydrous Ru oxide electrodes prepared by coating Ru oxide on the surface of carbon fibre paper with 5% Nafion binder showed the best performance. Specific capacitances (ca. 700 F/g) did not change significantly with increasing electrode loading (up to 51 mg/cm^2) due to the good proton conductivity of the Nafion binder and the high mechanical stability of the electrodes. The best power density for supercapacitors reached 130.5 kW/kg for half discharge, while the best energy densities

were 40.5 W h/kg and 31.2 W h/kg for the operating voltages of 1.3 V and 1.0 V, respectively. Their lifetimes were over 120000 cycles.

In order to improve the utilization of Ru, Ru oxide/CF composites were prepared by an impregnation method. Specific capacitances of the composites increased with Ru oxide loadings. However, the specific capacitance for the Ru oxide component decreased with increasing loading. An average specific capacitance of 1085 F/g based on the Ru oxide component was obtained for a 9.2% Ru oxide/CF supercapacitor. The high specific capacitance was ascribed to synergistic effects between functional groups on the CF surface and the Ru oxide component with high surface area.

Nanostructured Ru oxide/MWCNT, thin film Ru oxide/CF, thin film Mn oxide/CF, and thin film Mn-Ru oxide/CF composites were synthesized by a spontaneous reduction method. The sizes of Ru oxide particles for the nanostructured Ru oxide/MWCNT composites were less than 3 nm. Thin film structures were observed by SEM for all of the CF composites. The utilization of Ru in these composites was enhanced due to the thin film structure and nanostructured Ru oxide particles, which allows electrolytes to access the bulk Ru oxide. An average specific capacitance of 704±62 F/g for the hydrous Ru oxide component was obtained for a 25.1% hydrous Ru oxide/MWCNT composite. A maximum average specific capacitance of 824±152 F/g based on the Ru oxide component was obtained for a 7.4% Ru oxide/CF composite with a film structure. For an 11.6% Mn oxide/CF composite, the specific capacitance for the Mn oxide component in 2 M LiOH was over 1000 F/g, however, it quickly decreased with

cycling. The stability of Mn-Ru oxide/CF composites was sharply improved due to the introduction of Ru.

A few types of hybrid supercapacitors were tested by cyclic voltammetry and constant current discharging. The operating voltages for hybrid supercapacitors of Ru oxide/CF or Mn oxide/CF with the CF reached 2.0 V in 2 M KNO_3 electrolyte, and the maximum energy density was ca. 18 W h/kg. A Ru oxide//Pd/C supercapacitor exhibited a maximum energy density of 41.3 W h/kg. A hybrid supercapacitor with anthraquinone modified CF (the negative electrode) and Ru oxide (the positive electrode) electrodes requires 76.3% less Ru oxide relative to a symmetric Ru oxide supercapacitor to provide a similar energy

An approach for quickly predicting the energy and power from impedance spectroscopy is proposed. The usable energy ($E=\frac{1}{2}C_{re}(f)V^2$) is related to the real capacitance ($C_{re}(f)$) and operating voltage (V), while power ($P=2fE$) depends on E and the frequency (f). The predicted results at low frequencies greatly agreed with those from constant current discharging.

Acknowledgements

I would like to express my sincere thanks to my supervisor, Dr. Peter G. Pickup, for his guidance, encouragement and help.

I am grateful to Dr. Francesca M. Kerton and Dr. Travis D. Fridgen for their input as part of my supervisory committee.

I also would like to express my appreciation to NSERC (postgraduate scholarship), Defence Research and Development Canada, the Department of Chemistry, and the School of Graduate Studies for financial support.

Many thanks go to my colleagues in the Pickup group for their assistance, and to Mr. Michael Shaffer for SEM experiments, and to Dr. Trisha Huber for providing carbon nanotubes and TEM images.

I want to express my greatest gratitude to my wife, Minkun Lei, and my daughter, Alexia Liu, for their encouragement, patience and devotion; to my parents and parents-in-law for their encouragement.

Contents

List of Figures

List of Tables

List of Abbreviations

AMCF	anthraquinone modified carbon fabric
C	capacitance
C_{im}	imaginary capacitance
C_{re}	real capacitance
C_{series}	series capacitance
C_{sp}	specific capacitance
CF	carbon fabric
CFP	carbon fibre paper
CNT	carbon nanotube
CV	cyclic voltammetry
E	energy
EDX	energy-dispersive X-ray diffusion spectroscopy
ESR	equivalent series resistance
f	frequency
f_0	characteristic frequency
I	current
m	electrode mass
M	molar mass
MWCNT	multiwalled carbon nanotube
n	proton number

P	power
Q	charge
Q(V)	charge at V (voltage)
R_i	ionic resistance
SEM	scanning electron microscopy
t	time
T	temperature
TEM	transmission electron microscopy
TGA	thermogravimetric analysis
v	scanning speed
V	voltage
V_o	initial voltage
ΔV	voltage change
XRD	X-ray diffraction
Z' or Z_{re}	real impedance
Z'' or Z_{im}	imaginary impedance

Chapter 1 Introduction

1.1 Background

In recent years, public concerns about global warming, an energy crisis, and environmental pollution have risen sharply. Alternative energy solutions, such as electrochemical energy storage and conversion devices, are effective ways for solving these problems. These devices can be classified technically as batteries, fuel cells, and supercapacitors (also known as ultracapacitors or double layer capacitors) on the basis of their operating principles. Each type of device consists of two electrodes with an electrolyte separator, where energy-transforming processes occur at the interfaces between the two electrodes and the electrolyte.[1]

Each type of energy storage device has its own distinctive features. The electrical energy delivered by both batteries and fuel cells originates from chemical energy conversion. A battery is usually a closed system in which the energy storage materials are sealed into a container, while a fuel cell is an open system where fuel and air are pumped to the electrode interfaces. In contrast, a supercapacitor stores energy at the double layers of the electrodes or via fast surface Faradaic processes (see section 1.4).

In general, supercapacitors bridge the gap between batteries (or fuel cells) and conventional dielectric capacitors. Supercapacitors have much higher power densities and longer lifecycles (by at least two orders of magnitude) than batteries.[1, 2] However, batteries have higher energy densities than supercapacitors. Although fuel cells can provide high energy densities, the low power densities and high cost (due to the use of

precious metals catalysts) limit their applications. In contrast to conventional dielectric capacitors, supercapacitors have much higher energy densities (by at least three orders of magnitude). However, both supercapacitors and dielectric capacitors can provide similar maximum power densities.[3]

Supercapacitors are playing a vital role in the electrification of vehicles and in high performance electronics. For the energy supply of an electric vehicle, the combination of a supercapacitor with a battery or fuel cell can provide peak power for accelerating, braking and hill climbing. In addition, supercapacitors can also enhance the designs of circuits for consumer electronics and digital devices, thus meeting the requirements for peak power and good performance.

1.2 Definitions and equations

The following definitions and equations are used in this thesis.[1, 4]

A *supercapacitor* is a device that stores electrical energy at electrical double layers and/or by fast Faradaic processes.

An *electrolyte* is an ion conducting material.

A *separator* is a film material with negligible electronic conductivity between the two electrodes to prevent electrical shorting. For example, Nafion films, polymers, papers and glass fiber sheets are good separators.

Charging is an energy storage process in which the potential of the negative electrode moves to a lower value, while the potential of the positive electrode moves to a higher value.

Discharging is a process in which a supercapacitor delivers electrical energy to an external load.

Capacitance (*C*) is charge per applied voltage and is measured in farads (F). It is determined by Eq. 1.1. A supercapacitor capacitance depends on the capacitances of the negative electrode and the positive electrode (see Eq. 1.2). Its reciprocal value (1/C) is equal to the sum of the reciprocal values of the negative electrode ($1/C_n$) and the positive electrode ($1/C_p$).

$$C=Q/\Delta V \qquad \text{Eq. 1.1}$$

$$1/C=1/C_n+1/C_p \text{ or } C=C_nC_p/(C_n+C_p) \qquad \text{Eq. 1.2}$$

where C, Q, ΔV, C_n, and C_p represent capacitance, charge, voltage change, the capacitance of the negative electrode, and the capacitance of the positive electrode, respectively.

Specific capacitance is used to express the charge storage capability of an electrode material or device in farads per gram (gravimetric) or farads per square centimeter.

Cyclic voltammetry(CV) is a type of linear sweep voltammetry in which the potential of a working electrode is ramped linearly versus time. When the working electrode potential reaches a set potential, the scan direction is reversed.[4]

Cyclic voltammogram [4] is a plot in which the current response of the working electrode is plotted as a function of the applied potential in a cyclic voltammetry experiment. The capacitance, specific capacitance, and average capacitance of an

electrode or a supercapacitor can be obtained from a cyclic voltammogram. The capacitance at any potential is determined by Eq. 1.3

$$C=I/v \quad \text{Eq. 1.3}$$

where I is the current response in amperes, and v is a scan speed in volts per second. The average capacitance ($C_{average}$) can be obtained by Eq. 1.1.

Impedance (Z) is defined as the value of Ė/İ (where Ė and İ are alternating potential and current, respectively). A cell or an electrode impedance is often plotted as a function of frequency, and referred to *electrochemical impedance spectroscopy* (EIS).[4]

Constant current discharging is a discharge method in which a constant current is drawn from a cell. The graphical illustration of potential as a function of time is a *constant current discharging curve*.

The *energy* of a supercapacitor is its energy storage capability. It is determined by the initial voltage and capacitance as shown in Eq. 1.4, and is proportional to the square of the initial voltage.

$$E=\frac{1}{2}CV_o^2 \quad \text{Eq. 1.4}$$

where E, C, and V_o are energy, capacitance, and the initial voltage, respectively.

In addition, the energy of a supercapacitor can also be measured by constant current discharging. Eq. 1.5 shows the relationship of energy (E) to voltage (V), the constant discharging current (I), and the discharge time (t).

$$E=\int IVdt \quad \text{Eq. 1.5}$$

Energy density is the energy storage capability of an electrode material or supercapacitor by in watt-hours per kilogram (gravimetric) or watt-hours per litre (volumetric).

Power is the rate capability of energy delivery in watts (W). It is determined by Eq. 1.6. *Power density* is used for comparing the rate capability of energy delivery of a supercapacitor in watts per kilogram (gravimetric) or watts per litre (volumetric).

$$P=E/t \qquad \text{Eq. 1.6}$$

where P, E, and t are power, energy, and the time of energy delivery, respectively.

A *Ragone plot* is a plot of energy density as a function of power density, and provides power and energy capabilities of an energy storage device over a range of delivery rates.

1.3 Historical overview

The development of our understanding of the double layer at an electrode/electrolyte interface concept occurred over a long period of time. It was first developed and modeled by German physician, Hermann von Helmholtz in 1874.[3, 4] The principle was further developed by Gouy, Chapman, Stern and Grahame, therefore forming the modern theory of the electrical double layer at the end of the 1940s. Fig. 1.1 shows a schematic of a double layer at an electrode. It consists of a Helmholtz layer and a diffuse layer. The inner layer (also called the Stern layer or Helmholtz layer) consists of ions that are specifically adsorbed. However, the diffuse layer consists of nonspecifically

adsorbed ions due to the effects of thermal agitation in the solution, and extends from the Helmholtz plane into the bulk solution.[4]

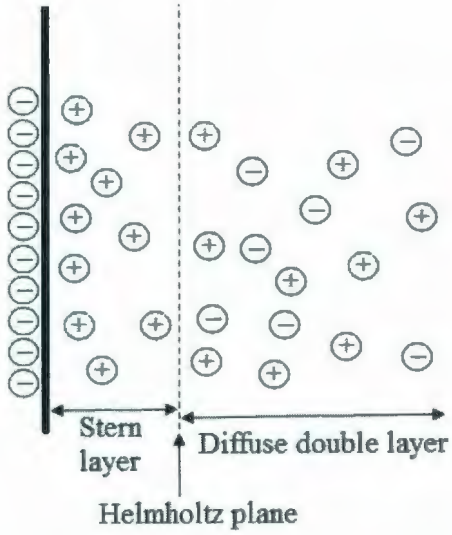

Fig. 1.1 A schematic of a double layer at an electrode

1.4 Mechanisms and classifications of supercapacitors

In general there are two types of supercapacitors on the basis of their charge storage mechanisms: double layer capacitors and pseudocapacitors. Charges are stored at the interfaces between electrodes and an electrolyte for double layer capacitors. Fig. 1.2 [5] shows the operating principles of a double layer supercapacitor. It can be seen that negative ions accumulate on the surface of the positive electrode during charging, while positive ions accumulate on the negative electrode. Electrons on the negative electrode flow through a load to the positive electrode during discharging, resulting in the release of energy. A double layer capacitor can be quickly charged or discharged due to this electrostatic storage mechansim.

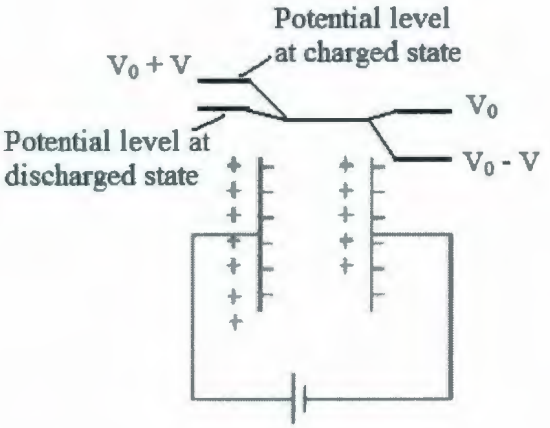

Fig. 1.2 Operating principle of a supercapacitor

Reprinted from "Experimental study of supercapacitor serial resistance and capacitance variations with temperature", vol 123, H. Gualous, D. Bouquain, A. Berthon and J. M. Kauffmann, page 86-93, Copyright (2003), with permission from Journal of Power Sources.

Fig. 1.2 also shows the potential changes of the positive and negative electrodes during charging and discharging. The potential of the positive electrode increases during charging owing to its extra positive charge given by a charging source. However, the potential of the negative electrode decreases due to the gain of electrons from the charging source.

Pseudocapacitors store charges by Faradaic processes, including fast intercalation reactions, electrosorption or redox reactions occurring on electrode surfaces.[2] The capacity to store charge strongly depends on the nature of these processes. The more electrons involved the reactions, the larger the capacities. The mechanism of pseudocapacitors is similar to that of rechargeable batteries except that the latter have much slower charging and discharging rates.

1.5 Materials for supercapacitors

Table 1.1 Summary of specific capacitances for selected electrode materials

Materials	Density (g/cm^3)	electrolyte	F/g	F/cm^3
Carbon cloth	0.35	KOH	200	70
		organic	100	35
Carbon black	0.2-1.0	KOH	95	95
Aerogel carbon	0.6	KOH	140	84
Small pore carbon [6]		organic	150	
Hydrous RuO_2	2.0-2.5	H_2SO_4	650	1300-1625
MnO_2		KOH	100-400	

Reprinted from "Ultracapacitors: why, how, and where is the technology", vol 91, A. Burke, page 37-50, Copyright (2000), with permission from Journal of Power Sources.

There are a variety of charge storage materials for supercapacitors. Table 1.1 [7] summarizes the specific capacitances of electrodes of the commonly used materials. Carbons and metal oxides are popular materials for supercapacitors. They are discussed in the following sections.

1.5.1 Carbon materials

Carbons are popular for double layer capacitors for many reasons.[3] Firstly, they are good electron conductors, thus allowing them to quickly store and deliver energy. Secondly, there are various types of carbon available for tailoring to specific purposes, such as activated carbon, carbon black, carbon fibre, carbon aerogel, carbon mat or fabric, carbon nanotubes, engineered carbon, etc. Thirdly, carbons are inexpensive compared

with metal oxides, and they are relatively stable in most acids, bases and organic solvents. Last but not least, carbons can be modified with functional groups or metal oxides, resulting in high capacitances and performances. So far, all current commercial supercapacitors employ carbon materials as electrodes.

The main limitations of carbons are their low specific capacitances relative to pseudocapacitive materials. In organic electrolytes, the specific capacitances for carbons with high surface area range from 80 F/g - 120 F/g (see Table 1.1), over 2.5 V - 3.5 V of nominal potential for a single cell.[3] This low gravimetric or volumetric capacitance limits their applications in some fields, such as medical devices, microdevices and electric vehicles.[8] Although carbon materials show high specific capacitances (over 200 F/g) in aqueous electrolytes (see Table 1.1),[9] the low usable cell voltage (ca. 1.2 V) means that it only provides low energy due to the relationship of the energy to the square of the cell voltage.[2] Modified carbons with anthraquinone functionality can provide higher specific capacitance, but they only show enhanced capacitances in aqueous electrolytes.[10, 11]

Chmiola *et al.* [6] developed a new carbide-derived method for preparing small pore carbons (<1 nm) which show a high specific capacitance of over 150 F/g in organic electrolytes. This enhanced capacitance is due to the higher surface area and the small pore distribution which allows the electrolyte to easily access small pores, thus enhancing the utilization of pores.

1.5.2 Ru(IV) oxide

Among the materials with pseudocapacitive behaviors, a few metal oxides, including Ru(IV) oxide, iridium oxide, manganese oxide and vanadium oxide show high specific capacitances. In particular, Ru(IV) oxide shows great promise as an electrode material for supercapacitors due to its high specific capacitance (over 650 F/g as shown in Table 1.1) and its three-dimension-network of electron and proton conductivity.[12-14]

Since Trasatti and Buzzanca [15] first reported that Ru oxide can be used as a capacitor material in 1971, Ru oxide has become an attractive topic. Most early research work focused on the formation of Ru oxide films, mechanisms of charging and discharging, and capacitive behaviors.[2] However, the specific capacitance was not enhanced significantly until 1995, when Zheng and Jow *et al.* [12, 14] synthesized hydrous Ru(IV) oxide with high specific capacitance (750 F/g) by a simple sol-gel method (the reaction between Ru chloride and base). In this way, they were able to double the best previously reported value. In more recent years, a few groups have synthesized Ru oxide for supercapacitors by a variety of different methods, such as electrophoretic deposition,[16] cyclic voltammetric deposition,[17-19] hydrothermal synthesis [20, 21] etc., but high specific capacitances are obtained only for electrodes with low loadings, and the specific capacitances quickly decrease with increasing loading.[16]

Ruthenium is an element that can form compounds with many oxidation states (see section 1.6). Hydrous Ru oxide is nonstoichiometric, making it unclear what valence states are involved in the charging and discharging. Generally speaking, there are two types of mechanisms that have been proposed for Ru(IV) oxide. The first one involves

the three redox couples/reactions shown in Eq. 1.7-1.9 [Ru(VI)/Ru(IV), Ru(IV)/Ru(III), and Ru(III)/Ru(II)].[2] Ruthenium with a valence state of VI is gradually reduced to lower valence states during discharging, while protons react with oxygen anions to form hydroxide anions (Eq. 1.10) for charge balance. The reverse of these processes occurs during charging.

$$Ru^{6+} + 2e^- \rightarrow Ru^{4+} \qquad \text{Eq. 1.7}$$

$$Ru^{4+} + e^- \rightarrow Ru^{3+} \qquad \text{Eq. 1.8}$$

$$Ru^{3+} + e^- \rightarrow Ru^{2+} \qquad \text{Eq. 1.9}$$

and

$$O^{2-} + H^+ \rightarrow OH^- \qquad \text{Eq. 1.10}$$

Zheng *et al.* [12] proposed a fast proton insertion mechanism. The reactions during charging and discharging can be expressed as follows (equation 1.11):

$$RuO_2 + nH^+ + ne^- \leftrightarrow RuO_{2-n}(OH)_n,\ 0 \le n \le 2 \qquad \text{Eq. 1.11}$$

Fig. 1.3 shows a typical cyclic voltammogram of a hydrous Ru oxide electrode. It can be seen that the voltammogram is very broad, which indicates that various redox couples are involved in the charging/discharging processes. For the charging process, protons are extracted from the bulk hydrous Ru oxide. In contrast, protons insert into the bulk Ru oxide during the discharging process. The charging and discharging curves are almost mirror images, which indicate that these processes are fast and reversible.

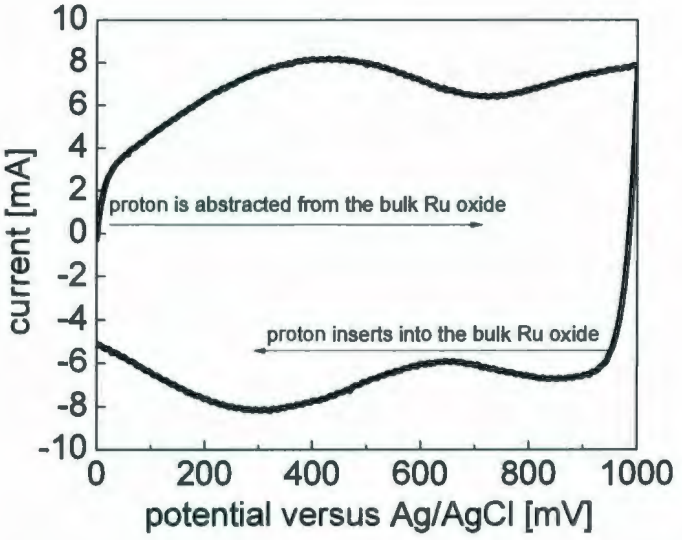

Fig. 1.3 Cyclic voltammogram at 20 mV/s for a hydrous Ru oxide electrode with a 0.89 mg/cm^2 loading in 1 M H_2SO_4.

1.5.3 Ru oxide composites

Applications of Ru oxide supercapacitors are limited to a few narrow fields due to the high price of Ru and the limited global resource. The combination of Ru oxide with carbons provides the characteristics of both double layer capacitors and pseudocapacitors, and can improve the utilization of Ru, thus decreasing the cost of Ru-based supercapacitors.

In recent years, there have been many publications on Ru oxide/carbon composites, including Ru oxide/activated carbon,[22-26] Ru oxide/carbon nanotube,[27-33] and Ru oxide/carbon nanofiber composites.[34, 35] Zhang *et al.*[22] reported that the specific capacitance of the Ru oxide component of a Ru oxide/activated carbon composite (with 10-20% Ru) electrode was over 1450 F/g, which is double the value for pure Ru oxide

(760 F/g). Ru oxide/carbon nanotube film composites also showed high specific capacitances (1170 F/g based on Ru oxide) and speed capacitances.[29] For Ru oxide/carbon nanofibre composites, the specific capacitance based on the Ru oxide component was 1017 F/g.[35] Although high specific capacitances have been obtained for Ru oxide/carbon composites, there are still issues that need further investigation, such as the mechanism for the improved utilization of Ru, why specific capacitances decrease with increasing loading, and the stability of composites.

Generally, Ru oxide/metal oxide composites have higher densities than Ru oxide/carbon based composites, and so can provide higher gravimetric and volumetric capacitances. Additive metal oxides, including vanadium oxide,[36, 37] tin oxide[21, 38-40] and tungsten oxide,[41] not only provide extra pseudocapacitance, but also function as dispersing agents for improving the surface area of the Ru oxide, resulting in its high utilization. Yokoshima *et al.*[37] synthesized nanoparticulate rutile-type $Ru_{1-x}V_xO_2$ by a polymerizable-complex method, obtaining a specific capacitance of 1210 F/g based on the Ru oxide when x was 0.9. Kou *et al.*[40] synthesized Ru oxide/SnO_2 composites by a cyclic voltammetric method, and obtained a specific capacitance of 930 F/g for the Ru oxide.

1.5.4 Mn oxide

Mn oxide has received extensive attention as a supercapacitor material due to its high gravimetric capacitance (see Table 1.1), low price, and high availability.[42-52] However, Mn oxide has low electron conductivity, so Mn-based materials with high

performances are normally Mn oxide/carbon composites due to the introduction of carbon with high conductivity. Lee *et al.* [45] synthesized a MnO_x/CNT/Ni nanocomposite by an anodic deposition method, and its specific capacitance (based on Mn oxide) was 415 F/g and 388 F/g at 5 mV/s and 100 mV/s, respectively. Furthermore, the specific capacitance based on the MnO_2 component of a Mn oxide/C composite increased to 458 F/g, and the composite exhibited very high stability (over 10,000 cycles) and reversibility.[52] Fischer et al. [53] synthesized birnessite ribbons and amorphous Mn oxide/carbon nanofoam composites by a self-limiting reaction between permanganate and carbon nanofoams. The specific capacitances for the Mn oxide components of these composites reached 170 F/g - 230 F/g. However, a symmetric MnO_2 supercapacitor showed low performance. It was reported that the negative electrode may suffer irreversible reactions, resulting in dissolution of the electrode (see section 1.7).[54] The reactions thought to be involved are as follows (see Eq. 1.12-1.13):

$$Mn^{4+} + 2e^- \rightarrow Mn^{2+} \qquad \text{Eq. 1.12}$$

$$MnO_a(OH)_b + nH^+ + ne^- \leftrightarrow MnO_{a-n}(OH)_{b+n} \qquad \text{Eq. 1.13}$$

A hybrid combination of Mn oxide (the positive electrode) and activated carbon (the negative electrode) can improve the operational voltage up to 2.2 V in aqueous media. The best energy density of a hybrid supercapacitor reached 12.6 W h/kg, which is close to the values for carbon supercapacitors with organic electrolytes.[54]

1.6 Ru and its oxides [55, 56]

Ruthenium is in group VIII of the 2nd transition series of the periodic table. The configuration of the outer electron subshells is $4d^7 5s^1$ with four unpaired electrons. This allows ruthenium to form various compounds with oxidation states from 0 to VIII, although the characteristic oxidation states are II, III, IV, VI, VII and VIII.[55]

Ruthenium oxides other than RuO_2 and RuO_4 do not have definite compositions and have not been widely investigated.[56] RuO_4 is a strong oxidizing agent with high volatility and high toxicity, and can be formed upon ignition of Ru metal in oxygen and in the air (see Eq. 1.14). RuO_2 is a stable oxide with the rutile structure (Ru-O 1.942 Å and Ru-O 1.984 Å), and is a metallic oxide with a resistivity of ca. 10^{-5} Ω·m at room temperature.[57] RuO_2 can be prepared by the disproportionation of Ru-oxy compounds with high oxidation states (see Eq. 1.15) and the precipitation of Ru(IV) with base (see Eq. 1.16). Fresh RuO_2 is readily soluble in hydrochloric acid, but difficult to dissolve in sulfuric and nitric acids. However, annealed RuO_2 cannot be dissolved in acids.[56]

$$Ru + 2O_2 \leftrightarrow RuO_4 \qquad \text{Eq. 1.14}$$

$$2H_2O + 3RuO_4^{2-} \rightarrow 2\ RuO_4^- + RuO_2 + 4OH^- \qquad \text{Eq. 1.15}$$

$$Ru^{4+} + 4OH^- \rightarrow RuO_2 + 2H_2O \qquad \text{Eq. 1.16}$$

The oxide Ru_2O_5 may possibly exist in the vapor phase between 1200 °C and 1500 °C, but is actually a mixture of Ru(IV) and Ru(VI).[56, 57] The existences of RuO, Ru_2O_3, Ru_5O_6, and Ru_4O_9 have not been proved. Recently RuO_3 has been prepared as a brown solid by photolysis (see Eq. 1.17).[58]

$$RuO_4 \xrightarrow[370-440\ nm]{} RuO_3 \qquad \text{Eq. 1.17}$$

1.7 Manganese and its oxides [59, 60]

Manganese is located in the 4th period of the periodic table. The configuration of the outer electrons is $4d^5 5s^2$ with five unpaired electrons.[59, 60] The outer electrons may be partly or completely lost, so the possible oxidation states are from 0 to VII.

There are a few manganese oxides. Mn_2O_7 is a very strong oxidizing agent and can be prepared by the reaction between $KMnO_4$ and concentrated sulfuric acid (see Eq. 1.18). It readily decomposes to MnO_2 and oxygen (see Eq. 1.19)

$$2KMnO_4 + 2H_2SO_4 \rightarrow Mn_2O_7 + 2KHSO_4 + H_2O \qquad \text{Eq. 1.18}$$

$$2Mn_2O_7 \rightarrow 4MnO_2 + 3O_2 \qquad \text{Eq. 1.19}$$

Mn(IV) oxide is a dark-brown solid. It does not dissolve in water or dilute acids, however, it dissolves slowly in base to form Mn(IV) compounds. MnO_2 can be prepared by strong heating of $Mn(NO_3)_2$ as shown in Eq. 1.20. MnO_2 can also be prepared by the reaction of Mn(VII) and organic compounds in base. The standard potential of the half reaction for Mn(VII)/Mn(IV) is 0.59 V (see Eq. 21).

$$Mn(NO_3)_2 \rightarrow MnO_2 + 2\ NO_2 \qquad \text{Eq. 1.20}$$

$$MnO_4^-(aq) + 2H_2O + 3e^- \rightarrow MnO_2(s) + 4OH^-(aq) \quad E^\circ = 0.59\ V \qquad \text{Eq. 1.21}$$

Hydrous Mn_2O_3 (brown) is prepared by the oxidation of $Mn(OH)_2$ in air (see Eq. 1.22), which gives MnO(OH) after drying (see Eq. 1.23).

When any manganese oxide or hydroxide is heated above 1000 °C, black Mn_3O_4, [manganese(II) dimanganese(III) oxide] is formed.[60]

$$4Mn(OH)_2 + O_2 + 2H_2O \rightarrow 4Mn(OH)_3 \qquad \text{Eq. 1.22}$$

$$Mn(OH)_3 \rightarrow MnO(OH) + H_2O \qquad \text{Eq. 1.23}$$

White hydrous $Mn(OH)_2$ can be obtained by adding base to a Mn^{2+} solution. In alkaline media, hydrous $Mn(OH)_2$ is readily oxidized by air to brown Mn_2O_3 (see Eq. 1.22). MnO can be obtained by heating of $MnCO_3$ (see Eq. 1.24). Eq. 1.25 shows the standard electrode potentials of Mn oxides.

$$MnCO_3 \rightarrow MnO + CO_2 \qquad \text{Eq. 1.24}$$

$$MnO_2 \xrightarrow{-0.1\ V} Mn_2O_3 \xrightarrow{-0.2\ V} Mn(OH)_2 \qquad \text{Eq. 1.25}$$

1.8 Impedance spectroscopy [61]

In electrochemical impedance experiments, a fixed DC-bias potential with a small sinusoidal oscillation is imposed on an electrochemical system and the resulting sinusoidal current response is analyzed and recorded by a frequency response analyzer and a computer.[61] The complex impedance (Z), which is frequency-dependent, consists of the real impedance (Z_{re}) and the imaginary impedance (Z_{im}) as shown in Eq. 1.26-1.29. j is the imaginary number ($\sqrt{-1}$) that indicates an anticlockwise rotation by $\pi/2$ relative to Z_{re} (see Eq. 1.30). θ is the phase difference between the voltage and current, and depends on Z_{re} and Z_{im} (see Eq. 1.31). When θ is zero, Z is equal to Z_{re}, indicating purely resistive behavior.

$$Z = Z_{re} + jZ_{im} \qquad \text{Eq. 1.26}$$

$$|Z| = [(Z_{re})^2 + (Z_{im})^2]^{1/2} \qquad \text{Eq. 1.27}$$

$$Z_{re} = |Z|\cos(\theta) \qquad \text{Eq. 1.28}$$

$$Z_{im} = |Z|\sin(\theta) \qquad \text{Eq. 1.29}$$

$$j \equiv \sqrt{-1} \equiv \exp(j\pi/2) \qquad \text{Eq. 1.30}$$

$$\theta = \tan^{-1}(Z_{im}/Z_{re}) \qquad \text{Eq. 1.31}$$

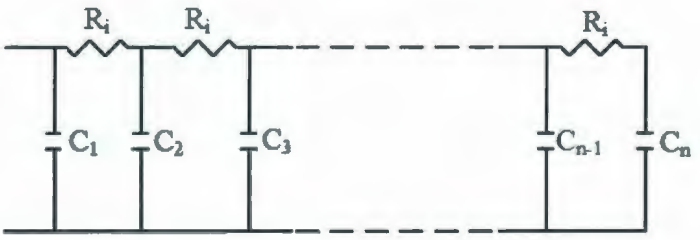

Fig. 1.4 A circuit for a transmission-line model of a porous electrode.

A Nyquist plot is a plot of Z_{im} as a function of Z_{re}. The impedance behavior of a porous electrode can be analyzed by using a transmission-line model circuit (see Fig. 1.4), which consists of parallel capacitances (C_1, C_2, C_3, … C_n) connected with pore-resistance elements (R_i). The impedance spectroscopy of the ladder circuit for a transmission-line model (see Fig. 1.4) exhibits a linear relationship between Z_{re} and Z_{im} with a -45° angle at high frequencies, which is the characteristic for a porous electrode. Fig. 1.5 shows a Nyquist plot for a porous Ru oxide supercapacitor. At relatively high frequencies, a ca. linear region with a near 45° slope is observed. This is characteristic of the transmission-line behavior of the porous Ru oxide electrodes. The Z_{re} at the highest frequency corresponds to the equivalent series resistance (ESR) of the supercapacitor. At lower frequencies, the Nyquist plot is close to a vertical (ideal) line, indicating pure capacitative behavior. Extrapolating the vertical section of the plot in Fig. 1.5 gives an intercept equal to ESR + $R_i/3$, where R_i represents ionic resistance of the porous electrodes.

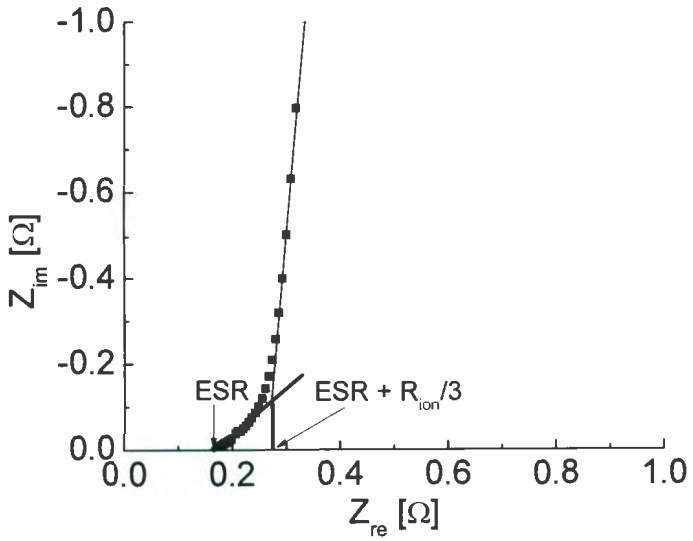

Fig. 1.5 Nyquist plot of a Ru oxide supercacitor with 10.72 mg (5.36 mg + 5.36 mg) Ru oxide and a NRE211 separator.

1.9 Objectives and outline of this thesis

1.9.1 Objectives

Based on literature work, ruthenium oxide-based composite materials for supercapacitors were selected for investigation. The following research objectives were set:

(1) Synthesis of hydrous Ru oxides and characterization of their properties by electrochemical methods and other instrumental techniques. Performances comparable with literature results were targeted and optimized;

(2) Synthesis and characterization of carbon-based Ru oxide composites to improve the utilization of Ru oxide;

(3) Synthesis and characterization of nanostructured Ru oxide/carbon nanotube composites to further improve the utilization of Ru oxide;

(4) Synthesis and characterization of thin film Ru oxide/carbon fabric (CF), thin film Mn oxide/CF, and binary Mn-Ru oxide /CF composites.

In order to meet these targets, a series of methods were used for synthesizing these electrode materials, including sol-gel, physical mixing, and spontaneous reduction methods. The properties of these materials were characterized by scanning electron microscopy (SEM), transmission electron microscopy (TEM), X-ray diffraction (XRD) and themogravimetric analysis (TGA) techniques. Their electrochemical properties were characterized by cyclic voltammetry, constant current discharging, and impedance spectroscopy.

1.9.2 Outline of this thesis

This thesis consists of 8 chapters. A brief outline for each chapter is as follows.

Chapter 1 introduces the background, mechanisms, definitions and equations of supercapacitors, and reviews materials for supercapacitors.

Chapter 2 mainly focuses on Ru oxide supercapacitors. Hydrous Ru oxide was synthesized by a modified sol-gel method, then annealed at various temperatures, and the effects of annealing temperature on capacitive behavior were investigated. Symmetric Ru oxide supercapacitors were constructed to model a real supercapacitor. Electrode preparation techniques, separator and loading effects on specific capacitance, low

temperature performance, long-term stability and self-discharge rate have been investigated in detail.

Chapter 3 covers Ru oxide/CF composites prepared by physical mixing. Hydrous Ru oxide powder was dispersed by sonication, then absorbed into carbon fabric to obtain the desired loadings. Capacitive properties of composites were characterized by potentiostatic and galvanostatic methods, and a synergic effect between Ru oxide and surface functional groups on the CF surface was discovered.

Chapter 4 describes Ru oxide/multiwall carbon nanotube (MWCNT) composites. These composite were prepared by a spontaneous reduction method using the reactions of Ru(VI or VII) compounds with functional groups on the MWCNT surface. Textures of composites were characterized by SEM and TEM. Electrochemical properties were characterized by cyclic voltammetry, constant current discharging and impedance spectroscopy.

Chapter 5 discusses thin film metal oxide/CF composites. Ru oxide/CF, Mn oxide/CF and binary Mn-Ru oxide/CF composites were synthesized by the spontaneous reduction method. Their textures were characterized by SEM. Their electrochemical properties were characterized by potentiostatic and galvanostatic methods.

Chapter 6 is about asymmetric supercapacitors, including thin film metal oxide/CF//CF, Ru oxide/anthraquinone-modified CF, Ru oxide//Pd/carbon supercapacitors. The properties of the supercapacitors were characterized by potentiostatic and galvanostatic methods.

Chapter 7 introduces a new method for evaluating supercapacitors. A novel method for predicting the energy density and power density of a supercapacitor by using impedance spectroscopy was developed.

Chapter 8 summarizes the whole thesis.

References

1. Winter, M.; Brodd, R. J., *Chemical Reviews* **2004,** *104* (10), 4245-4269.

2. Conway, B. E., *Electrochemical supercapacitors: scientific fundamentals and technological applications*. Plenum Press: New York, 1999.

3. Pandolfo, A. G.; Hollenkamp, A. F., *Journal of Power Sources* **2006,** *157* (1), 11-27.

4. Bard, A. J.; Faulkner, L. R., *Electrochemical methods : fundamentals and applications*. 2nd ed.; Wiley: New York, 2001; p xxi, 833 p.

5. Gualous, H.; Bouquain, D.; Berthon, A.; Kauffmann, J. M., *Journal of Power Sources* **2003,** *123* (1), 86-93.

6. Chmiola, J.; Yushin, G.; Gogotsi, Y.; Portet, C.; Simon, P.; Taberna, P. L., *Science* **2006,** *313* (5794), 1760-1763.

7. Burke, A., *Journal of Power Sources* **2000,** *91* (1), 37-50.

8. Huggins, R. A., *Solid State Ionics* **2000,** *134* (1-2), 179-195.

9. Niu, J. J.; Pell, W. G.; Conway, B. E., *Journal of Power Sources* **2006,** *156* (2), 725-740.

10. Algharaibeh, Z.; Liu, X. R.; Pickup, P. G., *Journal of Power Sources* **2009,** *187* (2), 640-643.

11. Kalinathan, K.; DesRoches, D. P.; Liu, X. R.; Pickup, P. G., *Journal of Power Sources* **2008,** *181* (1), 182-185.

12. Zheng, J. P.; Jow, T. R., *Journal of the Electrochemical Society* **1995,** *142* (1), L6-L8.

13. Jow, T. R.; Zheng, J. P., *Journal of the Electrochemical Society* **1998,** *145* (1), 49-52.

14. Zheng, J. P.; Cygan, P. J.; Jow, T. R., *Journal of the Electrochemical Society* **1995,** *142* (8), 2699-2703.

15. Trasatti, S.; Buzzanca, G., *Journal of Electroanalytical Chemistry* **1971,** *29* (2), A1-A5.

16. Jang, J. H.; Machida, K.; Kim, Y.; Naoi, K., *Electrochimica Acta* **2006,** *52* (4), 1733-1741.

17. Hu, C. C.; Chang, K. H., *Journal of Power Sources* **2002,** *112* (2), 401-409.

18. Hu, C. C.; Chang, K. H., *Electrochimica Acta* **2000,** *45* (17), 2685-2696.

19. Hu, C. C.; Chen, W. C.; Chang, K. H., *Journal of the Electrochemical Society* **2004,** *151* (2), A281-A290.

20. Chang, K. H.; Hu, C. C.; Chou, C. Y., *Chemistry of Materials* **2007,** *19* (8), 2112-2119.

21. Hu, C. C.; Chang, K. H.; Wang, C. C., *Electrochimica Acta* **2007,** *52* (13), 4411-4418.

22. Zhang, J. R.; Jiang, D. C.; Chen, B.; Zhu, J. J.; Jiang, L. P.; Fang, H. Q., *Journal of the Electrochemical Society* **2001,** *148* (12), A1362-A1367.

23. Zhang, J. R.; Chen, B.; Li, W. K.; Zhu, J. J.; Jiang, L. P., *International Journal of Modern Physics B* **2002,** *16* (28-29), 4479-4483.

24. He, X. J.; Geng, Y. J.; Oke, S.; Higashi, K.; Yamamoto, M.; Takikawa, H., *Synthetic Metals* **2009,** *159* (1-2), 7-12.

25. Su, Y. F.; Wu, F.; Bao, L. Y.; Yang, Z. H., *New Carbon Materials* **2007,** *22* (1), 53-58.

26. Wang, C. C.; Hu, C. C., *Materials Chemistry and Physics* **2004,** *83* (2-3), 289-297.

27. Cui, G. L.; Zhou, X. H.; Zhi, L. J.; Thomas, A.; Mullen, K., *New Carbon Materials* **2007,** *22* (4), 302-306.

28. Arabale, G.; Wagh, D.; Kulkarni, M.; Mulla, I. S.; Vernekar, S. P.; Vijayamohanan, K.; Rao, A. M., *Chemical Physics Letters* **2003,** *376* (1-2), 207-213.

29. Kim, I. H.; Kim, J. H.; Kim, K. B., *Electrochemical and Solid State Letters* **2005,** *8* (7), A369-A372.

30. Kim, J. D.; Kang, B. S.; Noh, T. W.; Yoon, J. G.; Baik, S. I.; Kim, Y. W., *Journal of the Electrochemical Society* **2005,** *152* (2), D23-D25.

31. Wang, X. F.; Ruan, D. B.; You, Z., *Chinese Journal of Chemical Physics* **2006,** *19* (6), 499-505.

32. Yan, S. C.; Qu, P.; Wang, H. T.; Tian, T.; Xiao, Z. D., *Materials Research Bulletin* **2008,** *43* (10), 2818-2824.

33. Yan, S. C.; Wang, H. T.; Qu, P.; Zhang, Y.; Xiao, Z. D., *Synthetic Metals* **2009,** *159* (1-2), 158-161.

34. Pico, F.; Ibanez, J.; Lillo-Rodenas, M. A.; Linares-Solano, A.; Rojas, R. M.; Amarilla, J. M.; Rojo, J. M., *Journal of Power Sources* **2008,** *176* (1), 417-425.

35. Lee, B. J.; Sivakkumar, S. R.; Ko, J. M.; Kim, J. H.; Jo, S. M.; Kim, D. Y., *Journal of Power Sources* **2007,** *168* (2), 546-552.

36. Takasu, Y.; Nakamura, T.; Ohkawauchi, H.; Murakami, Y., *Journal of the Electrochemical Society* **1997,** *144* (8), 2601-2606.

37. Yokoshima, K.; Shibutani, T.; Hirota, M.; Sugimoto, W.; Murakami, Y.; Takasu, Y., *Journal of Power Sources* **2006,** *160* (2), 1480-1486.

38. Yuan, C. Z.; Dou, H.; Gao, B.; Su, L. H.; Zhang, X. G., *Journal of Solid State Electrochemistry* **2008,** *12* (12), 1645-1652.

39. Wu, N. L.; Kuo, S. L.; Lee, M. H., *Journal of Power Sources* **2002,** *104* (1), 62-65.

40. Kuo, S. L.; Wu, N. L., *Electrochemical and Solid State Letters* **2003,** *6* (5), A85-A87.

41. Jeong, Y. U.; Manthiram, A., *Journal of the Electrochemical Society* **2001,** *148* (3), A189-A193.

42. Subramanian, V.; Zhu, H. W.; Vajtai, R.; Ajayan, P. M.; Wei, B. Q., *Journal of Physical Chemistry B* **2005,** *109* (43), 20207-20214.

43. Subramanian, V.; Zhu, H. W.; Wei, B. Q., *Journal of Power Sources* **2006,** *159* (1), 361-364.

44. Chang, J. K.; Tsai, W. T., *Journal of the Electrochemical Society* **2003,** *150* (10), A1333-A1338.

45. Lee, C. Y.; Tsai, H. M.; Chuang, H. J.; Li, S. Y.; Lin, P.; Tseng, T. Y., *Journal of the Electrochemical Society* **2005,** *152* (4), A716-A720.

46. Prasad, K. R.; Miura, N., *Electrochemistry Communications* **2004,** *6* (10), 1004-1008.

47. Chang, J. K.; Lin, C. T.; Tsai, W. T., *Electrochemistry Communications* **2004,** *6* (7), 666-671.

48. Raymundo-Pinero, E.; Khomenko, V.; Frackowiak, E.; Beguin, F., *Journal of the Electrochemical Society* **2005,** *152* (1), A229-A235.

49. Wang, G. X.; Zhang, B. L.; Yu, Z. L.; Qu, M. Z., *Solid State Ionics* **2005,** *176* (11-12), 1169-1174.

50. Subramanian, V.; Zhu, H. W.; Wei, B. Q., *Electrochemistry Communications* **2006,** *8* (5), 827-832.

51. Long, J. W.; Young, A. L.; Rolison, D. R., *Journal of the Electrochemical Society* **2003,** *150* (9), A1161-A1165.

52. Sharma, R. K.; Oh, H. S.; Shul, Y. G.; Kim, H., *Journal of Power Sources* **2007,** *173* (2), 1024-1028.

53. Fischer, A. E.; Pettigrew, K. A.; Rolison, D. R.; Stroud, R. M.; Long, J. W., *Nano Letters* **2007,** *7* (2), 281-286.

54. Barsukov, I. V.; North Atlantic Treaty Organization., *New carbon based materials for electrochemical energy storage systems: batteries, supercapacitors and fuel cells*. Springer: Dordrecht, 2006.

55. Ginzburg, S. I., *Analytical chemistry of platinum metals*. Wiley: New York, 1975; p xii, 673 p.

56. Avtokratova, T. i. a. D., *Analytical chemistry of ruthenium*. Ann Arbor-Humphrey Science Publishers: Ann Arbor,, 1969; p ix, 250 p.

57. Seddon, E. A.; Seddon, K. R., *The Chemistry of Ruthenium*. Elsevier: Amsterdam ; New York, 1984.

58. Cotton, S., *Chemistry of precious metals*. 1st ed.; Blackie Academic & Professional: London ; New York, 1997; p xii, 374 p.

59. Chambers, C.; Holliday, A. K., *Modern inorganic chemistry : an intermediate text*. Butterworths: London, 1975; p [10], 458 p.

60. Cotton, F. A.; Wilkinson, G.; Gaus, P. L., *Basic inorganic chemistry*. 3rd ed.; J. Wiley: New York, 1995; p xii, 838 p.

61. Barsoukov, E.; Macdonald, J. R., *Impedance spectroscopy : theory, experiment, and applications*. 2nd ed.; Wiley-Interscience: Hoboken, N.J., 2005; p xvii, 595 p.

Chapter 2 Hydrous ruthenium oxide for supercapacitors

This work has been published in the following journals: (1) Xiaorong Liu and Peter Pickup, (2008) *Ru oxide supercapacitors with high loadings and high power and energy density*, **Journal of Power Sources** 176: 410-416; (2) Xiaorong Liu and Peter Pickup, (2008) *Performance and low temperature behavior of hydrous ruthenium oxide supercapacitors with improved power densities*, **Energy Environ. Sci.** 1: 494-500. The experimental sections have been reproduced from these papers. This text was written in part by Dr. Peter Pickup

2.1 Introduction

In recent years, supercapacitors have received intensive attention due to their long life cycles, high energy efficiency and high power density.[1-10] The principles and categories of supercapacitors are discussed in section 1.4. Double layer capacitors electrostatically store charge at the interfaces between the electrodes and electrolyte, whereas pseudocapacitors store charge by fast Faradaic processes.[1, 11, 12]

Ru oxide has excellent pseudocapacitive behavior due to its high specific capacitance and good proton and electron conductivity. Although it was found that ruthenium oxide can be used as a capacitor material in 1971,[13] a major breakthrough in terms of specific capacitance (760 F/g) was made by Zheng and coworker in 1995 using a simple sol-gel method, which involved a chemical reaction of $RuCl_3$ with NaOH.[14, 15] Since then, many alternative preparation approaches, such as electrodeposition,[16]

oxidative synthesis with H_2O_2,[17] electrophoretic deposition,[18, 19] and cyclic voltammetric deposition,[20] have been investigated. However, the specific capacitance of RuO_2 has not been significantly enhanced by these methods, and high specific capacitances have normally only been obtained at low loadings. For example, Jang *et al.*[19] prepared Ru oxide electrodes by an electrophoretic deposition method, and its specific capacitance reached 734 F/g for an electrode with a loading of 0.19 mg/cm^2, while it sharply decreased with increasing loading. It was reported that the specific capacitances for Ru oxide electrodes decreased from 599 F/g to 350 F/g when their loadings increased from 0.64 mg/cm^2 to 1.7 mg/cm^2.[18,19] This shows that the performances of electrodes significantly depend on the Ru oxide loadings. The decreased performance may be due to poor mechanical stability of electrodes. The problem has been solved in this work by adding Nafion as a proton conducting binder, resulting in a constant specific capacitance of 700 F/g for loadings of Ru oxide up to 51 mg/cm^2.[21, 22]

In order to maintain a high specific capacitance for ruthenium oxide at high electrode loadings, a number of ruthenium oxide composites have been studied. Hu *et al.*[23] claimed that the specific capacitance for the ruthenium oxide component in ruthenium oxide/activated carbon composites reached 1340 F/g. The high specific capacitance was ascribed to the enhancement of the intra- and inter- particle electronic conductivity by the introduction of conductive carbon. Yokoshima *et al.*[24] synthesized binary Ru-V oxides with excellent performance. A specific capacitance of 1210 F/g for the ruthenium oxide component was obtained for a $Ru_{0.35}V_{0.65}O_2$ composite. In addition, Ru oxide/carbon nanotube composites were also found to enhance the utilization of

ruthenium oxide.[25, 26] However, it is not clear whether such high specific capacitances can obtain for electrodes with high loadings.

In this chapter, improvement and optimization of the performances of Ru oxide supercapacitors is documented. The following strategies were used for meeting the set goals. The morphology and structure of ruthenium oxide prepared by a modified sol-gel method was characterized by using scanning electron microscopy (SEM) and X-ray diffraction techniques. The effects of synthesis conditions, annealing temperature, electrode preparation, separator, and operating temperature on the performances of ruthenium oxide supercapacitors were investigated in detail by using cyclic voltammetry, impedance spectroscopy and constant current discharging.

2.2 Experimental

2.2.1 Materials

The following materials were used as purchased: Na_2CO_3 (Merck KGaA), H_2SO_4 (Fisher Scientific), Nafion film (NRE211, 25 μm; N115, 127 μm; and N112, 51 μm; all of them from Ion Power, Inc), 110A1 separator (110 μm, Nippon Sheet Glass Co., Ltd.), Celgard 3400 (25 μ, Celgard), titanium foil (25 μm, Aldrich), $RuCl_3 \cdot xH_2O$ (Precious Metals Online Pty Ltd.), tantalum foil (25 μm, ESPI Metals), carbon fibre paper (CFP; Toray™ Carbon Paper, TGP-H-090), 5% Nafion solution (DuPont).

2.2.2 Preparation of hydrous ruthenium oxide

Hydrous ruthenium oxide powders were prepared by a sol-gel method as described previously.[21, 22] Aqueous 1.5 M Na_2CO_3 was slowly added to an aqueous $RuCl_3$ solution (75 mL; 0.05 M) under stirring using a magnetic bar at either 5 °C or room temperature. Ruthenium oxide sol-gel started to form when the pH was ca. 3. The Ru was completely converted to Ru oxide until the pH was close to 7. The reaction end point was determined by pH indicator paper (Fisher Scientific). This sol-gel was heated to ca. 75 °C by using a hot plate at medium power, and then maintained at that temperature for ca. 5 min. The black precipitate completely or partly deposited on the bottom of the container (200 mL beaker) after a few minutes. The precipitate was collected by filtration (Whatman 4), and washed with copious deionized water until the filtrate had no chloride ion reaction with 0.01 M $AgNO_3$ (aq). Finally, the ruthenium oxide samples were annealed for 3 h at various temperatures in air to determine the best annealing temperature.

2.2.3 Physical characterization

Scanning electron microscopy (SEM) was performed with a FEI Quanta 400 environmental SEM at 25 kV.

X-ray diffraction patterns were obtained with a RIGAKU D/MAX 1400.

TGA of the samples were performed on a TA Instruments Q500 TGA analyzer under a N_2 atmosphere (sample gas, 60 mL/min; balance gas, 40 mL/min). The air trapped in the furnace of the TGA instrument was not removed before starting

experiments, so the actual gas atmosphere for experiments was a mixture of air and N_2. The samples were dried at room temperature for 72 h before measurements.

2.2.4 Preparation of electrodes

The preparation of standard Ru oxide electrodes employed in this work, designated as RuO_2/CFP/Ti is the same as described in our papers. [21, 22] A paste was prepared by mixing ruthenium oxide (2mg - 60 mg), an equal mass of 5% Nafion solution as binder and a few drops of deionized water in an agate mortar using a pestle. Electrodes were prepared by painting this paste onto the surface of CFP discs (or strips used in a conventional cell) with a surface area of ca. 1 cm^2 using a brush or a glass pipette. After electrodes were dried in air, they were dried for a further 10 min at the annealing temperature (for the samples whose annealing temperature was below 110 °C) or 110 °C (for the samples whose annealing temperatures was above 110 °C). Only the mass of Ru oxide was considered for calculating specific capacitance, energy density and power density of electrodes. The combined mass of both electrodes was used for estimating energy density and power density of a device. The specific capacitances of single electrodes are also reported for comparison purposes, as calculated according to Eq. 1.2 in Chapter 1. The ranges indicated are standard deviations for at least five measurements.

Although RuO_2/CFP/Ti provided high performances, the use of the CFP support increases not only the mass but also the cost of a device. In order to circumvent these shortcomings, Ru oxide was directly loaded onto a Ti plate (RuO_2/Ti). In addition, Ru oxide electrodes were also prepared by directly loading Ru oxide onto Ti plates that had

been modified to decrease the contact resistance with the Ru oxide (RuO_2/graphite/Ti and RuO_2/C/Ti). Ti plates were modified with graphite by manually rubbing their surface with a graphite rod. Ti plates were also modified with carbon (C/Ti), which were prepared by vapor deposition (thickness of a few nanometers) under high vacuum (5×10^{-5} torr) using a Denton Vacuum DV-502A. An arc discharge (50 A) between two closely spaced graphite electrodes was used to produce the graphite vapor. For RuO_2/Ta electrodes, Ru oxide was directly coated onto Ta plates.

2.2.5 The assembly of supercapacitors

Fig. 2.1 The assembly for Ru oxide supercapacitors

A piece of Nafion film (N115, N112 or NRE211, see section 2.2.1) or other film separator (Celgard 3400 or 110A1, see section 2.2.1) was first sandwiched between two similar Ru oxide/CFP electrodes or other electrodes (see section 2.2.4). Two polycarbonate blocks with titanium plates (as current collectors) were used as the case of the supercapacitor as shown in Fig. 2.1. The assembly was immersed in a 50 mL beaker with a small amount (ca. 10 mL) of 1 M or 5 M H_2SO_4 electrolyte. Air was not excluded

from the supercapacitor. In order to measure the capacitive behavior of a single electrode, an Ag/AgCl reference electrode was also immersed in the electrolyte.

2.2.6 Electrochemical characterization

The electrochemical properties of ruthenium oxide electrodes were initially characterized by using an EG&G 273A Potentiostat/Galvanostat. Cyclic voltammetry and constant current discharging experiments were conducted in a conventional three-electrode configuration (including a counter electrode (Pt wire), an Ag/AgCl reference electrode and 1 M H_2SO_4 electrolyte).

For electrochemical measurements on supercapacitors (two-electrode configuration), two identical ruthenium oxide electrodes were connected to the working electrode and counter electrode lead of the Potentiostat/Galvanostat separately, while the reference lead was connected to the counter electrode lead. Cyclic voltammetry and constant current discharging experiments were conducted by using the EG&G 273A, Solartron 1286 or Arbin Potentiostat/Galvanostat. For constant current discharging experiments, the supercapacitors were first charged at the operating potential of 1.0 V for 5 min -10 min, then completely discharged to 0 V using different currents.

Impedance spectroscopy measurements were conducted by using the EG&G 273A Potentiostat/Galvanostat, an EG&G 5210 lock-in amplifier and EG&G Powersuite software or a Solartron 1286/1250 combination with a Zplot software. The frequency range was from 10 kHz to 5 mHz or 0.1 mHz (for electrodes with high loadings), with a DC bias potential of 1 V and an amplitude of 10 mV.

For self discharge experiments, one supercapacitor was charge to 1 V for 30 min, then its voltage at open circuit was monitored using an EG&G 273A potentiostat.

2.3 Results and discussion

2.3.1 Scanning electron microscopy

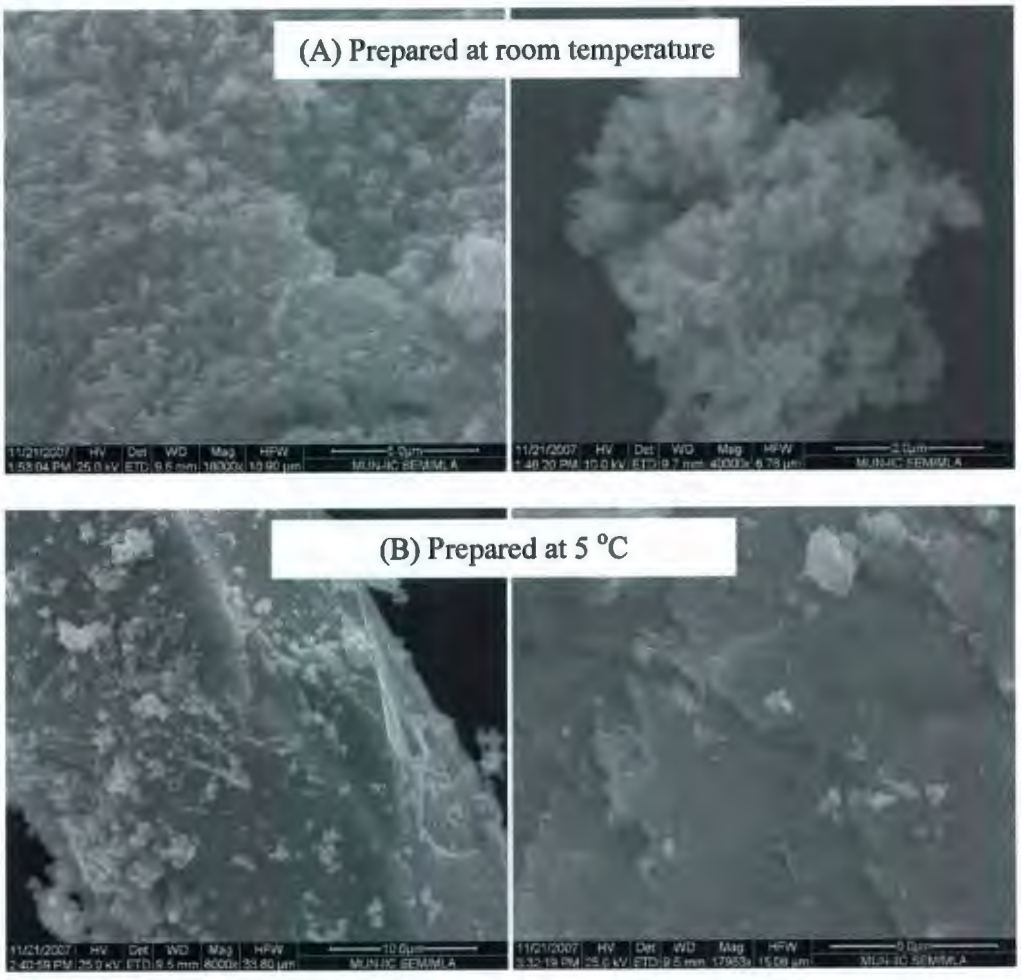

Fig. 2.2 SEM images of Ru oxide prepared at room temperature (A) and at 5 °C (B)

The morphology of ruthenium oxide powders annealed at 110 °C was examined by using SEM. Fig. 2.2(A) shows SEM images for ruthenium oxide prepared at room temperature. It can be seen that the sample exhibited a very porous morphology, consisting of aggregates of very small (ca. 100 nm) particles. In contrast, ruthenium oxide prepared at 5 °C displayed completely different morphology as shown in Fig. 2.2(B). This sample overwhelmingly consisted of very large (10 μm –100 μm) dense chucks with no visible porosity. Small amounts of material with similar morphology to the sample prepared at room temperature appear on the surface of the dense material. The different morphologies were ascribed to the formation and growth rate of crystal particles which depends on the system temperature. At higher temperature, the fast growth of crystal particles leads to a disordered structure, thus forming aggregate particles with abundant porosity.

2.3.2 X-Ray diffraction

The crystalline structures of hydrous Ru oxide annealed at different temperatures were characterized by X-ray diffraction as shown in Fig. 2.3. It can be seen that the as-prepared materials at either room temperature or 5 °C were completely amorphous. Some short range order began to develop at 50 °C, but crystallization did not begin until 200 °C. It is clear that the samples remained in an amorphous state at low annealing temperatures (≤150 °C).

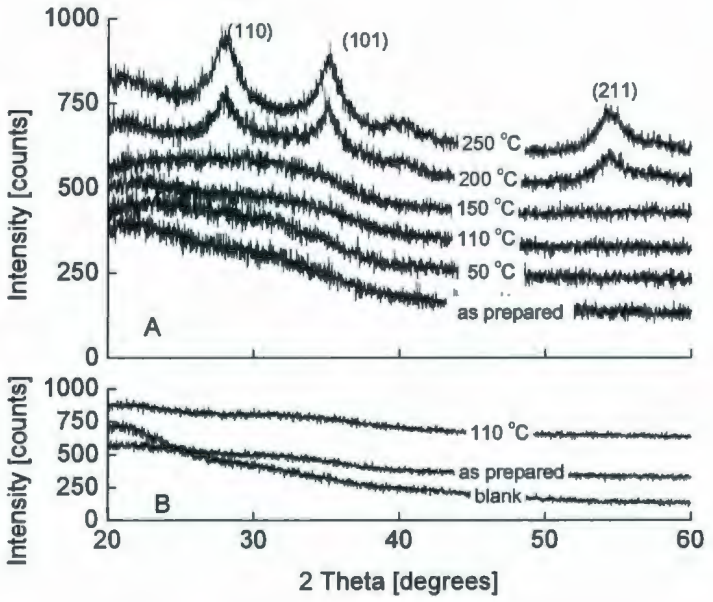

Fig. 2.3 XRD patterns of Ru oxide prepared at room temperature (A) and 5 °C (B). Annealing temperatures are indicated

2.3.3 Thermogravimetric analysis

The thermal dynamic properties of hydrous Ru oxide samples were characterized by TGA as shown in Fig. 2.4. Fig. 2.4(A) is the mass change as a function of temperature. It shows that the sample first gradually lost mass with increasing temperature until ca. 400 °C, and then the mass leveled off at ca. 78% with further increasing temperature. The differential results of mass loss (dm/dt) are plotted as a function of temperature for evaluating the rate of mass change as shown in Fig. 2.4(B). It can be seen that there is a broad peak at ca. 70 °C that can be attributed to the loss of water adsorbed on the surfaces of Ru oxide particles. The slow mass loss observed between 100 °C and 400 °C can be attributed to the slow dehydration process of bulk

hydrous Ru oxide. For the small peak at ca. 280 °C, it is not clear what caused the fast mass loss.

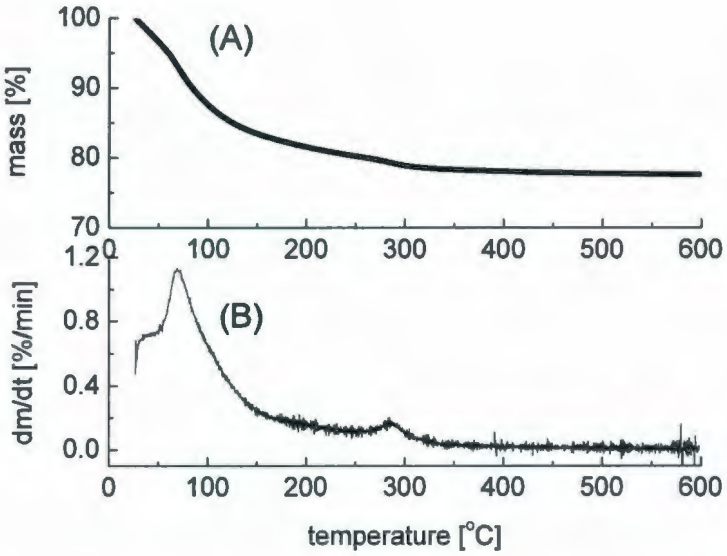

Fig. 2.4 TGA curve for hydrous Ru oxide prepared at room temperature (Initial sample, 6.52 mg; ramp, 5 °C/min to 600 °C)

The hydration number of the Ru oxide can be calculated by using its TGA data as follows. The mass of the sample at 600 °C is assumed to be due to anhydrous Ru oxide (RuO_2), and the mass difference between a specific temperature and 600 °C is attributed to water of hydration. Hydration numbers derived from the TGA data in Fig. 2.4(A) are given in Table 2.1. The hydration numbers were 0.93 and 0.56 for 100 °C and 150 °C, respectively, which are similar to the results reported by Zheng *et al.*[15] On the other hand, the hydration numbers at 200 °C and 250 °C are much higher than that of Zheng *et al.* The difference can presumably be ascribed to the different timescales employed since Zheng *et al.* annealed each sample for 17 h.[15]

Table 2.1 Hydration numbers and specific capacitances for hydrous Ru oxide

T (°C)	25	50	100	110	150	200	250	400	600
$RuO_2 \cdot xH_2O$ (mg)	6.52	6.30	5.71	5.64	5.44	5.32	5.23	5.09	5.06
Loss water (mg)	1.46	1.23	0.65	0.57	0.38	0.26	0.17	0.029	0
x	2.13	1.80	0.95	0.84	0.56	0.37	0.25	0.04	0
x (literature result)[15]	2.00		0.93		0.50	0.20	0.11	0.03	
C_{sp} (F/g)*	360	341	705	716±24	682±31	422	169		
C_{sp} (F/g) **	578	575		768	740	542	284		
C_{sp} (F/g) by CV [15]	527		670	720		144			

* measured by cyclic voltammetry
** measured by constant current discharging

2.3.4 Synthesis methods

Ru oxide samples prepared at room temperature and 5 °C exhibited extraordinarily different morphologies (section 2.3.1). Here, their capacitive behaviors as measured by cyclic voltammetry are presented.

Fig. 2.5 shows a typical cyclic voltammogram in a conventional glass cell for a Ru oxide (prepared at room temperature, and annealed at 110 °C) electrode, where the current response has been converted to specific capacitance according to Eq. 1.3 in Chapter 1. It can be seen from Fig. 2.5 that the voltammograms were featureless, which is the characteristic of capacitive behavior. The average specific capacitance was 597 F/g, 648 F/g and 654 F/g for the 1st, 10th and 25th cycle, respectively. It is clear that the average specific capacitance increased with cycling. This may be ascribed to the

development of electron or proton pathways with cycling. The average specific capacitance for seven electrodes annealed at 110 °C was 716±24 F/g, which is comparable to state-of-the-art results.[14, 15, 19]

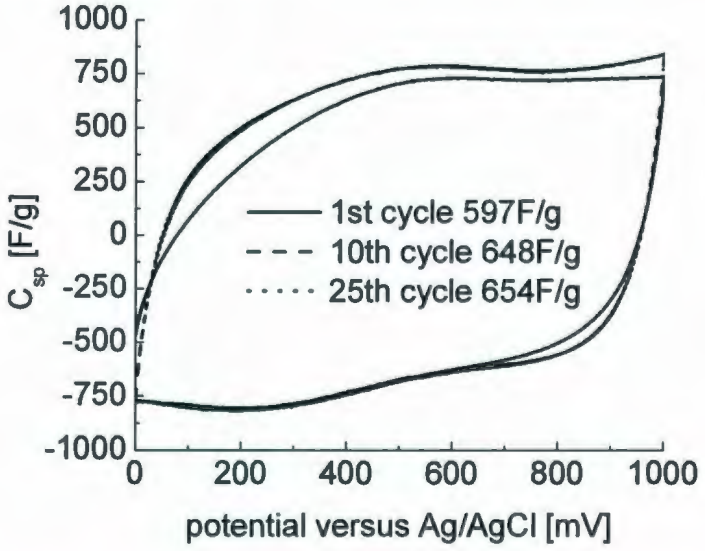

Fig. 2.5 Cyclic voltammograms at 20 mV/s for a Ru oxide electrode in 1 M H_2SO_4. The electrode loading was 1.43 mg/cm^2.

Fig. 2.5 also shows that the electrode possessed good reversibility except for the 1st cycle. The ratio of charging charge to discharging charge was 1.12:1, 0.99:1 and 1.00: 1 for the 1st, 10th and 25th cycle, respectively.

Voltammograms for Ru oxide prepared at 5 °C exhibited completely different shapes as shown in Fig. 2.6. They consisted of one pair of redox peaks, and the peak heights increased with cycling. The average specific capacitance of one sample annealed at 110 °C increased from 38 F/g to 88 F/g after 25 cycles. This can most likely be attributed to structure changes.[1] For example, the dense structure (see section 2.3.1) may convert to a less compact structure due to the repeated proton insertion-expulsion

processes. This would lead to access of the electrolyte to more Ru oxide particles.

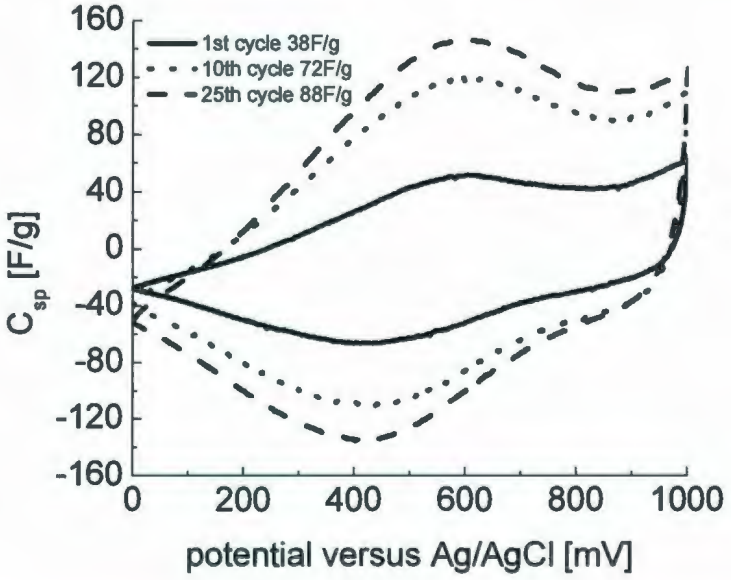

Fig. 2.6 Cyclic voltammograms at 20 mV/s for Ru oxide prepared at 5 °C. The Ru oxide loading was 1.33 mg/cm^2.

The best specific capacitance obtained for Ru oxide prepared at 5 °C was less than 100 F/g, which is much less than for Ru oxide prepared at room temperature (716±24 F/g). The different specific capacitances are believed to be due to the difference in surface morphologies. The high porosity of ruthenium oxide obtained at room temperature allows electrolyte to be accessible during charging and discharging, resulting in a high specific capacitance. In contrast, ruthenium oxide with a compact structure prohibits the full access of electrolyte, thereby leading to low specific capacitance. Overall, room temperature was found to be superior to 5 °C for the preparation of Ru oxide.

Jow *et al.*[27] thought that the charging/discharging efficiency of electrodes

decreased during the first few cycles due to hydrogen insertion and gas evolution, leading to damage of the electrodes. On the contrary, we observed that the specific capacitance for Ru oxide electrodes with either porous or compact structures increased with cycling. This is thought to be due to their structural adjustment for establishing better electron and proton pathways.[21]

2.3.5 Annealing temperature

2.3.5.1 Cyclic voltammetry

Ru oxide electrodes annealed at different temperatures were characterized by cyclic voltammetry in a conventional three-electrode cell as shown in Fig. 2.7. The current responses were converted to specific capacitance according to Eq. 1.3 (section 1.2). It is clear that the shapes of the voltammograms change with annealing temperature. For the as-prepared sample and the sample annealed at 50 °C, two specific capacitance peaks were observed at ca. 0.4 V and 0.9 V versus the Ag/AgCl reference electrode. It is believed that these peaks are due to two distinct redox reactions involved in the charging and discharging processes. However, it is not clear what redox couples are involved these processes. It is most likely that the two redox couples are Ru (IV/III) and Ru (III/II) or Ru (V/IV) couples at 0 V to 1.0 V versus an Ag/AgCl reference electrode.[28-30]

The voltammograms for Ru oxide annealed at 110 °C and 150 °C were completely different from those for samples annealed at low temperature (≤50 °C), since they were almost featureless. Average specific capacitances were 716±24 F/g (seven measurements) and 682±31 F/g (five measurements) for annealing temperatures of 110 °C and 150 °C,

respectively (see Table 2.1).

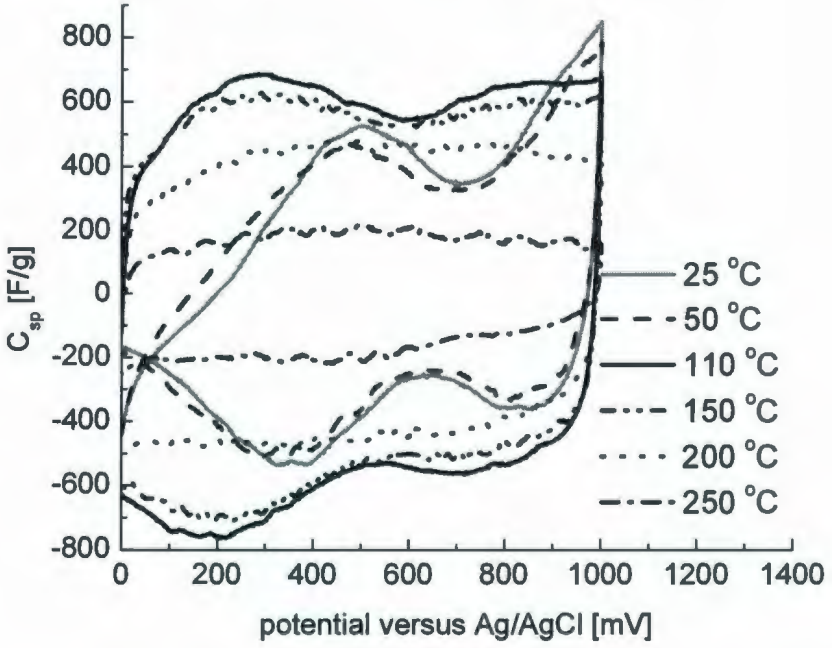

Fig. 2.7 Cyclic voltammograms at 5 mV/s for Ru oxide prepared with different annealing temperatures. The electrode loadings were 2.25, 1.83, 2.28, 2.08, 1.97 and 2.22 mg/cm^2 for Ru oxide annealed at 25, 50, 110, 150, 200 and 250 °C, respectively.

The voltammograms for the samples annealed at high temperatures ($\geq$ 200 °C) exhibit almost perfect rectangular shapes, but it is clear that the specific capacitance sharply decreased with increasing annealing temperature above 150 °C. The average specific capacitances were 422 F/g and 169 F/g for annealing temperatures of 200 °C and 250 °C (see Table 2.1), respectively. These are much lower than those for the samples annealed at either 110 °C or 150 °C. These low values are likely due to the formation of an ordered crystalline structure at high annealing temperatures (see section 2.3.2), resulting in blocking the accessibilty of protons to the bulk Ru oxide.

In summary, the best annealing temperature for hydrous Ru oxide was 110 °C, which is lower than the value of 150 °C reported by Zheng and coworkers.[14, 15] The difference may be due to the use of a different base (Na_2CO_3 vs NaOH), although the sensitivity of the morphology of Ru oxide to the preparation conditions (e.g. compare Fig. 2.1(A) and Fig. 2.1(B)) means that other factors could be involved. Use of NaOH as the precipitating reagent provides only OH^- ions for the deposition process. In contrast, a Na_2CO_3 solution was used as the precipitating reagent in this work, which provides not only OH^- ions but also HCO_3^- and CO_3^{2-}. Therefore the pristine Ru oxide may contain ruthenium carbonate or bicarbonate, resulting in different annealing properties.

2.3.5.2 Constant current discharging

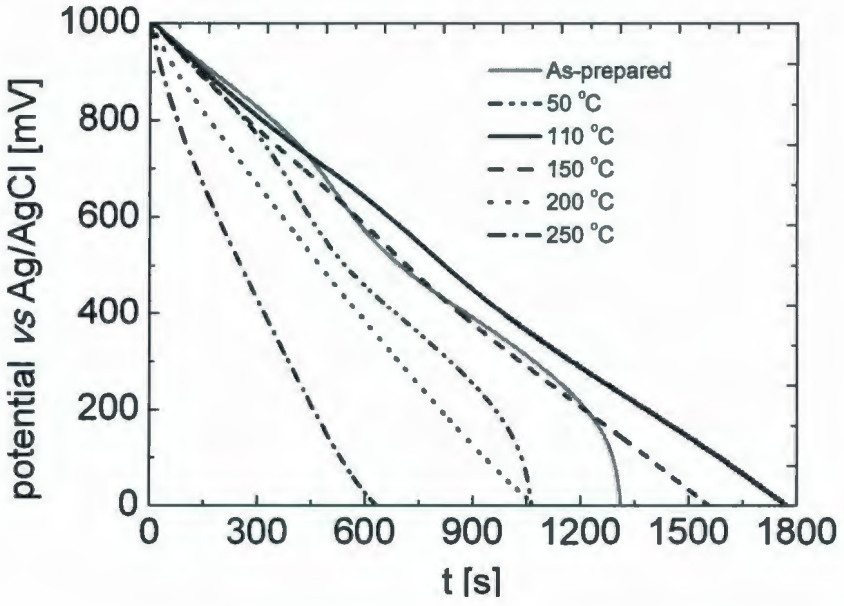

Fig. 2.8 Constant current discharging curves for the Ru oxide electrodes described in Fig. 2.7, with a current density of 1 mA/cm^2

The electrodes described in Fig. 2.7 were also characterized by constant current discharging as shown in Fig. 2.8. It can be seen that the curves for the samples annealed at low temperature (≤ 50 °C) are obviously different from the curves for the samples annealed at high temperature (≥ 110 °C). The latter shows good linear relationships between the voltage and discharge time. Their specific capacitances can be estimated by Eq. 2.1 based on constant current discharging data.

$$C_{sp} = \frac{It}{m\Delta V} \qquad \text{Eq. 2.1}$$

where C_{sp}, I, t, m and ΔV represent specific capacitance, discharge current, discharge time, electrode mass and potential change, respectively.

The specific capacitances of the electrodes measured by cyclic voltammetry and constant current discharging are plotted as a function of annealing temperature in Fig. 2.9, which shows that the specific capacitances from both methods increased with increasing annealing temperature, reached a maximum value at 110 °C, and then decreased. It is clear that the best annealing temperature is 110 °C. In comparison with the results from cyclic voltammetry, the specific capacitances for Ru oxide from constant current discharging were much higher. This difference should be due to the shorter timescale of the cyclic voltammetry. A shorter timescale means less electrode penetration depth during cyclic voltammetry measurements, resulting in lower capacitance.

In order to obtain high specific capacitance, it is very important to optimize the electron and proton conductivity of Ru oxide. It was reported that the low specific capacitances for Ru oxide electrodes annealed at high temperatures can be attributed to the loss of structural water involved in proton transport, resulting in an increase in

ordered RuO_6 octahedra structures which limit the access of protons.[31] However, the low specific capacitances for electrodes annealed at low temperatures are attributed to poor electron conductivity resulting from insufficient formation of Ru dioxo bridges to form a metallic band structure.[31] A great improvement in the specific capacitance for Ru oxide could be achieved if the conductivity of materials annealed at low temperatures could be improved.

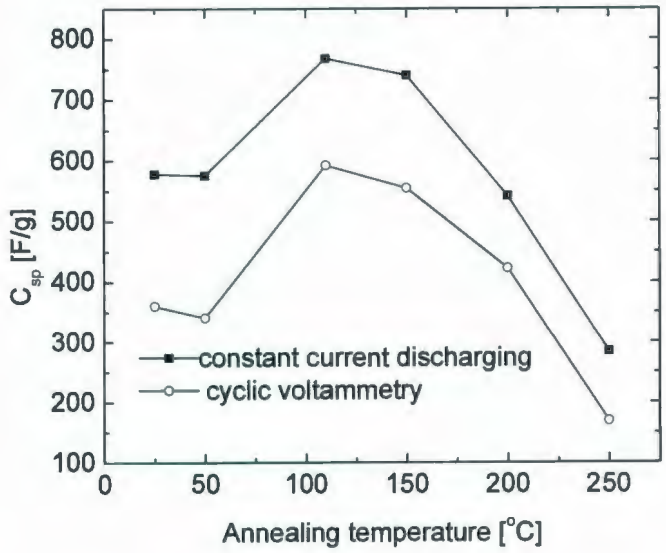

Fig. 2.9 Average specific capacitances of Ru oxide electrodes described in Fig. 2.7 & 2.8 versus annealing temperature.

2.3.6 Operating potential window

The operating potential window of Ru oxide was measured by cyclic voltammetry as shown in Fig. 2.10, which shows that the stable potential window for the Ru oxide electrode covers the range from -0.2 V to 1.2 V versus Ag/AgCl. No hydrogen or oxygen gas evolution was observed during scanning. However, the current responses strongly

depended on the potential of the electrode. The current responses sharply decreased with decreasing potential in the low potential range (< 0.2 V versus Ag/AgCl). Although we can obtain high current responses at 0.2 V to 1.1 V, there is a region with lower current response at ca. 0.7 V. As a consequence, the average specific capacitance (calculated by Eq. 1.1) depends on the potential window. For example, the average specific capacitances were 682 F/g, 753 F/g and 791 F/g for the potential windows of -0.2 V to 1.2 V, 0 V to 1.1 V, and 0.2 V to 1.1 V, respectively.

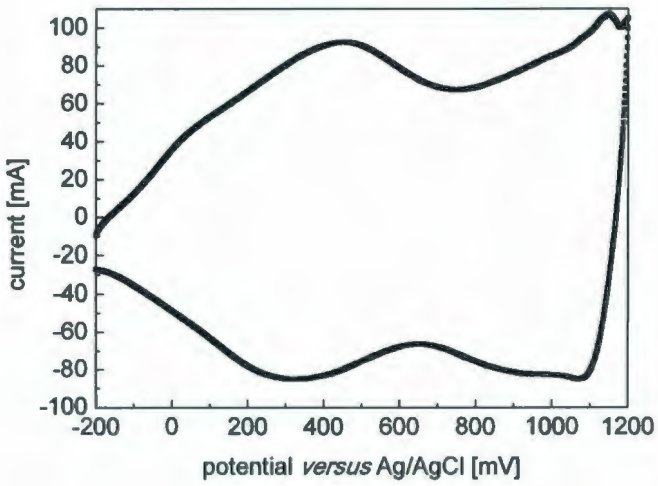

Fig. 2.10 Cyclic voltammogram at 20 mV/s of a Ru oxide electrode in 1 M H_2SO_4. The electrode loading (Ru oxide annealed at 110 °C) was 5.01 mg/cm^2.

Based on the stable potential window of a single electrode, the stable operating voltage for a symmetric device should reach -1.4 V to 1.4 V. Fig. 2.11 shows the cyclic voltammograms of a symmetric supercapacitor at different operating voltage windows. It shows that the device exhibited a stable voltage window of -1.4 to 1.4 V. When its potential limit was beyond 1.4 V, higher currents (at > 1.4 V) due to irreversible reactions

were observed. The ratios of the anodic charge to cathodic charge were 1:0.93, 1:0.83, and 1:0.71 for the potential limit of 1.4 V, 1.5 V and 1.6 V, respectively.

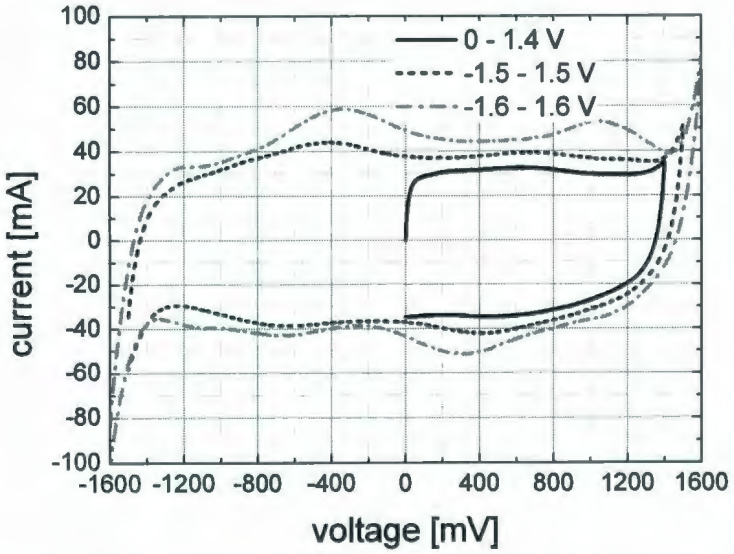

Fig. 2.11 Potential window at 20 mV/s of a symmetric supercapacitor in 1 M H_2SO_4. The supercapacitor consisted of 10.67 mg Ru oxide annealed at 110 °C, with a N112 separator.

Although the stable operation voltage window for a symmetric supercapacitor was up to 1.4 V, the work reported in this chapter was restricted to 1.0 V to avoid the effects of slow irreversible reactions.

2.3.7 Mechanism

The charge-discharge mechanism of Ru oxide electrodes is discussed in Chapter 1. Zheng *et al.* have represented proton insertion and extraction during charging and discharging as shown in Eq. 2.2.[14] The maximum proton transfer number was thought to be 2. Here, the proton transfer number (n) of our Ru oxide annealed at 110 °C was

estimated by Eq. 2.3 and 2.4 [27] based on the data in Fig. 2.10.

$$RuO_2 + nH^+ + ne^- \leftrightarrow RuO_{2-n}(OH)_n \quad 0 \leq n \leq 2 \qquad \text{Eq. 2.2}$$

$$Q(V) = \int_{V_0}^{V} \frac{I}{v} dV \qquad \text{Eq. 2.3}$$

$$n = \frac{\frac{Q(V)}{mF}}{M} \qquad \text{Eq. 2.4}$$

where n, I, v, F, m, M, Q(V), V_o and V are proton number, current response, scan speed during the CV measurements, Faraday's constant (96485 C/mol), electrode mass, molar mass of $RuO_2 \cdot 0.84H_2O$, charge at V, the starting potential of the Ru oxide electrode, and the final potential of the integration, respectively.

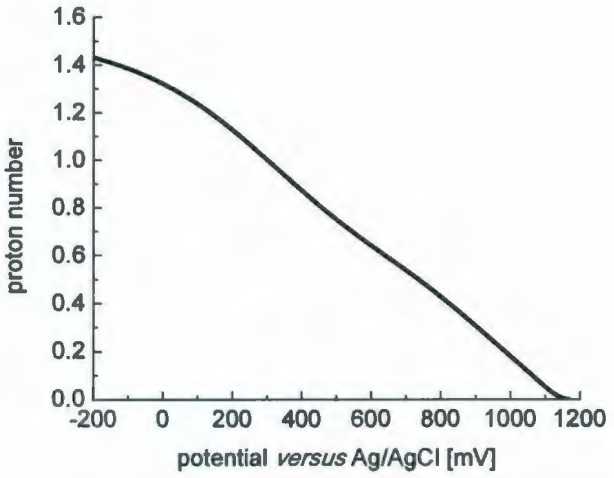

Fig. 2.12 Proton transfer number of Ru oxide from the data in Fig. 2.10

Eq. 2.3 was integrated from 1.168 V to -0.200 V, thus obtaining charge at different potentials. The proton number was calculated by using Eq. 2.4 and the charge derived from Eq. 2.3. The proton transfer number is plotted as a function of electrode potential in Fig. 2.12. It can be seen that the proton transfer number increases

approximately linearly with decreasing potential for the potential window of 0.1 to 1.1 V. The maximum proton transfer number was 1.43 per Ru, which is similar to literature results.[27]

2.3.8 Potential-dependent capacitance

Potential-dependent capacitances of Ru oxide electrodes are reported in section 2.3.5 and 2.3.6, where the discussion focuses on their cyclic voltammetry. Here, the capacitive behaviors of Ru oxide supercapacitors were measured by impedance spectroscopy as shown in Fig. 2.13, which can provide more information than cyclic voltammetry. Series specific capacitances (C_{series}= -1/2πfZ"m, where f, Z" and m are frequency, the imaginary impedance and electrode mass) for a Ru oxide electrode are plotted as a function of potential in Fig. 2.13(A). Fig. 2.13(A) shows that the series specific capacitance decreased approximately linearly with potential (< 0.3 V versus Ag/AgCl), while it leveled off at ca. 700 F/g for the potential window of 0.3 V to 1.1 V. Compared with the results from cyclic voltammetry (see Fig. 2.10), the capacitances were all lower. This may be ascribed to the much lower potential amplitude used in impedance spectroscopy, resulting in less electrode penetration depth

The specific capacitances of a symmetric supercapacitor are plotted as a function of potential in Fig. 2.13(B). Fig. 2.13(B) shows that specific capacitance increased from ca. 150 to 170 F/g with increasing potential from 0.0 V to 0.4 V, was then constant (170 F/g) until 0.8 V, and then quickly decreased to ca. 150 F/g when potential went up to 1.0

V. So the average specific capacitance (for a potential window of 0.0 V to 1.0 V) of a Ru oxide supercapacitor cannot be obtained by only one impedance measurement.

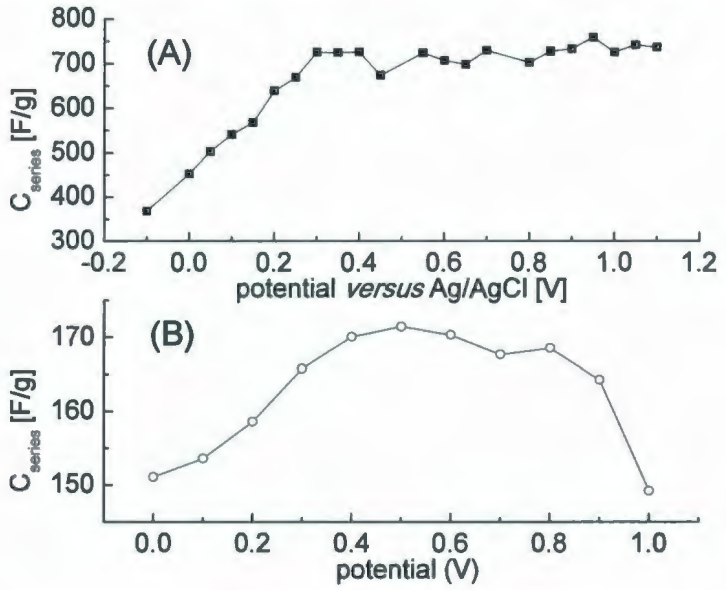

Fig. 2.13 Series specific capacitances of Ru oxide at different potentials measured by impedance spectroscopy at 5 mHz with 10 mV amplitude. (A) Three-electrode configuration, with 5.01 mg Ru oxide, (B) two-electrode configuration, with 10.04 mg Ru oxide.

It is clear that the specific series capacitances in Fig. 2.13(A) are much higher than those in Fig. 2.13(B). The difference is due to the different measurement methods (three-electrode configuration versus two-electrode configuration). For the two-electrode configuration, the capacitance measured for a symmetric device is one quarter of the value obtained in a three-electrode configuration according to Eq. 1.2.

2.3.9 Nafion binder

Ru oxide supercapacitors with Nafion binder were characterized by cyclic voltammetry, impedance spectroscopy, and constant current discharging as shown in Fig.

2.14. The Ru oxide mass in each supercapacitor was kept constant at ca. 10 mg, as specified in the caption in Fig. 2.14.

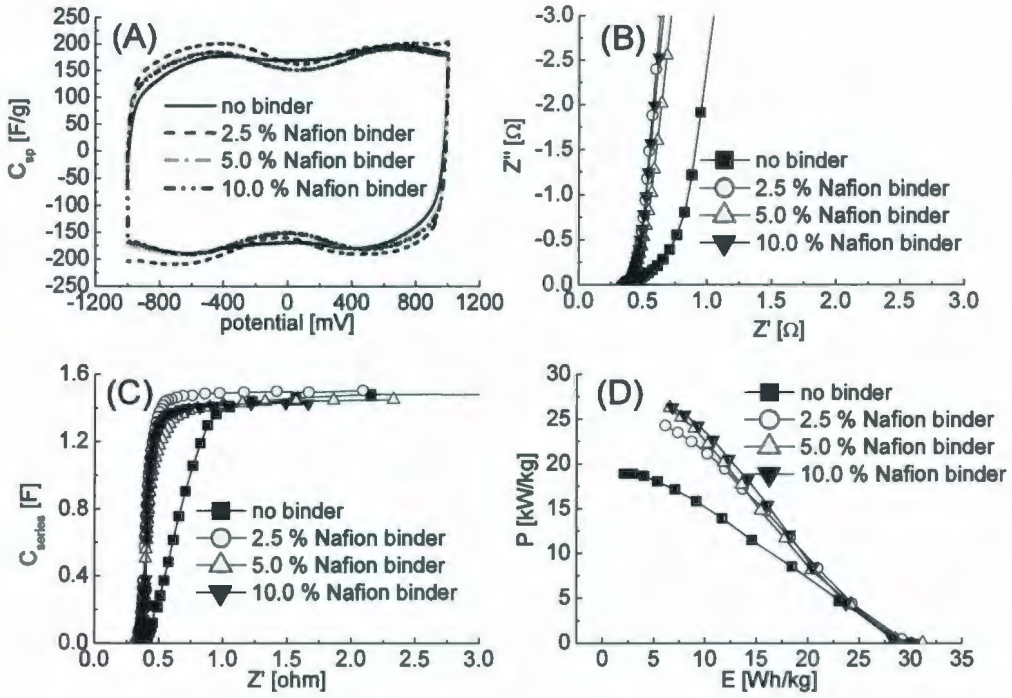

Fig. 2.14 Electrochemical data for Ru oxide supercapacitors with various amounts of Nafion binder, (A) cyclic voltammograms (B) Nyquist plots (C) capacitance plots (D) Ragone plots. The total mass of Ru oxide was 9.51, 10.35, 10.34, 10.14 mg for 0, 2.5%, 5%, and 10% Nafion binder, respectively.

The voltammograms of the Ru oxide supercapacitors (see Fig. 2.14(A)) exhibited similar shapes, even though the electrodes contained various amounts of Nafion binder. All of the supercapacitors showed high-quality capacitive behavior with excellent reversibility. The average specific capacitance for the potential window of -1.0 V to 1.0 V was ca. 167 F/g (based on the mass of the active electrode materials only) for all of the supercapacitors except with a 2.5% Nafion loading, which was 181 F/g. Obviously, the addition of 2.5% Nafion binder abruptly improved the specific capacitance, while no

higher performance was obtained for higher Nafion loadings. However, higher Nafion loadings can enhance the mechanical stability of the electrodes.

Fig. 2.14(B) shows the Nyquist plots of the supercapacitors. All of the plots show a 45 degree region at high frequencies, which is characteristic for a porous electrode.[32] At low frequencies, the curves are close to vertical, indicating purely capacitive behavior. Equivalent series resistances (ESR) were estimated by using the real impedance at the highest frequency (10 kHz), and were ca. 0.33 Ω for all of the supercapacitors. The ionic resistance of the electrodes (R_i) was estimated by using three times the difference between the real impedances at the highest frequency and the characteristic frequency at which the phase angle is minus 45 degree as shown in Eq. 2.5.

$$R_i = 3 \times (Z_{45}' - Z_{hf}') \qquad \text{Eq. 2.5}$$

Where R_i, Z_{45}', and Z_{hf}' represent ionic resistance, the real impedance at -45 degree phase angle, and the real impedance at 10 kHz.

The R_i changed insignificantly with Nafion loading, and was ca. 0.51 Ω for all of the supercapacitors with Nafion binder. However, R_i sharply increased to 1.39 Ω in the absence of binder. It is believed that the low R_i was due to the establishment of good proton conducting pathways within the Ru oxide particles. In addition, the binder also increases the mechanical stability of the electrodes, leading to lower electronic resistance.

Fig. 2.14(C) shows capacitance plots, which illustrate how the series capacitance increases with real impedance until it reaches a limiting capacitance. It is clear that the real impedance (Z') did not change greatly with decreasing frequency for the supercapacitors with Nafion binder before the series capacitance approached its limiting

value. However, Z' drastically increased with decreasing frequency for the supercapacitor without binder. It is believed that the high impedance originated from discontinuous electron conduction between the Ru oxide particles.

Ragone plots of the supercapacitors were constructed by using the results from constant current discharging and are shown in Fig. 2.14(D). It is clear that all of the supercapacitors had similar maximum energy densities (ca. 30 W h/kg) at a discharging current of 1 mA. Among these supercapacitors, the highest energy density was 31.2 W h/kg for the supercapacitor with 5% Nafion. In general, the usable energy densities decreased with increasing discharging current due to their shorter timescales. For example, when the discharging current increased to 1A, the usable energy density decreased to 6.6 W h/kg and 2.1 W h/kg for the supercapacitor with 5% Nafion and the supercapacitor without binder, respectively. However, the average power density increased with discharging current due to the quick delivery of energy. When the discharging current was increased from 0.3 A to 1 A, the power density increased from ca. 11.8 kW/kg to ca. 25.6 kW/kg for the supercapacitors with Nafion. In contrast, the power density increased from 11.5 kW/kg to only 18.9 kW/kg for the supercapacitor without binder. The power density at 1 A was lower by 26.2 % than for the supercapacitors with Nafion binder.

These results show that the addition of Nafion binder sharply improves the performance of Ru oxide supercapacitors. The high performance is ascribed to the formation of proton transfer pathways within the Ru oxide particles. Although 2.5%

Nafion binder can effectively improve performance, 5% Nafion is preferred because of the better mechanical stability that it provides.

2.3.10 Electrode loading

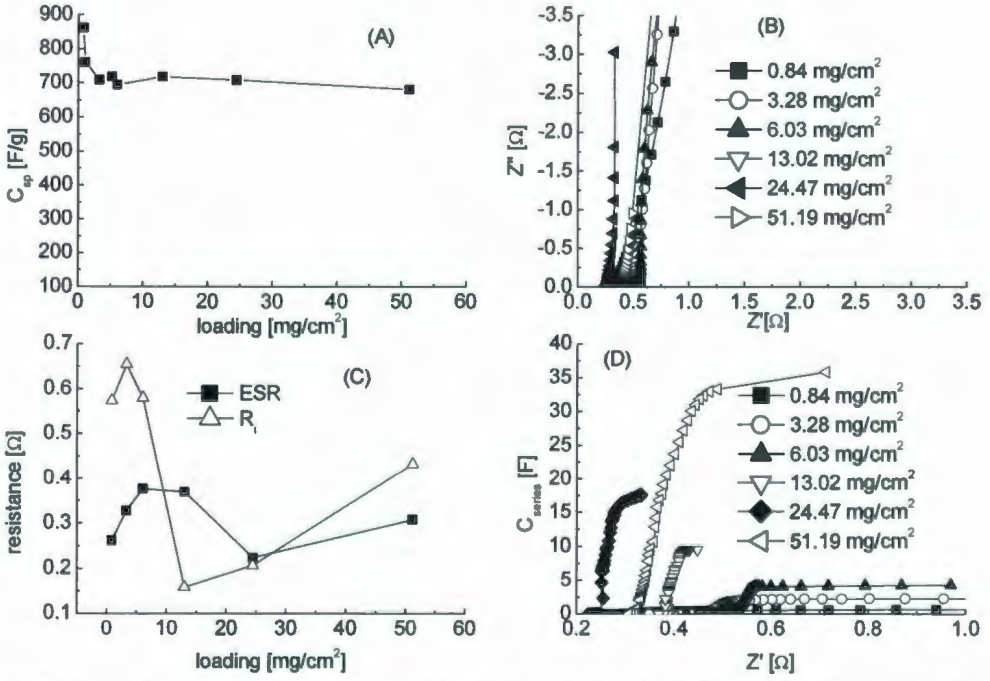

Fig. 2.15 Impedance results for Ru oxide electrodes with different loadings. (A) Specific capacitance versus electrode loadings (B) Nyquist plots (C) ESR and R_i as function of electrode loading (D) capacitance plots. The DC potential was 1 V versus Ag/AgCl, with 10 mV amplitude. The frequency ranged from10 kHz to 5 mHz or 1 mHz.

The effect of electrode loading on the performances of supercapacitors was evaluated by impedance spectroscopy as shown in Fig. 2.15, which shows the relationship between specific capacitance and electrode loading. The Ru oxide electrode with a 0.84 mg/cm^2 loading had a specific capacitance of 860 F/g. However, specific capacitances slightly decreased with increasing loading. For example, the specific capacitance decreased to 760 F/g for a 1.09 mg/cm^2 loading. Interestingly, the specific

capacitances leveled off at ca. 700 F/g for a wide loading range (3.28 mg/cm^2 to 51 mg/cm^2). These are much better than the results reported by Jang *et al.* as shown in Fig. 2.16.[18] Their specific capacitances drastically decreased with increasing electrode loading. The specific capacitance was ca. 700 F/g for 0.19 mg/cm^2, but decreased to ca. 300 F/g for ca. 1 mg/cm^2. Although the addition of PTFE (polytetrafluoroethylene) binder enhanced their specific capacitances, a specific capacitance of only ca. 400 F/g was obtained at 1.7 mg/cm^2.

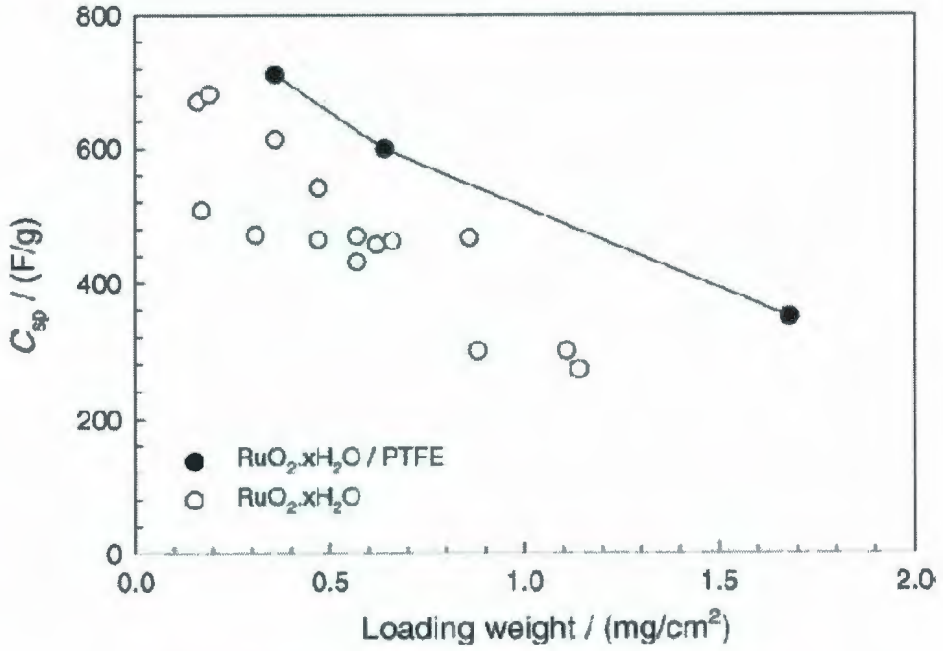

Fig. 2.16 Specific capacitance versus Ru oxide mass

Reprinted from "Electrophoretic deposition (EPD) of hydrous ruthenium oxides with PTFE and their supercapacitor performances", vol 52, J. H. Jang, K. Machida, Y. Kim, K. Naoi, page 1733-1741, Copyright (2006), with permission from Electrochimica Acta.

Fig. 2.15(B) shows Nyquist plots for electrodes with different loadings. There are 45 degree regions at high frequencies, which is the characteristic for a porous electrode, while at low frequencies, the plots are close to vertical.

ESR and R_i values for the electrodes are plotted versus electrode loading in Fig. 2.15(C). It can be seen that the ESR changed with increasing loading. The ESR mainly consists of contact resistances, and the resistances of the electrode materials and electrolyte. For supercapacitors with similar compaction, the ESR will depend on the resistance of the electrode materials (proportional to electrode thickness) and the electrolyte resistance. In this case, the ESR remained constant although the electrodes had different thicknesses. This indicates that the resistance of the Ru oxide materials is negligible due to its high electronic conductivity.

The ionic resistance of the electrodes, R_i, was ca. 0.6 Ω for low loadings ($\leq$ 6.03 mg/cm^2), but decreased with increasing loading to reach a minimum value (0.16 Ω) for 13.02 mg/cm^2, and then increased. It is not clear why R_i follows this complex change with loading. For a uniform porous electrode, R_i should increase linearly with increasing thickness (loading).

Capacitance plots (see Fig. 2.15(D)) show the change in specific capacitance versus Z' with decreasing frequency. It is clear that the electrode with 24.47 mg/cm^2 had the lowest real impedance before reaching the limiting capacitance. This is consistent with the low resistances seen in Fig. 2.15(C) for this electrode.

Although impedance spectroscopy can give very useful information for capacitance, ESR and R_i, it cannot provide performance information due to its limited

potential window (DC potential ± 14.1 mV) for one measurement. In contrast, constant current discharging experiments can provide energy storage capability for the whole operating potential window. Fig. 2.17 shows the discharge curves for supercapacitors with different electrode loadings at 10 mA. A similar discharging curve was obtained for the Ru oxide electrodes with loadings of 0.85 and 5.5 mg/cm^2 due to their similar active electrode masses. The discharge curves were integrated according to Eq. 1.5 described in Chapter 1. Although the electrode loadings ranged from 0.85 mg/cm^2 to 50.0 mg/cm^2, these supercapacitors possessed similar energy densities (ca. 26.5 W h/kg at low current density. This indicates that energy densities at low current density did not depend on electrode loadings.

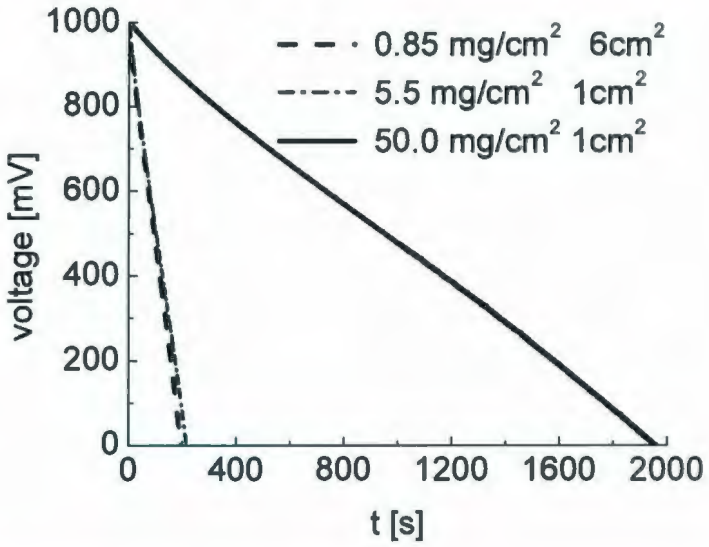

Fig. 2.17 Constant current discharging curves (10 mA) for supercapacitors with different electrode loadings.

2.3.11 Electrode preparation methods

In general, a supercapacitor consists of four components, including two electrodes, an electrode separator, and the electrolyte. The electrodes of a supercapacitor play a vital role during energy storage and energy delivery in that charges are stored at the interfaces between the electrodes and the electrolyte.[1] As a consequence, electrode structures can greatly influence supercapacitor performance. For example, the addition of Nafion binder greatly improves the performance of Ru oxide electrodes (section 2.3.8). In order to find the best electrode structure, various preparation methods for Ru oxide electrodes were investigated.

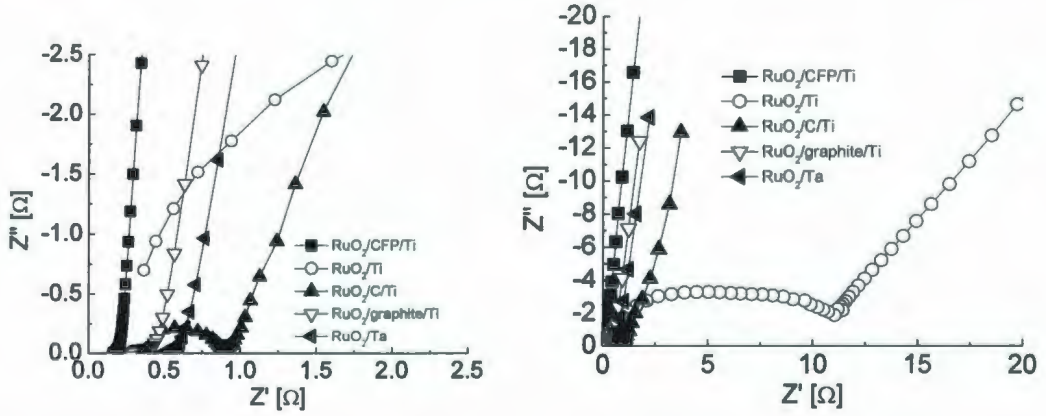

Fig. 2.18 Nyquist plots for symmetric supercapacitors with Ru oxide electrodes prepared by different methods. The electrode masses are specified in Table 2.2

Ru oxide supercapacitors constructed with different electrode structures were evaluated by impedance spectroscopy as shown in Fig. 2.18 (with different scales). There are semicircles at high frequencies for the supercapacitors constructed with RuO_2/Ti and RuO_2/C/Ti electrodes. These semicircles correspond to charge transfer

resistances due to the oxidation of current collectors, which will decrease the performance of the supercapacitors.

ESR and R_i values derived from Fig. 2.18 are given in Table 2.2. It can be seen that a similar ESR of ca. 0.48 Ω was obtained for the supercapacitor with RuO_2/C/Ti electrodes and the supercapacitor with RuO_2/Ta electrodes. However, the former had a much higher R_i value than the latter. Although the supercapacitors with RuO_2/graphite/Ti and RuO_2/Ta electrodes had different ESR values, they had a similar R_i value of ca. 0.7 Ω. The supercapacitor with RuO_2/Ti electrodes had the highest R_i (78 Ω). It is clear that the supercapacitor with RuO_2/CFP/Ti electrodes has the lowest ESR (0.16 Ω) and R_i (0.18 Ω) values. These differences in ESR and R_i can be attributed to their electrode structures, leading to different proton and electron pathways. In conclusion, RuO_2/CFP/Ti electrodes show the best characteristics for use in supercapacitors.

Table 2.2 Electrode mass, ESR and R_i values for supercapacitors with different electrode structures

	Electrodes for supercapacitors				
	RuO_2/ CFP /Ti	RuO_2/Ti	RuO_2/C/Ti	RuO_2/graphite /Ti	RuO_2 /Ta
Electrode mass (mg)	10.94	5.14	10.64	10.81	9.90
Separator	NRE211	Celgard 3400	NRE211	NRE211	NRE211
ESR (Ω)	0.16	0.37	0.49	0.27	0.47
R_i (Ω)	0.18	78	2.6	0.75	0.70

The performances of the supercapacitors described above (see Fig. 2.18) were determined by constant current discharging. Fig. 2.19 shows their Ragone plots derived

from the constant current discharging curves. It can be seen that there was discontinuity in energy and power densities, which caused by different potentiostat. Compared with the best energy density with the RuO_2/CFP/Ti electrode (27.5 W h/kg at 1 mA), the best energy densities decreased by 17% and 16% with the Ru oxide/graphite/Ti and the Ru oxide/Ta electrodes, respectively. In general, power densities increased with increasing current, while energy densities decreased. The best power densities were 59.7 kW/kg at 2.0 A, 24.2 kW/kg at 1.0 A, and 18.4 kW/kg at 1.0 A for the RuO_2/CFP/Ti, RuO_2/graphite/Ti and RuO_2/Ta electrodes, respectively, while the corresponding energy densities were 10.4 W h/kg, 5.6 W h/kg and 4.2 W h/kg. It is clear that the Ru oxide/CFP/Ti electrodes showed the best performance. This agrees with the results from impedance spectroscopy.

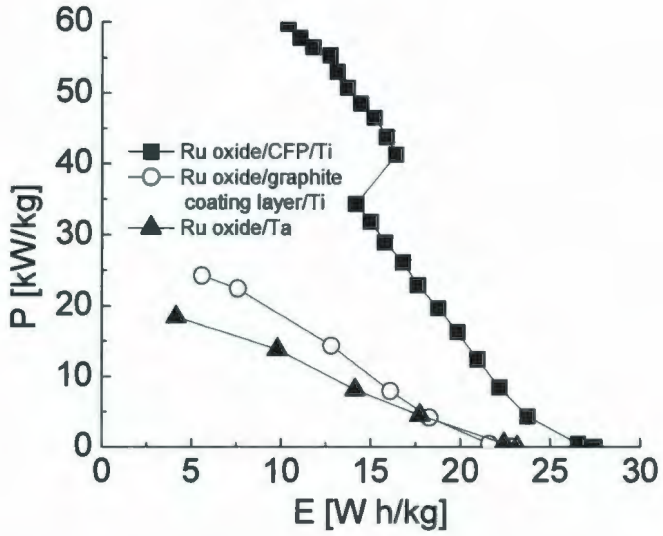

Fig. 2.19 Ragone plots for supercapacitors with different electrode structures. The discontinuity at high power was due to the use of a different potentiostat (Solartron 1286) with lower lead resistances for experiments at high currents (> 1A).

2.3.12 Separators

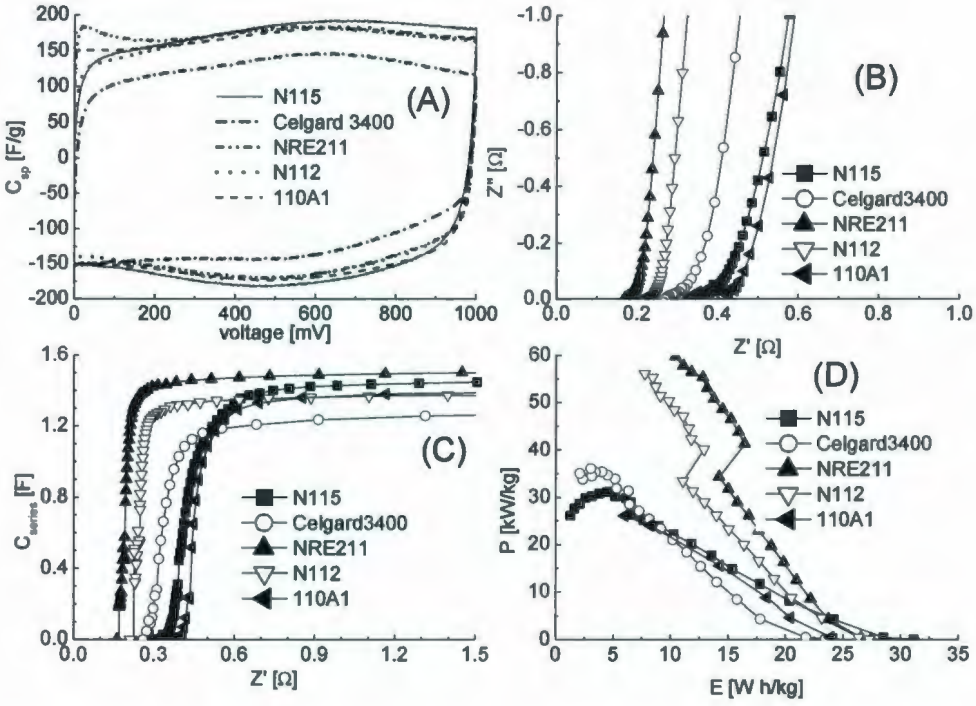

Fig. 2.20 Comparisons of supercapacitors with different separators. (A) Cyclic voltammograms at 20 mV/s, (B) Nyquist plots at 1 V DC potential and 10 mV amplitude, (C) capacitance plots, (D) Ragone plots derived from constant current discharging experiments. The electrode loadings are specified in Table 2.3.

The separator of a supercapacitor is a membrane between the two electrodes that prevents short circuits. In order to keep the ESR of the supercapacitor low, the separator has to be thin and highly porous.[33] For sulfuric acid electrolyte, thin Nafion films are excellent separators for Ru oxide supercapacitors because of their high proton conductivity. However, the high cost of Nafion films will limit their applications. The low cost porous Celegard 3400 (25 micron) and 110A1 membranes also have good

proton conductivity when saturated with sulfuric acid. In this work, Nafion films with different thicknesses, Celgard 3400 and 110A1 films were used as separators in Ru oxide supercapacitors and their performances were investigated by cyclic voltammetry, impedance spectroscopy and constant current discharging.

Cyclic voltammetry. The capacitive behaviors of the supercapacitors were measured by cyclic voltammetry as shown in Fig. 2.20(A). Here, the current responses were converted to specific capacitances. It can be seen that the voltammograms had similar shapes, and were rectangles over the 0.0 V to 1.0 V range employed. The extra current (or specific capacitance) for NRE211 and 110A1 can be contributed to different intial voltage of supercapacitors. It is clear that the supercapacitor with a Celgard 3400 separator gave an inferior performance compared to the other supercapacitors. Average specific capacitances for the four devices are given in Table 2.3. For Nafion separators, there were no significant difference in cyclic voltammograms. The supercapacitor with the Celgard 3400 separator had the lowest specific capacitance of 126 F/g (501 F/g for each electrode). In contrast, the supercapacitors with Nafion and 110A1 separators had specific capacitances of ca. 160 F/g (ca. 640 F/g for each electrode). It is not clear why the supercapacitor with the Celgard 3400 separator had such a low specific capacitance. It may have been due to poor wetting due to the hydrophobic nature of the separator.

Nyquist plots. Fig. 2.20(B) shows Nyquist plots for the supercapacitors. It can be seen that these had the characteristics of porous electrodes, including a ca. 45° intermediate region and a ca. vertical region at low frequencies.[32] ESR and R_i values derived from Fig. 2.20(B) are listed in Table 2.3. The ESR mainly originates from the

electrolyte, contact resistances, Nafion binder, separator, current collector and cables.[22] The resistance of the Nafion membrane increases with thickness, thus leading to an increase of the ESR. The supercapacitors with the N115 and the 110A1 separators had similar ESR (0.30 Ω) and R_i (ca. 0.67 Ω) values. NRE211 gave the lowest ESR (0.16 Ω) and R_i (0.18 Ω) values. The ESR and R_i values of the supercapacitor with the N112 were the same (0.21 Ω), and slightly higher than for the NRE211 supercapacitor due to the thicker separator. Although the thickness of the Celgard 3400 is the same as that of NRE211 (25 micron), it gave higher ESR (0.26 Ω) and R_i (0.39 Ω) values. This discrepancy may be attributed to differences in proton conductivity.

Table 2.3 Performance for supercapacitors with different separators

Mass of Ru oxide (mg)	Separator	Thickness (micron)	ESR (Ω)	R_i (Ω)	C_{sp} (F/g)*	C_{sp} (F/g)**
10.34	N115	127	0.30	0.66	141 (563)	165 (662)
10.24	Celgard 3400	25	0.26	0.39	125 (499)	126 (501)
10.94	NRE211	25	0.16	0.18	138 (552)	161 (642)
10.23	N112	51	0.21	0.21	135 (540)	157 (629)
10.10	110A1	110	0.30	0.68	135 (539)	160(635)

* Measured by impedance spectroscope, the values in parenthesis are for single electrodes.
** Measured by cyclic voltammetry, the values in parenthesis are for single electrodes.

Capacitance plots. Fig. 2.20(C) shows capacitance plots for the supercapacitors with different separators. Their series capacitances linearly increased with increasing resistance at high and medium frequencies. At lower frequencies (down to 5 mHz), the series capacitances were close to limiting values. The series capacitances at 5 mHz are listed in Table 2.3. Although the supercapacitors with the N115 and 110A1 separators

had high ESR values, their specific capacitances were quite high (over 135 F/g). Other supercapacitors with Nafion separators also showed high specific capacitances of over 135 F/g. However, the supercapacitor with the Celgard3400 separator had the lowest specific capacitance of 125 F/g. Compared to the specific capacitances measured by cyclic voltammetry, the results from impedance spectroscopy were systematically lower. The differences can be ascribed to the much smaller potential amplitude (see section 3.3.4.2). For cyclic voltammetry, the operating potential window was 0.0 V to 1.0 V, while the potential was confined to a narrow range (1± 0.0141 V) for impedance spectroscopy.

Ragone plots. Fig. 2.20(D) shows usable energy density versus average power density (Ragone) plots. It can be seen that the best usable energy density for the supercapacitor with the N115 separator was 31.2 W h/kg at 1 mA. However, the best usable energy densities were only 23.4 W h/kg and 24.2 W h/kg at 1 mA for the supercapacitors with the Celgard 3400 and 110A1 separators, respectively. In contrast, the supercapacitors with the NRE211 and N112 separators had maximum energy densities of ca. 27.4 W h/kg. The best energy density of the supercapacitor with the N115 separator was better by 33%, relative to the best energy density of the supercapacitor with the Celgard 3400 separator.

Usable energy densities decreased with increasing current in all cases. The usable energy density of the supercapacitor with the NRE211 separator decreased to 16.4 W h/kg and 10.4 W h/kg for 1.1 A and 2.0 A, respectively. In contrast, the energy densities of the supercapacitor with the N112 separator were 12.9 W h/kg and 7.7 W h/kg for 1.1 A

and 2.0 A, respectively. However, the energy density of the supercapacitor with the N115 separator decreased to 6.6 W h/kg and 1.3 W h/kg for 1.1 A and 2.0 A, respectively, while the supercapacitor with the Celgard 3400 separator still gave 6.3 W h/kg and 2.1 W h/kg at 1.1 A and 2.0 A, respectively. Only 6.0 W h/kg was obtained for the supercapacitor with the 110A1 separator at 1.0 A. It is clear that NRE211 was the best separator in that it gave the highest energy densities at high discharge currents. The discontinuities in the Ragone plots are due to the lower lead resistances (ca. 60 mΩ) of the Solartron 1286 potentiostat.

The average power density increased with increasing discharging current. The best power density was 59.7 kW/kg for the supercapacitor with the NRE211 separator at 2.0 A, whereas the supercapacitor with the N112 separator had a little lower power density (56.1 kW/kg) at the same current. However, we only obtained a best power density of 31.1 kW/kg for the supercapacitor with the N115 separator at 1.4 A. In contrast, the best power density was 36.0 kW/kg for the supercapacitor with the Celgard 3400 separator.

In conclusion, Nafion films are good separators due to their high proton conductivity. Ru oxide supercapacitors with thin Nafion films can obtain high performance in that they have lower ESR. The performance of Ru oxide supercapacitors with other separators depends on their proton conductivity and film thickness.

2.3.13 Operating temperature

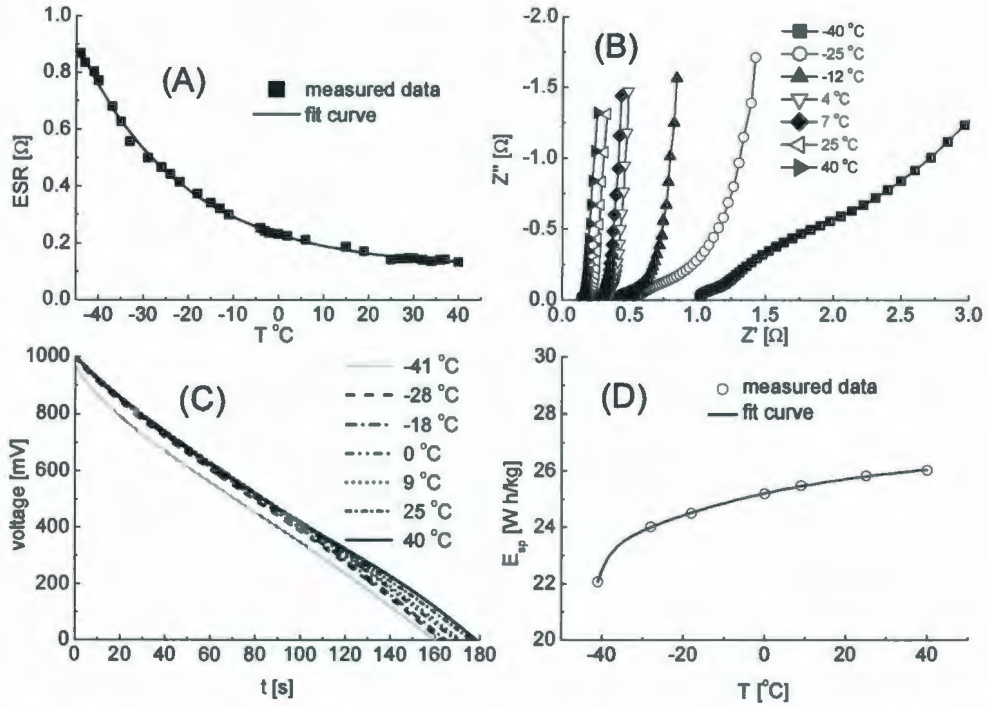

Fig. 2.21 Impedance data for a supercapacitor at different operating temperatures and constant current discharging results in 5 M H_2SO_4. (A) ESR versus operating temperature, (B) Nyquist plots, (C) constant current discharging curves, (D) specific energies versus operating temperature. The supercapacitor consisted of 9.2 mg Ru oxide with a Nafion NRE211 separator.

Operating temperature studies were conducted by using a low temperature bath (33% H_2SO_4 plus dry ice) to control the temperature of the cell. The temperature was varied by adjusting the amount of dry ice. ESR values were estimated by using the real impedance at 1 kHz with a DC bias of 1V, and 10 mV amplitude. The results plotted in Fig. 2.21(A) show that the ESR decreased with increasing operating temperature. The experimental data were modeled with a two term exponential decay function (see Table 2.4). The physical meaning of these parameters is unclear, but the simulated curve

matches the experimental results well. The two exponential variables are likely related to the dissociation of sulfuric acid and ion diffusion coefficients at different temperatures.

Table 2.4 Fit equations for ESR and specific capacitance (C_{sp}) versus operating temperature (T)

ESR (y) Fit function $y = A_1*\exp(-T/C_1) + A_2*\exp(-T/C_2) + y_0$		Specific capacitance (C_{sp}) Fit function $C_{sp} = A_1*\exp(-T/C_1) + A_2*\exp(-T/C_2) + C_{sp0}$	
constant	value	constant	value
y_0	0.11	C_{sp0}	26.7
A_1	0.058	A_1	-4.1E-7
C_1	23.4	C_1	2.8
A_2	0.058	A_2	-1.5
C_2	23.4	C_2	47.1
R	0.998	R	0.999

Note: y_0, C_{sp0}, A_1, C_1, A_2 and C_2 are constant. R is the sample correlation coefficient.

Table 2.5 ESR and R_i values for a supercapacitor at different operating temperatures

Temperature(°C)	ESR(Ω)	R_i(Ω)
-40	1.02	8.05
-25	0.52	2.62
-12	0.39	1.19
4	0.25	0.53
7	0.23	0.44
25	0.17	0.25
40	0.13	0.14

Nyquist plots. Nyquist plots (see Fig. 2.21(B)) can be used for estimating the ionic resistance of the supercapacitor at different operating temperatures as discussed previously. ESR and R_i values derived from Fig. 2.21(B) are given in Table 2.5, which shows that R_i increased with decreasing operating temperature. For example, the R_i was only 0.14 Ω at 40 °C, while it increased to 0.53 Ω and 8.05 Ω at 4 °C and -40 °C,

respectively. Although the ESR also increased with decreasing operating temperature, the increment was less than for R_i. For instance, the ESR was 0.13 Ω at 40 °C, and it increased to 1.02 Ω at -40 °C.

Constant current discharging. The energy storage capacity of the supercapacitor at different operating temperatures was measured by constant current discharging at 10 mA as shown in Fig. 2.21(C). It can be seen that the discharge curve at -41 °C had the highest voltage drop over the first few milliseconds. This is due to the high ESR at low temperature. Usable energy densities were obtained by integration using Eq. 1.5 in Chapter 1. The energy densities derived from Fig. 2.21(C) are plotted as a function of operating temperature in Fig. 2.21(D). It can be seen that the specific energy density increased with increasing operating temperature. The specific energy density increased from 22.1 W h/kg to 26.0 W h/kg when the operating temperature increased from -41 °C to 40 °C. The relationship between the specific energy density and operating temperature was simulated by using an exponential function. The parameters of the fit equation are listed in Table 2.4. It is clear that the fitted curve matched the experimental results very well.

In conclusion, the performance of supercapacitors strongly depends on operating temperatures. High performance can be obtained at high operating temperature for a supercapacitor due to its lower ESR and R_i. However, high operating temperature may cause other problems, such as device safety and lifecycles.

2.3.14 Stability

A supercapacitor consisting of two identical Ru oxide electrodes with a surface area of 6 cm^2 was soaked in 1 M H_2SO_4, then sealed using Parafilm. The supercapacitor was repeatedly charged to 1 V using 0.5 A, then discharged to 0 V using the same current. The total experiment time was 94 days, and included a cycling time of ca. 10 days. The supercapacitor was kept in a discharged state when it was not being cycled.

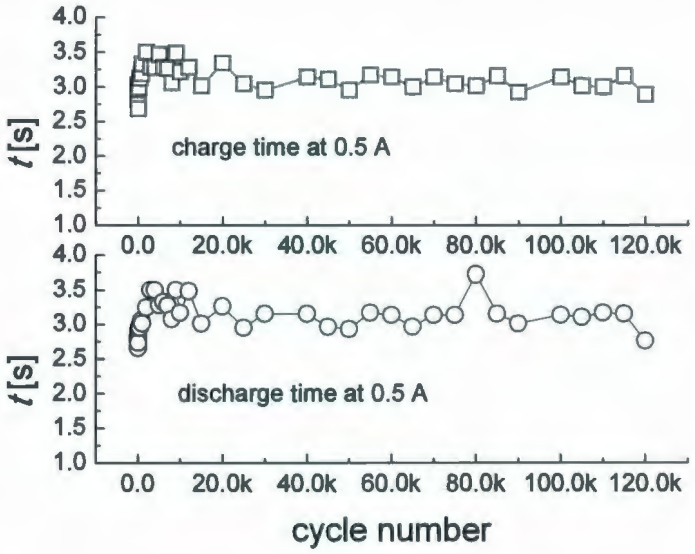

Fig. 2.22 Long-term stability of a Ru oxide supercapacitor in 1 M H_2SO_4. The supercapacitor consisted of 10.03 mg (two 6 cm^2 electrodes) Ru oxide with a NRE211 separator.

The charge time and discharge time are plotted as a function of cycle number in Fig. 2.22. The charge time and discharge time, which provide the charge and discharge energy storage capacity, first increased with cycling. For instance, the charge time and discharge time were both 2.81 s for the 5^{th} cycle, while the corresponding times increased

to 3.28 s and 3.50 s for the 3000th cycle. Subsequently, the charge time and discharge time dropped to 3 s at 115000-12000 cycles. It is clear that the Ru oxide supercapacitor possessed very high stability, and that its lifetime was over 120000 cycles.

Fig. 2.23 shows the charge and discharge curves for selected cycles. The voltage steps seen in this figure are due to the limited time resolution of the instrument at the very long timescale of the experiment. It can be seen that there was a fast potential drop over the first few milliseconds during discharging. The potential drop for all cycles was similar, indicating that the ESR did not change significantly during cycling. It is clear that the 5000th cycle had the highest discharge time, and that a little lower discharge time was obtained for the 50000th cycle and the 100000th cycle.

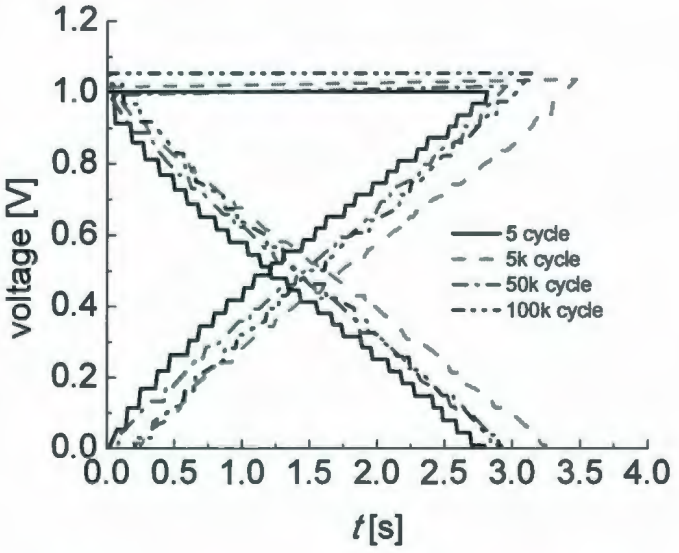

Fig. 2.23 Charge and discharge curves for selected cycles.

Another supercapacitor (with an electrode loading of ca. 5.2 mg/cm^2) was characterized using the methods employed for the supercapacitor (described above Fig.

2.22 and 2.23). Its energy storage capacity was tested by constant current discharging as described in section 2.2.6. Energy density and power density for the supercapacitor are plotted as a function of cycle number in Fig. 2.24. It can be seen that the energy density increased with cycling, and reached a maximum value of 16.9 W h/kg for the 1000th cycle, and then remained constant (16.7 W h/kg) until the 20000th cycle, followed by a slight decrease. The energy density (14.9 W h/kg) for the 50000th cycle was higher than the initial value (14.5 W h/kg), indicating good stability of the Ru oxide supercapacitor. The power density (ca. 3.5 kW/kg) did not change significantly with cycling.

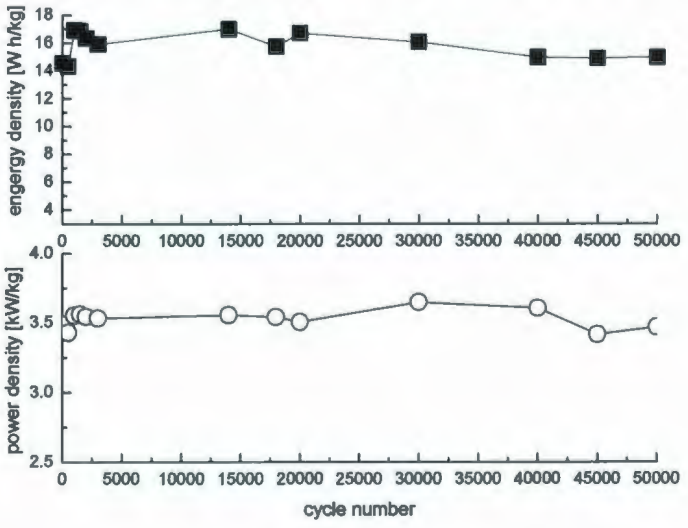

Fig. 2.24 Energy densities and power densities of a supercapacitor in 1 M H_2SO_4 versus cycle number. The supercapacitor with a NRE211 separator consisted of 62.24 mg Ru oxide annealed at 150 °C. The surface area of the electrodes was 6 cm^2.

2.3.15 Self-discharge

The self-discharge behavior of a supercapacitor was monitored by recording its potential change against time as shown in Fig. 2.25. It can be seen that the self-discharge

rate was high over the first hour, followed by a relatively slow self-discharge rate. For example, the voltage decreased from the initial value of 993 mV to 945 mV, 916 mV and 878 mV after 30 min, 1 h, and 2 h, respectively, corresponding to voltage losses of 3.9%, 7.8%, and 11.6%. In contrast, the voltage loss was only 29.2% (703 mV) after 24 h. The fast initial loss could be due to a reaction between the negative Ru oxide electrode and oxygen in the electrolyte because the supercapacitor was exposed to air. The Ru oxide on the positive electrode possessed a high valence after the supercapacitor was fully charged. On the other hand, the Ru oxide on the negative side had a low valence state. The lower valence Ru oxide may be oxidized by air in the electrolyte, accelerating the self-discharge process.

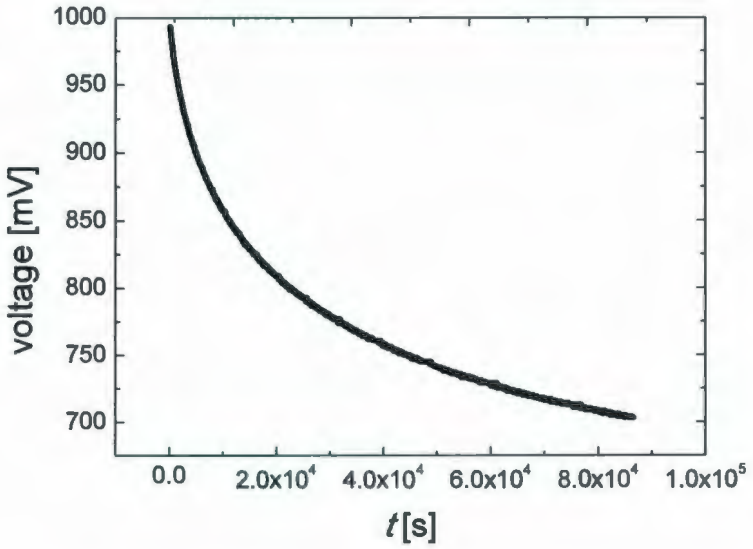

Fig. 2.25 Self-discharge curve for a supercapacitor in 1 M H_2SO_4. The supercapacitor consisted of 10.72 mg Ru oxide with a NRE211 separator.

2.3.16 A 1.3 V symmetric Ru oxide supercapacitor

Based on previous discussions in section 2.3.6, the operating voltage window for a symmetric Ru oxide supercapacitor can reach up to 1.4 V. A device was therefore tested at an operating voltage of 1.3 V. The supercapacitor was assembled by our optimum methods and tested by constant current discharging as shown in Fig. 2.26. The voltage quickly dropped over the first few milliseconds due to the ESR of the cell, and this drop increased with increasing discharge current. The internal resistance was estimated to be ca. 0.3 Ω from these initial voltage drops.

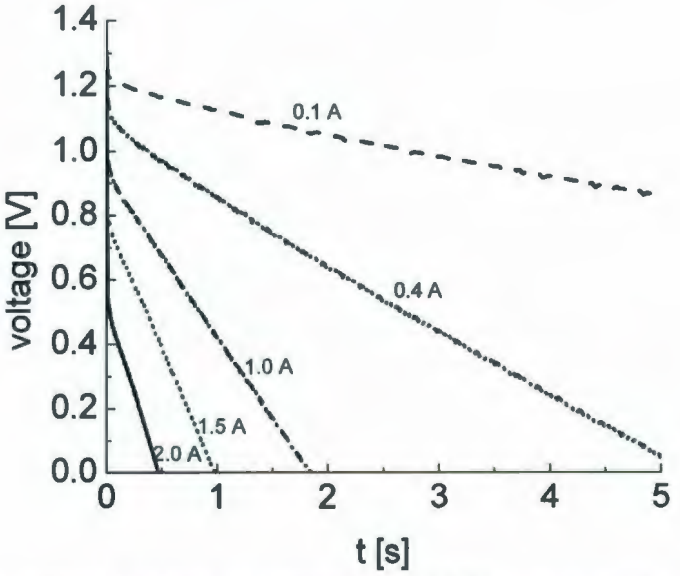

Fig. 2.26 Constant current discharging curves for a 1.3 V supercapacitor in 1 M H_2SO_4. The supercapacitor consisted of 10.14 mg Ru oxide with a NRE211 separator.

Fig. 2.27 shows the relationship between the energy density and power density derived from Fig. 2.26. It is clear that the energy density decreased with increasing discharging current, and the power density increased with current. The best energy

density was 40.5 W h/kg (with 0.6 kW/kg power density) for full discharge at 10 mA, while the energy density decreased to 23.4 W h/kg (with 45.5 kW/kg power density) at 1 A. The best power density increased to 59.9 kW/kg (with 11.3 W h/kg energy density) at 1.8 A.

For half-discharge, the best energy density was 26.1 W h/kg at 10 mA, which is similar to that for a 1 V supercapacitor at full discharge. An energy density of 11.9 W h/kg and a power density of 78.4 kW/kg at 1.0 A were obtained. The best power density was 130.5 kW/kg (with an energy density of 0.5 W h/kg).

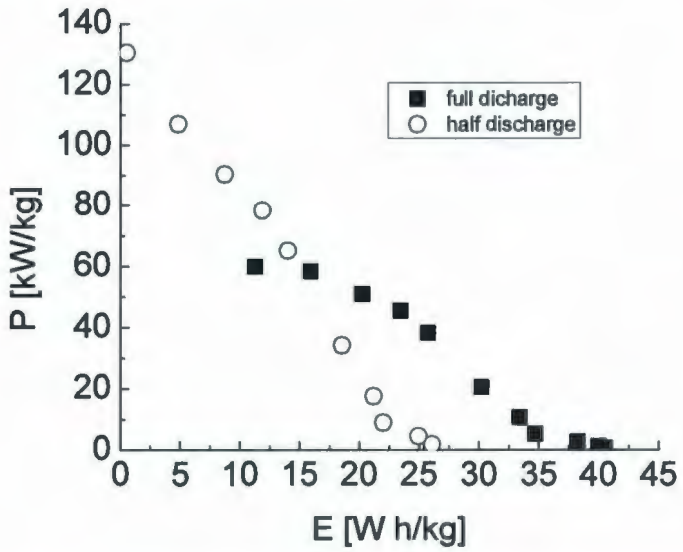

Fig. 2.27 Ragone plots for a 1.3 V Ru oxide supercapacitor.

2.4 Conclusions

Hydrous Ru oxide was prepared by a modified sol-gel method. Annealing experiments showed the optimal annealing temperature to be 110 °C, which is lower than the value of 150 °C reported in the literature.[15] The difference in optimum annealing

temperature may be contributed to the use of different bases (NaOH versus Na_2CO_3). XRD patterns showed that a crystalline structure started to form at ca. 200 °C.

The effects of electrode preparation, separator, and electrode loading on the performances of Ru oxide supercapacitors were investigated in detail by cyclic voltammetry, constant current discharging and impedance spectroscopy. Performances were found to depend significantly on the preparation techniques for the electrodes. The addition of Nafion binder sharply improved the performance of the supercapacitors due to the formation of proton conducting pathways. 5% Nafion binder can effectively enhance the performance and mechanical stability of Ru oxide electrodes. The best way for preparing electrodes was to load the Ru oxide onto carbon fibre paper, when a Ti plate current collector was used. For these electrodes, the specific capacitance did not change significantly with Ru oxide loading (up to 51 mg/cm^2). NRE211 was the best separator of those tested because of its low ESR (0.1 Ω/cm^2) and ionic resistance (0.2 Ω/cm^2). It provided a power density as high as 130.5 kW/kg for a 1.3 V operating voltage at half-discharge. The best energy densities were 40.5 W h/kg and 31.2 W h/kg for 1.3 V and 1V operating voltages, respectively. These are much higher than the value of 26 W h/kg reported by Zheng *et al.*[34] The high energy densities can be attributed to the addition of nafion binder with high proton conductivity, resulting in good proton pathway. The Ru oxide supercapacitors exhibited high stability. The performance did not change significantly over 120000 cycles at a constant current of 0.5 A. This is much better than the results of Zheng *et al.*[34] The capacitance of their device decreased by 15% within

10000 cycles. A slow decay rate was observed from 10000 to 50000 cycles. However, the capacitance quickly decreased again after 50000 cycles.

The performance of a ruthenium oxide supercapacitor at different operating temperatures was measured by impedance spectroscopy and constant current discharging. The ESR and R_i decreased with increasing operating temperature, leading to increased performance.

References

1. Conway, B. E., *Electrochemical supercapacitors: scientific fundamentals and technological applications*. Plenum Press: New York, 1999.

2. Winter, M.; Brodd, R. J., *Chemical Reviews* **2004,** *104* (10), 4245-4269.

3. Huggins, R. A., *Solid State Ionics* **2000,** *134* (1-2), 179-195.

4. Simon, P.; Gogotsi, Y., *Nature Materials* **2008,** *7* (11), 845-854.

5. Arico, A. S.; Bruce, P.; Scrosati, B.; Tarascon, J. M.; Van Schalkwijk, W., *Nature Materials* **2005,** *4* (5), 366-377.

6. Barsukov, I. V.; North Atlantic Treaty Organization., *New carbon based materials for electrochemical energy storage systems: batteries, supercapacitors and fuel cells*. Springer: Dordrecht, 2006.

7. Jeong, Y. U.; Manthiram, A., *Journal of the Electrochemical Society* **2001,** *148* (3), A189-A193.

8. Pandolfo, A. G.; Hollenkamp, A. F., *Journal of Power Sources* **2006,** *157* (1), 11-27.

9. Sugimoto, W.; Shibutani, T.; Murakami, Y.; Takasu, Y., *Electrochemical and Solid State Letters* **2002,** *5* (7), A170-A172.

10. Niu, J. J.; Pell, W. G.; Conway, B. E., *Journal of Power Sources* **2006,** *156* (2), 725-740.

11. Kim, I. H.; Kim, J. H.; Lee, Y. H.; Kim, K. B., *Journal of the Electrochemical Society* **2005,** *152* (11), A2170-A2178.

12. Lin, C. Q.; Popov, B. N.; Ploehn, H. J., *Journal of the Electrochemical Society* **2002,** *149* (2), A167-A175.

13. Trasatti, S.; Buzzanca, G., *Journal of Electroanalytical Chemistry* **1971,** *29* (2), A1-A5.

14. Zheng, J. P.; Jow, T. R., *Journal of the Electrochemical Society* **1995,** *142* (1), L6-L8.

15. Zheng, J. P.; Cygan, P. J.; Jow, T. R., *Journal of the Electrochemical Society* **1995,** *142* (8), 2699-2703.

16. Fang, W. C.; Huang, J. H.; Chen, L. C.; Su, Y. L. O.; Chen, K. H., *Journal of Power Sources* **2006,** *160* (2), 1506-1510.

17. Chang, K. H.; Hu, C. C., *Journal of the Electrochemical Society* **2004,** *151* (7), A958-A964.

18. Jang, J. H.; Machida, K.; Kim, Y.; Naoi, K., *Electrochimica Acta* **2006,** *52* (4), 1733-1741.

19. Jang, J. H.; Kato, A.; Machida, K.; Naoi, K., *Journal of the Electrochemical Society* **2006,** *153* (2), A321-A328.

20. Hu, C. C.; Chang, K. H., *Journal of Power Sources* **2002,** *112* (2), 401-409.

21. Liu, X. R.; Pickup, P. G., *Journal of Power Sources* **2008,** *176* (1), 410-416.

22. Liu, X. R.; Pickup, P. G., *Energy & Environmental Science* **2008,** *1* (4), 494-500.

23. Hu, C. C.; Chen, W. C.; Chang, K. H., *Journal of the Electrochemical Society* **2004,** *151* (2), A281-A290.

24. Yokoshima, K.; Shibutani, T.; Hirota, M.; Sugimoto, W.; Murakami, Y.; Takasu, Y., *Journal of Power Sources* **2006,** *160* (2), 1480-1486.

25. Lee, J. K.; Pathan, H. M.; Jung, K. D.; Joo, O. S., *Journal of Power Sources* **2006,** *159* (2), 1527-1531.

26. Kim, I. H.; Kim, J. H.; Kim, K. B., *Electrochemical and Solid State Letters* **2005,** *8* (7), A369-A372.

27. Jow, T. R.; Zheng, J. P., *Journal of the Electrochemical Society* **1998,** *145* (1), 49-52.

28. Hu, C. C.; Huang, Y. H., *Journal of the Electrochemical Society* **1999,** *146* (7), 2465-2471.

29. Seddon, E. A.; Seddon, K. R., *The Chemistry of Ruthenium*. Elsevier: Amsterdam ; New York, 1984.

30. Stefan, I. C.; Mo, Y. B.; Antonio, M. R.; Scherson, D. A., *Journal of Physical Chemistry B* **2002,** *106* (48), 12373-12375.

31. McKeown, D. A.; Hagans, P. L.; Carette, L. P. L.; Russell, A. E.; Swider, K. E.; Rolison, D. R., *Journal of Physical Chemistry B* **1999,** *103* (23), 4825-4832.

32. Lefebvre, M. C.; Martin, R. B.; Pickup, P. G., *Electrochemical and Solid State Letters* **1999,** *2* (6), 259-261.

33. Kotz, R.; Carlen, M., *Electrochimica Acta* **2000,** *45* (15-16), 2483-2498.

34. Zheng, J. P.; Jow, T. R., *Journal of Power Sources* **1996,** *62* (2), 155-159.

Chapter 3 Carbon fabrics and Ru oxide/carbon fabric composites for supercapacitors

This work has been published in Journal of Solid State Electrochemistry: Xiaorong Liu and Peter Pickup, (2010) *Ru oxide/carbon fabric composites for supercapacitors*, Journal of Solid State Electrochemistry 14 (2): 231-240. The experimental sections have been reproduced in part from this paper. The text was written in part by Dr. Peter Pickup

3.1 Introduction

The experimental results presented in Chapter 2 demonstrate that Ru oxide is an excellent material for supercapacitors. However, the high price and a limited supply of ruthenium prevent it from meeting the requirements for widespread use.[1] In order to circumvent these disadvantages, one of the strategies is to enhance the utilization of Ru by combining it with other electrode materials, such as carbon-based materials. Among these, carbon fabrics (or fibers) and activated carbons are promising materials for supercapacitors due to their high surface areas (up to 2500 m^2/g) and high specific capacitances (up to 200 F/g).[2, 3]

Composites of Ru oxide and carbon-based materials can effectively improve the utilization of Ru. Hu *et al.*[4] report that a specific capacitance of 1340 F/g was obtained for the Ru oxide component in a Ru oxide/conductive activated carbon composite. Zhang *et al.*[5] have reported specific capacitances exceeding 1450 F/g based on the Ru oxide

components of electrodes with 10-20 wt% Ru. In addition, the specific capacitance for the Ru oxide component in Ru oxide/carbon nanofiber composites also improved to 1017 F/g.[6] Although these composites enhanced the utilization of ruthenium, the reasons were not completely understood.

In the work described in this chapter, Ru oxide/carbon fabric composites were prepared by an impregnation method. Their electrochemical properties were characterized by cyclic voltammetry, impedance spectroscopy and constant current discharging. Interactions (or synergistic effects) between the carbon fabric (CF) and Ru oxide were investigated in detail.

3.2 Experimental

3.2.1 Materials

The following materials were used as purchased: carbon fabric (CF; Spectracarb 2225 from Engineered Fibers Technology), H_2SO_4 (Fisher Scientific), Nafion film (NRE211 from Ion Power, Inc), titanium foil (25 micron, Aldrich), $RuCl_3 \cdot xH_2O$ (Precious Metals Online Pty Ltd.), carbon fibre paper (CFP; Toray™ Carbon Paper, TGP-H-090), 5% Nafion solution (DuPont).

3.2.2 Preparation of Ru oxide/CF composites

Preparation of hydrous Ru oxide. Hydrous ruthenium oxide powder was prepared by a modified sol-gel method as described in Chapter 2.[1, 7, 8] The as-prepared hydrous ruthenium oxide was annealed for 3 h at 150 °C in air.

Preparation of composites. Ru oxide powder (0.01g - 0.5g) was dispersed in deionized water (10 ml -100 mL) by sonicating for approximately 30 min. For low loadings of Ru oxide (< 30 %), Spectracarb 2225 CF (typical size 4 cm × 4 cm), that had been dried for 24 h at 150 °C, was immersed in this suspension for ca. 30 min, then dried for ca. 10 min at 150 °C. This immersion/drying procedure was repeated until the targeted mass loading of Ru oxide was reached. Finally, the composite was dried for 1 h to 2 h at 150 °C to obtain a stable mass. For high loadings of Ru oxide (> 30 %), the Ru oxide suspension was added dropwise to a piece of CF (2 cm x 4 cm) on a hotplate at ca. 50 °C. The loadings were estimated from the increase in dry mass of the CF sample.

3.2.3 Thermogravimetric analysis (TGA)

Thermal dynamic properties of the composites were performed on a TA Instruments Q500 TGA analyzer under a N_2 atmosphere (sample gas, 60 mL/min; balance gas, 40 mL/min). Air was not completely purged from the TGA instrument before starting experiments.

3.2.4 Scanning electron microscopy

Scanning electron microscopy was performed with a FEI Quanta 400 environmental SEM.

3.2.5 Assembly of supercapacitors

Supercapacitors were constructed by sandwiching a NRE211 film between two equivalent Ru oxide/CF electrodes (1 cm^2). Two titanium plates built into polycarbonate blocks were used as current collectors. A piece of CFP was placed between each titanium plate and electrode to minimize the contact resistance. The assembly was immersed in a 50 mL beaker with ca. 10 mL of 1 M H_2SO_4 in air.

3.2.6 Electrochemical characterization

The properties of electrodes were characterized by using three-electrode and two-electrode configurations. In the three-electrode configuration, identical Ru oxide/CF composite electrodes were connected to the working electrode and the counter electrode leads of the potentiostat while the reference electrode lead was connected to an Ag/AgCl reference electrode immersed in the external 1 M H_2SO_4 electrolyte. In the two-electrode (supercapacitor) configuration the reference electrode lead was connected to the counter electrode lead. Cyclic voltammetry and constant current discharging experiments were conducted using an EG&G 273A potentiostat/galvanostat. For constant current discharging experiments, the supercapacitors were first charged at 1.0 V for 5 min, then completely discharged to 0 V at different currents.

Impedance spectroscopy measurements were conducted with a Solartron 1286 potentiostat, 1250 Frequency Response Analyser and a Zplot software. The measurement frequency range was usually from 10 kHz to 10 mHz or 5 mHz, with an amplitude of 10 mV and 0.5 V DC bias potential.

3.3 Results and discussion

3.3.1 Thermogravimetric analysis

TGA can be used for characterizing thermal dynamic properties of composites and measuring Ru oxide loadings. Fig. 3.1(A) shows TGA curves for a 19.7% Ru oxide/CF composite and an as received sample of CF. It can be seen that the composite slowly lost mass as the temperature was increased to 200 °C. This can be attributed to the loss of adsorbed water from the CF surface and the slow dehydration of the hydrous Ru oxide component. In contrast, the mass loss rate sharply increased at temperatures above 200 °C. This can be attributed to the oxidation of the CF, which is catalyzed by the Ru oxide.[9,10] The sample finally reached a residual mass of 20.4% at ca. 700 °C, corresponding to anhydrous Ru oxide and the trace ash content of the CF. In contrast only a very slow mass loss was observed for the CF at temperatures up to 600 °C. A rapid mass loss, corresponding to the oxidation of the CF, occurred above 600 °C. It is clear that the CF had a much higher oxidation temperature than the Ru oxide/CF composite. The residual mass of the CF was negligible, so the residual masses of the composites can be used directly for estimating Ru oxide loadings.

Fig. 3.1(B) shows the differential mass loss against sample temperature. It is clear that the first peak (at < 100 °C) of the composite is due to the loss of adsorbed water that is easy to lose at low temperature. The peaks between 200 °C and 700 °C can be attributed to the oxidation of the CF and the dehydration of the hydrous Ru oxide. The peak located between 600 °C and 950 °C can be ascribed to the oxidation of the CF. [9, 10]

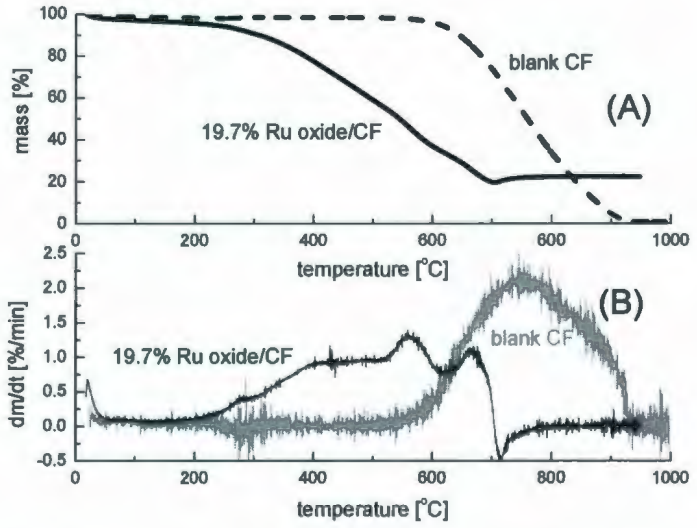

Fig. 3.1 TGA curves for samples of 19.7% Ru oxide/CF (5.03 mg) and CF (1.76 mg) (ramp 5 °C/min to 1000 °C). (A) Mass loss plots (B) differential plots of mass loss

For a Ru oxide /CF composite with a 19.7% Ru oxide loading estimated from the mass difference during preparation, the average (6 measurements) residual mass from TGA was 18.6%, corresponding to a hydrous Ru oxide (based on a hydration number of 0.5) loading of 19.8%. It is clear that the loading measured by TGA agrees with that from the increase in the mass during the preparation of the composite.

3.3.2 Scanning electron microscopy

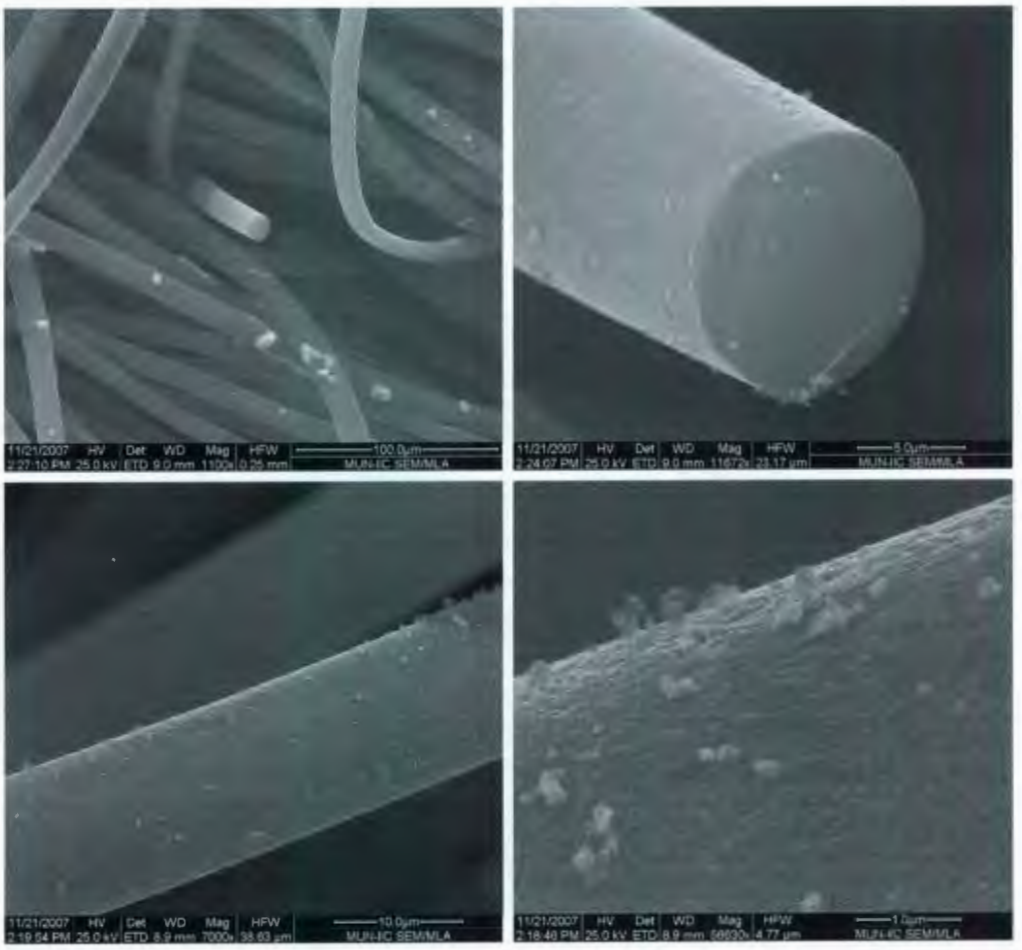

Fig. 3.2 SEM images of a 9.1 % Ru oxide/CF composite

The texture of a 9.1% Ru oxide/CF sample is shown in the SEM images in Fig. 3.2. It can be seen that the composite consists of porous cylinder fibres with diameters of ca. 10 micron. The rough surfaces of the fibres provide anchor sites for small Ru oxide particles which cover parts of the CF surface. The Ru oxide particle sizes ranged from

tens to hundreds of nanometers. There may have been some smaller particles that are not visible on the scale of this image.

Fig. 3.3 shows SEM images of 19.7% Ru oxide/CF and 59.2% Ru oxide/CF samples. Large clumps of Ru oxide were observed with increasing loading, and most of the Ru oxide particles occupy the spaces between the fibres.

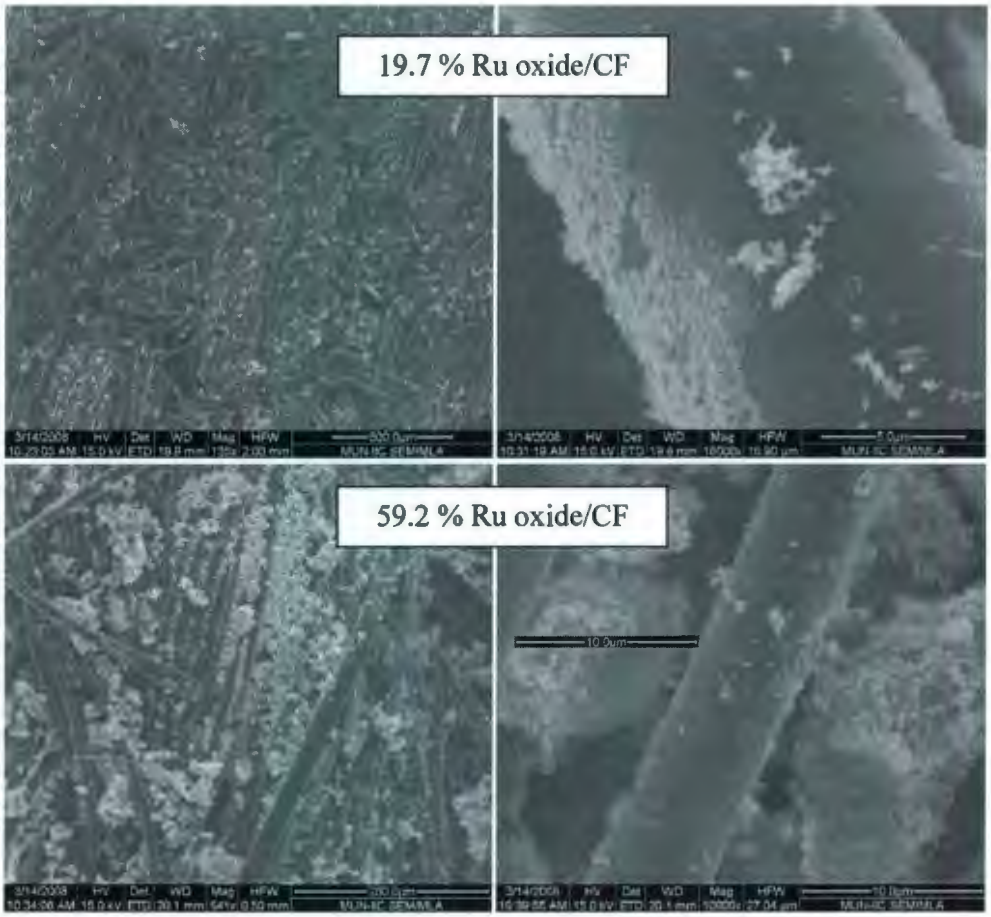

Fig. 3.3 SEM images of Ru oxide/CF composites with high loadings

3.3.3 CF supercapacitors

3.3.3.1 Cyclic voltammetry

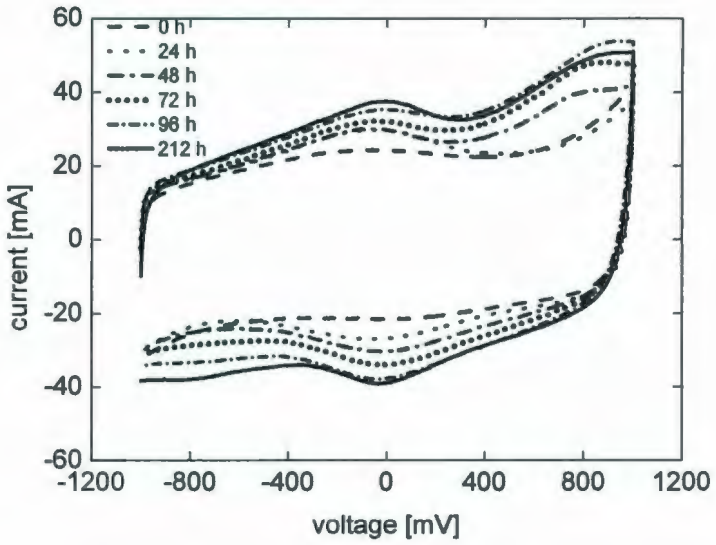

Fig. 3.4 Cyclic voltammograms at 20 mV/s for a CF (13.44 + 13.66 mg) supercapacitor at different soaking times.

The capacitive behavior of a CF supercapacitor was characterized by cyclic voltammetry as shown in Fig. 3.4. It is clear that the current responses increased with soaking time in the 1 M H_2SO_4 electrolyte. For the immediate measurement, the shape of the voltammogram was quite featureless over the voltage window of -1.0 V to 1.0 V. A wide current peak at ca. 0 V was observed after a period of soaking, and the peak height sharply increased with time. Clearly, the increase can be attributed to the changes of the surface functionality on the CF caused by soaking and cycling. However, irreversible peaks also developed at ca. +0.9 V. This may be ascribed to redox of the carbon surface.

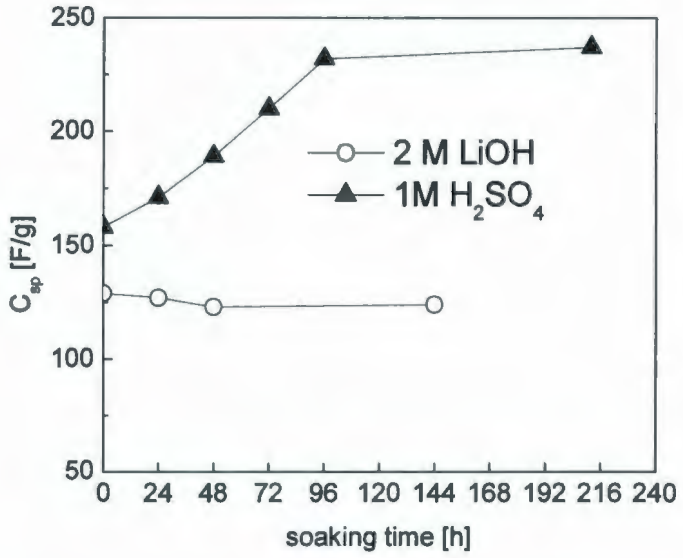

Fig. 3.5 Average specific capacitances (based on single electrodes) of CF in different electrolytes at different soaking times.

Average specific capacitances derived from Fig. 3.4 are plotted as a function of soaking time as shown in Fig. 3.5. It can be seen that the average specific capacitance increased by 46.8% (232 F/g) after 96 h, as compared with the initial value of 158 F/g. However, the specific capacitance did not change significantly thereafter, and a maximum specific capacitance of 237 F/g was obtained at 212 h.

A supercapacitor with a 2 M LiOH electrolyte (with lower density compared to other 2 M base) was also characterized by cyclic voltammetry as shown in Fig. 3.6 and Fig. 3.5. Obviously, its current responses did not change significantly with time. Its average specific capacitances were 129, 127, 123, and 124 F/g for 0, 24, 48, and 144 h, respectively. This indicated that the air trapped on the surface of CF was not an issue.

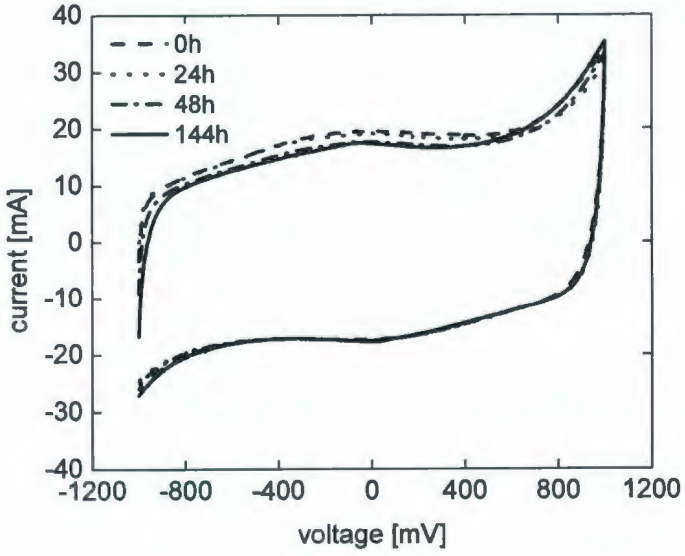

Fig. 3.6 Cyclic voltammograms at 20 mV/s for a CF (13.0 mg + 13.2 mg) supercapacitor in 2 M LiOH (aq) at different soaking times.

For the CF supercapacitor with a 1 M H_2SO_4 electrolyte, it appears that the increase in specific capacitances was due to the changes in surface functionality. The changes in the shape of the voltammograms with time (see Fig. 3.4) suggest that the increase in specific capacitances was due to an increase in functional groups with psedoucapacitive behavior.

Various surface redox reactions have been proposed to explain the specific capacitance peak seen in voltammograms of carbon-based materials in H_2SO_4 electrolyte.[11, 12] The increase in specific capacitances is most likely due to the oxidation of functional groups on the carbon surface.[13-15] The broadness of the peaks suggests that a series of redox reactions are involved in the electrochemical processes. Quinone/hydroquinone-type couples with different surface structures, such as those

shown in Scheme 3.1,[16] seem to be the most plausible functional groups. The peak at ca. 0 V for the CF supercapacitor shown in Fig. 3.4 can be explained by the fact that both electrodes have open circuit potentials of ca. 0.3 V versus Ag/AgCl due to quinone/hydroquinone-type couples..

Five CF supercapacitors were tested by cyclic voltammetry after 17 h, and an average specific capacitance of 175±6 F/g was obtained. This shows that the measurement method has good reproducibility.

Scheme 3.1 Proposed process occurring on CF at ca. 0.3 V versus Ag/AgCl

3.3.3.2 Impedance spectroscopy

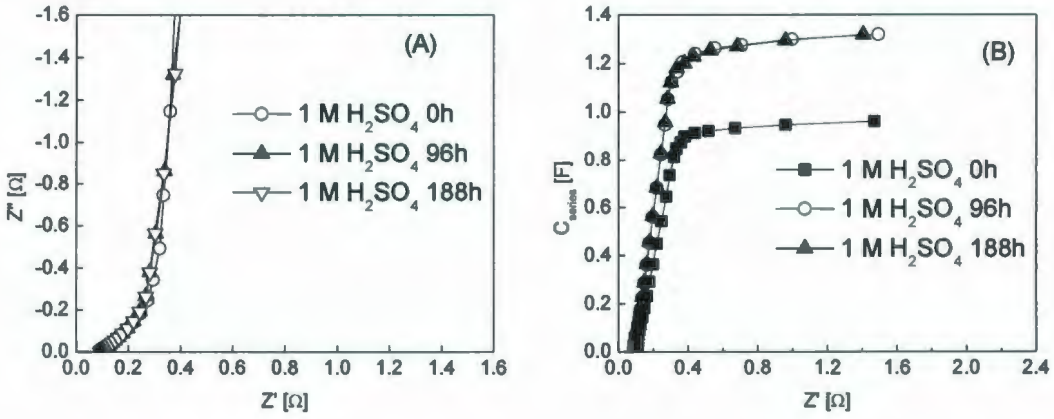

Fig. 3.7 Nyquist plots (A) and capacitance plots (B) for the supercapacitor described in Fig. 3.4.

The supercapacitor described in Fig. 3.4 was also characterized by impedance spectroscopy as shown in Fig. 3.7. It can be seen from Fig. 3.7(A) that all of the Nyquist plots have the expected characteristics for porous electrodes, consisting of a 45 degree region at high frequencies and a vertical line at low frequencies. Although the soaking time was different, a similar ESR value of 0.092 Ω was obtained at 0 h, 96 h and 188 h; while the R_i was 0.54 Ω, 0.53 Ω and 0.52 Ω at the corresponding soaking times, respectively. This indicates that the impedance behavior of the CF supercapacitor had no significant change with time

Capacitance plots (see Fig. 3.7(B)) show that the series capacitances linearly increased with the real impedance at high frequencies, and reached limiting values at low frequencies. The changes in the capacitance and resistance are due to the increasing penetration depth of the ac signal as the frequency is decreased.[17] It can be seen from Fig. 3.7(B) that the limiting capacitance increased from 0.96 F to 1.32 F after 96 h.

3.3.4 Ru oxide/CF composite supercapacitors

3.3.4.1 Cyclic voltammetry

The capacitive behaviors of symmetric supercapacitors with various loadings of Ru oxide on the CF electrodes were characterized by cyclic voltammetry as shown in Fig. 3.8. It can be seen that all of the supercapacitors illustrated high quality capacitive behaviors over the -1.0 V to 1.0 V (symmetric devices) range employed. Average specific capacitances derived from Fig. 3.8 are given in Table 3.1, which shows that the average specific capacitances increased with Ru oxide loading.

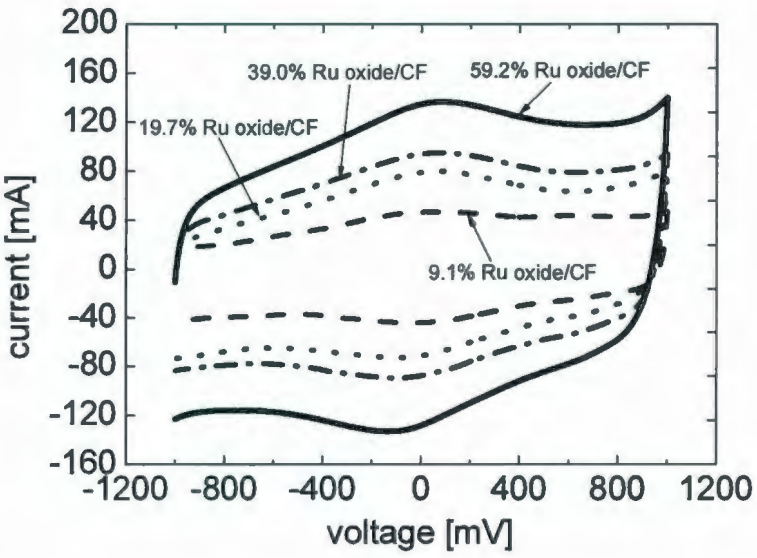

Fig. 3.8 Cyclic voltammograms (20 mV/s) for Ru oxide/CF composites with the specified loadings in 1 M H_2SO_4 after 17 h. The masses of the electrodes are specified in Table 3.1

Table 3.1 Specific capacitances for Ru oxide/CF composites in 1 M H_2SO_4 after soaking for 17 h

Ru oxide loading (%)	Electrode mass (mg)	C_{sp}(F/g) at 10 mA discharge	C_{sp} (F/g) by CV(20mV/s)	C_{sp}*(F/g) based on Ru oxide
9.1	14.4+14.5	280	248	978±60
19.7	19.9+19.9	264	294	779±24
39.0	21+21.5	383	340	599±9
59.2	26+26.5	427	402	559±4

* Based on C_{sp} =175±6 F/g for the CF and C_{sp} from cyclic voltammetry.

When the specific capacitances based on the Ru oxide components of the composites were calculated, the specific capacitances of the CF components of the composites were assumed to be the same as for the pristine CF. In fact, the specific capacitance of the CF component may decrease with increasing Ru oxide loading due to a

decrease in the available surface area. This simplification could therefore make the calculated results less than the true contributions of the Ru oxide components of the composites with high Ru oxide loadings.

Compared to pure Ru oxide (see Table 2.1) measured under similar conditions, the specific capacitance based on the Ru oxide component increased from 716±24 F/g to 978±60 F/g for the composite with a 9.1% loading. It is clear that the electrochemical utilization of Ru oxide was enhanced. This high utilization of Ru can be attributed to the high surface area of the CF and synergistic effects (see section 3.3.4.6). The high surface area not only allows Ru oxide to distribute as small particles on the CF surface, giving the electrolyte easy access to the bulk Ru oxide, but also provides possibilities for synergistic effects. The synergistic effects are discussed in section 3.3.4.6.

3.3.4.2 Impedance spectroscopy

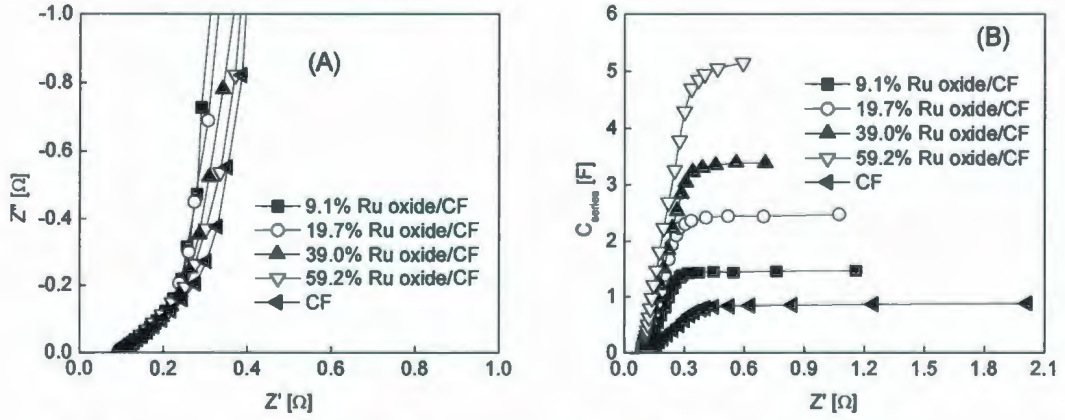

Fig. 3.9 Nyquist plots (A) and capacitance plots (B) for the Ru oxide/CF composite supercapacitors described in Fig. 3.8

The supercapacitors described in Fig. 3.8 were also characterized by impedance spectroscopy as shown in Fig. 3.9. Fig. 3.9(A) shows that all of the Nyquist plots have the characteristics for porous electrodes, including a ca. 45° linear region at high frequencies and a ca. vertical line at low frequencies. The ionic resistance (R_i) of the electrodes corresponds to three times the real impedance of the 45° region, while the equivalent series resistance (ESR) is given by the real impedance at high frequency (10 kHz).[18] ESR and R_i values derived from Fig. 3.9 are given in Table 3.2. All of the supercapacitors had a similar ESR of ca. 100 mΩ. Interestingly, the supercapacitors with Ru oxide/CF composite electrodes exhibited lower R_i values than the unmodified CF supercapacitor, and the R_i of the composite supercapacitors increased with increasing Ru oxide loading.

Table 3.2 Specific capacitances, ESR and R_i values for Ru oxide/CF composite supercapacitors

	ESR (Ω)	R_i (Ω)	C_{sp} (F/g)	C_{sp} (F/g) (based on Ru oxide)
0	0.11	0.62	144±9	
9.1%	0.099	0.45	203	798±87
19.7%	0.097	0.46	249	678±35
39.0%	0.099	0.51	319	593±17
59.2%	0.099	0.54	392	564±7

The decrease in the R_i was most likely due to the introduction of Ru oxide with high conductivity. It has been reported that the conductivity of Ru oxide is two orders of magnitude greater than the conductivity of the CF.[2, 19] As a consequence, the Ru oxide/CF composites should have higher conductivity than the CF, and the composites with higher Ru oxide loadings should have higher conductivity than those with low

loadings. However, the results from impedance spectroscopy show that the R_i increased with Ru oxide loading. This is presumably due to increased resistance due to the thicker Ru oxide layer on the carbon fibres.

Fig. 3.9(B) shows capacitance plots for the composite supercapacitors and the CF supercapacitor. It can be seen that the series capacitances increased with decreasing frequency, and reached limiting values at low frequencies. The real impedance also increased with decreasing frequency in that the parallel resistance mainly contributed to the total resistance.[17] The limiting specific capacitances derived from Fig. 3.9 are given in Table 3.2. They parallel the voltammetric results shown in Table 3.1, although all the values were lower. These differences in the series capacitances can be attributed to the voltage ranges of the measurements. The voltage range was -1 to 1 V for cyclic voltammetry, while it was 0.5±0.014 V for impedance spectroscopy. Fig. 3.8 shows that a relatively low capacitance was obtained from cyclic voltammety at cell voltages of ca. 0.5 V which used in the impedance measurement. In addition, the small amplitude excitation (10 mV) used in impedance spectroscopy usually gives a significantly lower capacitance for an electrochemical system, compared to the results from cyclic voltammetry.[7] An average specific capacitance of 144±9 F/g (six measurements) for the CF was used to calculate the specific capacitances based on the Ru oxide components of the composites shown in Table 3.2. It can be seen that the utilization of Ru oxide has been enhanced for the composites with low Ru oxide loadings (< 20%).

3.3.4.3 Constant current discharging

A supercapacitor with the 9.1% Ru oxide/CF composite electrodes was tested by constant current discharging as shown in Fig. 3.10. It can be seen that the discharge curves have sharp potential drops over the first few milliseconds due to the ESR of the cell. It is clear that the supercapacitor exhibited a potential-dependent capacitance, which agrees with cyclic voltammetry. Energy densities and power densities of the supercapacitor are discussed in the following section.

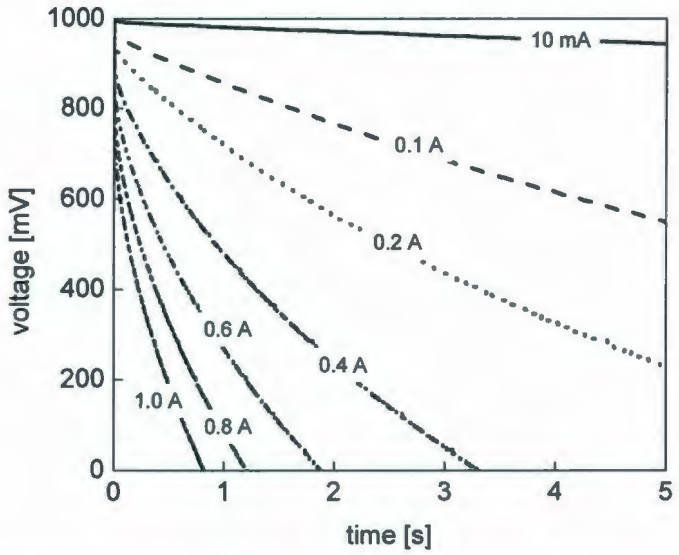

Fig. 3.10 Constant current discharging curves for a supercapacitor with 9.1% Ru oxide/CF composite electrodes and a NRE211 separator.

The average specific capacitances of the supercapacitors described in Fig. 3.8 were tested by constant current discharging at 10 mA and are given in Table 3.1. They parallel the results from cyclic voltammetry.

3.3.4.4 Addition of Nafion

Based on the discussion in Chapter 2, it was found that the addition of Nafion to Ru oxide electrodes significantly enhanced the performances of Ru oxide supercapacitors.[7, 8] Nafion provides good proton conduction pathways between the Ru oxide particles, thus increasing both the proton conductivity of the electrodes and the utilization of Ru oxide.

A piece of the 9.1% Ru oxide/CF sheet was immersed in a 1.5% Nafion solution for ca. 2 min, and was then dried for 2 h at 110 °C. The Nafion loading was estimated from the mass difference during the preparation. The resulting sheet contained 3.6% Nafion and 8.8% Ru oxide. Its electrochemical properties were characterized by cyclic voltammetry, impedance spectroscopy and constant current discharging as shown in Fig. 3.11. For comparison purposes, a 9.1% Ru oxide/CF supercapacitor was also characterized by these electrochemical methods.

Fig. 3.11(A) shows the Nyquist plots of the two supercapacitors. It can be seen that the Nyquist plots had distinct characteristics. The ESR values derived from Fig. 3.11(A) were 0.093 Ω and 0.13 Ω for the supercapacitors with 0% and 3.6% Nafion loadings, respectively. In contrast, R_i increased from 0.45 Ω to 2.02 Ω with the introduction of Nafion.

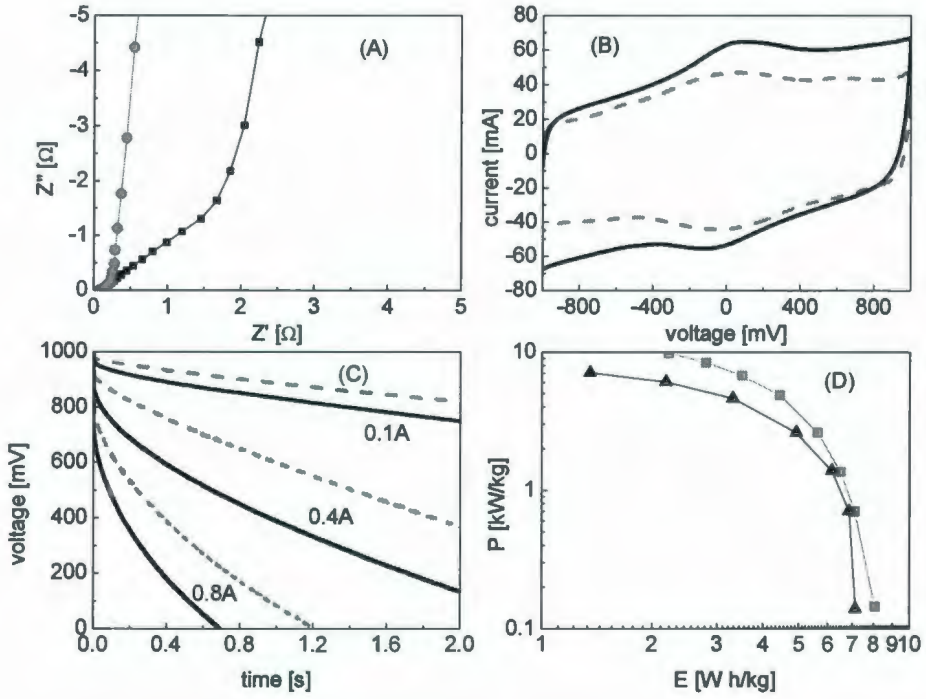

Fig. 3.11 Comparisons of the performances of two supercapacitors with Nafion (black color) and without Nafion (gray color). (A) Nyquist plots, (B) cyclic voltammograms, (C) capacitance plots, (D) Ragone plots. The electrode masses were 28.9 mg (14.4 mg +14.5 mg) for 9.1% Ru oxide/CF without Nafion and 30.1 mg (15.1 mg + 15.0 mg) for 8.76% Ru oxide/CF with 3.6 % Nafion.

Fig. 3.11(B) shows cyclic voltammograms of the two supercapacitors. The average specific capacitance of the supercapacitor with 3.6 % Nafion loading was better by 31 % than for the supercapacitor without Nafion. The increase in specific capacitance may be due to the establishment of proton conduction pathways between the Ru oxide particles. However, the increases in ESR and R_i are likely due to the presence of Nafion in pores (the ion conducting channels), because Nafion has much lower electronic conductivity than 1 M H_2SO_4.[1]

Constant current discharging curves (see Fig. 3.11(C)) show that the supercapacitor with Nafion exhibited a much higher voltage drop over the first few milliseconds due to the high ESR. The energy densities and power densities were calculated according to Eq. 1.5 and Eq. 1.6 in Chapter 1.

Ragone plots (see Fig. 3.11(D)) shows that both the usable energy and power densities for the supercapacitor with Nafion were lower than those for the supercapacitor without Nafion at the same discharge current. The maximum energy densities were 7.1 W h/kg and 8.1 W h/kg for the supercapacitors with Nafion and without Nafion, respectively, while the best power densities were 7.1 kW/kg and 9.8 kW/kg for the corresponding supercapacitors. It is clear that the addition of Nafion cannot improve the performance of the Ru oxide/CF supercapacitor due to the high ESR and R_i.

3.3.4.5 Cycling rate

Supercapacitors with 9.1% Ru oxide/CF composite, Ru oxide and CF electrodes were characterized by cyclic voltammetry over a range of scan speeds as shown in Fig. 3.12, in order to determine how fast they could be cycled. Fig. 3.12(A) shows cyclic voltammograms for a 9.1% Ru oxide/CF composite, while Fig. 3.12(B) shows specific capacitances as a function of scan speed. It is clear that the specific capacitances for both the Ru oxide component of the composite and the pure Ru oxide decreased with increasing scan speed. Apparently, the Ru oxide component exhibited much higher specific capacitances than pure Ru oxide at the same scan rates. For example, the specific capacitances based on the Ru oxide component were 1071, 897 and 579 F/g at 20, 100

and 400 mV/s, respectively, while the specific capacitances for the pure Ru oxide electrodes were 543, 451 and 325 F/g at the corresponding scan rates. The high rate specific capacitances may be attributed to the high surface area of the CF, allowing Ru oxide to distribute as small particles. This distribution allows Ru oxide to be available to the electrolyte even at high scan rates, resulting in high capacitances.

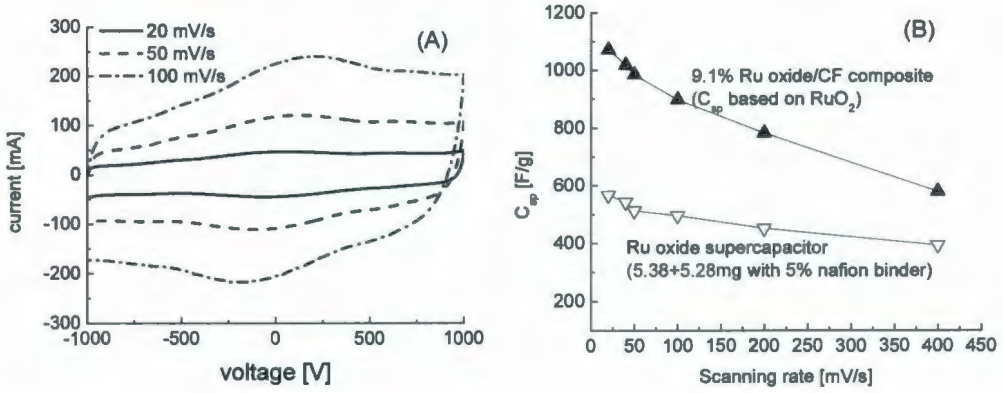

Fig. 3.12 Cyling rate, (A) cyclic voltammograms of 9.1% Ru oxide/CF composite (B) comparisons of capacitances as a function of scan rate for various capacitors.

3.3.4.6 Synergistic effects

In order to investigate synergistic effects (interactive effects, which include physical and chemical processes between two materials) between the CF and the Ru oxide component, a CF supercapacitor and a Ru oxide/CF composite supercapacitor were characterized by cyclic voltammetry and impedance spectroscopy using three-electrode and two-electrode configurations. Impedance experiments were conducted at different DC bias potentials. The performances of the supercapacitors were tested by constant current discharging experiments at 10 mA.

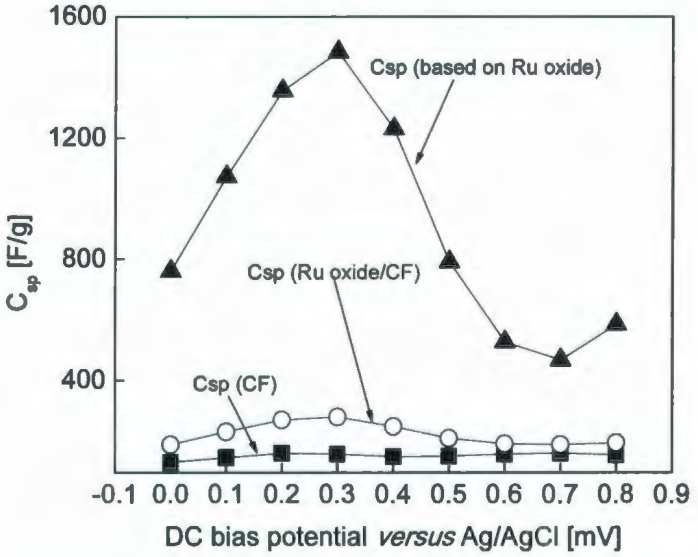

Fig. 3.13 Potential-dependence of the capacitances for a 9.2% Ru oxide/ CF composite (13.9 mg) and a CF electrode (15.29 mg)

Impedance spectroscopy. The capacitances of the CF and 9.2% Ru oxide/CF composite electrodes were characterized at 10 mHz at different DC bias potentials. Their specific capacitances and the specific capacitances for the Ru oxide component are plotted as a function of DC bias potential in Fig. 3.13. It can be seen that there was a wide specific capacitance peak over the potential range of 0.0 V to 0.5 V versus Ag/AgCl. The peak specific capacitance for the Ru oxide component reached 1485 F/g at 0.3 V versus Ag/AgCl, which is higher than the theoretical value of 1280 F/g (based on $RuO_2 \cdot H_2O$) for a two-proton intercalation process. This high specific capacitance may be due to a synergistic effect between the Ru oxide component and the CF, resulting in an increase in functional groups (such as quinone groups) with pseudocapacitance. A variety of functional groups exist on the CF surface as discussed in section 3.3.3.1. Among these

groups, quinone structures are most likely involved in the synergistic effects, because the peak position is close to the redox peak of quinone/hydroquinone-type couples in H_2SO_4.

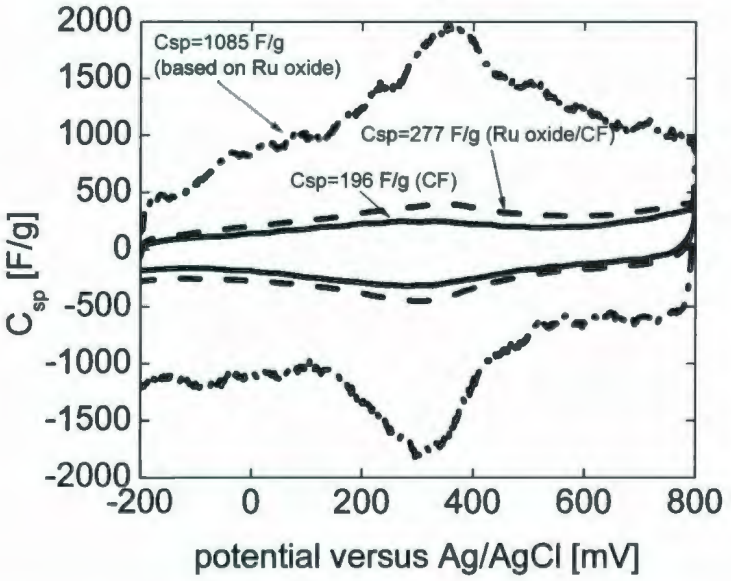

Fig. 3.14 Cyclic voltammograms (5 mV/s) for 9.2% Ru oxide/CF composite and CF electrodes.

Cyclic voltammetry. The CF and the 9.2% Ru oxide/CF composite electrodes were also characterized by cyclic voltammetry using a three-electrode configuration as shown in Fig. 3.14. Here, the current responses were converted to specific capacitance. It can be seen that there was a specific capacitance peak for the Ru oxide component at ca. 0.3 V versus Ag/AgCl. The peak specific capacitances were 1984 F/g and 1824 F/g at 368 mV (anodic) and 296 mV (cathodic), respectively. An average specific capacitance of 1085 F/g based on the Ru oxide component was obtained, while the average specific capacitance of the symmetric supercapacitor was 1313 F/g over the voltage window of -1.0 V to 1.0 V. These values are comparable with results in the literature.[4, 20-23]

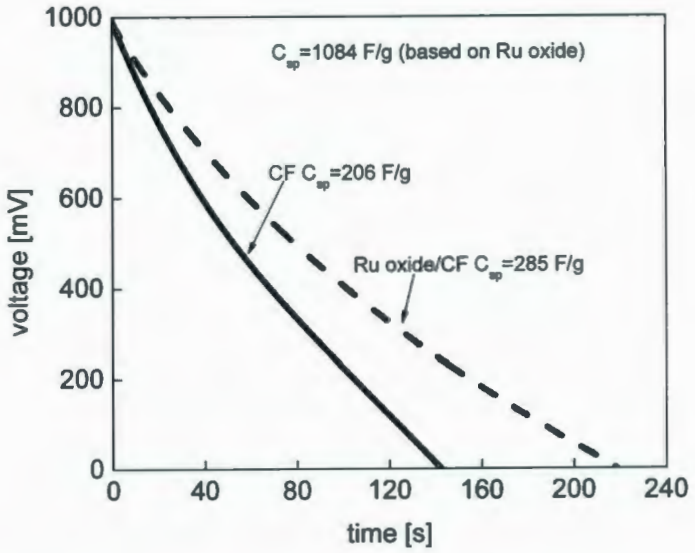

Fig. 3.15 Discharging curves for CF and 9.2% Ru oxide/CF composite supercapacitors. The CF supercapacitor consisted of 27.8 mg (13.9 mg +13.9 mg) CF, while the composite supercapacitor consisted of 30.76 mg (15.29 mg + 15.47 mg) of 9.2% Ru oxide/CF.

Constant current discharging. The charge storage capacities of the CF and 9.2% Ru oxide/CF supercapacitors were also tested by constant current discharging at 10 mA as shown in Fig. 3.15. It can be seen that the 9.2% Ru oxide/CF supercapacitor had a much longer discharge time than the CF supercapacitor. The specific capacitances were 206 F/g and 285 F/g for the CF and 9.2% Ru oxide/CF composite supercapacitors, respectively. The specific capacitance based on the Ru oxide component was 1084 F/g, which agrees with the result from cyclic voltammetry.

In summary, the high utilization of Ru in the composite is due to the synergistic effects between the CF and Ru oxide component with high surface area. The Ru oxide component with high surface area enhances not only the accessibility of the sulfuric acid electrolyte, but also the synergistic effects.

3.3.4.7 Stability

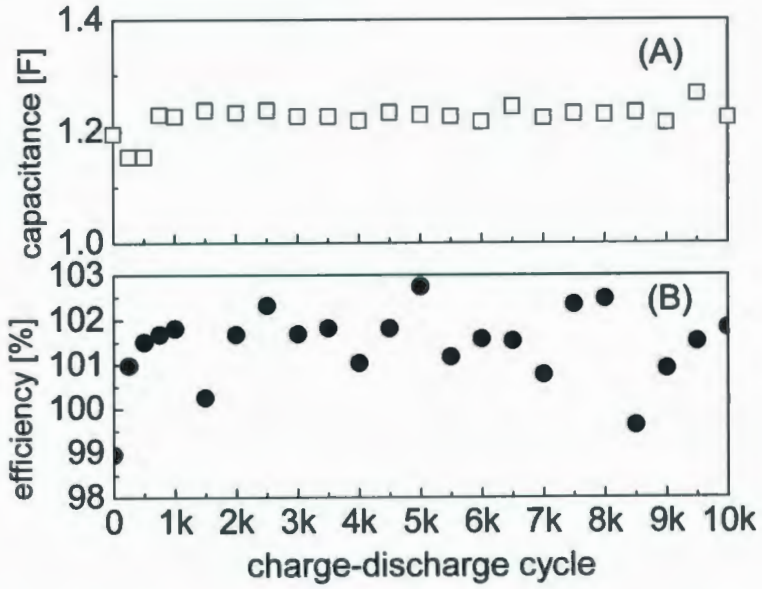

Fig. 3.16 Reversibility of a 10.0% Ru oxide/CF composite supercapacitor at 100 mA/cm^2. (A) Capacitance versus cycle number (B) charge-discharge efficiency. The electrode mass was 27.6 mg (13.7 mg +13.9 mg).

A supercapacitor consisting of a 10.0% Ru oxide/CF composite was repeatedly charged to 1.0 V at 100 mA/cm^2, then discharged to 0 V using the same current. The capacitances are plotted as a function of cycle number in Fig. 3.16(A). It can be seen that the supercapacitor had a slightly lower capacitance (ca 1.15 F) over the first 500 cycles. However, the capacitance increased to 1.23 F by ca. 750 cycles, then maintained this value until 10000 cycles. This shows that the composite supercapacitor had good stability. The increase in capacitances may have been due to a shift of the open circuit potential and the fact that CF develops its quinone peaks over the first 500 cycles.

Fig. 3.16(B) shows the relationship between the charge-discharge efficiency and cycle number. It can be seen that the efficiencies were between 99% and 103%. This indicates that the supercapacitor has very good reversibility.

3.4 Conclusions

Ru oxide/CF composites were prepared by impregnating the CF with a colloidal hydrous Ru oxide solution. Their textural properties were characterized by SEM which showed that Ru oxide particles evenly deposited on the CF surface for a composite with a low loading of Ru oxide (below 20%). However, most Ru oxide particles occupy the spaces between the fibers for composites with high loadings (above 20%).

The capacitive behaviors of the CF and Ru oxide/CF composite electrodes were characterized by cyclic voltammetry, impedance spectroscopy and constant current discharging. The specific capacitance of CF increased with soaking time in the sulfuric acid electrolyte, and this was attributed to an increase in pseudocapacitive quinone-type groups on the CF surface. A maximum specific capacitance of 237 F/g was obtained after soaking for 212 h. The specific capacitances of the composites increased with Ru oxide loading. However, the specific capacitances based on the Ru oxide component decreased with increasing loading. A specific capacitance of 1085 F/g based on the Ru oxide component was obtained for a 9.2% Ru oxide/CF supercapacitor measured by cyclic voltammetry. The high specific capacitance was ascribed to the synergistic effects between functional groups on the CF surface and the Ru oxide component with high surface area. The conductivity of the CF composites was enhanced by the introduction of

Ru oxide. Although the addition of Nafion can enhance the capacitances of composites, only low performance was obtained due to the high ESR and R_i.

References

1. Liu, X. R.; Pickup, P. G., *Journal of Solid State Electrochemistry* **2010,** *14* (2), 231-240.

2. Pandolfo, A. G.; Hollenkamp, A. F., *Journal of Power Sources* **2006,** *157* (1), 11-27.

3. Kotz, R.; Carlen, M., *Electrochimica Acta* **2000,** *45* (15-16), 2483-2498.

4. Hu, C. C.; Chen, W. C.; Chang, K. H., *Journal of the Electrochemical Society* **2004,** *151* (2), A281-A290.

5. Zhang, J. R.; Jiang, D. C.; Chen, B.; Zhu, J. J.; Jiang, L. P.; Fang, H. Q., *Journal of the Electrochemical Society* **2001,** *148* (12), A1362-A1367.

6. Lee, B. J.; Sivakkumar, S. R.; Ko, J. M.; Kim, J. H.; Jo, S. M.; Kim, D. Y., *Journal of Power Sources* **2007,** *168* (2), 546-552.

7. Liu, X. R.; Pickup, P. G., *Journal of Power Sources* **2008,** *176* (1), 410-416.

8. Liu, X. R.; Pickup, P. G., *Energy & Environmental Science* **2008,** *1* (4), 494-500.

9. Jang, J. H.; Han, S.; Hyeon, T.; Oh, S. M., *Journal of Power Sources* **2003,** *123* (1), 79-85.

10. Panic, V.; Vidakovic, T.; Gojkovic, S.; Dekanski, A.; Milonjic, S.; Nikolic, B., *Electrochimica Acta* **2003,** *48* (25-26), 3805-3813.

11. Kim, Y. T.; Ito, Y.; Tadai, K.; Mitani, T.; Kim, U. S.; Kim, H. S.; Cho, B. W., *Applied Physics Letters* **2005,** *87* (23), -.

12. Frackowiak, E.; Beguin, F., *Carbon* **2001,** *39* (6), 937-950.

13. Rafiee, M.; Nematollahi, D., *Electroanalysis* **2007,** *19* (13), 1382-1386.

14. Garten, V. A.; Weiss, D. E., *Australian Journal of Chemistry* **1955,** *8* (1), 68-95.

15. Qu, D. Y., *Journal of Power Sources* **2002,** *109* (2), 403-411.

16. Liu, X. R. a. P., G.P., *Journal of Solid State Electrochemistry* **2009**.

17. Rafik, F.; Gualous, H.; Gallay, R.; Crausaz, A.; Berthon, A., *Journal of Power Sources* **2007,** *165* (2), 928-934.

18. Lefebvre, M. C.; Martin, R. B.; Pickup, P. G., *Electrochemical and Solid State Letters* **1999,** *2* (6), 259-261.

19. Zheng, J. P.; Cygan, P. J.; Jow, T. R., *Journal of the Electrochemical Society* **1995,** *142* (8), 2699-2703.

20. Pico, F.; Ibanez, J.; Lillo-Rodenas, M. A.; Linares-Solano, A.; Rojas, R. M.; Amarilla, J. M.; Rojo, J. M., *Journal of Power Sources* **2008,** *176* (1), 417-425.

21. Park, J. H.; Ko, J. M.; Park, O. O., *Journal of the Electrochemical Society* **2003,** *150* (7), A864-A867.

22. Kim, H.; Popov, B. N., *Journal of Power Sources* **2002,** *104* (1), 52-61.

23. Kim, I. H.; Kim, J. H.; Kim, K. B., *Electrochemical and Solid State Letters* **2005,** *8* (7), A369-A372.

Chapter 4 Nanostructured Ru oxide/carbon nanotube composites for supercapacitors

This work has been published in Electrochimica Acta: Xiaorong Liu, Trisha A. Huber, Michael C. Kopac, and Peter G. Pickup, (2009), *Ru oxide/carbon nanotube composites for supercapacitors prepared by spontaneous reduction of Ru(VI) and Ru(VII)*, Electrochimica Acta, 54 (27): 7141-7147.

The experimental sections have been reproduced in part from our paper which is a published account of the work described in this chapter.[22] This text was written in part by Dr. Peter Pickup.

4.1 Introduction

Carbon nanotubes (CNTs), as one of the allotropes of carbon, were first discovered by Sumio Iijima in 1991.[1] The diameters of CNTs are on the order of a few nanometers, and their length may be a few millimeters. CNTs are one of most promising energy storage materials, and receive extensive attention due to their nanostructures and excellent electrical properties, and especially their potential applications in Li-ion batteries,[2-5] hydrogen storage[6-9] and supercapcitors.[10-19]

There are two types of CNTs, single-walled and multi-walled nanotubes consisting of concentric tubes of graphene. Their structures depend on the synthesis method. Single-walled carbon nanotubes (SWCNTs) possess higher specific surface areas (typically > 1000 m^2/g) than multi-walled carbon nanotubes (MWCNTs). Both types of

CNTs can be used as electrode materials for supercapacitors. However, the charge storage capabilities (typically < 100 F/g) of CNTs are relatively low due to their low surface area (typically below 1000 m^2/g), compared to engineered carbon materials (up to 200 F/g in aqueous media). In addition, CNTs are much more expensive than other carbon-based materials, so there is still a long way to go before the commercialization of supercapacitors built on CNTs.

The functionalization of CNTs is a good way to overcome some of these shortcomings. Functionalized materials not only possess the advantages of both CNTs and the modifying compounds or functional group, but also can provide high specific capacitances.

Among these functionalized nanotube composites, Ru oxide/CNTs are the most promising materials for supercapacitors due to the high specific capacitance and excellent proton and electronic conductivity of Ru oxide. Kim *et al.*[14, 16] prepared Ru oxide/CNT films by an electrochemical deposition method. The specific capacitances for the Ru oxide components of composites with low loadings (<17%) were over 1170 F/g. The high specific capacitance can be attributed to the thin and uniform deposition of Ru oxide on the surfaces of the thin CNT films.

Nanostructured Ru oxide should improve the utilization of Ru in composites because of its high accessibility to electrolytes. Park *et al.*[20] prepared Ru oxide/CNT composites by a heat-treatment process using ruthenium ethoxide as a precursor. The Ru oxide nanoparticles were as small as 1 nm in diameter. Ru oxide/CNT composites prepared using CNTs that had been treated with nitric acid showed much higher

capacitances than the pristine CNT; 900 F/g and 500 F/g based on the Ru oxide components were obtained, respectively. This enhancement of the apparent utilization of ruthenium was attributed to hydrophilic functional groups produced by acid-treatment. The hydrophilic groups increase not only the specific capacitance of the CNT, but also the number of Faradaic reaction sites of the Ru oxide nanoparticles. However, the best specific capacitance obtained for the Ru oxide component was less than for some other carbon-based composites. For instance, the specific capacitance of the Ru oxide component reached 1450 F/g for a Ru oxide/activated carbon composite.[21] Nonetheless, Ru oxide/CNT composites are still very promising materials for supercapacitors due to the potential of their 3-D nanostructures to maximize the utilization of Ru.

In this chapter, a novel method for preparing Ru oxide/CNT is described. Ru(VI) and Ru(VII) compounds were spontaneously reduced by functional groups on the CNTs in order to deposit hydrous Ru(IV) oxide on their surfaces. One advantage of this novel method is that uniform deposition of Ru oxide particles can be obtained because the deposition processes are strongly dependent on the presence of suitable functional groups on the nanotubes. Another advantage is that the CNTs do not need to be pretreated by acid, since the Ru(VI) and Ru(VII) compounds are strong oxidizing agents that can oxidize the CNTs, thus increasing the number of functional groups with pesduocapacitive behaviors.

Composites were also prepared by sol-gel and physical mixing methods (see chapters 2 and 3) for comparison purposes. The properties of the Ru oxide/CNT

composites were characterized by SEM, TEM, TGA, cyclic voltammetry, impedance spectroscopy, and constant current discharging.

4.2 Experimental

4.2.1 Materials

Purified and functionalized Nanocyl multiwalled carbon nanotubes (MWCNTs) were provided by Dr. Trisha Huber's lab at DRDC Atlantic Pacific Dockyard. The residual metal content of the purified MWCNT (Fe and Co) was ca. 0.02%.[23] The degree of acid functionality of the fuctionalized MWCNT was reported to be 4.1 ± 0.4 mequiv/g, which indicates that roughly 1 in 20 carbon atoms were functionalized.[22]

The following materials were used as purchased: Na_2O_2 (Aldrich), $KRuO_4$ (Alfa Aesar), Na_2CO_3 (MERCK KGaA), H_2SO_4 (Fisher Scientific), Nafion film (N115 from Ion Power, Inc), Ti plate (25 micron, Aldrich), $RuCl_3 \cdot xH_2O$ (Precious Metals Online Pty Ltd.), and carbon fibre paper (CFP; Toray™ Carbon Paper, TGP-H-090), nickel crucible (Aldrich), glass fibre paper (Nippon Sheet Glass Co., Ltd.).

4.2.2. Preparation of composites by spontaneous reduction of Ru(VI) and Ru(VII)

Both purified (p-MWCNT) and functionalized multiwalled carbon nanotubes (f-MWCNTs) were used for preparing Ru oxide/MWCNT composites. Ru (VI) solutions were prepared as follows.[24] Ru oxide (0.43 g) prepared by a sol-gel method [25] mixed with a large excess of NaOH (4.6 g) using an agate mortar with a pestle was placed in a 50 mL

nickel crucible with a cover, which was then placed in a preheated oven at 550 °C. After fusion for ca. 20 min, Na_2O_2 (0.95 g) was added with light agitation of the Ni crucible. The sample was then heated at 550 °C for a further 10 min. The cooled product was dissolved in deionized water (200 mL), and the solution was filtered through glass fibre paper.

p-MWCNTs (0.125 g) were added to 50 mL of Ru(VI) solution, and the mixture was stirred using a magnetic bar until the supernatant solution was colorless (typically within 24 h). The resulting Ru oxide/p-MWCNT was collected by filtration and washed with deionized water until the filtrate was neutral. The composite was then allowed to age in ca. 1 mL of deionized water for 2 weeks in order to form a stable film structure.

Table 4.1 Details of the preparation and TGA results of Ru oxide/p-MWCNT composites prepared with $KRuO_4$

Sample #	MWCNT(g)	$KRuO_4$ (g)	reaction time (h)	TGA residue (%)	$RuO_2 \cdot 2H_2O$%
090212	0.16	0.089	23	26.1	30.4
090303	0.14	0.082	43	27.6	32.3
090309	0.16	0.041	23	14.6	17.2

Ru oxide (0.2 g) prepared by a sol-gel method,[25] NaOH (6.6 g) and Na_2O_2 (1.8 g) was used to prepare a 200 mL Ru(VI) solution as described above. f-MWCNTs (0.25 g) were soaked in 100 mL of this Ru(VI) solution under stirring for 1 week, which did not cause bleaching of the solution. 2.4 M HCl was slowly added until pH ~ 7, and the mixture was heated to 70-80 °C for 5 min. The resulting Ru oxide/f-MWCNT composite was collected by filtration (Whatman 4) and washed with copious deionized water until

the filtrate was neutral. Unlike the Ru oxide/p-MWCNT composites, which were obtained as powders, the Ru oxide/f-MWCNT composite was gelatinous.

Ru oxide/p-MWCNT composites were also prepared by reaction with commercial $KRuO_4$. The p-MWCNTs were dispersed in water by sonicating for 2 h, and then a 0.05 M solution of $KRuO_4$ in 0.1 M KOH was added. Following stirring for 23 h or 43 h, the resulting Ru oxide/p-MWCNT was collected by filtration (Whatman 4) and washed with deionized water. Details of the preparations are given in Table 4.1.

4.2.3 Composites prepared by sol-gel and physical mixing methods

For comparison purposes, a composite was also prepared by preparing hydrous Ru oxide[25] *in situ* by a sol-gel method. Thus, p-MWCNTs (65 mg) were added to a $RuCl_3$ solution (12 mL with 2.26 mg $RuCl_3.xH_2O$ per mL), and the mixture was stirred using a magnetic bar for ca. 30 min. 1.5 M Na_2CO_3 (aq) was then slowly added until pH ~ 7. The mixture was then heated to 70-80 °C for 5 min. The composite was collected by filtration and washed with copious deionized water until the filtrate was neutral. The final composite was aged in deionized water for 1 week.

Some colloidal Ru oxide particles passed through the filter paper (Whatman 4) during the filtration. The filtrate was collected in a beaker and evaporated to dryness. The resulting gel was then dried at room temperature for 2 days, and washed 10 times with a small amount of deionized water to remove salts. The final powder was dried at room temperature until a stable mass (8.53 mg) was obtained. This mass was subtracted from the theoretical mass of ruthenium oxide when the loading was calculated.

In order to measure the mass of Ru oxide added to the p-MWCNTs, another 12 mL of $RuCl_3$ solution (2.26 mg/mL) was used to prepare hydrous Ru oxide in the absence of CNTs, and a dry mass (RT) of 19.16 mg was obtained. A Ru oxide loading of 14.1% was thereby estimated for the composite (based on 19.16 mg - 8.53 mg = 10.63 mg Ru oxide).

A Ru oxide/p-MWCNT composite was also prepared by a physical mixing method (see section 3.2).[26] Hydrous Ru oxide prepared by a sol-gel method was first annealed at 110 °C for 3 h. Hydrous Ru oxide powder (13.16 mg) was placed in a 5 mL vial with 4 mL of deionized water, then sonicated for 1 h. The hydrous Ru oxide suspension was then added to 52.89 mg p-MWCNTs in a 20 mL vial, and stirred using a magnetic bar for 30 min. The mixture was slowly evaporated to dryness with stirring, and then dried in an oven at 150 °C for 1 h. The final loading of the composite was 19.9 %.

4.2.4. Transmission electron microscopy (TEM) and scanning electron microscopy

TEM images were acquired on a Hitachi H-7000 transmission electron microscope by Dr. Trisha Huber. SEM images were obtained on a FEI Quanta 400 environmental SEM at different magnification.

4.2.5. Energy Dispersive X-Ray Emission Spectroscopy (EDX)

EDX was utilized to confirm the presence of ruthenium and semi-quantitatively determine the ruthenium content. EDX was conducted on a FEI Quanta 400 environmental SEM at 25 kV.

4.2.6. Thermogravimetric analysis (TGA)

TGA of samples was performed on a TA Instruments Q500 TGA analyzer under a N_2 atmosphere (sample gas, 60 mL/min; balance gas, 40 mL/min). The air trapped in the furnace of the TGA instrument was not removed completely before starting experiments, so the actual atmosphere of experiments was a mixture of air and N_2.

4.2.7. Electrodes and supercapacitors

Electrodes (1 cm^2) were prepared by spreading a weighed amount of wet composite onto a CFP disc. For powder electrode materials, they were first mixed with a few drops of deionized water to form a paste. Electrodes were prepared by smearing the paste onto a CFP disc. The assembly of supercapacitors (Nafion N115 as separator) was the same as for the Ru oxide supercapacitors described in Chapter 2.

4.2.8. Electrochemical measurements

Electrochemical measurements were made on supercapacitors immersed in 1 M H_2SO_4 in the presence of air. An Ag/AgCl reference electrode in this electrolyte solution was used to provide a reference potential in 3-electrode experiments. After all measurements were completed, the Ru oxide/MWCNT composite was carefully collected, washed until neutral, dried at room temperature, and then weighed.

4.3 Results and discussion

4.3.1 Spontaneous reduction methods

Spontaneous reduction methods are very attractive for preparing nanostructured Ru oxide/carbon composites in that the deposition of Ru oxide is a self-assembly process, which is controlled by redox reactions between Ru(VI) or Ru(VII) and functional groups on the carbon surface. On the other hand, the functional groups act as positioning and reduction agents. These may be carboxyls, phenols, lactones, and carbonyls as well as quinones and quinone-like structures, carboxylic anhydrides, lactols and others.[27] It is unclear what reactions will occur while Ru oxide is depositing, because a variety of groups may be involved in the processes. However, we can modify carbon with desirable groups, and thus should be able to control the deposition processes. Obviously, Ru oxide/carbon composites with different structures can be obtained by adjusting either the concentration of Ru(VI) or Ru(VII) or modifying carbon surfaces.

4.3.1.1 Thermogravimetric analysis

The thermal dynamic properties of Ru oxide/p-MWCNT composites and blank p-MWCNT were characterized by TGA as shown in Fig. 4.1 and Fig. 4.2. It can be seen that the Ru oxide/p-MWCNT composites gradually lost mass with increasing sample temperature until they reached stable masses (residual mass). The mass losses can be attributed to the loss of water adsorbed on the surfaces of the composites, dehydration of the hydrous Ru oxide and the oxidation of the p-MWCNT component. The residual

masses of the composites should be due to anhydrous Ru oxide and the trace ash content of the p-MWCNT component, and can be used to estimate Ru oxide loading. The residual mass was negligible for the blank p-MWCNT as shown in Fig. 4.1.

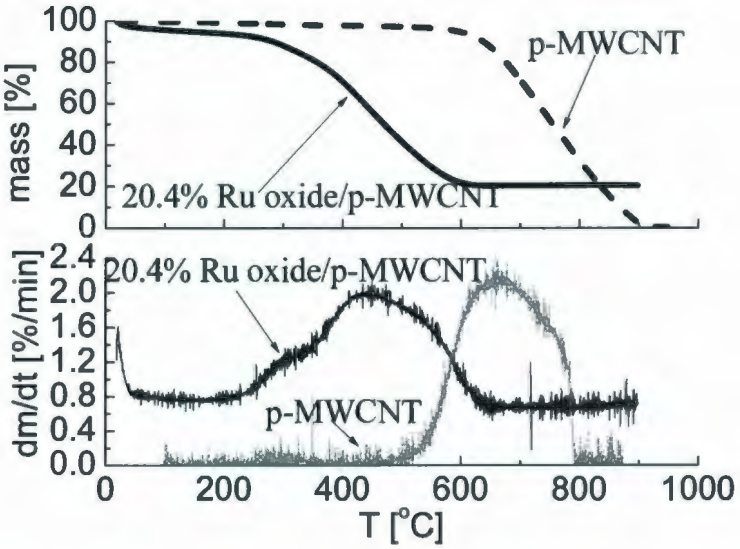

Fig. 4.1 TGA curves for a 20.4% Ru oxide/p-MWCNT composite (2.73 mg, ramp 5 °C/min to 900 °C) prepared with Ru(VI) and p-MWCNT (1.93 mg, ramp 5 °C/min to 1000 °C)

The rate of the mass change can further be evaluated by the differential mass loss as shown in Fig. 4.1 and 4.2. It can be seen that the differential curves for the composites possessed two peaks. The peak at low temperatures (< 100 °C) can be attributed to the loss of water adsorbed on the surfaces of the composite. The wide peak with a shoulder between 200 °C and ca. 600 °C can be ascribed to the slow dehydration of the hydrous oxide and the oxidation of the p-MWCNT component. The p-MWCNT only showed one differential peak between 500 °C and 800 °C, corresponding to the oxidation of the p-

MWCNT. It is clear that the composites have much lower oxidation temperatures. This can be attributed to the catalytic effect of the Ru oxide components.[28, 29]

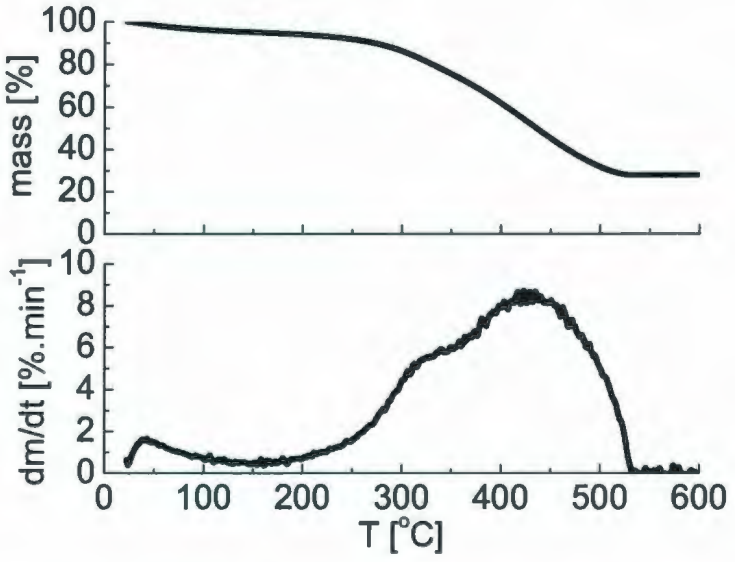

Fig. 4.2 TGA curve for a 27.6% Ru oxide/p-MWCNT composite prepared with $KRuO_4$ (4.00 mg, ramp 25 °C/min to 800 °C)

It has been reported that the hydration number is 2.00 for as-prepared hydrous Ru oxide.[30] This can be used to estimate the hydrous Ru oxide loading of composites according to TGA results. Fig. 4.1 shows a residual mass of 20.4%, which is taken to be the anhydrous Ru oxide (RuO_2). This corresponds to a hydrous oxide ($RuO_2 \cdot 2H_2O$) loading of 25.1%. A theoretical $RuO_2 \cdot 2H_2O$ loading of 25.9% was obtained based on the amount of Ru(VI) employed in the synthesis. The TGA result therefore agrees with the target composition. This shows that the Ru(VI) was completely deposited on the p-MWCNT. For the composite prepared with Ru(VII), the $RuO_2 \cdot 2H_2O$ loading (32.3%)

from TGA was similar to the targeted loading (32.7%) calculated by the mass of $KRuO_4$ employed in this synthesis.

Comparing the results in Fig. 4.1 and Fig. 4.2 shows that there were no significant differences between the TGA curves of the two composites. This indicates that they had similar thermal stabilities.

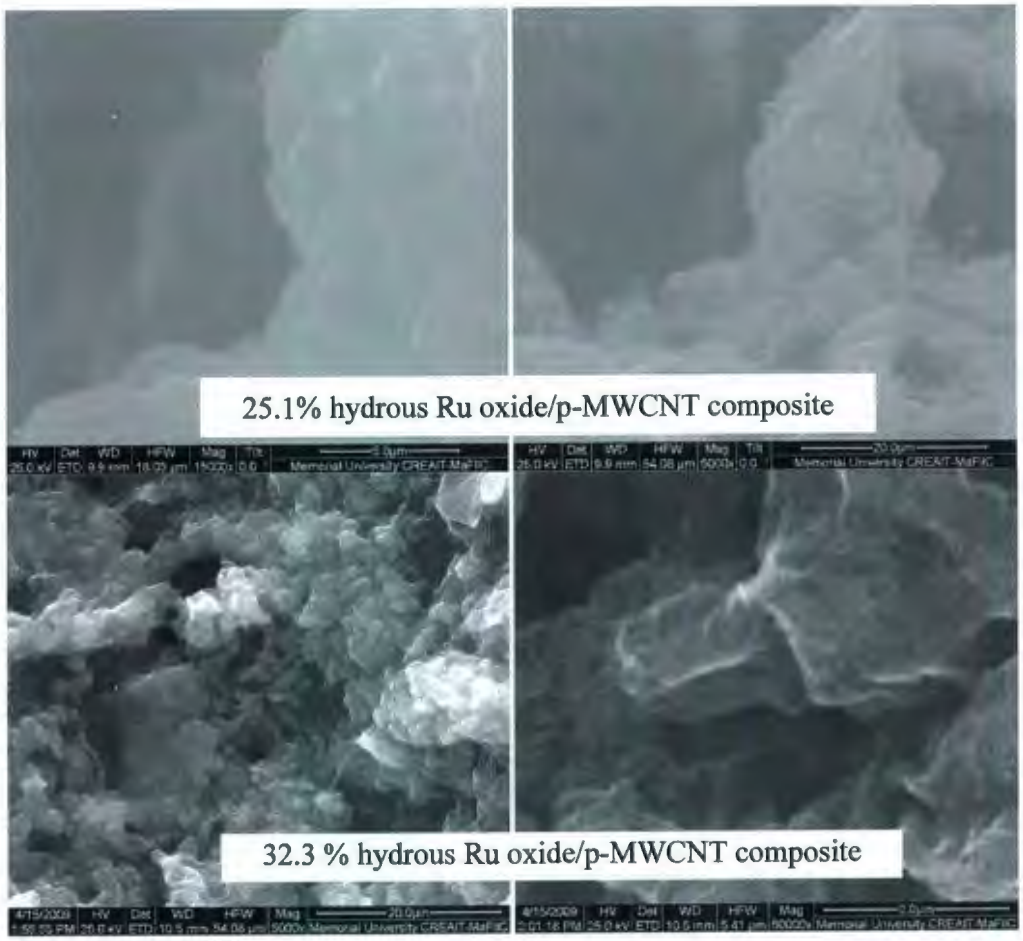

Fig. 4.3 SEM images of Ru oxide/p-MWCNT composites

4.3.1.2 Scanning electron microscopy

Textural characteristics of Ru oxide/p-MWCNT composites prepared with either Ru(VI) or Ru(VII) were characterized by SEM (Fig. 4.3). It can be seen that both of the composites consisted of small particles with porous structures. No expected nanotube structures were observed due to the resolution limitation of the SEM instrument.

4.3.1.3 Transmission electron microscopy

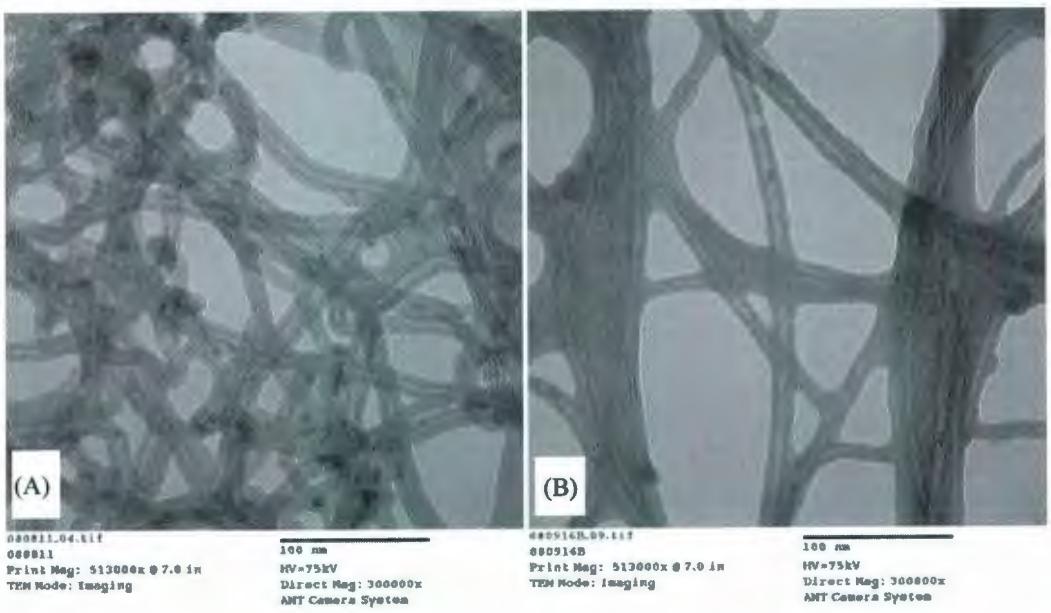

Fig. 4.4 TEM images of Ru oxide/MWCNT composites. (A) 25.1% hydrous Ru oxide/p-MWCNT (B) 15.6% hydrous Ru oxide/f-MWCNT.

High resolution images of both Ru oxide/p-MWCNT and Ru oxide/f-MWCNT composites were obtained by TEM (see Fig. 4.4). It can be seen that both samples displayed nanotube structures with diameters of ca. 15 nm. The small dark spots with

nanometer dimensions can be attributed to Ru oxide, which distributed mainly at the intersections of the nanotubes. A greater uniformity in the distribution of Ru oxide particles was observed for the Ru oxide/p-MWCNT composite, and the particle size ranged from < 1 nm to ca. 3 nm, as illustrated in Fig. 4.4(A). Unlike the Ru oxide/p-MWCNT, the Ru oxide/f-MWCNT composite illustrated much less homogeneity as for the distribution of Ru oxide particles, which ranged from 1 nm to 9 nm as shown in Fig. 4.4(B). The difference in Ru oxide particle size distribution may suggest that the surface functionality influenced the Ru oxide deposition process in that the surface functionality has different redox properties.

The TEM images also show different appearances for the composites. The Ru oxide/f-MWCNT composite exhibited apparent coating layer structures, whereas these were less pronounced for the Ru oxide/p-MWCNT composite. The apparent coating layers can be attributed to the deposition of Ru oxide particles. The difference in appearances may be ascribed to the different deposition rate of Ru oxide particles. For the f-MWCNT, the deposition rate of Ru oxide was very slow, thus leading to apparent coating layer structures.

4.3.1.4 Energy dispersive X-ray emission spectroscopy

EDX was used to confirm the presence of ruthenium and estimate the Ru oxide loading. Fig. 4.5 shows the EDX of a 32.3% hydrous Ru oxide/p-MWCNT composite. It can be seen that the composite consisted of the expected C, O and Ru, but also had a K impurity (from $KRuO_4$). The qualitative analysis results are given in Table 4.2. It can be

seen that the total percentage of oxygen was higher than the targeted value (as RuO_2). The functionalization of the MWCNT by $KRuO_4$ and water also contribute to the total O percentage. The mass concentration of Ru is 11.7%, which is lower than the result from TGA (21.0%). This deviation may be attributed to the small amount of sample for EDX. Overall, EDX only provides semiquantitative results, and accurate loadings should be obtained by chemical analysis or TGA.

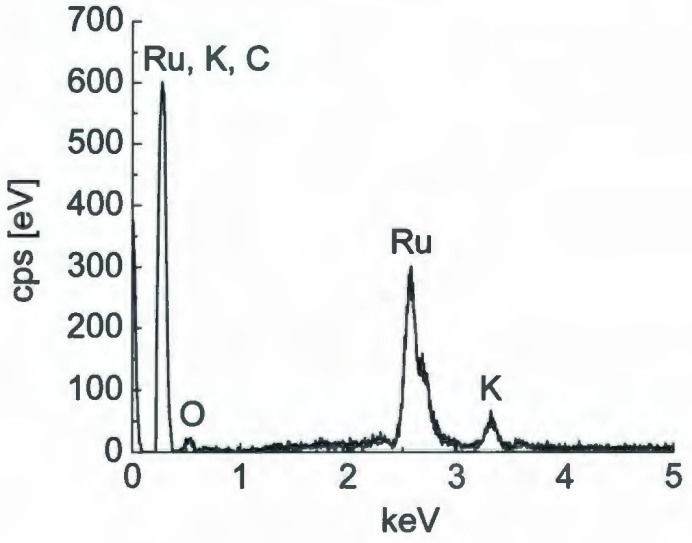

Fig. 4.5 EDX for a 27.6% Ru oxide/p-MWCNT composite

Table 4.2 EDX analysis for a 27.6% Ru oxide/p-MWCNT composite

Element	Series	Unnormalized. Concentration [mass %]	Normalized. Concentration [mass %]	Atomic. Concentration [atomic %]
Ruthenium	L-series	11.70	11.70	1.64
Carbon	K-series	69.89	69.89	82.57
Potassium	K-series	1.03	1.03	0.37
Oxygen	K-series	17.38	17.38	15.41

4.3.1.5 Cyclic voltammetry

The capacitive behavior of the 25.1% Ru oxide/p-MWCNT composite was characterized by cyclic voltammetry as shown in Fig. 4.6. It can be seen that a symmetric capacitance peak at ca. 0.45 V versus Ag/AgCl was observed. The peak capacitances for the Ru oxide component were 1326 F/g and 1300 F/g at 471 mV (anodic) and 430 mV (cathodic), respectively. The average specific capacitance based on the hydrous Ru oxide was 722 F/g, which is higher than that of as-prepared pure hydrous Ru oxide (see Chapter 2).

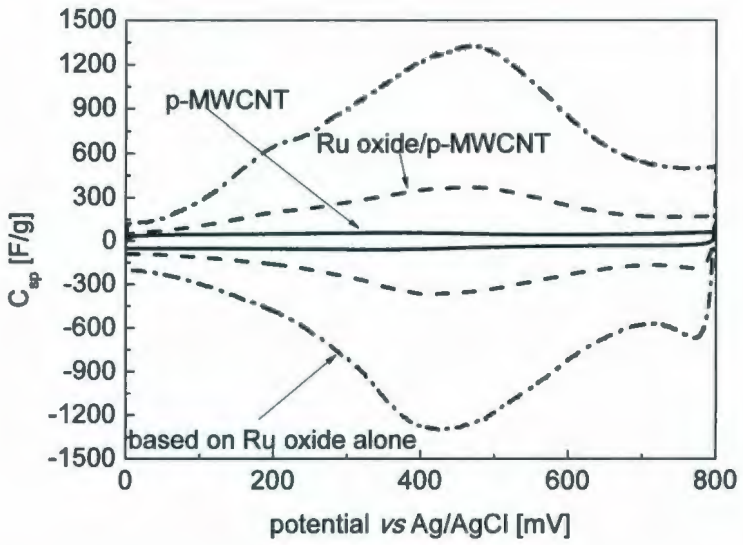

Fig. 4.6 Cyclic voltammogram at 20 mV/s for a 25.1% Ru oxide/p-MWCNT composite

Fig. 4.7 shows that the 25.1% Ru oxide/p-MWCNT composite had a stable potential window of -0.2 V to 1.0 V. The specific capacitances were improved over the

whole potential window, compared with the blank p-MWCNT. The high specific capacitance was due to the introduction of hydrous Ru oxide with pseduocapacitances.

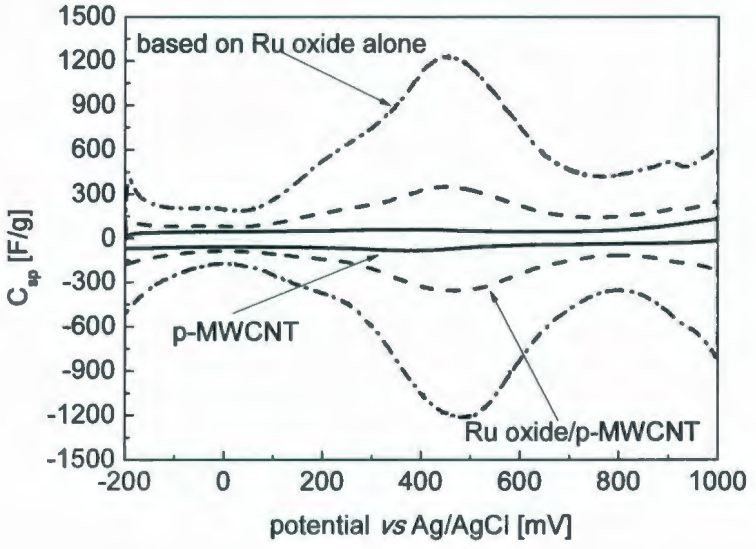

Fig. 4.7 Stable potential window for a 25.1% Ru oxide/p-MWCNT (at 20 mV/s) eletrode

More results for composite samples from cyclic voltammetry are listed in Table 4.3. All of the wet composites prepared with Ru(VII) exhibited high specific capacitances (over 621 F/g) based on their hydrous Ru oxide components. However, the specific capacitance for composites dried at room temperature decreased by ca. 10%, compared with the wet composites. This may be attributed to damage of the thin film structures (cracking off) due to surface tension when the samples were dried, thus increasing the proton and electronic resistances. In addition, the specific capacitance for the 25.1% Ru oxide/p-MWCNT composite annealed at 150 °C sharply decreased from 213 ± 16 F/g to 141 ± 6 F/g (ca. 33.8% loss). This indicates that the specific capacitance based on the Ru oxide component sharply decreased with increasing annealing temperature for

composites prepared by the spontaneous reduction method. This is different from as-prepared Ru oxide, whose specific capacitance increased with annealing temperature (below 110 °C), and does not change significantly at annealing temperatures between 110 °C and 150 °C (see section 2.3.5 in Chapter 2). The difference in annealing properties may be attributed to the crystalline structures. For the composites prepared by the spontaneous reduction method with Ru(VI) or Ru(VII), the Ru oxide components are initially deposited as hydrous Ru(VI) oxide that may have more ordered RuO_6 octahedra structures than the Ru oxide (with Ru(III) and Ru(VI)) prepared by a sol-gel method.[31] Crystallization will begin when the Ru(VI) oxide component is annealed. The crystallization will limit the access of protons, thus leading to low specific capacitance.

Table 4.3 Specific capacitances for Ru oxide/MWCNT composites

	Hydrous Ru oxide loading (%)	TGA (%)	C_{sp} (F/g)	C_{sp} based on hydrous Ru oxide (F/g)	Method
Blank p-MWCNT			49±1		
Ru oxide/p-MWCNT	25.1	20.4	213 ±16	704±62	Ru(VI)
Ru oxide/p-MWCNT	30.4	26.1	244±8	689±26	Ru(VII)
Ru oxide/p-MWCNT*	32.3	27.6	209±30	545±92	Ru(VII)
Ru oxide/p-MWCNT	32.3	27.6	234±8	621±24	Ru(VII)
Ru oxide/p-MWCNT*	17.2	14.6	135±9	555±55	Ru(VII)
Ru oxide/p-MWCNT	17.2	14.6	146±1	621±9	Ru(VII)
Ru oxide/ p-MWCNT	25.1	20.4	141±6	502±30	150 °C
Ru oxide/ p-MWCNT	19.9		165±12	632±62	physical mixture
Ru oxide/ p-MWCNT	14.1		107±4	459±27	sol-gel
Blank f-MWCNT			69±1		
Ru oxide/ f-MWCNT	15.6		184±11	803±72	Ru(VI)

*The composite samples were dried at room temperature before starting measurements

Fig. 4.8 shows a cyclic voltammogram of a 15.6% Ru oxide/f-MWCNT composite. It can be seen that the voltammogram was similar to Fig. 4.6 with a broad specific capacitance peak. The peak values based on the Ru oxide were 1482 F/g and 1452 F/g at 524 mV (anodic) and 482 mV (cathodic) versus Ag/AgCl, respectively. An average specific capacitance of 867 F/g for the hydrous Ru oxide component was obtained over the potential window of 0.0 V to 0.8 V. The high specific capacitance may be due to the lower Ru oxide loading.

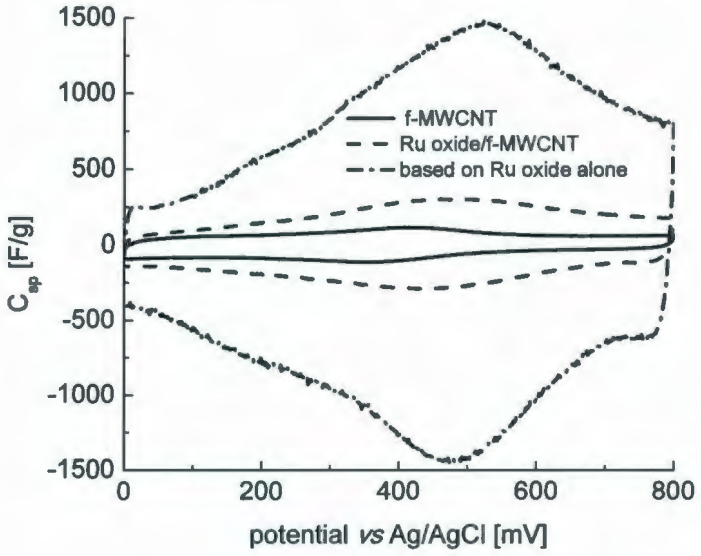

Fig. 4.8 Cyclic voltammogram for a 15.6% Ru oxide/f-MWCNT composite and f-MWCNT

Fig. 4.9 shows voltammograms of the blank MWCNTs. It is clear that the f-MWCNT has a much larger capacitance peak at ca. 0.4 V versus Ag/AgCl. The peaks can be attributed to pseudocapacitance of quinone groups on the f-MWCNT surface. The

average specific capacitance was 48 ± 1 F/g (five measurements) for the p-MWCNT, while it increased to 69 ± 1 F/g (four measurements) for the f-MWCNT.

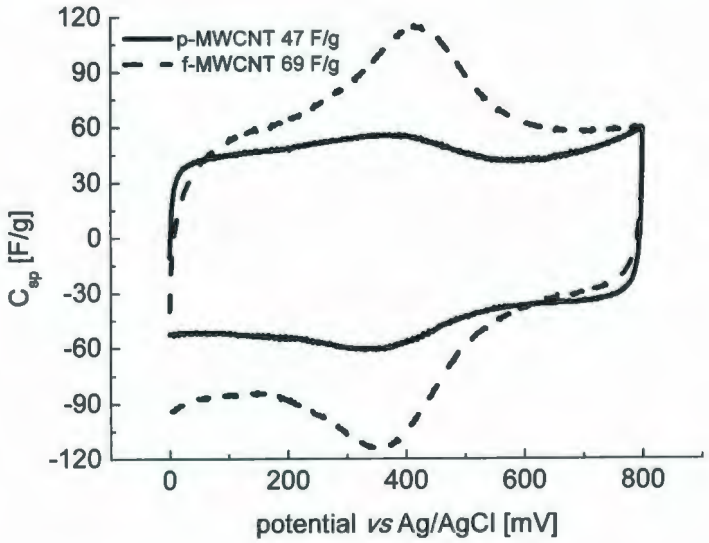

Fig. 4.9 Cyclic voltammograms (20 mV/s) of the blank p-MWCNT and f-MWCNT

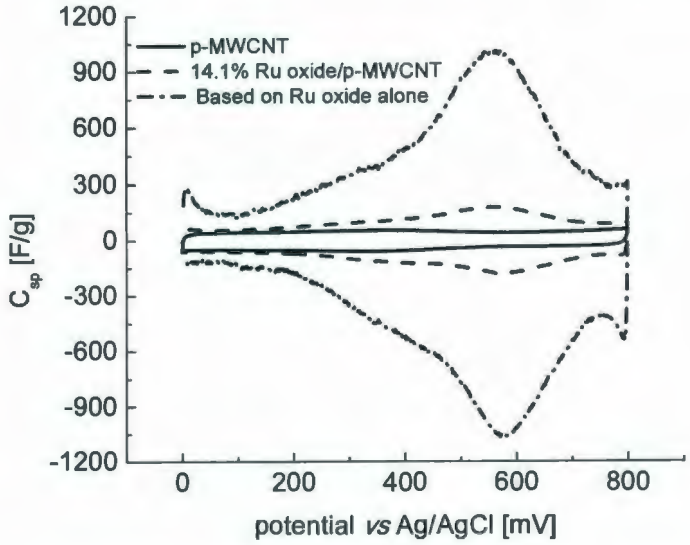

Fig. 4.10 Cyclic voltamograms (20 mV/s) for a 14.1% Ru oxide/p-MWCNT composite prepared by a sol-gel method

In general, the utilization of Ru in Ru oxide/MWCNT composites was sharply improved. As shown in Table 4.3, the average specific capacitance for the hydrous Ru oxide component was 704±62 F/g (four measurements) and 803±72 F/g (two measurements) for the 25.1% Ru oxide/ p-MWCNT composite and the 15.6% Ru oxide/ f-MWCNT composite, respectively. The specific capacitances based on the Ru oxide components are higher than that of as-prepared hydrous Ru oxide. The high utilization can be ascribed to nanostructured Ru oxide which increases the accessibility of the sulfuric acid electrolyte.

4.3.2 Modified sol-gel methods

For comparison purposes, a Ru oxide composite with 14.1% loading was prepared by a modified sol-gel method.[25, 32] The properties of the composite were characterized by cyclic voltammetry as shown in Fig. 4.10. It can be seen that the shape of the voltammogram was similar to that for Ru oxide/p-MWCNT composites prepared by the spontaneous reduction method, with a broad specific capacitance peak. The peak values were 1017 F/g and 1070 F/g at 557 mV (anodic) and 570 mV (cathodic), respectively. It is clear that the peak values were much less than for the composite described in Fig. 4.6. In addition, the peak potentials shifted to more positive positions due to the change of Ru oxidation state. The average specific capacitance of the Ru oxide component was only 459±27 F/g (three measurements), which is much less than the specific capacitance of 704±62 F/g for the hydrous Ru oxide component of the 25.1% Ru oxide/p-MWCNT composite prepared with Ru(VI).

Fig. 4.11 shows changes in the voltammogram of the 14.1% Ru oxide/p-MWCNT caused by a series of electrochemical experiments, including impedance spectroscopy, constant current discharging and cyclic voltammetry. Three pairs of redox peaks were observed at 421 mV and 411 mV, 557 mV and 563 mV, 724 mV and 708 mV versus Ag/AgCl, respectively. These presumably correspond to three distinct redox reactions during charging and discharging, although it is not clear what they are.

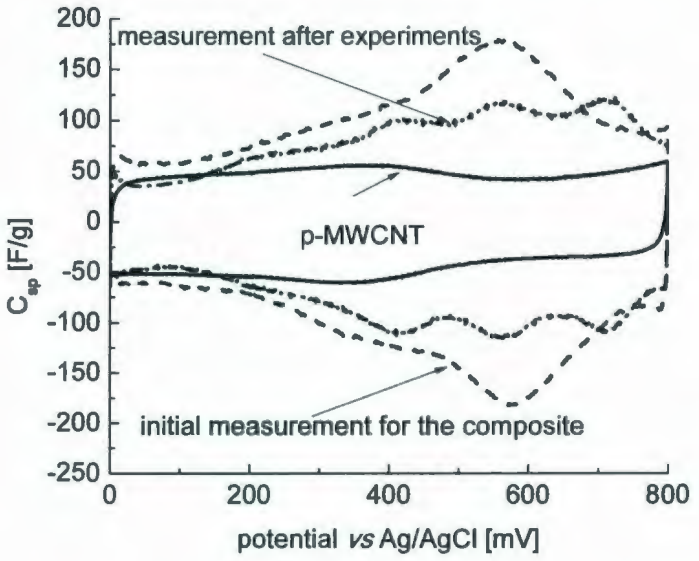

Fig. 4.11 Changes in the cyclic voltammetry (20 mV/s) of a 14.1% Ru oxide/ p-MWCNT composite caused by a series of experiments.

Although the electrochemical behavior of solid Ru oxide is different from that of aqueous Ru(VI), we can obtain some clues from the latter. Wallace *et al.*[33] proposed that Ru(IV) exists in $HClO_4$ as a tetrameric species that can be reversibly reduced by two, one-electron processes to tetrameric species with formal oxidation states of 3.75 and 3.5. Atwood *et al.*[34] reported reduction potentials for Ru(IV) perchlorate of 0.42 V, 0.56 V,

and 0.49 V versus calomel electrode for the Ru(3.5)/Ru(III), Ru(IV)/Ru(3.5), and Ru(IV)/Ru(II) couples, respectively. Based on the peak potentials of Fig. 4.11, there are at least two redox couples, Ru(3.5)/Ru(III) and Ru(IV)/Ru(3.5) involved in the charging and discharging processes.

4.3.3 Physical mixing methods

Chapter 3 has demonstrated that physical mixing is a good method for preparing Ru oxide/CF composites with low loadings. Here, the method was used to prepare carbon nanotube composites for comparison purposes.

The capacitive behavior of a 19.9% Ru oxide/p-MWCNT composite was characterized by cyclic voltammetry as shown in Fig. 4.12. It can be seen that the voltammogram for the Ru oxide component was featureless, which is similar to that for pure Ru oxide as described in Chapter 2. The average specific capacitance for the Ru oxide component was 632±62 F/g (three measurements), which is similar to values for the composites prepared by the spontaneous reduction method. The specific capacitance based on the Ru oxide components was higher by 25.8% and 37.7% for composites prepared by the physical mixing (with 19.9% loading) and spontaneous reduction (with 25.1% loading) methods, respectively, as compared with the specific capacitance (502 ± 30 F/g) for the Ru oxide component of the composite (prepared by the spontaneous reduction method) annealed at 150 °C.

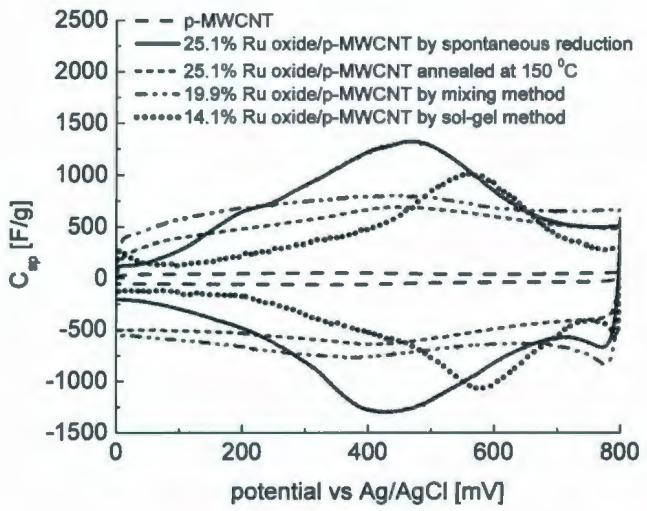

Fig. 4.12 Comparisons of cyclic volatmmograms for composites prepared by different methods.

4.3.4 Impedance spectroscopy

The impedance behavior of composite supercapacitors was characterized by impedance spectroscopy as shown in Fig. 4.13. It can be seen that all of the Nyquist plots displayed the expected characteristics for porous electrodes, including a 45 degree region at high frequencies and a vertical region at low frequencies. ESR and R_i values derived from Fig. 4.13 are given in Table 4.4. The R_i for the supercapacitor with the 19.9% Ru oxide/p-MWCNT composite was 0.67 Ω, while the R_i of the supercapacitors with composites prepared by the spontaneous reduction method were higher (1.04 Ω – 2.57 Ω). The high conductivity for the 19.9% Ru oxide/MWCNT composite can be attributed to the introduction of Ru oxide (annealed at 110 °C) with high electronic conductivity.[30, 35]

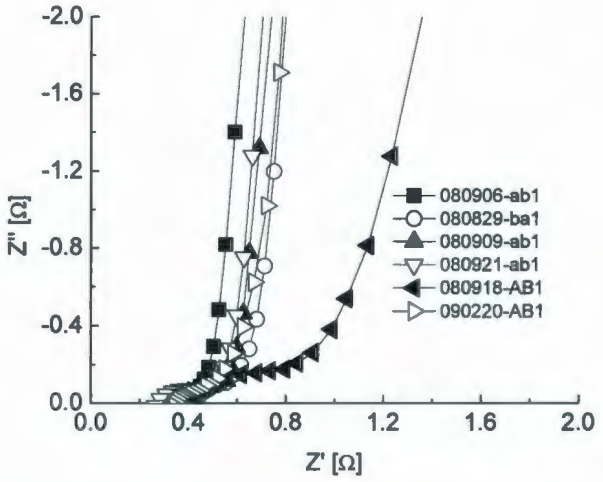

Fig. 4.13 Nyquist plots for Ru oxide/MWCNT composites and the MWCNT. The electrode materials are specified in Table 4.4

Table 4.4 ESR and R_i values for MWCNTs and their composites

	Composites	ESR (Ω)	R_i (Ω)
080906-ab1*	19.9% hydrous Ru oxide/p-MWCNT	0.30	0.67
080905-ab1**	25.1% hydrous Ru oxide/p-MWCNT annealed at 150 °C	0.34	1.07
080829-ba1**	25.1% hydrous Ru oxide/p-MWCNT	0.36	1.04
090220-ab1***	30.4% hydrous Ru oxide/p-MWCNT	0.33	1.01
0903142-ba1***	17.2% hydrous Ru oxide/p-MWCNT	0.35	1.06
080909-ab1	blank p-MWCNT	0.30	1.05
080921-ab1	blank f-MWCNT	0.25	1.13
080918-ab1**	15.6% hydrous Ru oxide/f-MWCNT	0.38	2.57

* prepared by physical mixing
** prepared by the spontaneous reduction method with Ru(VI)
*** prepared by the spontaneous reduction method with Ru(VII)

For composites prepared by the spontaneous reduction method, the introduction of Ru oxide should enhance the conductivity of the composites because Ru oxide has high conductivity. However, the electronic conductivity of MWCNTs will decrease due

to the loss of conjugation during the Ru oxide deposition process. That is why the 19.9% hydrous Ru oxide/p-MWCNT prepared by physical mixing has much lower R_i than the others. It can be seen from Table 4.4 that R_i values for the composites of Ru oxide and the p-MWCNT were not significantly different from those for the p-MWCNT.

The conductivity of Ru oxide has been shown to increase with increasing annealing temperature.[30] However, Table 4.4 shows that the composite annealed at 150 °C and the as-prepared composite gave similar R_i values, indicating that the change due to annealing was insignificant.

The R_i for the 15.6% hydrous Ru oxide/f-MWCNT composite was 2.57 Ω, which was much higher than for the Ru oxide/p-MWCNT composites and the f-MWCNT. The high R_i may be due to the introduction of defects in the extended pi system introduced during the preparation process.

4.3.5 Constant current discharging

The performance of a symmetric supercapacitor with two similar composite electrodes was evaluated by constant current discharging. Fig. 4.14 shows typical constant current discharging curves. It can be seen that the initial voltage quickly dropped over the first few milliseconds due to the ESR of the cell. Based on the initial potential drop, the ESR of the supercapacitor can be estimated by Equation 4.1

$$ESR = V_{drop} / I \qquad \text{Eq. 4.1}$$

where V_{drop}, I and ESR represent the initial voltage drop, constant current and the equivalent series resistance of the supercapacitor, respectively.

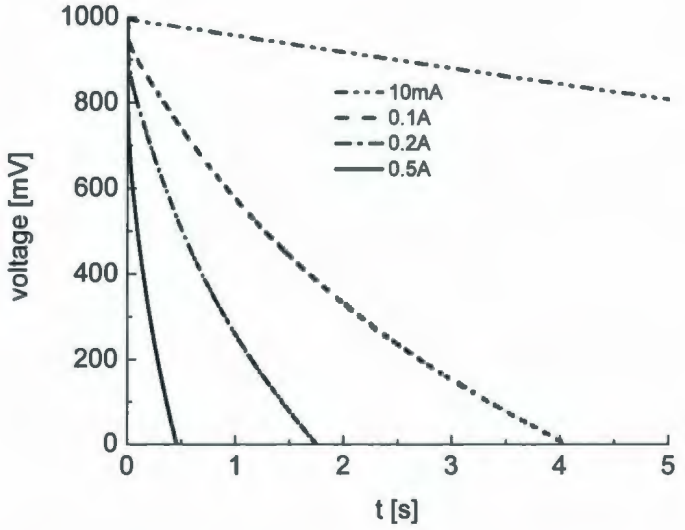

Fig. 4.14 Constant current discharging curves for a symmetric 25.1% Ru oxide/p-MWCNT composite (5.11 mg + 5.99 mg) supercapacitor.

The ESR of the supercapacitor derived from Fig. 4.14 was ca. 0.4 Ω, which agrees with the result from impedance spectroscopy. The discharging curves exhibited lower slopes over the low voltage range, indicating higher specific capacitances. This is due to the potential-dependence of the specific capacitance (see section 4.3.1.5).

Energy densities derived from Fig. 4.14 are plotted as a function of power density in Fig. 4.15, which also shows the Ragone plot of the supercapacitor with the 19.9% Ru oxide/p-MWCNT composite. It can be seen that the maximum energy density was 4.5 W h/kg for the supercapacitor with the 25.1% hydrous Ru oxide/p-MWCNT composite. In contrast, the maximum energy density was 6.1 W $h.kg^{-1}$ for the supercapacitor with the 19.9% Ru oxide/p-MWCNT composite. The higher energy density was attributed to the low R_i (see Table 4.4) and high capacitances at the high potential range (see Fig. 4.12).

At a similar average power density (ca. 14 kW. kg^{-1}), the energy densities were 3.1 W $h.kg^{-1}$ and 1.7 W $h.kg^{-1}$, respectively, for the 19.9% and 25.1% Ru oxide/p-MWCNT supercapacitors. Although the 25.1% Ru oxide/p-MWCNT composite exhibited high average specific capacitance over the potential window of 0.0 V to 0.8 V, most of the charge is stored at ca. 0.4 V versus Ag/AgCl, resulting in low performance.

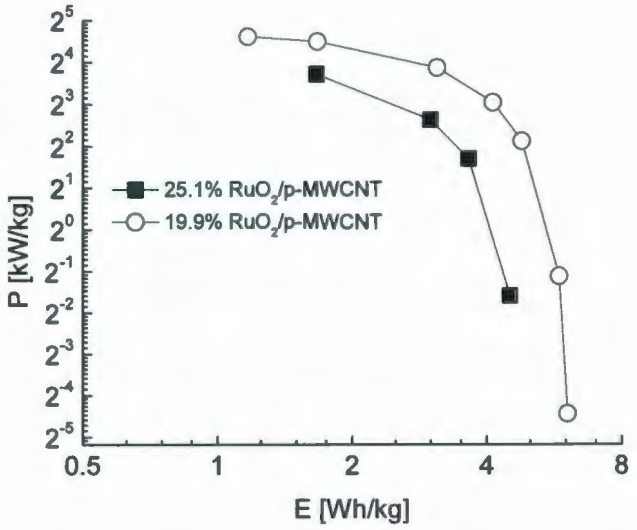

Fig. 4.15 Ragone plots for Ru oxide/p-MWCNT composite supercapacitors. Solid squares: 11.5 mg composite prepared by the spontaneous reduction method; open circles: 10.18 mg composite prepared by the physical mixing method.

4.3.6 Stability

The stability of a supercapacior was tested by repeated charging and discharging at 100 mA/cm^2. Fig. 4.16(A) shows charging-discharging curves for selected cycles. It is clear that the initial voltage drop for the 10^{th} cycle was much higher than for the 1000^{th} cycle. This indicates that the ESR decreased with cycling, which may have resulted from

the development of proton and/or electron pathways within Ru oxide particles. In addition, the ESR could gradually decrease due to the increase of small pores available for the electrolyte with cycling due to longer soaking time.[22]

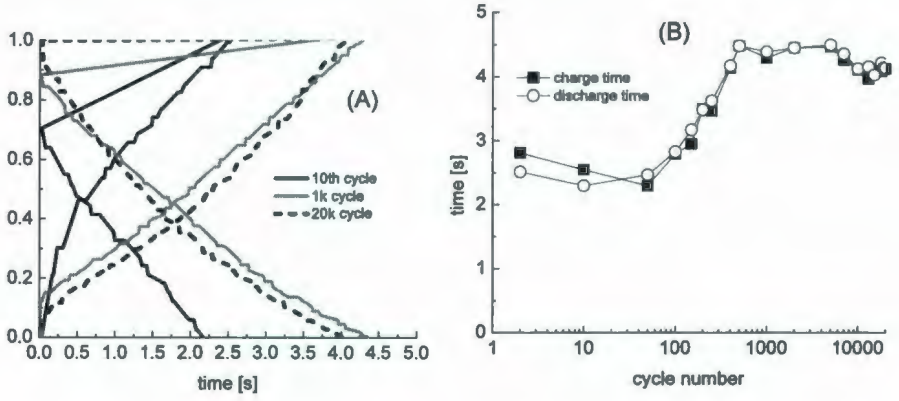

Fig. 4.16 Stability of a Ru oxide/p-MWCNT supercapacitor. (A) Charge-discharge curves for selected cycles (B) charge time and discharge time versus cycle number. The combined electrode mass was 11.5 mg (25.1% Ru oxide/p-MWCNT composite).

The charge and discharge times for selected cycles are plotted as a function of cycle number in Fig. 4.16(B). It can be seen that the discharge time (proportional to the capacitance) increased with cycling and reached the maximum value at 5,000 cycles (4.5 s), then followed a slight decrease between the 5,000th and 20,000th cycle (4.1 s). The discharge time at the 20,000th cycle was still higher than that during the first 400 cycles, showing excellent long-term stability of the supercapacitor.

The increase in discharging time with cycling is most likely related to changes in the open circuit potentials of the electrodes. Fig. 4.17 shows cyclic voltammograms recorded before and after the charging/discharging experiments. It is clear that the potential (424 mV) of the specific capacitance peak shifted to a higher value (474 mV)

during cycling. This shift will result in a combined cyclic voltammogram with high capacitance at high potential region for a supercapacitor, thus leading to high energy storage capacity because energy relates to the square of volatge. This change should increase the energy storage capacity of the supercapacitor.

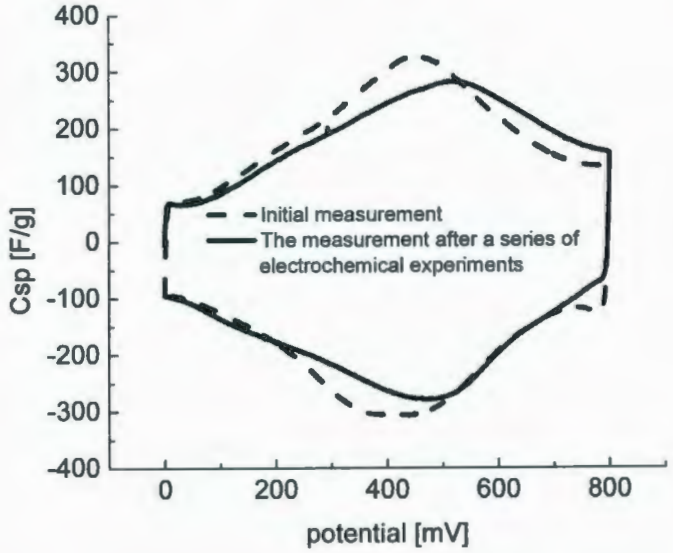

Fig. 4.17 Changes of cyclic voltammograms (current was normalized to specific capacitance) for a 25.1% Ru oxide/p-MWCNT electrode

4.4 Conclusions

Nanostructured Ru oxide/p-MWCNT and Ru oxide/f-MWCNT composites were synthesized by the spontaneous reduction of Ru(VI) and Ru(VII), a modified sol-gel method and physical mixing. Their properties were characterized by cyclic voltammetry, constant current discharging and impedance spectroscopy. The Ru oxide/p-MWCNT composites prepared by the spontaneous reduction method exhibited much higher capacitance than those prepared by the modified sol-gel and physical mixing methods.

Average specific capacitances of 704±62 F/g and 803±72 F/g for the Ru oxide components were obtained for the 25.1% Ru oxide/p-MWCNT and 15.6% Ru oxide/f-MWCNT composites, respectively. However, the specific capacitance decreased to 502±30 F/g when the 25.1% Ru oxide/p-MWCNT was annealed at 150 ^{0}C. For symmetric supercapacitors, a composite prepared by the physical mixing method exhibited much higher performance than one prepared by the spontaneous reduction method. The composite materials prepared by the spontaneous reduction method showed good stability. A lifetime of over 20,000 cycles was demonstrated. The low resistance pathways will develop during long term cycling.

References

1. Iijima, S., *Nature* **1991,** *354* (6348), 56-58.

2. Morris, R. S.; Dixon, B. G.; Gennett, T.; Raffaelle, R.; Heben, M. J., *Journal of Power Sources* **2004,** *138* (1-2), 277-280.

3. Udomvech, A.; Kerdcharoen, T.; Osotchan, T., *Chemical Physics Letters* **2005,** *406* (1-3), 161-166.

4. Zhao, J.; Buldum, A.; Han, J.; Lu, J. P., *Physical Review Letters* **2000,** *85* (8), 1706-1709.

5. Chen, W. X.; Lee, J. Y.; Liu, Z. L., *Carbon* **2003,** *41* (5), 959-966.

6. Williams, K. A.; Eklund, P. C., *Chemical Physics Letters* **2000,** *320* (3-4), 352-358.

7. Wang, Q. Y.; Johnson, J. K., *Journal of Physical Chemistry B* **1999,** *103* (23), 4809-4813.

8. Yin, Y. F.; Mays, T.; McEnaney, B., *Langmuir* **2000,** *16* (26), 10521-10527.

9. Han, S. S.; Lee, H. M., *Carbon* **2004,** *42* (11), 2169-2177.

10. Xiao, Q. F.; Zhou, X., *Electrochimica Acta* **2003,** *48* (5), 575-580.

11. Lee, C. Y.; Tsai, H. M.; Chuang, H. J.; Li, S. Y.; Lin, P.; Tseng, T. Y., *Journal of the Electrochemical Society* **2005,** *152* (4), A716-A720.

12. Yoon, B. J.; Jeong, S. H.; Lee, K. H.; Kim, H. S.; Park, C. G.; Han, J. H., *Chemical Physics Letters* **2004,** *388* (1-3), 170-174.

13. Beguin, F.; Szostak, K.; Lota, G.; Frackowiak, E., *Advanced Materials* **2005,** *17* (19), 2380-+.

14. Kim, I. H.; Kim, J. H.; Lee, Y. H.; Kim, K. B., *Journal of the Electrochemical Society* **2005,** *152* (11), A2170-A2178.

15. Kim, I. H.; Kim, J. H.; Cho, B. W.; Lee, Y. H.; Kim, K. B., *Journal of the Electrochemical Society* **2006,** *153* (6), A989-A996.

16. Kim, I. H.; Kim, J. H.; Kim, K. B., *Electrochemical and Solid State Letters* **2005,** *8* (7), A369-A372.

17. Wang, Y. G.; Wang, Z. D.; Xia, Y. Y., *Electrochimica Acta* **2005,** *50* (28), 5641-5646.

18. Du, C. S.; Pan, N., *Nanotechnology* **2006,** *17* (21), 5314-5318.

19. Du, C. S.; Pan, N., *Journal of Power Sources* **2006,** *160* (2), 1487-1494.

20. Park, J. H.; Ko, J. M.; Park, O. O., *Journal of the Electrochemical Society* **2003,** *150* (7), A864-A867.

21. Zhang, J. R.; Jiang, D. C.; Chen, B.; Zhu, J. J.; Jiang, L. P.; Fang, H. Q., *Journal of the Electrochemical Society* **2001,** *148* (12), A1362-A1367.

22. Xiaorong Liu, T. A. Huber., Michael C. Kopac and Peter G. Pickup, *Electrochimica Acta* **2009,** *54* (27), 7.

23. Huber, T. A.; Kopac, M. C.; Chow, C., *Canadian Journal of Chemistry-Revue Canadienne De Chimie* **2008,** *86* (12), 1138-1143.

24. Ginzburg, S. I., *Analytical chemistry of platinum metals*. Wiley: New York, 1975; p xii, 673 p.

25. Liu, X. R.; Pickup, P. G., *Journal of Power Sources* **2008,** *176* (1), 410-416.

26. Liu, X. R.; Pickup, P.G., *Journal of Solid State Electrochemistry* **2009**.

27. Toles, C. A.; Marshall, W. E.; Johns, M. M., *Carbon* **1999,** *37* (8), 1207-1214.

28. Jang, J. H.; Han, S.; Hyeon, T.; Oh, S. M., *Journal of Power Sources* **2003,** *123* (1), 79-85.

29. Panic, V.; Vidakovic, T.; Gojkovic, S.; Dekanski, A.; Milonjic, S.; Nikolic, B., *Electrochimica Acta* **2003,** *48* (25-26), 3805-3813.

30. Zheng, J. P.; Cygan, P. J.; Jow, T. R., *Journal of the Electrochemical Society* **1995,** *142* (8), 2699-2703.

31. McKeown, D. A.; Hagans, P. L.; Carette, L. P. L.; Russell, A. E.; Swider, K. E.; Rolison, D. R., *Journal of Physical Chemistry B* **1999,** *103* (23), 4825-4832.

32. Liu, X. R.; Pickup, P. G., *Energy & Environmental Science* **2008,** *1* (4), 494-500.

33. Richard M. Wallace, R. C. P., *J. Am. Chem. Soc.* **1969,** *91*, 7.

34. D. K. Atwood, T. D. V., *J. Am. Chem. Soc.* **1962,** *84* (14), 3.

35. Pandolfo, A. G.; Hollenkamp, A. F., *Journal of Power Sources* **2006,** *157* (1), 11-27.

Chapter 5 Thin film metal oxide/carbon fabric composites for supercapacitors

5.1 Introduction

Carbon fabrics (CFs) are excellent materials for supercapacitors. They typically consist of woven fibers with diameters of ca.10 μm and a relatively narrow pore-size distribution (<2 nm).[1] There are a variety of advantages of CFs as supercapacitor materials, such as high surface area, good electrical conductivity, high stability in various electrolytes, a wide potential window in non-aqueous electrolytes, and ease of electrode formation.[1-4] Niu *et al.*[3] reported that the specific capacitance of Spectracarb 2225, a CF with a surface area of ca. 2500 m^2/g, reached 230 F/g - 485 F/g over the potential range of −0.40 V to +1.15 V vs. RHE (reversible hydrogen electrode).

Ru oxide/CF composites have good capacitive behaviors in that they combine the advantages of both Ru oxide and the CF. The experiment results presented in Chapter 3 demonstrate that Ru oxide/CF composites with different Ru oxide loadings are excellent materials for supercapacitors. However, the specific capacitance based on the Ru oxide component of these composites was found to decrease with increasing Ru oxide loading.[5]

Manganese oxide (MnO_2) is an attractive material for supercapacitors due to its high specific capacitance and the abundance of Mn as a resource.[6-11] However, high specific capacitances are usually only obtained for very thin films, or by combining MnO_2 with materials with high conductivity, such as activated carbons, carbon nanotubes

(CNT), carbon fabrics etc. In addition, the specific capacitance of the MnO_2 component of composites quickly decreases with cycling.[12-16] Chang *et al.*[12] investigated the decay of the specific capacitances of hydrous manganese oxide and its composites after 600 cycles. The losses in specific capacitances were 25.7%, 22.0% and 19.5% for pure hydrous manganese oxide, multi-layer composites and co-deposited composites, respectively.

Nanostructured MnO_2 composites have higher stability than the materials prepared by traditional methods.[10, 17] Zhang *et al.*[10] synthesized manganese oxide nanoflower/carbon nanotube array composites with hierarchical porous structures. The composite electrodes had very high stability, with only a 3% capacity loss after 20000 charge/discharge cycles.

In the work described in this chapter, the spontaneous reduction method developed in Chapter 4 was used to prepare thin film Ru oxide/CF, thin film hydrous Mn oxide/CF and Mn-Ru oxide/CF composites. Their physical properties were characterized by SEM and TGA, and their electrochemical properties in different electrolytes were characterized by cyclic voltammetry, impedance spectroscopy and constant current discharging.

5.2 Experimental

5.2.1 Materials

The following materials were used as purchased: Spectracarb 2225 (Engineered Fibers Technology) with a specific area of 2500 m^2/g, KNO_3 (BDH Chemical Inc.), KOH

(ACP Chemical Inc), H_2SO_4 (Fisher Scientific), NaOH (BDH Chemical Inc.), LiOH (Sigma), Na_2O_2 (Sigma-Aldrich), Nafion NRE211 (Ion Power), 110A1 (Nippon Sheet Glass Co., Ltd.), $KMnO_4$ (MERCK KGaA) and $KRuO_4$ (Alfa Aesar), Carbon fibre paper (CFP; Toray™ TGP-H-090).

5.2.2 Preparation of Ru(VI) and Ru(VII) solutions

A Ru (VI) solution was prepared as described in Chapter 4.[18, 19] Hydrous Ru oxide (0.085g) prepared by a modified sol-gel method,[20, 21] NaOH (1.97g) and Na_2O_2 (1.00 g) were used to prepare 200 mL of Ru(VI) solution.

Ru(VII) solutions were prepared as follows: $KRuO_4$ (typically 100 mg) was dissolved in 0.1 M KOH(aq) to give 0.05 M Ru(VII).

5.2.3 Preparation of thin film Ru oxide/CF composites

A piece of CF with a known mass was soaked in a Ru(VI) or Ru(VII) solution for typically 24 h with stirring. Hydrous Ru oxide spontaneously deposited on the CF surface due to reaction between Ru(VI) or Ru(VII) and functional groups on the CF surface. Details of the syntheses are given in Table 5.1. The composites were removed and washed with copious deionized water until the supernatant solution was neutral, and then allowed to age in deionized water for a period of typically 1 week. The Ru oxide loadings were estimated by TGA.

5.2.4 Preparation of thin film Mn oxide/CF composites

Table 5.1 Details for the preparation of hydrous Ru oxide/CF, hydrous Mn oxide/CF, and Mn-Ru oxide/CF composites

	CF (g)	Ru or Mn source	Reaction time	Residual TGA mass (%)
Hydrous Ru oxide/CF	0.33	70 mL Ru(VI)	8 h	7.4
	0.30	0.068 g $KRuO_4$	3 h	11.5
	0.48	0.303 g $KRuO_4$	24 h	27.4
Hydrous MnO_2/CF	0.51	40 mL 0.05 M $KMnO_4$	2 h	17.1
	0.28	10 mL 0.05 M $KMnO_4$	20 min	11.6
	0.63	21 mL 0.05 M $KMnO_4$	1 h	22.4*
	0.62	0.50 g $KMnO_4$ in 20 mL H_2O	10 min	34.3*
Multilayer composite	0.29	10 mL 0.05 M $KMnO_4$ and 30.6 mg $KRuO_4$	1.5 h	10.8
$MnRu_{0.18}O_x$/CF	0.38	20 mL 0.05 M $KMnO_4$ and 37.1 mg $KRuO_4$	20 h	25.0
$MnRu_{0.32}O_x$/CF	0.39	10 mL 0.05 M $KMnO_4$ and 33.0 mg $KRuO_4$	19.5 h	14.8

*Loadings were calculated by the mass difference during preparation.

The preparation of hydrous Mn oxide/CF composites was similar to that of the hydrous Ru oxide/CF composites, and based on a previous report of the spontaneous deposition of Mn oxide on carbon (see Eq. 1.21).[11] Details are provided in Table 5.1. The deposition time was typically shorter than for the hydrous Ru oxide/CF composites. Mn oxide loadings were estimated by TGA.

5.2.5 Preparation of thin film Mn-Ru oxide/CF composites

A thin film Mn-Ru oxide/CF composite was prepared by a multistep deposition method. A piece of CF with a known mass was first soaked in 0.05 M $KMnO_4$ for 1.5 min, and then removed and washed until the supernatant solution was colorless. Secondly, the Mn oxide/CF sheet was soaked in 0.05 M $KRuO_4$ for 5 min, followed by removing and washing until the supernatant solution was colorless. The soaking procedures in the $KMnO_4$ and $KRuO_4$ solutions were repeated 9 times. Finally the sheet was washed with copious deionized water until the supernatant solution was neutral. The metal oxide loading was estimated by TGA.

Thin film Mn-Ru oxide/CF composites were also prepared by a spontaneous co-deposition method using a mixed solution of $KMnO_4$ and $KRuO_4$. Typically the deposition time was 24 h. The theoretical ratio of Mn to Ru was calculated by using the amounts of Ru and Mn employed in the synthesis. The resulting composites were washed with copious water until the supernatant solution was neutral, and aged in deionized water for typically 1 week. Metal oxide loadings were evaluated by TGA.

5.2.6 Thermogravimetric analysis

The thermal dynamic properties of the composites were measured with a TA Instruments Q500 TGA analyzer under a N_2 atmosphere (sample gas, 60 mL/min; balance gas, 40 mL/min). Air was not completely purged from the TGA instrument furnace before starting experiments.

5.2.7 Scanning electron microscopy and energy dispersive X-ray spectroscopy (EDX)

SEM images were obtained on a *FEI Quanta 400* environmental SEM at different magnifications. EDX was utilized to confirm the presence of Ru or Mn. Analysis was performed on a *FEI Quanta 400* environmental SEM at 25 kV.

5.2.8 Electrochemical characterization

The composite sheets were punched into disc electrodes (1 cm^2). Supercapacitors were assembled with two similar electrodes, a Nafion NRE211 or 110A1 membrane separator, and Ti current collectors. A piece of CFP disc was placed between each Ti plate and electrode to minimize the contact resistance. Electrochemical measurements (using an EG&G 273A potentiostat/galvanostat) were made on supercapacitors immersed in different electrolytes (1 M H_2SO_4, 2 M KOH, and 2 M LiOH) in the presence of air. An Ag/AgCl reference electrode in these electrolyte solutions was used to provide a reference potential in 3-electrode experiments.

The specific capacitances of Mn oxide/CF composites in different electrolytes (2 M LiOH, 2 M KOH, and 1 M Na_2SO_4) were measured by cyclic voltammetry (using the EG&G 273A potentiostat/galvanostat) using two-electrode (with a Celgard 3400 or 110A1 separator) and three-electrode configurations. For constant current discharging, the supercapacitors were first charged to 1.0 V for 5 min, then completely discharged to 0 V using different constant currents. Impedance spectroscopy (using the EG&G 273A Potentiostat/Galvanostat, an EG&G 5210 lock-in amplifier and EG&G Powersuite software) was conducted at a DC bias potential of 0.5 V with an amplitude of 10 mV.

5.3 Results and discussion

5.3.1 Thin film Ru oxide/CF composites

5.3.1.1 Scanning electron microscopy and energy dispersive X-ray emission spectroscopy

Fig. 5.1 SEM images of a 11.5% Ru oxide/CF composite

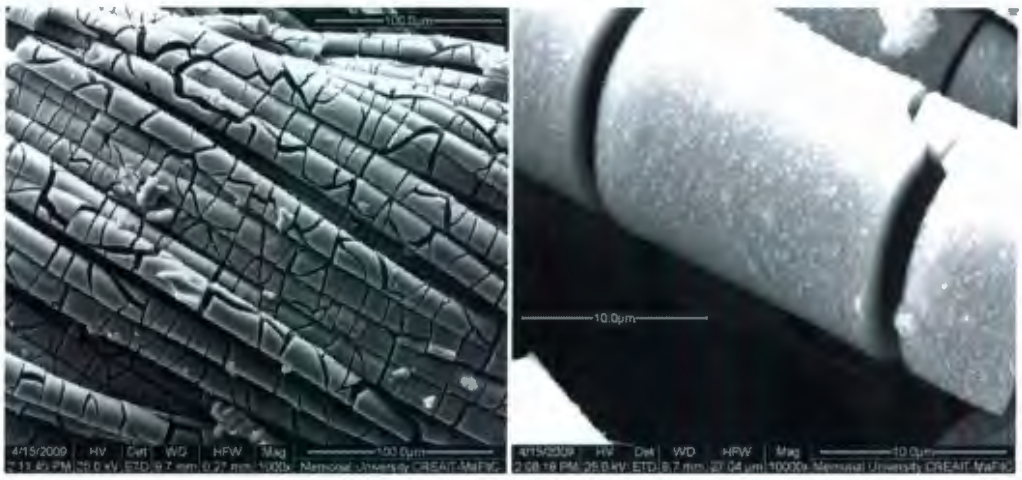

Fig. 5.2 SEM images of a 27.4% Ru oxide/CF composite

Fig. 5.1 and Fig. 5.2 show SEM images of hydrous Ru oxide/CF composite samples that were dried at ambient temperature. It can be seen that Ru oxide with a smooth film structure was evenly deposited on the CF fibers. The cracks in the Ru oxide layers of both composites are presumably due to capillary forces during drying, or by handling of the dried composites.[22] Capillary forces should cause cracks on all fibers, while many appear to be crack-free. These were most likely due to the variation of capillary forces with location. The thickness of the Ru oxide layer can be estimated to be ca. 0.9 μm for the 27.4% Ru oxide/CF composite.

Since freeze-drying and critical-point drying methods can effectively decrease the capillary forces during drying, hydrous Ru oxide/CF composites without cracks may potentially be obtained by these methods.[22] However, these methods were not available for this work. Therefore, in order to obtain electrochemical properties of Ru oxide/CF composites without cracks, they were used without drying.

The 27.4% Ru oxide/CF composite was also characterized by EDX as shown in Fig. 5.3. It can be seen that the composite consisted of the expected Ru, O, and C, but also had a K impurity which must come from the $KRuO_4$ + KOH solution that was used as the Ru source.

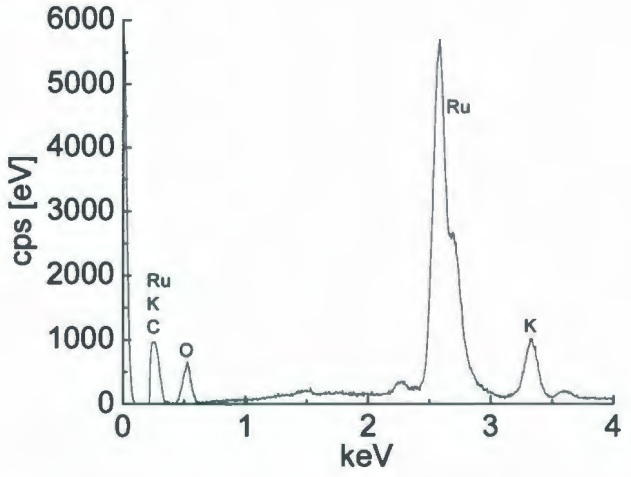

Fig. 5.3 EDX of the 27.4% Ru oxide/CF composite

Table 5.2 EDX results for a 27.4% Ru oxide/CF composite

Element	Series	unnormalized concentration [mass %]	normalized concentration [mass %]	The atomic ratios of other elements to ruthenium
Ruthenium	L-series	50.49	56.23	1.00
Carbon	K-series	4.80	5.35	0.80
Potassium	K-series	7.36	8.19	0.38
Oxygen	K-series	27.15	30.24	3.40

Table 5.2 shows quantitative results for the 27.4% Ru oxide/CF composite from EDX. It can be seen that the main components were Ru and O. In order to estimate the empirical formula of the composite, the mass concentrations based on atomic ratios were calculated, and $K_{0.38}RuO_{3.40}C_{0.80}$ was obtained. This suggests that the average oxidation state of the Ru may have been above VI.

5.3.1.2 Thermogravimetric analysis

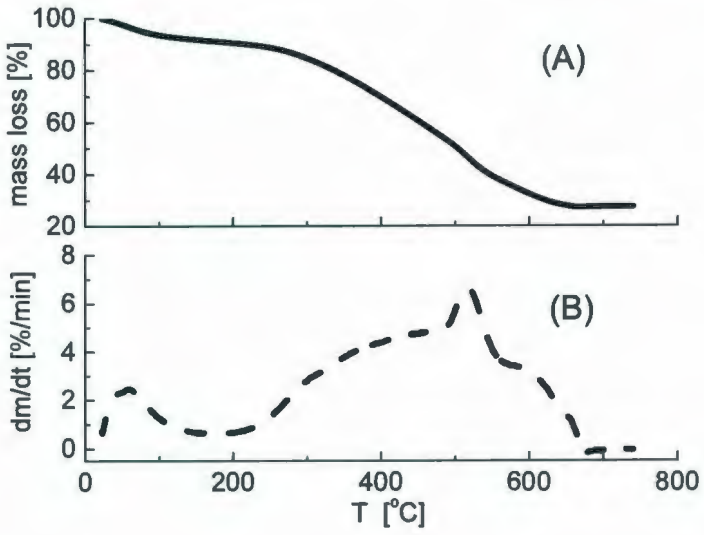

Fig. 5.4 TGA curve for a hydrous Ru oxide/CF composite (8.75 mg sample, ramp 25.00 °C/min to 750.00 °C)

The thermal dynamic properties of a Ru oxide/CF composite were characterized by TGA as shown in Fig. 5.4. It can be seen from Fig. 5.4(A) that the sample gradually lost mass with increasing sample temperature, and finally reached a stable residual mass of 27.4%, corresponding to anhydrous Ru oxide and the trace ash content of the CF. The

differential mass losses are plotted as a function of time in Fig. 5.4(B), and can be used for comparing the rate of the mass loss. It can be seen that there are two wide peaks in the differential plot. The low temperature peak (<100 °C) can be attributed to the loss of water adsorbed on the surface of the composite. The wide peak between 200 °C and 660 °C can be attributed to the slow dehydration of the hydrous Ru oxide and the oxidation of carbon.

5.3.1.3 Capacitive behavior

5.3.1.3.1 Sulfuric acid

Hydrous Ru oxide/CF composite electrodes were characterized by cyclic voltammetry in 1 M H_2SO_4 as shown in Fig. 5.5. It can be seen from Fig. 5.5(A) that the current responses of the composite electrodes increased with Ru oxide loading. Average specific capacitances based on the Ru oxide component derived from Fig. 5.5(A) are given in Table 5.3, which shows that they decreased with increasing Ru oxide loading. The average specific capacitance based on the Ru oxide component was 824±152 F/g for the composite with 7.4% Ru oxide loading, which is the same within experimental error as that of pure Ru oxide described in Chapter 2. The high specific capacitance (high utilization of ruthenium) can be ascribed to the fact that the very thin film allows the electrolyte (1 M H_2SO_4) to easily access the bulk Ru oxide. The decrease with increasing Ru oxide loading is most likely due to the increase of the thickness of the Ru oxide film. As a consequence, the Ru oxide film may be in part unavailable for the electrolyte, thus leading to a low specific capacitance.

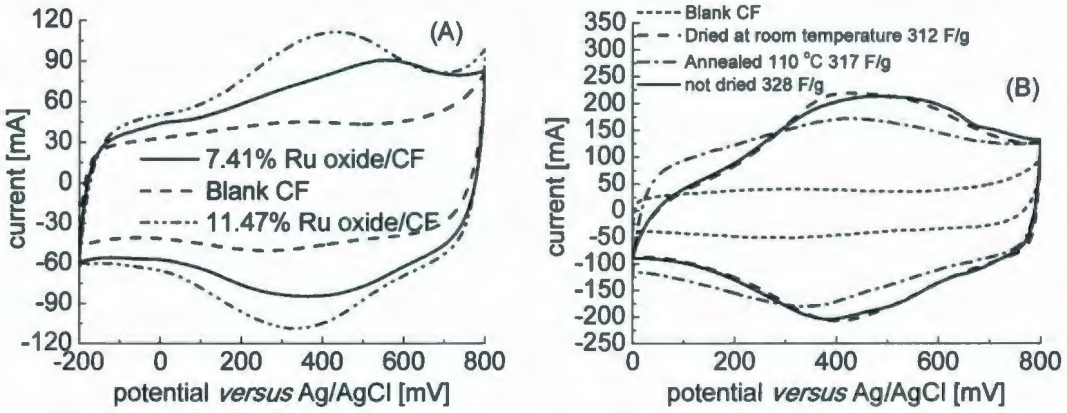

Fig. 5.5 Cyclic voltammograms for hydrous Ru oxide/CF composites (not dried) with different loadings (A) and a 27.4% Ru oxide/CF composite at various stages of drying (B)

Fig. 5.5(B) shows cyclic voltammograms of a 27.4% Ru oxide/CF composite at various stages of drying. It can be seen that the voltammograms for the sample that had not been dried (C_{sp}=328 F/g) and the sample dried at room temperature (C_{sp}=312 F/g) were similar, although drying did cause a slight (5.1%) decrease in capacitance. This decrease in capacitance for the sample dried at room temperature can be attributed to the crack of the Ru oxide flim. In contrast, the voltammogram of the sample annealed at 110 °C had less prominent peaks, and larger currents at potentials below 0.3 V due to high conductivity of Ru oxide. However, it gave an average specific capacitance of 317 F/g, which is not significantly different from the values for the other two samples. Thus, unlike for pure hydrous Ru oxide, annealing does not significantly increase the specific capacitance of the Ru oxide component of the composite. The difference in annealing properties is likely due to the ordered crystalline structure of the Ru oxide produced by spontaneous deposition, as described in Chapter 4 (see section 4.3.1.5).

Table 5.3 Specific capacitances (from cyclic voltammetry) for the metal oxide components of metal oxide/CF composites

Composites	C_{sp} (F/g) 1 M H_2SO_4	2 M KOH	2 M LiOH
7.4% Ru oxide/CF	824±152*[a]		
11.5% Ru oxide/CF	718±164 767±105*[a]		
27.4% Ru oxide/CF	679±109 725±141*[b]	575±26	576±42
11.6% Mn oxide/CF		1044±60	1080±63
17.1% Mn oxide/CF			957±58

Note: the average specific capacitance of the CF was 145 ± 7 F/g (four measurements), 123 ± 7 F/g (six measurements), and 134 ± 7 F/g (four measurements) in 1 M H_2SO_4, 2 M LiOH and 2 M KOH electrolytes, respectively.
*Samples that had not been dried. Specific capacitances were calculated based on the masses of other samples from the same sheet that had been dried at room temperature.
[a] The potential window was -0.2 V to 0.8 V versus Ag/AgCl.
[b] The potential window was 0.0 V to 0.8 V versus Ag/AgCl.

More results for specific capacitances of composite samples dried at room temperature are given in Table 5.3, which shows similar specific capacitances of ca. 700 F/g (based on the Ru oxide) for composite samples (dried at room temperature) with 11.5% and 27.4% loadings. The samples that had not been dried had higher specific capacitances than those dried at room temperature. Presumably, the cracking observed in the SEM images results in loss of contact between some of the Ru oxide and the carbon fibers.

Compared to hydrous Ru oxide/CF composites with low loadings prepared by physical mixing (see Table 3.1 in Chapter 3), the composites prepared by the spontaneous reduction method have lower specific capacitances. For example, the specific capacitance of the Ru oxide component of the 7.4% Ru oxide/CF composite prepared by spontaneous reduction was 15.7% lower than for a 9.1% hydrous Ru oxide/CF composite prepared by physical mixing.

5.3.1.3.2 Basic electrolytes

Fig. 5.6 shows cyclic voltammograms of the 27.4% Ru oxide/CF in 2 M LiOH. It can be seen from Fig. 5.6(A) that the composite electrodes showed much higher specific capacitances over the potential window of -1.0 V to 0.0 V than the CF electrode. For both the composite samples (annealed at 110 °C or dried at room temperature), the voltammograms have similar shapes with only minor features. This indicates again that annealing does not significantly influence the capacitive behavior of hydrous Ru oxide prepared by spontaneous deposition on CF. The differences in currents at -1.0 V to -0.8 V (anodic scan) are most likely due to differences in conductivity. The sample dried at room temperature would be expected to have lower electronic conductivity than the annealed sample since the electronic conductivity of hydrous Ru oxide increases with annealing.[23] Fig. 5.6(B) shows a cyclic voltammogram based on the Ru oxide component, which is similar to that of pure Ru oxide annealed at 110 °C in 1 M H_2SO_4.

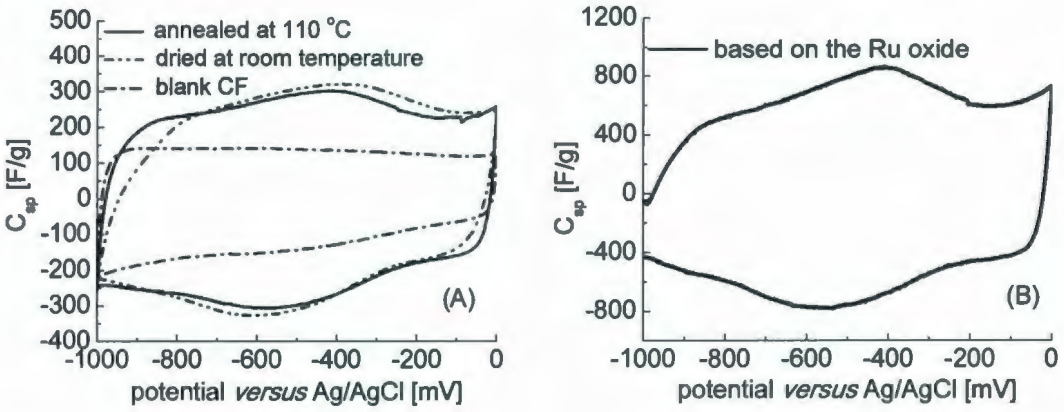

Fig. 5.6 Cyclic voltammograms (5 mV/s) for a 27.4% Ru oxide/CF composite and CF electrodes in 2 M LiOH. (A) Cyclic voltammograms for composites and the CF, (B) cyclic voltammogram for the Ru oxide component of the composite annealed at 110 °C. The electrode masses were 19.68 mg and 21.46 mg for the composite samples annealed at 110 °C and dried at room temperature, respectively.

The capacitive behavior in 2 M KOH of the 27.4% Ru oxide/CF composite dried at room temperature was also characterized by cyclic volytammetry, and a specific capacitance of ca. 575 F/g was obtained for the Ru oxide component, which is similar to that in 2 M LiOH (Table 5.3). It is clear (see Table 5.3) that the specific capacitances of composites in basic media were less than those in 1 M H_2SO_4. This can be attributed to different charge storage mechanisms (proton insertion versus alkali ion insertion). In basic media, cations (K^+ or Li^+) insert into Ru oxide during reduction, and are expelled during discharging (see Eq. 5.1), which is similar to the behavior of Mn oxide in basic electrolytes.[24] The processes are also similar to the proton insertion mechanism in sulfuric acid electrolyte (see Eq. 2.2 in Chapter 2). In addition, OH^- could be reversibly absorbed/desorbed as shown in Eq. 5.2.[25]

$$RuO_2 \cdot xH_2O + nA^+ + n\,e^- \leftrightarrow A_nRuO_2 \cdot xH_2O \quad (0 \le n \le 2) \qquad \text{Eq. 5.1}$$

$$RuO_2 \cdot xH_2O + nOH^- \leftrightarrow H_{2x}RuO_{2+x}(OH)_n + ne^- \qquad (0 \leq n \leq 2) \qquad \text{Eq. 5.2}$$

where A is an alkali metal, such as K, Li and Na.

5.3.1.4 Impedance spectroscopy

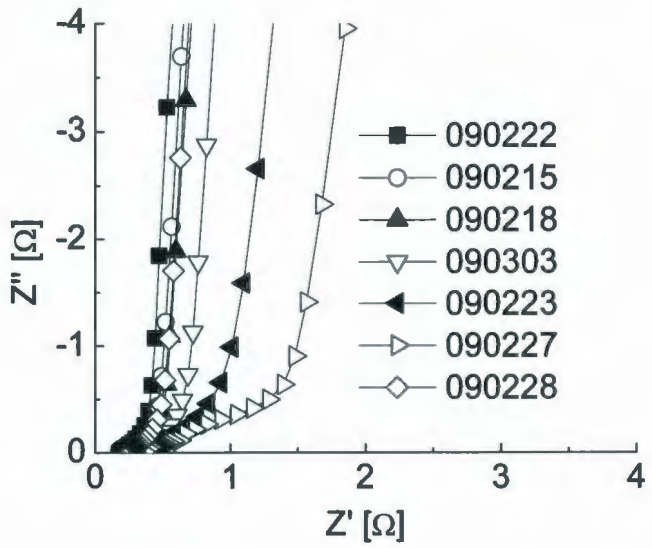

Fig. 5.7 Nyquist plots for CF and hydrous Ru oxide/CF composite supercapacitors in 1 M H_2SO_4. The details for the supercapacitors are given in Table 5.4.

The impedance behavior of hydrous Ru oxide/CF composites was characterized by impedance spectroscopy as shown in Fig. 5.7. It can be seen that all of the Nyquist plots had the expected characteristics for porous electrodes, including a ca. 45 degree region at high frequencies and a ca. vertical region at low frequencies. ESR (the real impedance at 10 kHz) and R_i values derived from Fig. 5.7 are given in Table 5.4.

It can be seen from Table 5.4 that the ESR and R_i values of the supercapacitors were higher than those for the unmodified CF supercapacitor, and that the composite

samples dried at room temperature had much higher R_i values than the samples that had not been dried. It is also clear that the R_i for the samples that had not been dried increased with Ru oxide loading. Thus it appears that the ionic resistance of the Ru oxide coating on each fibre contributes to the total ion resistance of the electrode.

Table 5.4 ESR and R_i values for hydrous Ru oxide/CF composite supercapacitors in 1 M H_2SO_4

Sample	Sample #	Electrode treatment	Electrode mass (mg)	ESR (Ω)	R_i (Ω)
CF	090222		14.09+14.19	0.17	0.66
7.4% Ru oxide/CF	090215*	not dried sample	16.4+16.4	0.21	0.78
11.5% Ru oxide/CF	090218*	not dried sample	17.12+17.12	0.21	0.95
	090303	Dried at RT	17.05+17.18	0.26	1.30
27.4% Ru oxide/CF	090223*	not dried sample	21.37+21.37	0.28	2.19
	090227	Dried at RT	22.08+22.28	0.34	3.67
	090228	Annealed at 110 °C	19.83+20.85	0.22	0.80

* The electrode masses were average values for several electrodes dried at room temperature from the same sheet that had been dried at room temperature.

Compared to the 27.4% Ru oxide/CF composite sample dried at room temperature, the ESR decreased by 35.2% and the R_i decreased by 78.1% for the composite annealed at 110 °C. The higher conductivity was likely due to the enhancement of the electronic conductivity of the hydrous Ru oxide after annealing.[23] Increasing the conductivity of the Ru oxide can decrease R_i. The decrease in R_i suggests that the electronic resistance of the Ru oxide does indeed contribute to R_i.

The R_i of the 27.4% Ru oxide/CF composite annealed at 110 °C was 61% higher than for Ru oxide/CF composites (R_i was ca. 0.5 Ω for 20% - 40% loadings) prepared by physical mixing (see Chapter 3).

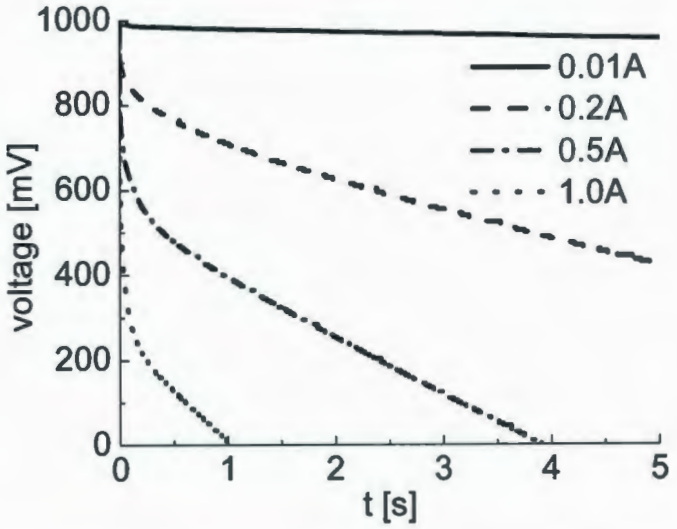

Fig. 5.8 Constant current discharging curves for a supercapacitor with 27.4% Ru oxide/CF composite electrodes annealed at 110 °C in 1 M H_2SO_4.

5.3.1.5 Constant current discharging

The performances of composite supercapacitors were characterized by constant current discharging. Fig. 5.8 shows typical discharge curves for a symmetric supercapacitor. It can be seen that the initial voltage quickly decreased over the first few milliseconds due to the ESR of the cell. It is clear that the supercapacitor exhibited a potential-dependent capacitance.

Table 5.5 Energy densities and power densities for 27.4% Ru oxide/CF composite supercapacitors in 1 M H_2SO_4.

Current (A)	dried at room temperature		annealed at 110 °C	
	E (W h/kg)	P (kW/kg)	E (W h/kg)	P (kW/kg)
0.01	7.9	0.088	9.0	0.10
0.1	5.5	0.73	7.5	0.95
0.2	3.6	1.2	6.3	1.8
0.5	0.88	2.0	3.6	3.4
1.0	0.062	2.9	1.0	3.6

Table 5.5 lists the energy and power densities of the supercapacitor described in Fig. 5.8 and a supercapacitor with the 27.4% Ru oxide/CF composite electrodes dried at room temperature. It can be seen that annealing the electrodes at 110 °C increased the maximum energy density by 13.9%, from 7.9 W h/kg to 9.0 W h/kg. The power densities at 1 A were 2.9 kW/kg and 3.6 kW/kg, respectively, for the supercapacitors with electrodes dried and annealed at 110 °C. Furthermore, the energy density was ca. 16 times higher after annealing. It is clear that the annealing sharply improved the performance of the composite supercapacitor. This can be attributed to the high conductivity of the annealed Ru oxide.

5.3.1.6 Stability

The stability of the 27.41% Ru oxide/CF composite in 2 M KOH was evaluated by cyclic voltammetry at 5 mV/s as shown in Fig. 5.9. It can be seen from Fig. 5.9(A) that the voltammograms did not change significantly with cycling. The average specific capacitances derived from Fig. 5.9(A) are plotted against cycle number in Fig. 5.9(B).

The average specific capacitance was almost constant at ca. 255 F/g for the 200 cycles employed, indicating that the composite supercapacitor had good stability in 2 M KOH.

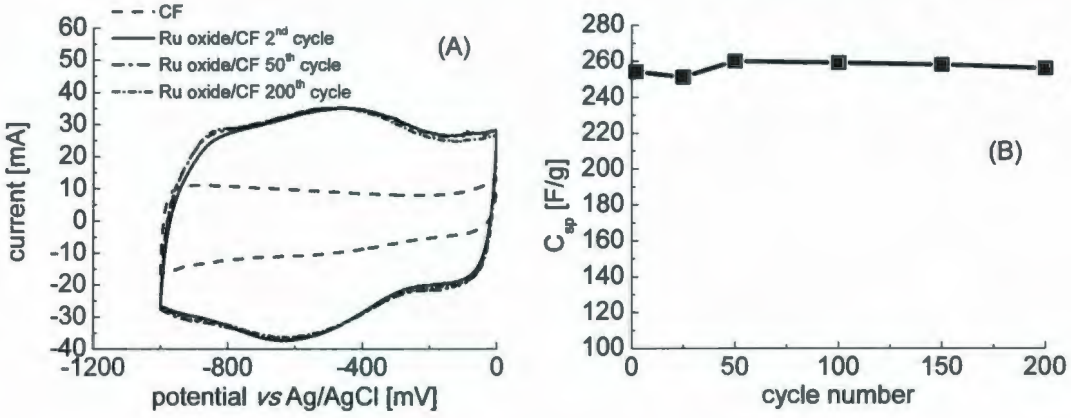

Fig. 5.9 Stability of a 27.4% Ru oxide/CF composite (21.9 mg) electrode in 2 M KOH. (A) cyclic voltammograms and (B) C_{sp} vs cycle number plot.

The Ru oxide/CF composite electrodes (either not dried or dried at room temperature) were not stable in 1 M H_2SO_4, although they had very high specific capacitance. The electrolyte solution became slightly colored (light yellow) after cycling or a period of soaking due to dissolution of the hydrous Ru oxide component in 1 M H_2SO_4. In contrast, nanostructured hydrous Ru oxide/MWCNT composites (see Chapter 4) prepared by the same method were found to exhibit good stability in 1 M H_2SO_4. It is not clear what caused this difference in stabilities. The differences in textures of the Ru oxide components (small particles stabilized by carbon nanotubes vs. relatively thick films) may result in the different stabilities. However, the annealed composite at 110 °C was quite stable in 1 M H_2SO_4.

5.3.2 Thin film Mn oxide/CF composites

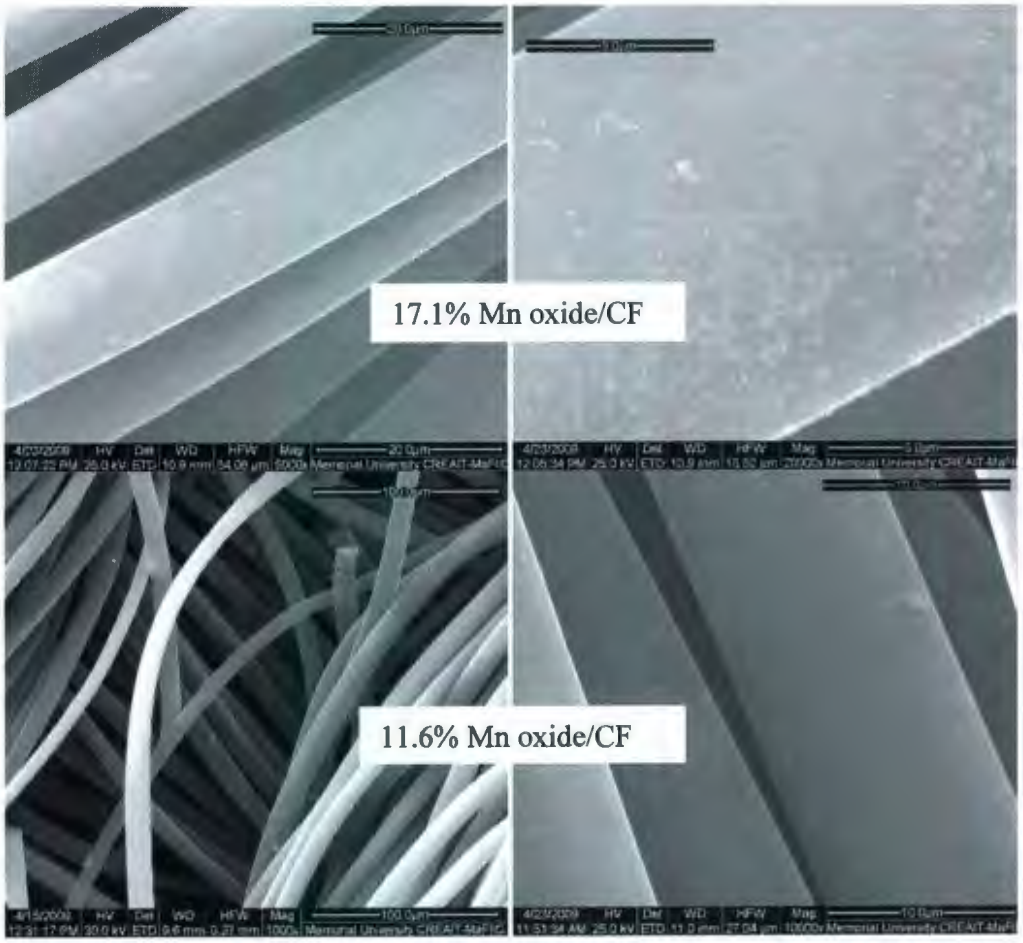

Fig. 5.10 SEM images of hydrous Mn oxide/CF composites

Thin film Mn oxide/CF composites were prepared by the spontaneous reduction method using reaction between Mn(VII) and functional groups on the CF surface.[11] The properties of the Mn oxide/CF composites were characterized by TEM, TGA, cyclic voltammetry, impedance spectroscopy and constant current discharging.

5.3.2.1 Textures

The textures of Mn oxide/CF composites were characterized by SEM as shown in Fig. 5.10. It can be seen that uniform Mn oxide layers were coated on the CF surfaces. These are different from the Ru oxide coating layers of Ru oxide/CF composites, whose surfaces have cracks. The uniform film structure will be of benefit to charge transfer between the Mn oxide particles. The absence of cracking suggests that the Mn oxide film has low surface tension. For the 17.1% Mn oxide/CF composite, small amounts of particles with diameters of ca. 200 nm appear on the surface of the Mn oxide film.

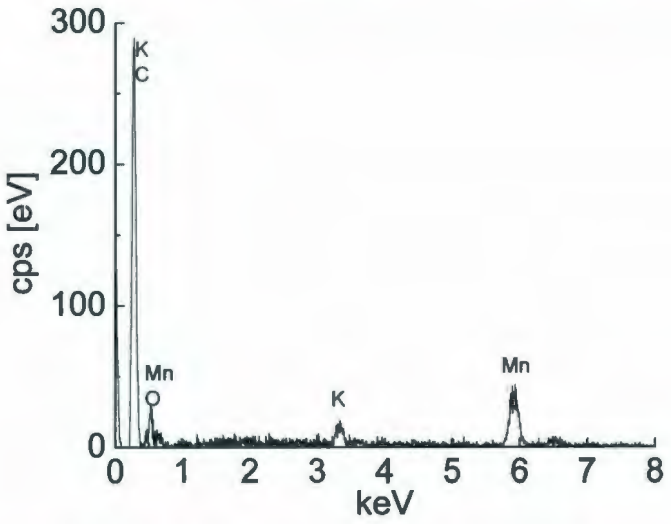

Fig. 5.11 EDX of an 11.6% MnO2/CF composite

Fig. 5.11 shows EDX of an 11.6% Mn oxide/CF composite. It can be seen that the composite consisted of the expected Mn, O and C, but also had a K impurity from the $KMnO_4$ as the source of Mn.

5.3.2.2 Thermogravimetric analysis

The thermal dynamic properties of a MnO_2/CF composite were characterized by TGA as shown in Fig. 5.12. It can be seen that the Mn oxide/CF composite lost mass with increasing sample temperature, and finally reached a stable mass (residual mass) of 17.1% at ca. 660 °C. The differential mass loss plot shows a peak at low temperatures (<100 °C), which can be attributed to the loss of water adsorbed from the composite surface. The broad series of peaks and shoulders between 100 °C to 700 °C, can be attributed to the dehydration of the hydrous Mn oxide and the oxidation of carbon.

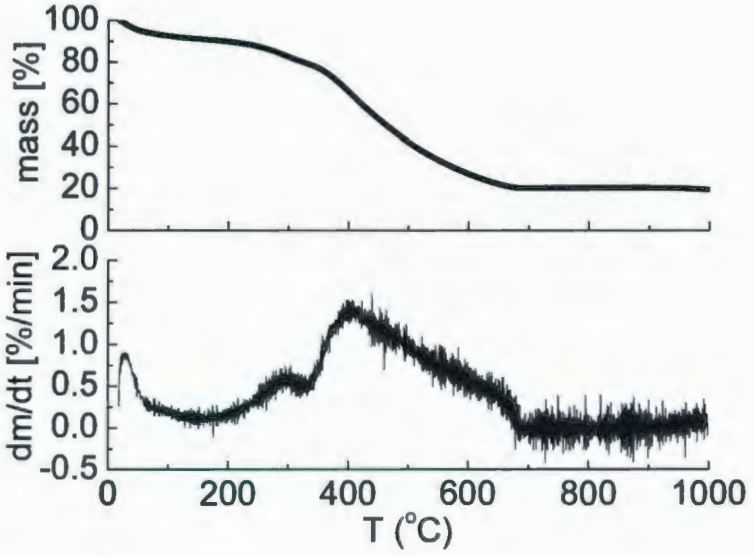

Fig. 5.12 TGA curves for a Mn oxide/CF composite (3.83 mg, ramp 5 °C/min to 1000 °C)

5.3.2.3 Capacitive behavior

5.3.2.3.1 Three-electrode configuration

The capacitive behavior of an 11.6% Mn oxide/CF composite electrode in 2 M LiOH was characterized by cyclic voltammetry as shown in Fig. 5.13. It can be seen that there were two anodic peaks at -332 mV and -52 mV versus Ag/AgCl, with peak specific capacitances of 502 F/g and 456 F/g, respectively; however, only one cathodic peak was observed at -558 mV with a specific capacitance of 409 F/g due to slow redox reactions. The mechanisms will be discussed in section 5.3.2.4. An average (both anodic and cathodic) specific capacitance of 264 F/g was obtained for the first cycle, but the specific capacitance decreased with cycling. This is discussed in section 5.3.2.7.

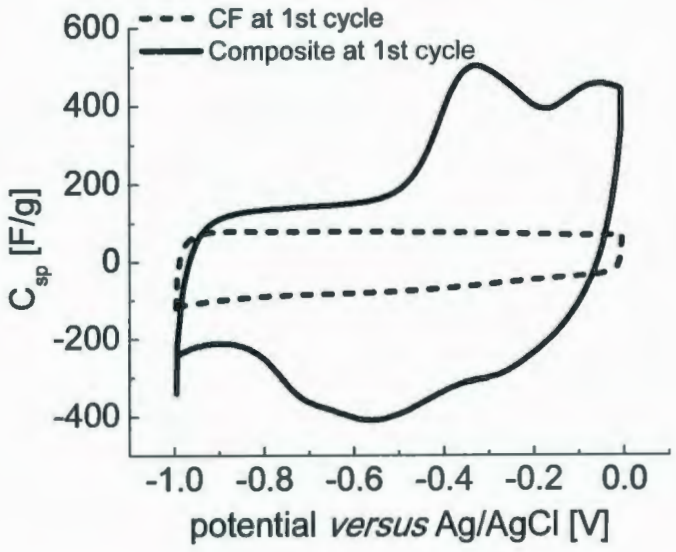

Fig. 5.13 Cyclic voltammograms (5 mV/s) of an 11.6% Mn oxide/CF composite (17.22 mg) and CF in 2 M LiOH.

Table 5.3 summarizes specific capacitances calculated for the Mn oxide component of the composites. The specific capacitance of the Mn oxide component of the 11.6% Mn oxide/CF composite was over 1000 F/g in both 2 M LiOH and 2 M KOH, which is higher than the specific capacitance of Ru oxide. The specific capacitance of the Mn oxide component of the 17.1% MnO_2/CF composite (958 F/g) was slightly lower, but still very high. The decrease in specific capacitance with increasing Mn oxide loading can be attributed to the low conductivity of the Mn oxide component.

5.3.2.3.2 Two-electrode configuration

The capacitive behaviors of Mn oxide/CF composite supercapacitors were also characterized by cyclic voltammetry as shown in Fig. 5.14. Fig. 5.14(A) shows that the supercapacitor in 2 M LiOH had two specific capacitance peaks, and that these peaks exhibited very high specific capacitances.

In 1 M Na_2SO_4, the voltammogram for the Mn oxide/CF composite had a different shape (see Fig. 5.14(B)). It is clear that the specific capacitance based on the Mn oxide component in 1 M Na_2SO_4 was less than that in 2 M LiOH, and there were no significant capacitance peaks over the useable operating potential window. The difference in cyclic voltammograms between 2 M LiOH and 1 M Na_2SO_4 can be attributed to the different ions and pH.

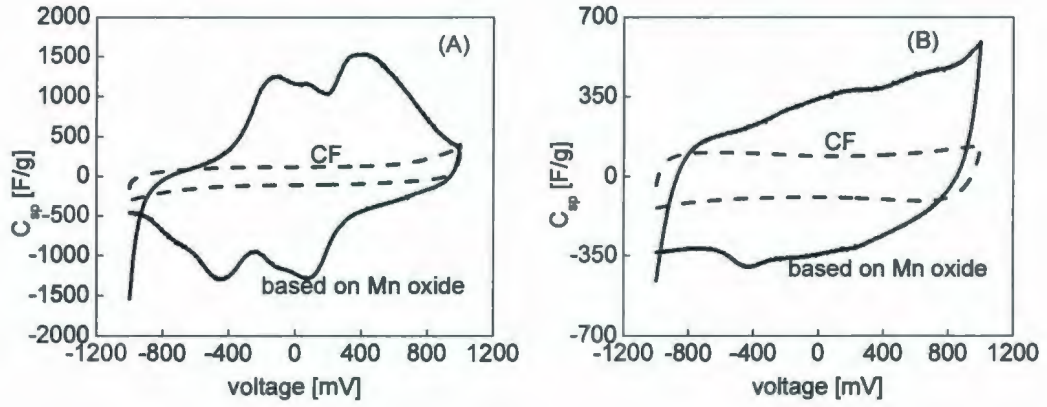

Fig. 5.14 Cyclic voltammograms (2 mV/s) for 22.4% Mn oxide/CF composite supercapacitors in 2 M LiOH (A) and 1 M Na_2SO_4 (B). The electrode masses are specified in Table 5.6.

Table 5.6 Specific capacitances for Mn oxide/CF composite supercapacitors in 2 M LiOH and 1 M Na_2SO_4 (two-electrode configurations)

	Loading (%)	Electrolyte	Mass (mg)	C_{sp} (F/g)	C_{sp} based on Mn oxide (F/g)
CF		2M LiOH	14.48+14.41	124	
composite	22.4	2M LiOH	19.22+19.07	264	751
composite	34.3	2M LiOH	21.37+21.26	322	702
CF		1M Na_2SO4	12.59+12.07	98	
composite	22.4	1M Na_2SO4	18.86+19.98	143	297

Specific capacitances based on the combined masses of both electrodes of each supercapacitor derived from Fig. 5.14 (and other results) are listed in Table 5.6, together with single electrode specific capacitances calculated for the Mn oxide component. It can be seen that the Mn oxide capacitance in 2 M LiOH decreased with increasing Mn oxide

loading. In addition, changing the electrolyte to 1 M Na_2SO_4 decreased the Mn oxide specific capacitance by 60%.

5.3.2.4 Mechanisms

The high specific capacitances for the Mn oxide components of the composites in basic electrolytes can be attributed to an alkali metal ion insertion mechanism. The following equations (see Eq. 5.3) show the reactions involved in charging and discharging.[24, 26, 27]

$$MnO_2 + A^+ + e^- \leftrightarrow MnOOA \quad \text{Eq. 5.3}$$

where A is an alkali metal, such as Li, Na, and K.

The maximum specific capacitance for the Mn oxide component should be ca. 1110 F/g, based on the above mechanism. For the composites prepared here by the spontaneous reduction method, the specific capacitances (over 1000 F/g) based on the Mn oxide components are close to this theoretical value. The high electrochemical utilization of the Mn oxide can be attributed to the thin film structure, which will allow the electrolyte to access the whole Mn oxide layer. Importantly, this thin film structure enhanced contact between the Mn oxide and the carbon fibres, leading to high electron access.

5.3.2.5 Annealing temperature

The capacitive behaviors in 2 M LiOH of Mn oxide/CF composites annealed at different temperatures in air were characterized by cyclic voltammetry as shown in Fig.

5.15. It can be seen from Fig. 5.15(A) that all of the voltammograms had similar shapes, including two specific capacitance peaks. Fig. 5.15(B) shows calculated voltammograms for the Mn oxide component of each composite. It can be seen that the composites annealed at 100 °C and 150 °C showed slightly higher specific capacitances than those that were annealed at 50 °C and dried at room temperature. The increase in specific capacitance with annealing can be mainly attributed to the loss of water, which decreases the mass of Mn oxide.

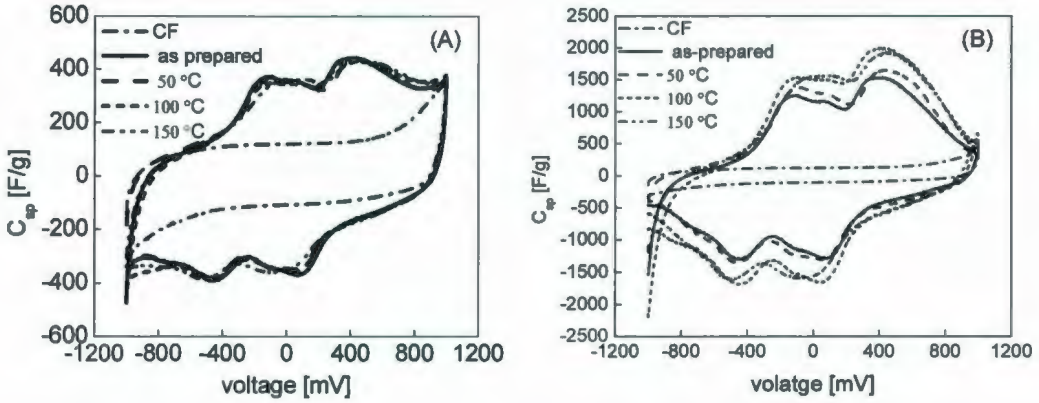

Fig. 5.15 Cyclic voltammograms (2 mV/s) in 2 M LiOH for Mn oxide/CF supercapacitors with 22.4% Mn oxide/CF composite electrodes annealed at different temperatures. (A) For the composites and (B) based on the Mn oxide alone. The electrode masses are specified in Table 5.7.

Average specific capacitances derived from Fig. 5.15 are given in Table 5.7. All of the composites gave similar specific capacitances of ca. 267 F/g for the 1st cycle. However, the specific capacitance calculated for the Mn oxide component increased with increasing annealing temperature (≤100 °C), followed by a slight decrease. It is clear that the best annealing temperature range was between 100 °C and 150 °C.

Table 5.7 Electrochemical data for supercapacitors constructed with CF and 22.4% Mn oxide/CF composites annealed at different temperatures

	Loading	Mass(mg)	C_{sp} (F/g)	C_{sp} (F/g) based on the Mn oxide component	ESR (Ω)	R_i (Ω)
CF		14.48+14.41	124		0.78	2.14
As-prepared	22.36%	19.22+19.22	264	751	1.07	10.8
50 °C	20.20%	16.26+16.20	268	838	1.92	14.8
100 °C	16.28%	17.24+17.68	269	1017	1.49	18.3
150 °C	16.80%	15.30+14.79	267	973	1.61	22.5

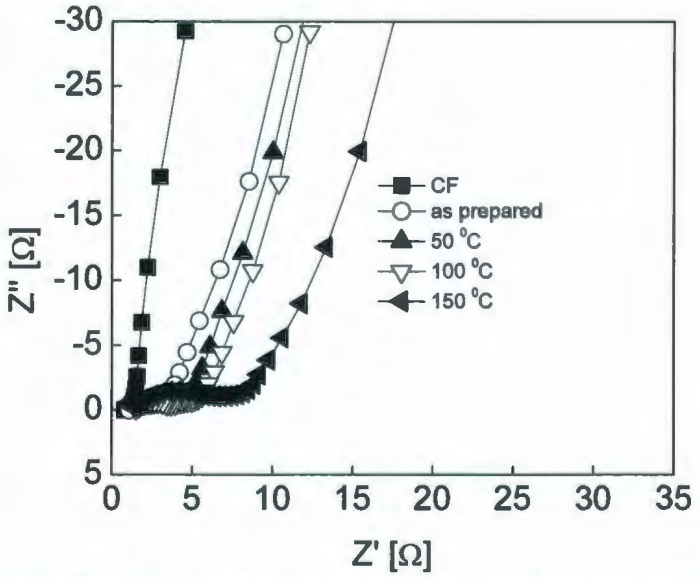

Fig. 5.16 Nyquist plots for the supercapacitors described in Fig. 5.15.

The supercapacitors described in Fig. 5.15 were also characterized by impedance spectroscopy as shown in Fig. 5.16. It can be seen that all of the Nyquist plots showed the

characteristics for porous electrodes, including a ca. 45 degree region at high frequencies and a near vertical region at low frequencies. ESR and R_i values derived from Fig. 5.16 are given in Table 5.7. It is clear that the ESR of the CF supercapacitor was far less than for the composite supercapacitors. This can be attributed to the low electronic conductivity of the Mn oxide component.[9] The ESR of the composite supercapacitors did not change significantly with increasing annealing temperature. However, R_i sharply increased with increasing annealing temperature, which is different from the results of Xu *et al.* On the contrary, the ionic conductivity of Mn oxide decreased with annealing temperature.[16] The change in R_i for Mn oxide/CF composites is most likely due to deformation of Mn oxide film during annealing, leading to loss of contact between some of Mn oxide film and the carbon fibers. This process should decrease the specific capacitance of Mn oxide components. However, the composite also lost water content during annealing, and this will increase its specific capacitance. So the specific capacitance at different annealing temperatures depends on the net contribution of both factors.

5.3.2.6 Constant current discharging

The performance of a symmetric composite supercapacitor was characterized by constant current discharging as shown in Fig. 5.17. It can be seen that the initial voltage quickly decreased over the first few milliseconds due to the ESR of the cell. Energy densities and power densities derived from Fig. 5.17 are given in Table 5.8, which indicates that the maximum energy density was 16.8 W h/kg, and that the energy density

decreased with increasing current. The maximum power density measured was 5.8 kW/kg. However, the performance of Mn oxide supercapacitor will decrease with cycling (see section 5.3.2.7).

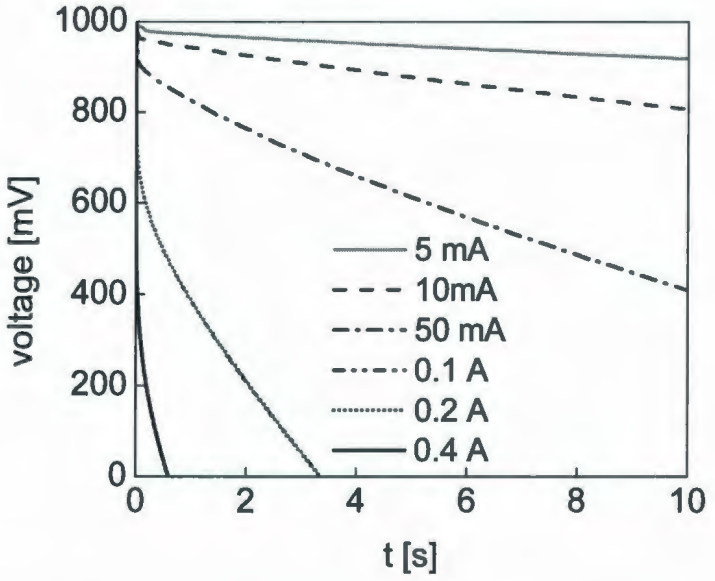

Fig. 5.17 Constant current discharging curves for a 22.4% Mn oxide/CF composite (dried at room temperature, 19.22 mg + 19.07 mg) supercapacitor with a Celgard 3400 separator .

Table 5.8 Energy and power densities for a 22.4% Mn oxide/CF supercapacitor

current (A)	-0.005	-0.01	-0.05	-0.1	-0.2	-0.4
E (W h/kg)	16.8	11.9	11.1	8.8	4.9	0.9
P (kW/kg)	0.2	0.4	1.9	3.4	5.3	5.8

5.3.2.7 Stability

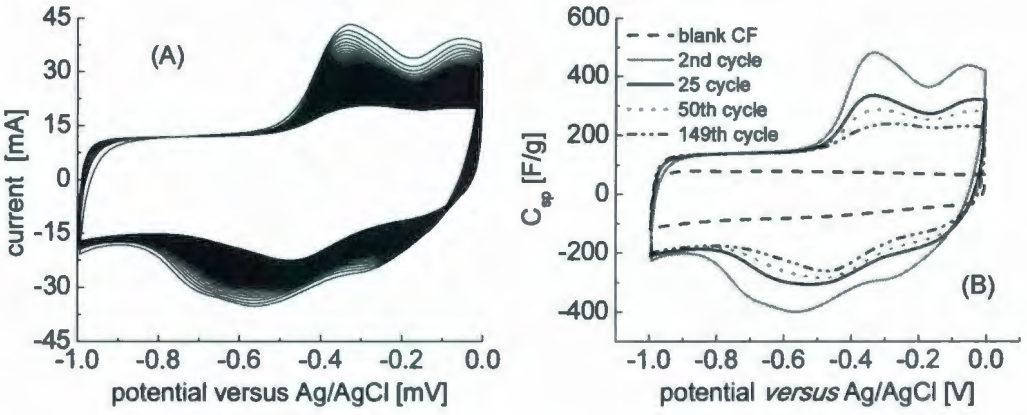

Fig. 5.18 Long-term cyclic voltammograms (5 mV/s) of an 11.6% Mn oxide/CF composite electrode (17.22 mg) (using a Pine potentiostat).

The stability of an 11.6% MnO_2/CF composite electrode was tested by long-term cyclic voltammetry as shown in Fig. 5.18. Fig. 5.18(A) shows the voltammograms for all 149 cycles. It can be seen that the current responses between -0.4 V and 0 V (anodic scan) and between -0.1 V and -0.8 V (cathodic scan) gradually decreased with cycling, while the current response did not change significantly between -1 V and 0.4 V (anodic scan). Fig. 5.18(B) shows the voltammograms for selected cycles for which the currents have been converted to specific capacitances. The average specific capacitances quickly decreased during the first 25 cycles, followed by a slower decrease with cycling. The average specific capacitance had decreased by 20.5% and 34.5% at the 25th and the 149th cycles, respectively. The quick decrease in specific capacitances may be ascribed to the irreversible Mn(IV) to Mn(II) reaction, leading to the dissolution of Mn oxide.[28]

Although the specific capacitance of the Mn oxide component decreased with cycling, it was still significantly higher than for the CF alone.

5.3.3 Binary Ru-Mn oxide /CF composites

Binary Mn-Ru oxide/CF composites were prepared by multistep spontaneous deposition and spontaneous co-deposition methods. TGA was used to determine the loading of the binary Mn-Ru oxide/CF composites (see Table 5.10) based on the residual mass. The properties of these composites were characterized by SEM, EDX, and cyclic voltammetry.

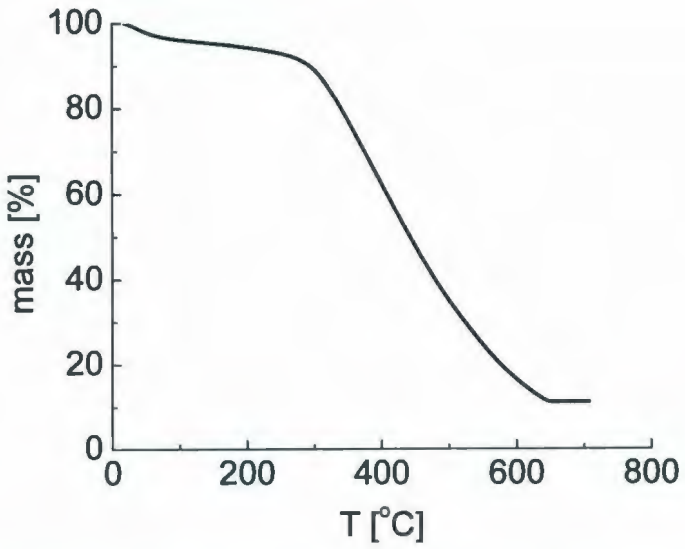

Fig. 5.19 TGA curve of a binary Mn-Ru oxide/CF sample prepared by multistep deposition

One binary Mn-Ru oxide/CF composite was prepared by repetitive deposition of Mn and Ru oxide layers (10 of each): a piece of CF sheet was first allowed to react for

1.5 min in 0.05 M $KMnO_4$, then 5 min in 0.05 M $KRuO_4$. The deposition procedures in the $KMnO_4$ and $KRuO_4$ solutions were repeated 9 times. As a consequence, the first layer of the CF was Mn oxide, followed by a Ru oxide layer, and the composite included 10 repeated structures (Mn oxide/Ru oxide layers). The metal oxide loading of the composite was 10.8% from TGA (see Fig. 5.19).

5.3.3.1 Thermogravimetric analysis

The thermal dynamic properties of a binary Mn-Ru composite prepared by multistep deposition were characterized by TGA as shown in Fig. 5.19. It can be seen that the sample gradually lost mass with increasing sample temperature (< 350 °C). The decreases in mass can be attributed to the loss of adsorbed water on the surface of the composite and the dehydration of hydrous Mn-Ru oxide. However, the sample quickly lost mass at high temperature (350 °C - 620 °C). This can be attributed to the oxidation of the carbon. Finally, the sample reached a residual mass of 10.8%, which corresponds to anhydrous Mn-Ru oxide and the ash content of the CF. The residual mass can be considered as the loading of the composite because the ash content is negligible (see Chapter 3).

5.3.3.2 Multistep deposition

The texture of the 10.8% Ru-Mn oxide/CF composite sample was characterized by SEM as shown in Fig. 5.20. According the deposition procedures, multilayers should form on the CF surface. However, only two distinct layers of oxides can be seen to be

evenly deposited on the CF surface. This can be attributed to thinness of the individual layers which cannot be viewed by SEM. Unlike the hydrous Ru oxide/CF composite (see Fig. 5.1 and Fig. 5.2), the coating layers of the 10.8% Ru-Mn oxide/CF composite show only very minor cracks following drying at room temperature.

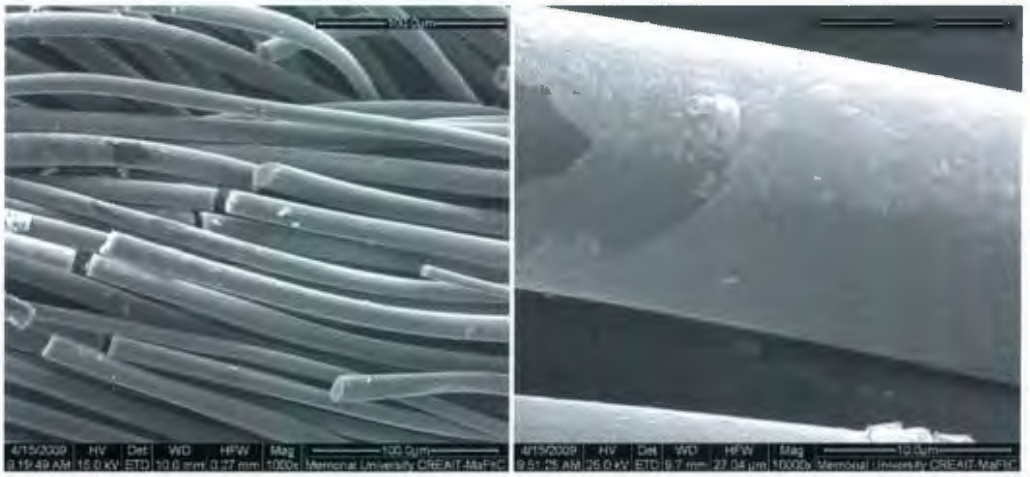

Fig. 5.20 SEM images of a 10.8% Mn-Ru oxide/CF composite prepared by repetitive deposition of Mn and Ru oxide layers (10 of each)

Fig. 5.21 shows an EDX of the 10.8% Mn-Ru oxide/CF composite prepared by repetitive deposition. It can be seen that Mn, Ru, and O were present in the coating layers as expected, and that there was residual K from $KMnO_4$, $KRuO_4$, and KOH. Semiqualitative compositions from this spectrum are given in Table 5.9, which shows that the ratio of Mn to Ru was 1.50:1. The oxygen concentration was much higher than expected for the designated metal(IV) oxides, which can be attributed to the hydration of the oxides, adsorbed water, and oxygen functionality on the CF.

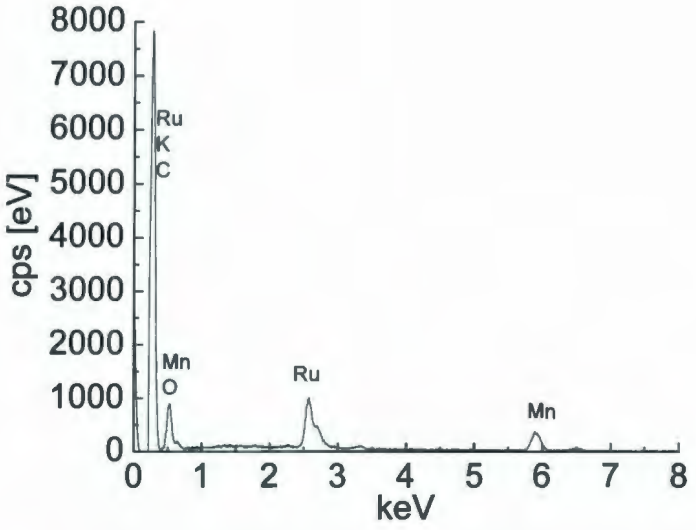

Fig. 5.21 EDX of a 10.8% Mn-Ru oxide/CF composite sample prepared by repetitive deposition of Mn and Ru oxide layers (10 of each)

Table 5.9 Composition of a 10.8% Mn-Ru oxide/CF composite prepared by repetitive deposition of Mn and Ru oxide layers (10 of each) measured by EDX

Element	Series	Measured concentration [mass %]	Normalized concentration [mass %]	Ratios to Ru
Ruthenium	L-series	14.64	22.23	1.00
Manganese	K-series	11.95	18.14	1.50
Carbon	K-series	0.00	0.00	0.00
Potassium	K-series	0.47	0.72	0.08
Oxygen	K-series	38.79	58.91	16.74

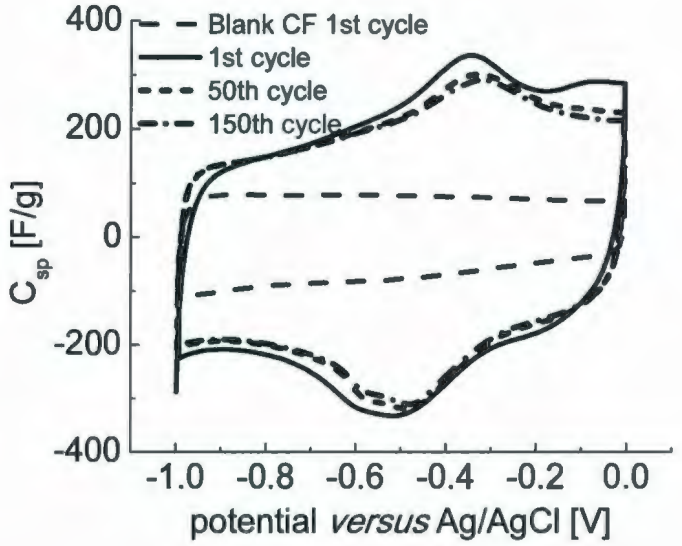

Fig. 5.22 Cyclic voltammograms (5 mV/s) in 2 M LiOH for a 10.8% Mn-Ru oxide/CF sample (16.68 mg; dried at room temperature) prepared by repetitive deposition.

The capacitive behavior of the 10.8% Mn-Ru oxide/CF composite (prepared by repetitive deposition) electrode in 2 M LiOH was characterized by long-term cyclic voltammetry as shown in Fig. 5.22. It can be seen that the shapes of the voltammograms are different from those for both the hydrous Mn oxide/CF and hydrous Ru oxide/CF composites (see Fig. 5.6 and Fig. 5.13). There are peaks at ca. -0.3 V (anodic) and -0.5 V (cathodic) versus Ag/AgCl for the 10.8% Mn-Ru oxide/CF composite prepared by multistep deposition, and the average specific capacitance decreased only slightly with cycling, as summarized in Table 5.10. The loss of capacitance over 150 cycles (9.1%) was far less than that for an 11.6% Mn oxide/CF composite (34.5% loss; see Fig. 5.18). This indicates that the stability of the Mn oxide/CF composite was sharply enhanced by

the introduction of Ru oxide. The enhancement in stability is likely due to the barrier layer (Ru oxide layer) between Mn oxide and LiOH.

Table 5.10 Specific capacitances and stabilities for Mn-Ru oxide/CF composites prepared by different deposition methods

deposition methods		Multistep deposition	$MnRu_{0.18}O_x$/CF by co-deposition	$MnRu_{0.32}O_x$/CF by co-deposition
Loading		10.8%	25.0%	14.8%
C_{sp} (F/g) in 2 M KOH			661±53*	621±28*
C_{sp} (F/g) in 2 M LiOH		677±66*		
stability	1st cycle (F/g)	220 **	240**	210**
	150th cycle (F/g)	200**	200**	179**
	Loss (%)	9.1	16.7	14.8

*based on oxide component only
** based on composites

5.3.3.3 Spontaneous co-deposition methods

Binary Mn-Ru oxide/CF composites were prepared by spontaneous co-deposition using solutions containing both $KMnO_4$ and $KRuO_4$. The metal oxides loadings were measured by TGA (see Table 5.10). The ratios of Mn to Ru were estimated by the amounts of Mn and Ru employed in the syntheses.

5.3.3.3.1 $MnRu_{0.18}O_x$/CF composite

The texture of a 25.0% $MnRu_{0.18}O_x$/CF composite prepared by spontaneous co-deposition of Mn and Ru oxides was characterized by SEM as shown in Fig. 5.23. It can

be seen that the Mn-Ru oxide component evenly coated the CF surface. Compared to the texture of the 10.8% Mn-Ru oxide/CF composite prepared by repetitive deposition shown in Fig. 5.20, the coating layer of the 25.0% $MnRu_{0.18}O_x$/CF composite prepared by co-deposition consisted of much larger particles with diameters of ca. 500 nm.

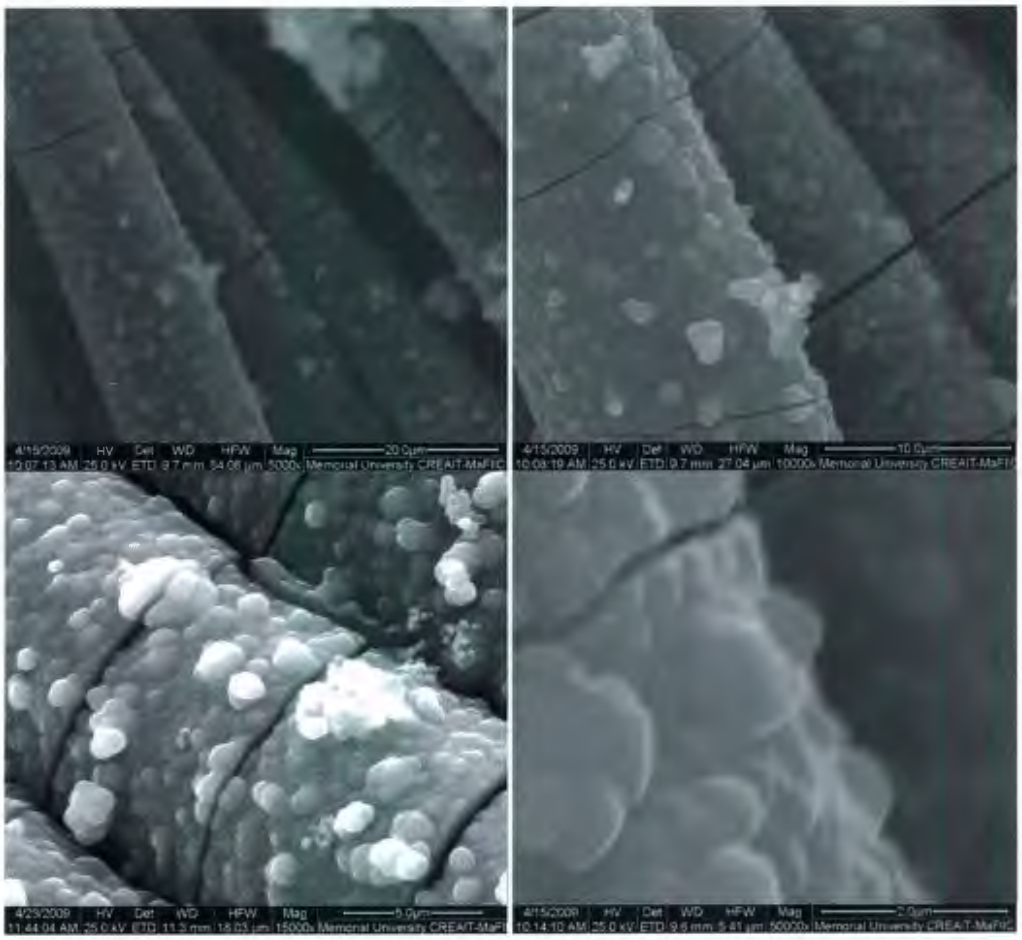

Fig. 5.23 SEM images of a 25.0% $MnRu_{0.18}O_x$/CF composite prepared by co-deposition.

The capacitive behavior of a 25.0% $MnRu_{0.18}O_x$/CF composite (prepared by co-deposition) electrode in 2 M KOH was characterized by cyclic voltammetry as shown in Fig. 5.24. It is clear that the shapes of the voltammograms were different from those for

the composites with a single metal oxide (see Fig. 5.6 and Fig. 5.13) and binary Mn-Ru oxide prepared by repetitive deposition (Fig. 5.22). It can be seen from Fig. 5.24 that the voltammogram had specific capacitance peaks at ca -0.257 V (anodic) and -0.476 V (cathodic), and that the anodic peak position shifted to lower potentials with cycling while the cathodic peak did not change significantly. It is not clear what redox reactions occur during cycling.

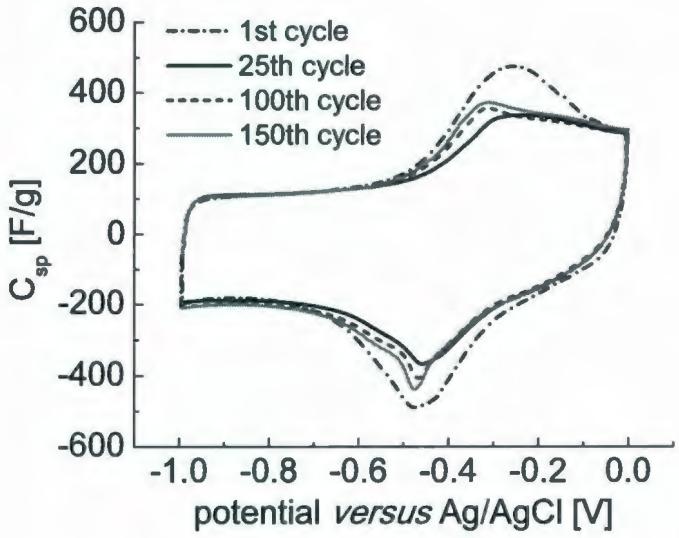

Fig. 5.24 Cyclic voltammograms at 5 mV/s for a 25.0% $MnRu_{0.18}O_x$/CF composite prepared by co-deposition (20.3 mg) in 2 M KOH.

Fig. 5.24 also shows that the changes in specific capacitances were insignificant over the potential range from -1.0 V to -0.5 V (anodic) and -1 V to -0.6 V (cathodic). However, the average specific capacitance over the full potential range (-1.0 to 0 V) first decreased with cycling, reaching a minimum value at roughly the 25th cycle, and then increased slightly. These complex changes in specific capacitances are most likely due to

structural changes in the metal oxide layer caused by repeated K^+ insertion-extraction. Table 5.10 shows that the loss of specific capacitance was only 16.7% after 150 cycles, which is less than for a similar hydrous Mn oxide/CF composite (34.5%).

5.3.3.3.2 14.8% $MnRu_{0.32}O_x$/CF composite

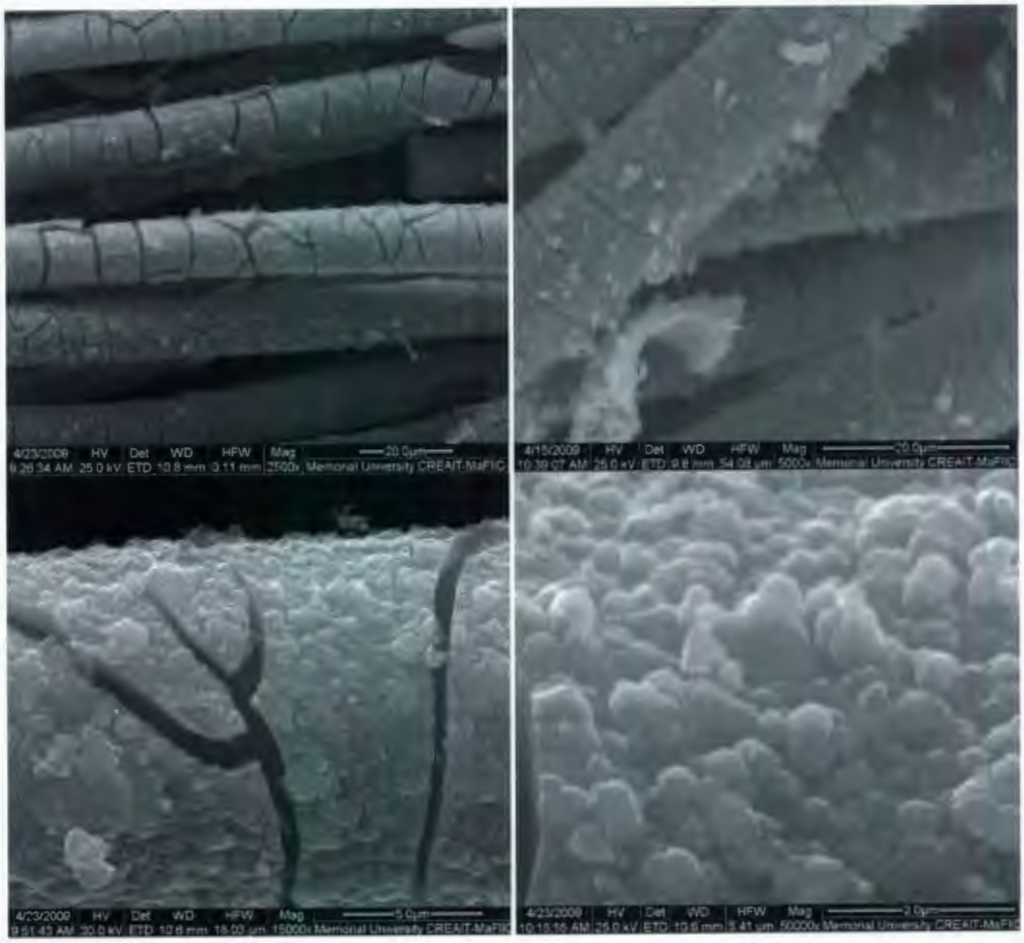

Fig. 5.25 SEM images of a 14.8% $MnRu_{0.32}O_x$/CF composite prepared by co-deposition

The texture of a 14.8% $MnRu_{0.32}O_x$/CF composite prepared by co-deposition was characterized by SEM as shown in Fig. 5.25. It can be seen that the Mn-Ru oxide layer

(thickness of ca. 1.3 μm) evenly coated the CF surface, but was heavily cracked. The coating layer consisted of small particles with diameters of ca. 220 nm, which are smaller than for the $MnRu_{0.18}O_x$/CF composite prepared by co-deposition.

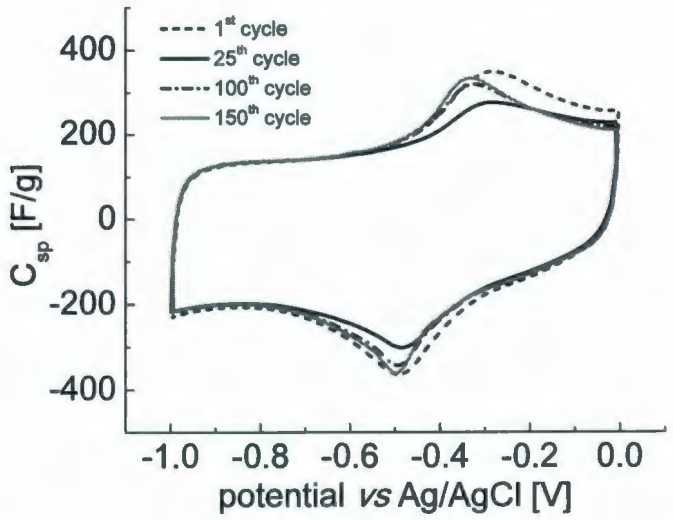

Fig. 5.26 Cyclic voltammograms (5 mV/s) for a 14.8% $MnRu_{0.32}O_x$/CF composite (16.3 mg) prepared by co-deposition in 2 M KOH.

Fig. 5.26 shows cyclic voltammograms for the 14.8% $MnRu_{0.32}O_x$/CF composite prepared by co-deposition, which are similar to those of the 25.0% $MnRu_{0.18}O_x$/CF composite. The average specific capacitance decreased with cycling, and reached a minimum value at ca. cycle 25, and then increased with cycling. Table 5.10 shows the loss of the specific capacitance of the composite to be 14.8% after 150 cycles, which is slightly lower than for the $MnRu_{0.18}O_x$/CF composite (16.7%).

5.4 Conclusions

Thin film metal oxide/CF composites were synthesized by spontaneous reduction methods. Their properties were characterized by SEM, EDX, TGA, cyclic voltammetry, constant current discharging, and impedance spectroscopy. SEM images showed that thin oxide layers were evenly deposited on the carbon fibres. Specific capacitances based on the hydrous Ru oxide components of Ru oxide/CF composites in 1 M H_2SO_4 decreased with increasing loading. The maximum average specific capacitance was 824±152 F/g (based on metal oxide alone) for a 7.4% Ru oxide/CF composite. This high specific capacitance was ascribed to the thin film structure of the Ru oxide. The specific capacitance of the composites decreased with damage of the film structure due to drying or annealing. For example, the specific capacitance of a 27.4 % Ru oxide/CF composite decreased by 5.1%, and the electrode was dried at room temperature. ESR and R_i values increased with increasing Ru oxide loading. Drying the composites at room temperature increased R_i, but annealing at 110 °C caused a sharp decrease in R_i due to an increase in the electronic conductivity of the hydrous Ru oxide.

The Ru oxide/CF composites showed very high stability in basic electrolytes. The specific capacitance in 2 M LiOH did not change significantly during 200 cycles. However, the hydrous Ru oxide oxide/CF was not stable in 1 M H_2SO_4, although its stability can be improved by annealing at 110 °C.

Mn oxide/CF composites had high quality Mn oxide film structures. The specific capacitance based on the Mn oxide component decreased only slightly with increasing loading. However, specific capacitances quickly decreased with cycling. For instance, the

specific capacitance for an 11.6% Mn oxide/CF composite in 2 M LiOH was 264 F/g (over 1000 F/g for the Mn oxide component) for the first cycle, whereas it had decreased to 173 F/g by the 149th cycle. Composites annealed at 110 °C showed the highest specific capacitance for the Mn oxide component (1017 F/g), but R_i sharply increased with annealing.

Binary Mn-Ru oxide/CF composites show high stability due to the introduction of the Ru component. A 10.8% Mn-Ru oxide/CF composite prepared by a multistep deposition method exhibited good stability in 2 M LiOH with only a 9.1% loss of specific capacitance over 150 cycles. The binary Mn-Ru composites prepared by co-deposition methods showed that the specific capacitance decreased with cycling, and reached a mimnum value at ca. 25 cycles, then increased with further cycling.

References

1. Pandolfo, A. G.; Hollenkamp, A. F., *Journal of Power Sources* **2006,** *157* (1), 11-27.

2. Conway, B. E., *Electrochemical supercapacitors: scientific fundamentals and technological applications*. Plenum Press: New York, 1999.

3. Niu, J. J.; Pell, W. G.; Conway, B. E., *Journal of Power Sources* **2006,** *156* (2), 725-740.

4. Kalinathan, K.; DesRoches, D. P.; Liu, X. R.; Pickup, P. G., *Journal of Power Sources* **2008,** *181* (1), 182-185.

5. Liu, X. R.; Pickup, P. G., *Journal of Solid State Electrochemistry* **2010,** *14* (2), 231-240.

6. Lee, H. Y.; Goodenough, J. B., *Journal of Solid State Chemistry* **1999,** *144* (1), 220-223.

7. Reddy, R. N.; Reddy, R. G., *Journal of Power Sources* **2003,** *124* (1), 330-337.

8. Reddy, R. N.; Reddy, R. G., *Journal of Power Sources* **2004,** *132* (1-2), 315-320.

9. Raymundo-Pinero, E.; Khomenko, V.; Frackowiak, E.; Beguin, F., *Journal of the Electrochemical Society* **2005,** *152* (1), A229-A235.

10. Zhang, H.; Cao, G. P.; Wang, Z. Y.; Yang, Y. S.; Shi, Z. J.; Gu, Z. N., *Nano Letters* **2008,** *8* (9), 2664-2668.

11. Fischer, A. E.; Pettigrew, K. A.; Rolison, D. R.; Stroud, R. M.; Long, J. W., *Nano Letters* **2007,** *7* (2), 281-286.

12. Chang, J. K.; Lin, C. T.; Tsai, W. T., *Electrochemistry Communications* **2004,** *6* (7), 666-671.

13. Lee, C. Y.; Tsai, H. M.; Chuang, H. J.; Li, S. Y.; Lin, P.; Tseng, T. Y., *Journal of the Electrochemical Society* **2005,** *152* (4), A716-A720.

14. Subramanian, V.; Zhu, H. W.; Wei, B. Q., *Electrochemistry Communications* **2006,** *8* (5), 827-832.

15. Nagarajan, N.; Humadi, H.; Zhitomirsky, I., *Electrochimica Acta* **2006,** *51* (15), 3039-3045.

16. Xu, M. W.; Zhao, D. D.; Bao, S. J.; Li, H. L., *Journal of Solid State Electrochemistry* **2007,** *11* (8), 1101-1107.

17. Sugimoto, W.; Iwata, H.; Murakami, Y.; Takasu, Y., *Journal of the Electrochemical Society* **2004,** *151* (8), A1181-A1187.

18. Ginzburg, S. I., *Analytical chemistry of platinum metals*. Wiley: New York, 1975; p xii, 673 p.

19. Xiaorong Liu, T. A. Huber., Michael C. Kopac and Peter G. Pickup, *Electrochimica Acta* **2009,** *54* (27), 7.

20. Liu, X. R.; Pickup, P. G., *Journal of Power Sources* **2008,** *176* (1), 410-416.

21. Liu, X. R.; Pickup, P. G., *Energy & Environmental Science* **2008,** *1* (4), 494-500.

22. Brinker, C. J.; Scherer, G. W., *Sol-gel science: the physics and chemistry of sol-gel processing*. Academic Press: Boston, 1990; p xiv, 908 p.

23. Zheng, J. P.; Cygan, P. J.; Jow, T. R., *Journal of the Electrochemical Society* **1995,** *142* (8), 2699-2703.

24. Toupin, M.; Brousse, T.; Belanger, D., *Chemistry of Materials* **2004,** *16* (16), 3184-3190.

25. Juodkazyte, J.; Vilkauskaite, R.; Sebeka, B.; Juodkazis, K., *Transactions of the Institute of Metal Finishing* **2007,** *85* (4), 194-201.

26. Ghaemi, M.; Ataherian, F.; Zolfaghari, A.; Jafari, S. M., *Electrochimica Acta* **2008,** *53* (14), 4607-4614.

27. Pang, S. C.; Anderson, M. A.; Chapman, T. W., *Journal of the Electrochemical Society* **2000,** *147* (2), 444-450.

28. Barsukov, I. V.; North Atlantic Treaty Organization., *New carbon based materials for electrochemical energy storage systems: batteries, supercapacitors and fuel cells*. Springer: Dordrecht, 2006.

Chapter 6 Hybrid supercapacitors

6.1 Introduction

In recent years, hybrid supercapacitors (also called as asymmetric supercapacitors) have been a new trend for the development of supercapacitors due to integration of the advantages of different positive and negative electrodes.[1-3] This hybrid combination of electrodes can provide high energy density.[4, 5]

Hybrid combinations that have been investigated include carbon/metal oxide,[6-13] carbon/polymer,[14-16] metal oxide/metal oxide,[17] and polymer/metal oxide[18] combinations. A hybrid supercapacitor consisting of an anthraquinone modified carbon fabric (CF) electrode (the negative electrode) and an unmodified CF positive electrode was shown to provide a 40% higher average capacitance, 56% – 86% higher energy density, and improved power duration relative to a symmetric CF supercapacitor.[4] A hybrid supercapacitor with anthraquinone modified CF (the negative electrode) and Ru oxide (the positive electrode) electrodes requires 64% less Ru oxide relative to a symmetric Ru oxide supercapacitor to provide a similar energy.[5] Thin film metal oxide/CF composites, including hydrous Ru oxide/CF and Mn oxide/CF composites, are excellent electrode materials for supercapacitors (see Chapter 5) and attractive candidates for use in asymmetric supercapacitors.

In the work described in this chapter, hybrid supercapacitors consisting of thin film metal oxide/CF and CF electrodes were characterized by cyclic voltammetry and constant current discharging. In addition, a hybrid supercapacitor with Ru oxide (the

positive electrode) and 40% Pd/C (the negative electrode) electrodes was also characterized by electrochemical methods. The performances of anthraquinone modified CF/Ru oxide hybrid supercapacitors were also further improved by increasing the anthraquinone loading.

6.2 Experimental

6.2.1 Thin film metal oxide/CF//CF supercapacitors

Thin film Ru oxide/CF and Mn oxide/CF composites, were prepared as described in Chapter 5. The assembly of hybrid supercapacitors with a 2 M KNO_3 electrolyte was similar to that described for Ru oxide supercapacitors (see Chapter 2). Here, a thin film metal oxide/CF composite disc was employed as the positive electrode, while the negative electrode was unmodified CF. The separator was a 110A1 membrane (Nippon Sheet Glass Co., Ltd.) or a NRE211 membrane (Ion Power, Inc.)

6.2.2 Hybrid combinations of Ru oxide and Pd/C composite electrodes

A hybrid supercapacitor was constructed by sandwiching a Nafion N115 separator between a negative electrode consisting of a 9.0 mg 40% Pd/C composite (E-TECK) loaded on a 1 cm^2 CFP disc and a positive electrode consisting of 4.08 mg Ru oxide loaded on a 1 cm^2 CFP disc. Two titanium plates built into a polycarbonate block were used as current collectors. The assembly was immersed in a 1 M H_2SO_4 electrolyte in air.

6.2.3 Hybrid combinations of anthraquinone modified CF and Ru oxide electrodes

Preparation of anthraquinone modified carbon fabric (AMCF). The preparation of AMCF followed literature reports with only minor changes.[4, 5] Hypophosphorous acid (8.85 g, 50 % from Aldrich) was added to a mixture of 42 mL water and 30 mL acetone, which was then cooled to 0 °C using an ice-water bath. A piece of CF with known mass (5.0 cm x 5.5 cm) and 0.85 g of Fast Red Al salt (Acros, anthraquinone-1-diazonium chloride 0.5 $ZnCl_2$) were added to this cooled solution under stirring. After reaction for ca. 20 min, a further 10 mL H_2O and 20 mL acetone were added, and the reaction was continued for a further 40 min. The resulting modified CF sheet was removed and washed with copious deionized water until the supernatant was neutral, then dried at 110 °C in air for 1.5 h. The anthraquinone loading was 15.9% based on the increase in dry mass of the CF, which is much higher than reported in the literature (7% - 10%).[4, 5]

The assembly of Ru oxide/AMCF hybrid supercapacitors. The assembly of hybrid supercapacitors was the same as for Ru oxide supercapacitors. A NRE211 separator was used. The Ru oxide electrode was maintained at positive potentials relative to the AMCF electrode in all experiments. The electrolyte was 1 M H_2SO_4.

6.2.4 Electrochemical characterization

Electrochemical properties of the hybrid supercapacitors were characterized by cyclic voltammetry and constant current discharging using an EG&G 273A potentiostat/galvanostat. For constant current discharging experiments, the

supercapacitors were charged to the operating voltage for 5 min, then discharged to 0 V using different constant currents.

6.3 Results and discussion

6.3.1 Thin film metal oxide/CF//CF supercapacitors

Ru oxide/CF//CF and Mn oxide/CF//CF supercapacitors were characterized in 2 M KNO_3 by cyclic voltammetry and constant current discharging. Their stabilities were evaluated by long-term cyclic voltammetry.

6.3.1.1 Ru oxide/CF//CF hybrid supercapacitors

The capacitive behavior of a hybrid supercapacitor consisting of Ru oxide/CF composite and CF electrodes was characterized in 2 M KNO_3 by cyclic voltammetry as shown in Fig. 6.1(A). It can be seen that the Ru oxide/CF electrode had a stable potential window of -0.6 V to 1.0 V versus Ag/AgCl, while the stable potential window for the CF electrode was -1.0 V to 0.2 V. The voltammogram of the hybrid supercapacitor shows a higher operating voltage (up to 2.0 V) than either electrode individually.

Fig. 6.1(B) shows discharge curves for the Ru oxide/CF//CF hybrid supercapacitor. It can be seen that the initial voltage quickly decreased over the first few milliseconds due to the ESR of the cell, and then decreased almost linearly with time. Energy densities and power densities derived from Fig. 6.1(B) are plotted in Fig. 6.1(C). It can be seen that the best energy density of the hybrid supercapacitor was 17.9 W h/kg,

which is much higher than the best energy density of 7.9 W h/kg for the symmetric supercapacitor with 27.4% Ru oxide/CF composite electrodes in 1 M H_2SO_4 described in section 5.3.1.5. The maximum power density measured was 3.4 kW/kg at a discharge current of 0.5 A.

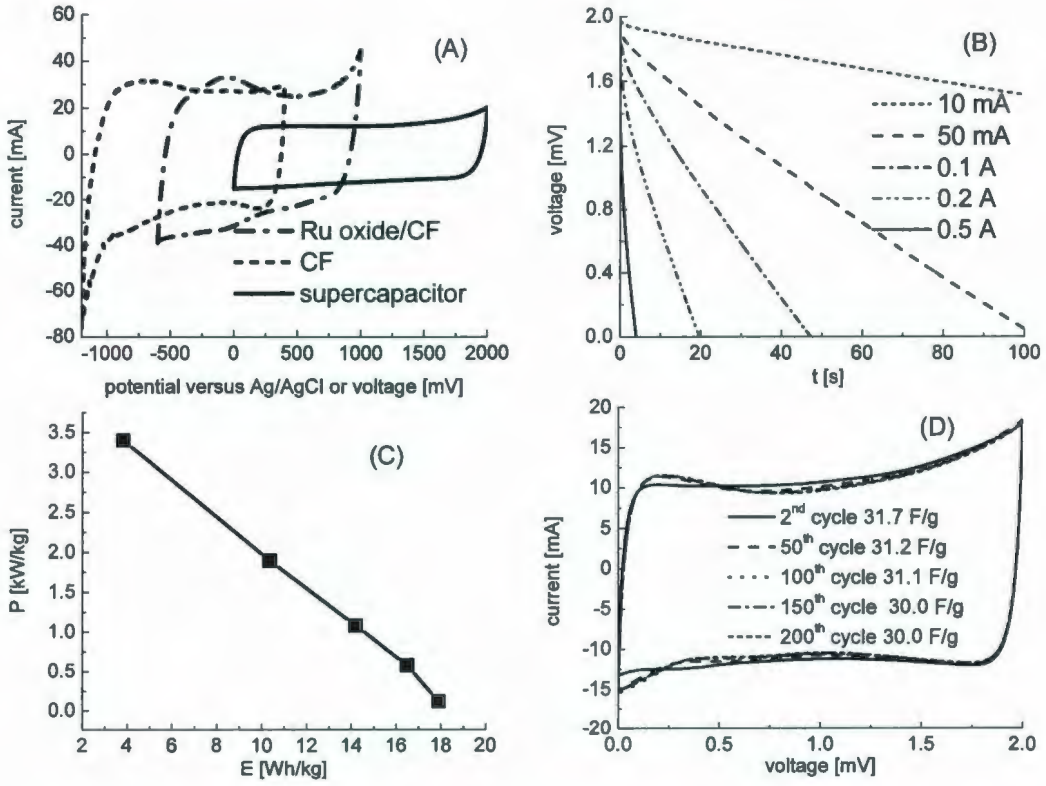

Fig. 6.1 Cyclic voltammograms at 5 mV/s (A), constant current discharging curves (B), and Ragone plots (C) for a hybrid supercapacitor with 7.4% Ru oxide/CF composite (32.8 mg) and CF (43.76 mg) electrodes and a NRE211 separator. Long-term stability at 10 mV/s (D) for a hybrid supercapacitor with 27.4% Ru oxide/CF composite (21.37 mg) and CF (15.0 mg) electrodes and a NRE211 separator.

The stability of a Ru oxide/CF//CF hybrid supercapacitor was evaluated by continuous cyclic voltammetry as shown in Fig. 6.1(D). It can be seen that the voltammograms did not change significantly with cycling. A 5.4% decrease in the

average specific capacitance was observed during the 200 cycles. This indicates that the Ru oxide/CF//CF hybrid combination has good stability.

6.3.1.2 Mn oxide/CF//CF hybrid supercapacitors

The experimental results presented in Chapter 5 demonstrate that the specific capacitance of Mn oxide/CF composites quickly decreased with cycling. This shortcoming could be overcome by a hybrid combination of Mn oxide/CF composite with an unmodified CF electrode if the instability is caused by low potentials.[3]

Fig. 6.2(A) shows voltammograms for CF and Mn oxide/CF electrodes, and a Mn oxide/CF//CF hybrid supercapacitor in 2 M KNO_3. The stable potential windows were -1.0 V to 0.2 V and -0.2 V to 1.0 V for the CF and the composite electrodes, respectively. The operating voltage of the hybrid supercapacitor was increased up to 2.0 V, which is similar to that of a Ru oxide/CF//CF supercapacitor.

Fig. 6.2(B) shows discharge curves of the Mn oxide/CF//CF hybrid supercapacitor. It can be seen that the initial voltage quickly decreased over the first few milliseconds due to the ESR of the cell, and then decreased almost linearly with time. Energy densities and power densities derived from Fig. 6.2(B) are plotted in Fig. 6.2(C). It can be seen that a maximum energy density of 18.3 W h/kg was obtained at 5 mA, and that the energy density decreased with increasing current. However, the power density increased with increasing current, and a power density of 14.2 kW/kg was obtained at 0.5 A. Compared to a symmetric supercapacitor with 22.4% MnO_2/CF composite electrodes in 2

M LiOH (16.8 W h/kg; see Chapter 5), the maximum energy density for the hybrid supercapacitor in 2 M KNO_3 was higher by 8.9%.

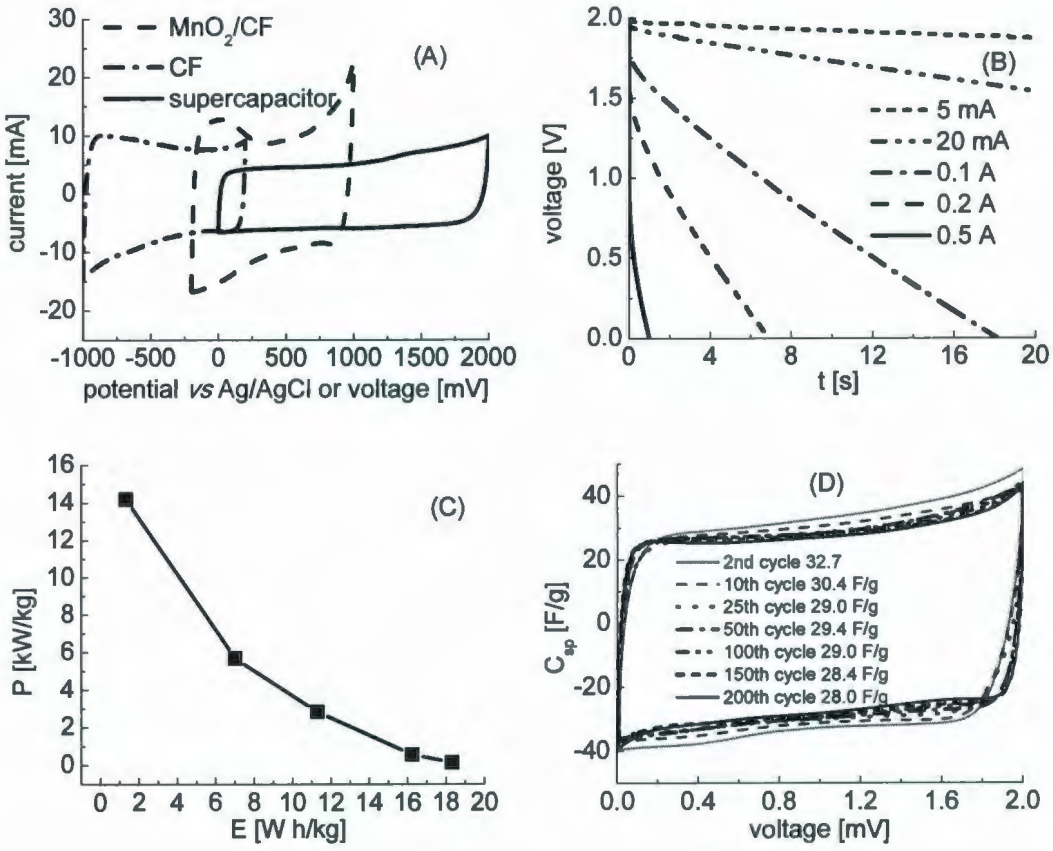

Fig. 6.2 Cyclic voltammograms at 5 mV/s (A), constant current discharging curves (B) and Ragone plot (C) for a hybrid supercapacitor with 17.1% Mn oxide/CF composite (20.8 mg) and CF (14.4 mg) electrodes and a NRE211 separator. Long-term stability at 10 mV/s (D) for a hybrid supercapacitor with 11.6% Mn oxide/CF composite (17.96 mg) and CF (14.32 mg) electrodes and an 110A1 separator

The stability of a 2.0 V Mn oxide/CF//CF hybrid supercapacitor was evaluated by long-term cyclic voltammetry as shown in Fig. 6.2(D). The voltammograms changed slightly with cycling. It can be seen that the average specific capacitance decreased with cycling. The specific capacitance of the hybrid supercapacitor was 33 F/g for the 2nd

cycle, and decreased by 7.0%, 11.3% and 14.3% for the 10^{th}, 25^{th} and 200^{th} cycles, respectively. It is clear that the main loss in specific capacitance occurred during the first 25 cycles. The main loss can be attributed to the dissolution of Mn oxide.

6.3.2 Pd/C//Ru oxide hybrid supercapacitors

6.3.2.1 Cyclic voltammetry

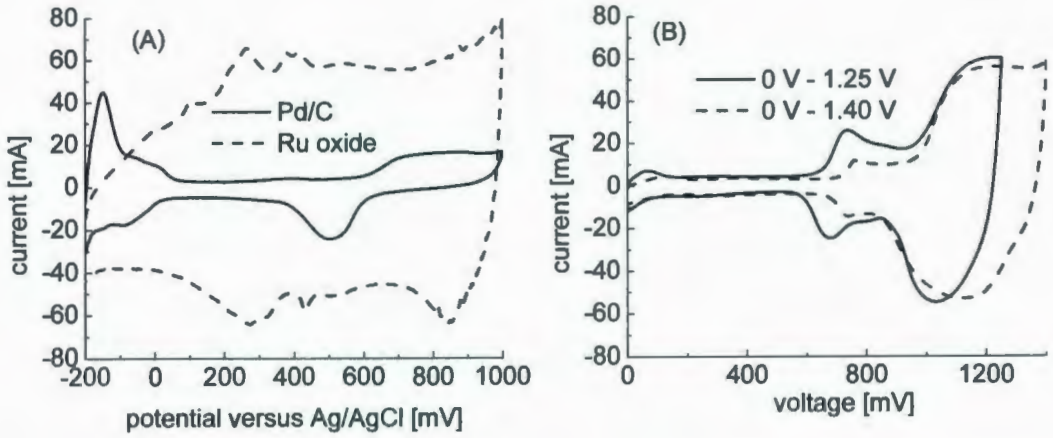

Fig. 6.3 Cyclic voltammograms at 20 mV/s for a Pd/C//Ru oxide hybrid supercapacitor with 40% Pd/C composite (9.0 mg) and Ru oxide annealed at 110 °C (4.08 mg) electrodes and a NRE211 separator. (A) Three-electrode configuration (B) two-electrode configuration.

Fig. 6.3(A) shows voltammograms of Ru oxide and Pd/C composite electrodes. It can be seen that the voltammogram of the Ru oxide electrode was somewhat different from those for Ru oxide electrodes in symmetric Ru oxide supercapacitors.[19] Two small peaks were observed in the from 0.2 V to 0.5 V potential range versus Ag/AgCl, which is similar to the voltammogram of ruthenic acid (designated as $H_{2x}RuO_{2+x}\cdot nH_2O$) as shown

in Fig. 6.4.[20] The formation of ruthenic acid is likely due to reaction between Ru oxide and hydrogen produced at the counter electrode (see Eq. 6.1 and 6.2). The voltammogram for the Pd/C composite electrode shows that the Pd component started to be oxidized slowly at above 0.6 V versus Ag/AgCl (anodic scan), while Pd oxide was reduced at potentials above 0.6 V (cathodic scan), and a peak was observed at ca. 0.5 V. Hydrogen was reversibly absorbed and extracted over the potential range of -0.2 V to 0 V.

$$2H_2O \rightarrow H_2 + O_2 \qquad \text{Eq. 6.1}$$

$$xH_2 + RuO_2 \cdot nH_2O \leftrightarrow H_{2x}RuO_{2+x} \cdot nH_2O \qquad \text{Eq. 6.2}$$

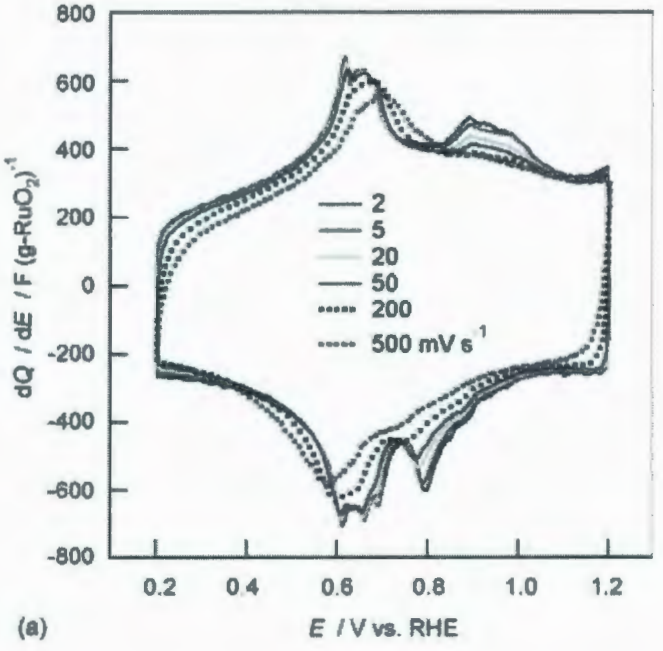

Fig. 6.4 Cyclic voltammograms at various scan rates for a layered $H_{0.2}RuO_{2.1} \cdot nH_2O$ thin film electrode (40 μg) in 0.5 M H_2SO_4

Reprinted from "Charge storage mechanism of nanostructured anhydrous and hydrous ruthenium-based oxides", vol 52, Wataru Sugimoto, Katsunori Yokoshima, Yasushi Murakami and Yoshio Takasu, page 1742-1748, Copyright (2006), with permission from Electrochimica Acta.

Fig. 6.3(B) shows that voltammograms of the hybrid supercapacitor have a guitar-like shape. It is clear that the supercapacitor has high current responses over the high potential range (>0.6 V). This kind of energy storage distribution is beneficial to deliver high energy since supercapacitors are usually only partially discharged in true applications.

6.3.2.2 Constant current discharging

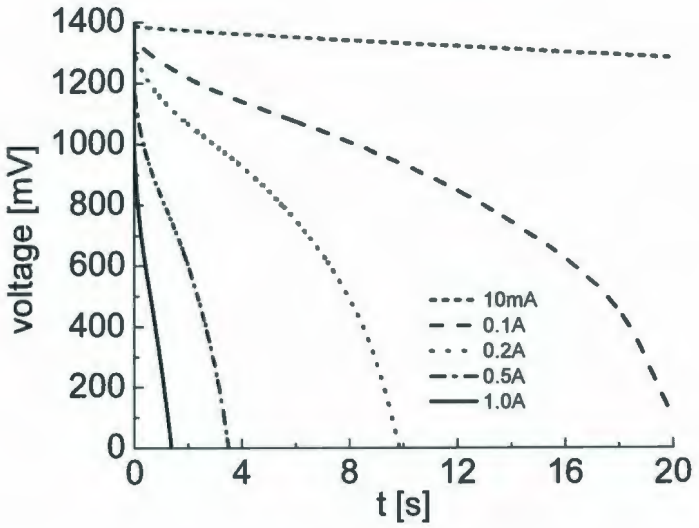

Fig. 6.5 Constant current discharging curves for a Pd/C//Ru oxide hybrid supercapacitor with an operating voltage of 1.4 V

The performance of the hybrid supercapacitor described in Fig. 6.3 was also tested by constant current discharging as shown in Fig. 6.5. It can be seen that the voltage of the supercapacitor decreased relatively slowly with time at high potentials (0.7 V - 1.4 V), corresponding to the high capacitance seen in Fig. 6.3(B). However, at low potentials

(<0.7 V), the voltage quickly decreased to 0 V, again in agreement with the cyclic voltammetry.

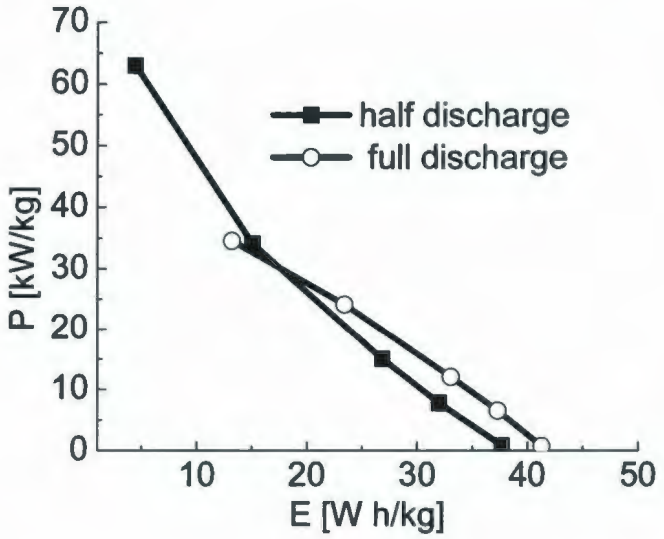

Fig. 6.6 Ragone plot for a 1.4 V hybrid Pd/C//Ru oxide supercapacitor

Energy and power densities derived from Fig. 6.5 are plotted in Fig. 6.6. It can be seen that the best energy densities were 41.3 W h/kg and 37.7 W h/kg based on full discharge and half discharge, respectively. The best energy density for half discharge was much higher than that for a symmetric Ru oxide supercapacitor (21.8 W h/kg based on half discharge).[21] It can be seen from Fig. 6.6 that the energy density of the hybrid supercapacitor decreased with increasing discharge current. The energy density decreased from 26.9 W h/kg (33.1 W h/kg based on full discharge) to 4.43 W h/kg (13.2 W h/kg based on full discharge) when the current was increased from 0.2 A to 1.0 A. However, the power density increased with increasing discharge current. The best power density

was 63 kW/kg (34.6 kW/kg based on full discharge) at 1.0 A, which is comparable to the literature result for a symmetric Ru oxide supercapacitor.[21]

6.3.2.3 Stability

The stability of the hybrid supercapacitor described in Fig. 6.3 was tested by repeated charge/discharge cycling. The operating voltage was 1.35 V with a constant current of 0.1 A for the first 500 cycles, while the operating voltage was decreased to 1.25 V for the second 500 cycles. Further 92 cycles were run at an operating voltage of 1.25 V and a current of 10 mA. The discharge times for selected cycles are given in Table 6.1. The discharge times, which relate to the energy storage capability of the hybrid supercapacitor, decreased with cycling for all conditions tested here.

Table 6.1 Discharge times for long-term experiments on a hybrid Pd/C//Ru oxide supercapacitor

The first 500 cycles Operating voltage: 1.35 V Constant current: 0.1 A		The second 500 cycles Operating voltage: 1.25 V Constant current: 0.1 A		Further 92 cycles Operating voltage: 1.25 V Constant current: 10 mA	
Cycle #	Discharge time (s)	Cycle #	Discharge time (s)	Cycle #	Discharge time (s)
2	12.58	2	6.58	2	91.53
50	12.34	50	6.48	10	89.75
100	11.69	100	6.48	50	81.34
200	11.03	200	6.45	92	74.40
300	10.52	300	6.06		
400	10.33	400	6.19		
500	9.84	500	5.92		

The performance changes were further investigated by cyclic voltammetry and constant current discharging after long-term cycling. Fig. 6.7(A) shows a comparison of

voltammograms recorded before and after long-term cycling. It can be seen that the voltammograms did not change significantly over the voltage range of 0.8 to 1.4 V, and that the main change occurred at 0.6 V to 0.8 V. Energy densities derived from Fig. 6.7(B) are listed in Table 6.2, which shows that the energy density loss for half discharge was 3.7 % (7.3% for full discharge) after 1092 cycles, indicating good stability. It can be seen from Table 6.2 that the discharge times were significantly different before and after long-term cycling, while the energy was fairly stable. These differences can be attributed to the potential-dependent capacitance of the Pd/C//Ru oxide hybrid supercapacitor (see Fig. 6.7). Although the discharge time for the initial measurement was longer than that after long-term cycling due to the higher capacitance over the potential range of 0.8 to 0.6 V, the impact on the whole energy storage was relatively small.

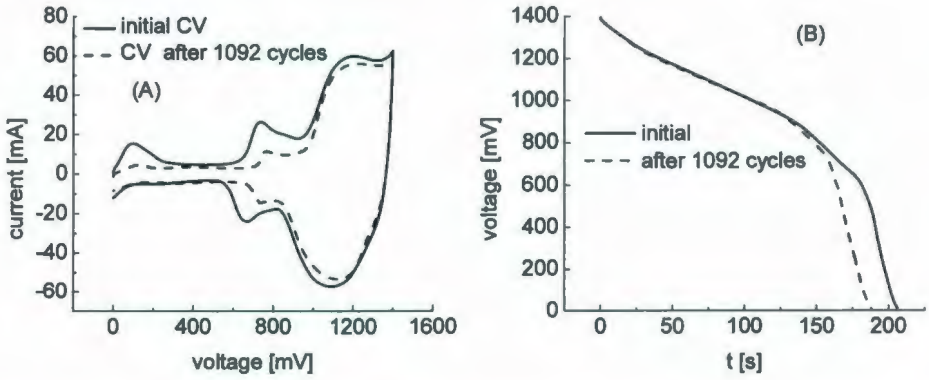

Fig. 6.7 Performance changes for the hybrid supercapacitor described in Fig. 6.3. (A) Cyclic voltammetry at 20 mV/s and (B) constant current discharging curves at 10 mA.

Table 6.2 Performance (at 10 mA) changes over 1092 cycles for a Pd/C//Ru oxide supercapacitor

Discharge for before or after long-term cycling	Potential window	Discharge time (s)	Energy density for full or half discharge (W h/kg)
Initial discharge	1.4 V to 0 V	206.8	41.3
Discharge after 1092 cycles	1.4 V to 0 V	188.6	38.3
Initial discharge	1.4 V to 0.7 V	167.3	37.7
Discharge after 1092 cycles	1.4 V to 0.7 V	159.2	36.3

6.3.3 AMCF/Ru oxide hybrid supercapacitors

6.3.3.1 Cyclic voltammetry

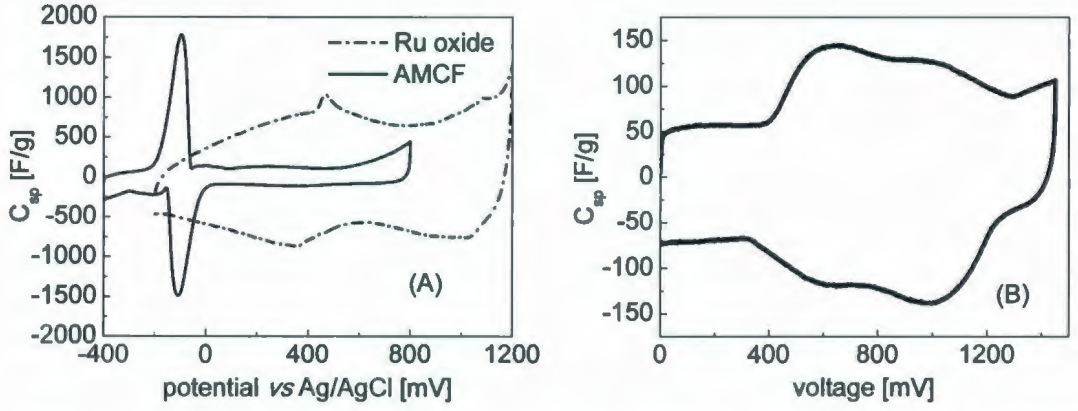

Fig. 6.8 Cyclic voltammograms at 5 mV/s for an AMCF/Ru oxide supercapacitor with 15.9% AMCF (17.14 mg) and Ru oxide (5.29 mg) and a NRE211 separator in 1 M H_2SO_4. (A) Three-electrode configuration and (B) two-electrode configuration.

The capacitive behavior of an AMCF/Ru oxide supercapacitor was characterized by cyclic voltammetry as shown in Fig. 6.8. Fig. 6.8(A) shows voltammograms for the positive electrode and the negative electrode separately. It can be seen that the AMCF

electrode had very high peak specific capacitances of 1783 F/g and 1489 F/g at -98 mV (anodic) and -109 mV (cathodic) versus Ag/AgCl, respectively. These specific capacitance peaks are due to the redox of the anthraquinone component as shown in Schematic 6.1. The voltammogram for the Ru oxide electrode is similar to those electrodes shown in Chapter 2. Fig. 6.8(B) shows a voltammogram of the hybrid supercapacitor. It can be seen that there was a wide specific capacitance peak between 0.4 and 1.2 V.

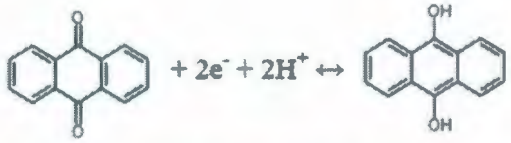

Schematic 6.1 Proposed process occurring for AMCF at ca. -0.1 V versus Ag/AgCl.

6.3.3.2 Constant current discharging

The performance of the hybrid supercapacitor described in Fig. 6.8 was tested by constant current discharging as shown Fig. 6.9(A). It can be seen that the supercapacitor had a potential-dependent capacitance, which agrees with the cyclic voltammetry. Energy and power densities derived from Fig. 6.9(A) are plotted in Fig. 6.9(B). For comparison purposes, energy and power densities for a symmetric Ru oxide supercapacitor (with an operating voltage of 1.2 V) are also plotted in Fig. 6.9(B). It can be seen that the best energy densities were similar, at 34.9 W h/kg and 32.1 W h/kg for the hybrid and the symmetric Ru oxide supercapacitors, respectively. However, the hybrid supercapacitor requires 76.3 % less Ru oxide relative to a symmetric Ru oxide supercapacitor to provide a similar energy density. This represents a further improvement in the performance of the

hybrid combination as compared to previous results.[5] At 1.0 A discharge current, the power densities were 25.6 kW/kg (with energy density of 15.7 W h/kg) and 31.2 kW/kg (with energy density of 12.7 W h/kg) for the hybrid and the Ru oxide supercapacitors, respectively.

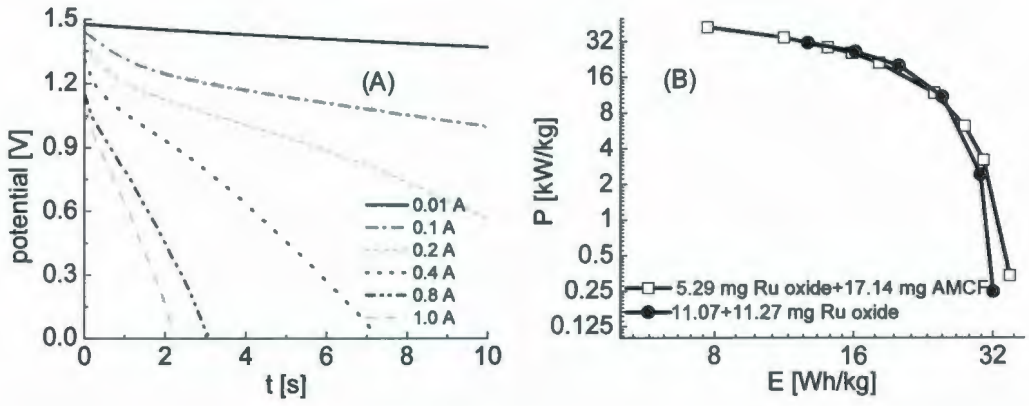

Fig. 6.9 Constant current discharge curves for an AMCF/Ru oxide supercapacitor as described in Fig 6.8 (A) and Ragone plots for the hybrid supercapacitor described in Fig. 6.8 and a symmetric supercapacitor with 22.34 mg of Ru oxide annealed at 110 °C and a NRE211 separator (B).

6.3.3.3 Long-term stability

The stability of an AMCF/Ru oxide supercapacitor was tested by a continuous charge/discharge method. Charge and discharge times for selected cycles are plotted against cycle number in Fig. 6.10. It can be seen that both decreased slightly with cycling. For example, the discharge times were 3.50 s, 3.48 s, 3.28 s and 3.15 s for the 5th, 2000th, 6000th and 9989th cycles, respectively. It is clear that the change in discharge time was insignificant during the first 2000 cycles. The loss of the discharge time was only 10 % after 9989 cycles, indicating good stability.

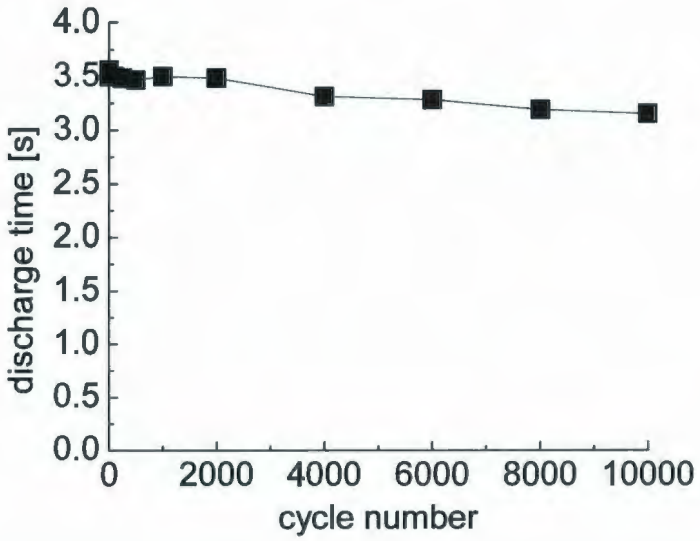

Fig. 6.10 Stability at 0.5 A/cm^2 for a hybrid supercapacitor (with an operating voltage of 1.3 V) with AMCF (16.50 mg) and Ru oxide (5.30 mg) electrodes.

6.4 Conclusions

Four types of hybrid supercapacitors were investigated by cyclic voltammetry and constant current discharging. The CF//Ru oxide/CF and CF//MnO_2/CF hybrid supercapacitors in 2 M KNO_3 have high operating voltages up to 2.0 V, thus providing high energy densities. Compared to a symmetric supercapacitor with 27.4% Ru oxide/CF composite electrodes in 1 M H_2SO_4 (E_{max}= 7.9 W h/kg), the maximum energy density for the CF//7.4% Ru oxide/CF supercapacitor was increased to 17.9 W h/kg. The maximum energy density for CF//MnO_2/CF supercapacitors in 2 M KNO_3 was also enhanced as compared to symmetric supercapacitors. Both the CF//Ru oxide/CF and CF//MnO_2/CF hybrid supercapacitors exhibited high stability. The loss of specific capacitance was only 5.4% for a CF//Ru oxide/CF supercapacitor after 200 cycles.

A Ru oxide//Pd/C hybrid supercapacitor has a maximum energy density of 41.3 W h/kg measured based on full discharge and excellent stability. Its energy loss was only 3.7 % based on half discharge (from 37.7 W h/kg to 36.3 W h/kg) after 1092 cycles. The best energy density was 34.9 W h/kg for a 1.5 V AMCF/Ru oxide hybrid supercapacitor, which requires 76.3 % less Ru oxide relative to a symmetric Ru oxide supercapacitor with 1.2 V operating voltage to provide a similar energy density. AMCF/Ru oxide supercapacitors have high stability, with an energy density loss of only 10 % observed over 9989 cycles.

References

1. Conway, B. E., *Electrochemical supercapacitors: scientific fundamentals and technological applications*. Plenum Press: New York, 1999.

2. Wang, Q.; Wen, Z. H.; Li, J. H., *Advanced Functional Materials* **2006,** *16* (16), 2141-2146.

3. Barsukov, I. V.; North Atlantic Treaty Organization., *New carbon based materials for electrochemical energy storage systems: batteries, supercapacitors and fuel cells*. Springer: Dordrecht, 2006.

4. Kalinathan, K.; DesRoches, D. P.; Liu, X. R.; Pickup, P. G., *Journal of Power Sources* **2008,** *181* (1), 182-185.

5. Algharaibeh, Z.; Liu, X. R.; Pickup, P. G., *Journal of Power Sources* **2009,** *187* (2), 640-643.

6. Du Pasquier, A.; Plitz, I.; Gural, J.; Menocal, S.; Amatucci, G., *Journal of Power Sources* **2003,** *113* (1), 62-71.

7. Wang, Y. G.; Yu, L.; Xia, Y. Y., *Journal of the Electrochemical Society* **2006,** *153* (4), A743-A748.

8. Sun, Z. H.; Yuan, A. B., *Chinese Journal of Chemical Engineering* **2009,** *17* (1), 150-155.

9. Du, X. A.; Wang, C. Y.; Chen, M. M.; Jiao, Y., *Journal of Inorganic Materials* **2008,** *23* (6), 1193-1198.

10. Wang, Y. G.; Xia, Y. Y., *Electrochemistry Communications* **2005,** *7* (11), 1138-1142.

11. Chen, L. M.; Lai, Q. Y.; Hao, Y. J.; Huang, J. H.; Ji, X. Y., *Ionics* **2008,** *14* (5), 441-447.

12. Khomenko, V.; Raymundo-Pinero, E.; Beguin, F., *Journal of Power Sources* **2006,** *153* (1), 183-190.

13. Brousse, T.; Marchand, R.; Taberna, P. L.; Simon, P., *Journal of Power Sources* **2006,** *158* (1), 571-577.

14. Laforgue, A.; Simon, P.; Fauvarque, J. F.; Mastragostino, M.; Soavi, F.; Sarrau, J. F.; Lailler, P.; Conte, M.; Rossi, E.; Saguatti, S., *Journal of the Electrochemical Society* **2003,** *150* (5), A645-A651.

15. Balducci, A.; Henderson, W. A.; Mastragostino, M.; Passerini, S.; Simon, P.; Soavi, F., *Electrochimica Acta* **2005,** *50* (11), 2233-2237.

16. Machida, K.; Suematsu, S.; Tamamitsu, K., *Electrochemistry* **2007,** *75* (8), 601-603.

17. Yuan, C. Z.; Gao, B.; Zhang, X. G., *Journal of Power Sources* **2007,** *173* (1), 606-612.

18. Song, R. Y.; Park, J. H.; Sivakkumar, S. R.; Kim, S. H.; Ko, J. M.; Park, D. Y.; Jo, S. M.; Kim, D. Y., *Journal of Power Sources* **2007,** *166* (1), 297-301.

19. Liu, X. R.; Pickup, P. G., *Journal of Power Sources* **2008,** *176* (1), 410-416.

20. Sugimoto, W.; Yokoshima, K.; Murakami, Y.; Takasu, Y., *Electrochimica Acta* **2006,** *52* (4), 1742-1748.

21. Liu, X. R.; Pickup, P. G., *Energy & Environmental Science* **2008,** *1* (4), 494-500.

Chapter 7 A new approach for predicting the energy and power of a supercapacitor using impedance spectroscopy

7.1 Introduction

Supercapacitors are emerging as alternative energy solutions. They have received intensive attention due to their current and potential applications in portable devices and electrical vehicles.[1-5] There are two kinds of supercapacitors based on different charge storage mechanisms, double layer capacitors and pseudocapacitors as described in Chapter 1.[5]

In order to discover new electrode materials with high performance for supercapacitors, various electrochemical techniques are used to evaluate the properties of these materials. These electrochemical techniques include cyclic voltammetry, constant current charging/discharging, constant power discharging and impedance spectroscopy.[6-8] Capacitance and energy values from cyclic voltammetry are usually lower than those from constant current discharging due to shorter timescales.[7] Constant current charging/discharging and constant power methods provide the most useful measures of supercapacitor performances, but are time-consuming. Impedance spectroscopy provides rapid measurement of the electrochemical properties of supercapacitors in the frequency domain, and allows the rapid separation of the various resistive and capacitive components of the cell.[9-11] Although various equivalent circuits, such as RC circuits and

transmission line models (see Fig. 1.3) are used to analyze impedance data, these methods are usually only approximations due to the complexity of the true circuits.[9, 12]

In an attempt to use impedance spectroscopy as a simple tool for evaluating supercapacitors, Miller[13] defined a characteristic frequency as the frequency at which the real impedance is equal to the imaginary impedance. Maximum energy and power densities were estimated by using a combination of the capacitance at low frequencies and the characteristic frequency (see section 7.3.1). Taberna *et al.*[14] and Kurzwell[15] also proposed methods that predict the energy and power of a supercapacitor from impedance spectroscopy (see section 7.3.1), but the reliability of these methods needs further investigation.

In the work described in this chapter, commercial, carbon fabric and Ru oxide supercapacitors were characterized by impedance spectroscopy and constant current discharging. A simple approach for predicting energy and power from the impedance data is proposed, and its reliability is evaluated by comparison with the results from constant current discharging.

7.2 Experimental

7.2.1 Commercial supercapacitor

A Bcap0140 (Maxwell Technologies) supercapacitor with a rated capacitance of 140 F, a rated voltage of 2.5 V and an internal resistance of 7.20 mΩ was used.

7.2.2 Carbon fabric supercapacitor

A piece of Spectracarb 2225 carbon fabric (CF) sheet (Engineered Fibers Technology) was cut into squares of ca. 6 cm^2. A CF supercapacitor was constructed by sandwiching a Nafion film (NRE211, from Ion power, Inc.) between two identical CF squares. Two titanium plates built into a Teflon block were used as current collectors. The assembly was dried at 145 °C for 10 min, and then immediately immersed in a beaker with 15 mL of acetonitrile saturated with tetraethylammonium tetrafluoroborate (Alfa-Aesar), and wrapped in parafilm to exclude air and moisture.

7.2.3 Ru oxide supercapacitors

The preparation of electrodes and the assembly of Ru oxide supercapacitors were the same as described in Chapter 2.[7,8] Hydrous ruthenium oxide annealed at 110 °C in air for 3 h was used.

7.2.4 Electrochemical characterization

Three-electrode and two-electrode configurations were used for characterizing the properties of the supercapacitors. For three-electrode configurations, two identical electrodes were used as the working electrode and the counter electrode, and an Ag/AgCl reference electrode was placed in the external electrolyte solution. In contrast, the reference electrode lead of the potentiostat was connected to the counter electrode in two-electrode configurations.

Cyclic voltammetry and constant current discharging measurements for the CF and Ru oxide supercapacitors were conducted by using an EG&G 273A Potentiostat/Galvanostat. For constant current discharging, the supercapacitors were first charged to 1.0 V (for the Ru oxide supercapacitor) or 2.5 V (for the CF supercapacitor), and then completely discharged to 0 V using different constant currents. The charge time was 5 min for both the Ru oxide and the CF supercapacitors, while it was 10 min for the Bcap0140 supercapacitor using a Solartron 1286 Potentiostat/Galvanostat.

Impedance spectroscopy for the CF and Ru oxide supercapacitors was conducted by using the EG&G 273A Potentiostat/Galvanostat, an EG&G 5210 lock-in amplifier and EG&G PowerSuite software with different DC bias voltages and an amplitude of 10 mV. The frequency range was from 10 kHz to 5 mHz.

Impedance spectroscopy measurements for the Bcap0140 supercapacitor were conducted with a Solartron 1286 potentiostat, 1250 Frequency Response Analyser and a Zplot software. The measurement frequency range was usually from 1.0 kHz to 0.5 mHz, with an amplitude of 10 mV and different DC bias potentials.

7.3 Results and discussion

7.3.1 Prediction of energy and power from impedance data

Electrochemical impedance spectroscopy imposes a DC-bias potential with a small sinusoidal voltage on an electrochemical system. The resulting sinusoidal current is analyzed and recorded by a frequency response analyzer and a computer (see Chapter 1).[9]

Impedance spectroscopy quickly provides frequency domain characteristics of an electrochemical system. Impedance spectroscopy can be used to predict the energy and power of a supercapacitor.[13-16]

Taberna *et al.*[14] utilized the frequency (ω), real capacitance (C_{re}), imaginary capacitance (C_{im}) and root mean square (rms) voltage (ΔU) to calculate the complex power of a supercapacitor (see Eq. 7.1-7.3.)

$$S(\omega) = P(\omega) + jQ(\omega) \quad \text{Eq. 7.1}$$

$$P(\omega) = \omega C_{im}(\omega)(\Delta U)^2 \quad \text{Eq. 7.2}$$

$$Q(\omega) = -\omega C_{re}(\omega)(\Delta U)^2 \quad \text{Eq. 7.3}$$

where S(ω), P(ω) and Q(ω) are the complex power, the active power (watt) and the reactive power (Volt-Ampere-reactive, VAR), respectively. C_{re} and C_{im} can be obtained by Eq. 7.4 and 7.5, respectively.

$$C_{re}(\omega) = \frac{-Z_{im}(\omega)}{\omega|Z(\omega)|^2} \quad \text{Eq. 7.4}$$

$$C_{im}(\omega) = \frac{Z_{re}(\omega)}{\omega|Z(\omega)|^2} \quad \text{Eq. 7.5}$$

where $Z_{im}(\omega)$ and $Z_{re}(\omega)$ are the imaginary and real impedance, respectively. $C_{re}(\omega)$ at low ω is equivalent to capacitances measured by constant current discharging. $C_{im}(\omega)$ corresponds to energy dissipation by irreversible processes.

|P|/|S| and |Q|/|S| values are used for charactering a supercapacitor's resistive and capacitive behaviors. |P|/|S| reaches a maximum value at high frequency, while the |Q|/|S| value increases with decreasing frequency. The supercapacitor behaves like a resistor and a pure capacitor at high and low frequencies, respectively. P|/|S| and |Q|/|S| values are the

same $(1/\sqrt{2})$ at a -45 degree phase angle, which corresponds to the transition between resistive and capacitive behaviors.

Kurzweil defined a complex power based on voltage and admittance,[15] as described by Eq. 7.6-7.8.

$$S = P + jQ \qquad \text{Eq. 7.6}$$

$$P = (\Delta U)^2 Y_{re} \qquad \text{Eq. 7.7}$$

$$Q = -(\Delta U)^2 Y_{im} \qquad \text{Eq. 7.8}$$

where S, P, Q, ΔU, Y_{re} and Y_{im} are complex power, the active power, the reactive power, rms potential, the real admittance and the imaginary admittance, respectively. The energy (E) is determined by Eq. 7.9

$$E = \frac{1}{2} C (\Delta U)^2 \qquad \text{Eq. 7.9}$$

where C is the capacitance at low frequencies.

Comparison of the equations proposed by Taberna *et al.*[14] and Kurzweil [15] reveals that the formulae for energy and power are related by replacing admittance with frequency (ω) and capacitance. However, the validities of these methods have not been verified by other electrochemical methods, such as cyclic voltammetry and constant current discharging.

There are a number of other methods for predicting the energy and power of a supercapacitor from impedance spectroscopy. Sawai *et al.*[17] converted frequency-domain responses to time-domain responses by performing a Fourier transform and the use of Ohm's law. Although this method does not require a specific modeling circuit, the complicated calculations limit its application. Miller [13] employed a characteristic

response time [t_0; the reciprocal of characteristic frequency (f_0)] to determine the maximum energy ($E_{max}=\frac{1}{2}CV^2$; where C is $-1/2\pi f_0 Z_{im}$ and V is the rated voltage of the supercapacitor) of a supercapacitor. However, this method cannot give the energy and power over a range of discharge rates, which are very important for evaluating the performance of a supercapacitor.

In this work, a simple approach to use impedance spectroscopy to predict the energy (E) and power (P) for a supercapacitor is proposed. The predicted results are compared with results from constant current discharging.

The energy delivered by a supercapacitor at a certain discharge rate depends on the usable capacitance ($C_{re}(f)$) and the operating voltage (V) as shown in Eq. 7.10.

$$E = \frac{1}{2} C_{re}(f) V^2 \quad \text{Eq. 7.10}$$

Here f represents the frequency at which $C_{re}(f)$ from an impedance experiment is equal to the magnitude of the capacitance that is available at a certain (but unknown) discharge rate. The average power (P) can then be obtained by dividing the energy by the discharge time, which depends on the selected frequency (f). The reciprocal of frequency ($1/f$) represents the time for one complete charge/discharge cycle,[12, 16] and so it is proposed that the appropriate time is $1/2f$, and that the power can be obtained by Eq. 7.11.

$$P = \frac{E}{t} = 2fE = fC_{re}(f)V^2 \quad \text{Eq. 7.11}$$

7.3.2 Bcap0140 supercapacitor

The impedance of a Bcap0140 supercapacitor was measured at different DC bias potentials and an amplitude of 10 mV. Series capacitances (C_{series}) were calculated by using Eq. 7.12 and the real components of capacitances (C_{re}) were obtained from Eq. 7.4.

$$C_{series} = \frac{1}{-2\pi f Z_{im}} \quad \text{Eq. 7.12}$$

Fig. 7.1(A) shows capacitance plots for the Bcap0140 supercapacitor. It can be seen that both C_{series} and C_{re} were relatively low at high frequencies since the supercapacitor behaves like a resistor. However, both of them increased with decreasing frequency, and reached a similar limiting value at low frequencies. The limiting value (ca. 135 F) is close to the rated capacitance. However, C_{series} starts to approach the limiting value at a much higher frequency than C_{re}.

Fig. 7.1(B) shows that the phase angle was positive at high frequencies, which can be attributed to the inductive behavior of the contacts and leads. The phase angle decreased gradually to zero degrees with decreasing frequency, and finally approached -90 degree at low frequencies. A peak value for C_{im} was obtained at a phase angle of -45 degree where $|Z_{im}|$ is equal to $|Z_{re}|$ or $\frac{\sqrt{2}}{2}|Z|$.[9] At the characteristic frequency (f_0), the $|C_{im}|$ value is half of the C_{series} value as expected from Eq. 7.12 and Eq. 7.5, and the C_{re} value is equal to the $|C_{im}|$ value as expected from Eq. 7.4 and Eq. 7.5.

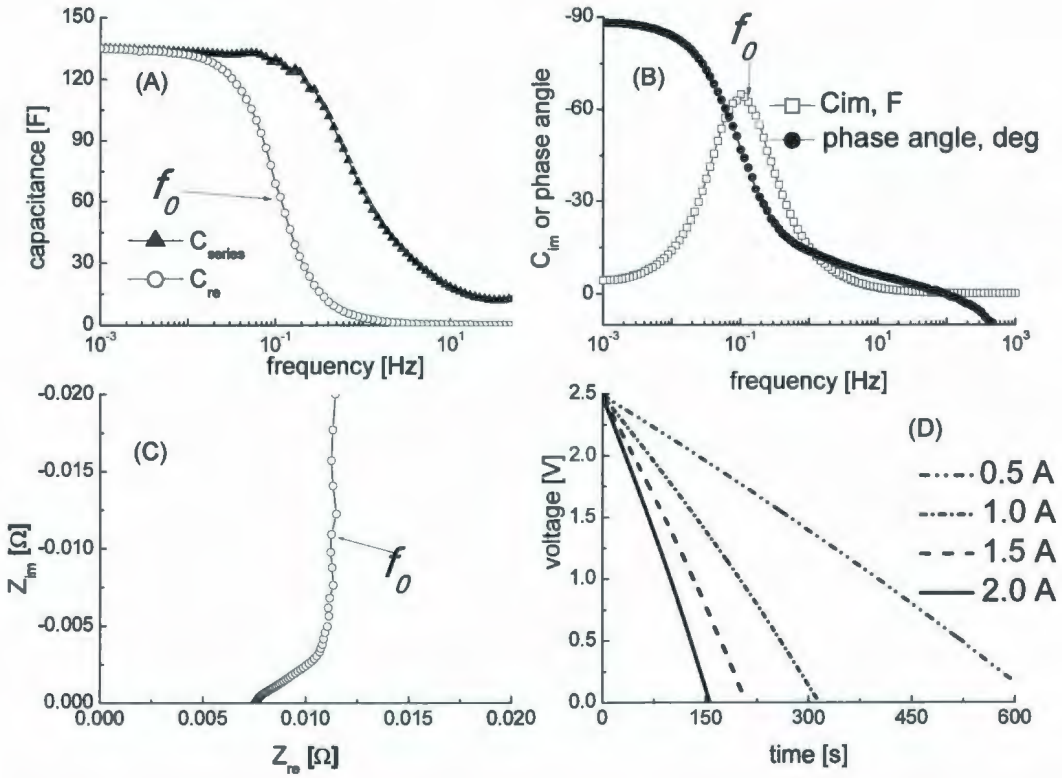

Fig. 7.1 Electrochemical data for a Bcap0140 supercapacitor. (A) Series and real capacitance plots, (B) imaginary capacitance and phase angle plots, (C) Nyquist plots (D) constant current discharging curves. The measurement of impedance spectroscopy was conducted with a DC potential of 2.0 V and 10 mV amplitude.

Fig. 7.1(C) shows a Nyquist plot for the Bcap0140 supercapacitor. It can be seen that the ESR value (the real impedance at 1 kHz) was ca. 7.4 mΩ, which is similar to the rated value of 7.2 mΩ. The Nyquist plot also shows that the electrode materials have the impedance characteristics for porous electrodes, including a ca. 45 degree region at high frequencies and a nearly vertical region at low frequencies.[9]

Fig. 7.1(D) shows discharge curves. It can be seen that the initial voltage decreased nonlinearly with time, indicating that the supercapacitor had a potential-

dependent capacitance. The average capacitances at 0.5 A were 135 F and 120 F for the potential ranges of 2.5 V to 1.25 V and 1.25 to 0.0 V, respectively.

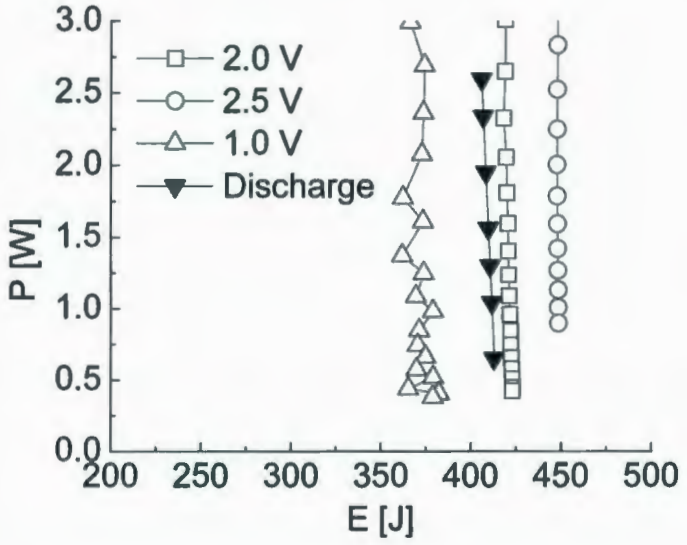

Fig. 7.2 Ragone plots for the Bcap0140 supercapacitor. ▼, constant current discharging results; Δ, □ and○ present the predicted results from impedance spectroscopy with DC potentials of 1.0 V, 2.0 V and 2.5 V, respectively.

Fig. 7.2 shows Ragone plots for the Bcap0140 supercapacitor. It can be seen that the energies predicted (by using Eq. 7.10) from the impedance spectroscopy at each DC potential changed slightly with frequency at low frequencies. However, power almost linearly increased with increasing frequency. It is clear that the three series of predicted values paralleled each other, and that the series of data with a DC potential of 2.5 V have the highest values. The differences in the predicted results can be attributed to the potential-dependent capacitance of the Bcap0140. It can also be seen from Fig 7.2 that the results from constant current discharging were close to the predicted values from the impedance spectroscopy with a DC potential of 2.0 V. The differences can be attributed

to the different voltage ranges employed. For constant current discharging, the employed voltage range was from 0 to 2.5 V, while it was 2.0±0.014 V for impedance spectroscopy. In order to obtain good predicted results, we should choose a voltage in which specific capacitance is close to average specific capacitance over the whole voltage range.

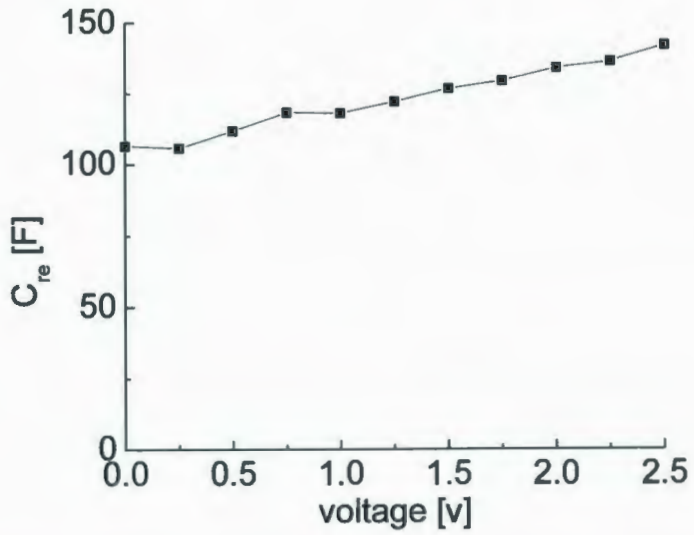

Fig 7.3 Potential-dependent capacitance for the Bcap0140 supercapacitor

In order to measure the validity of the discharge time ($t=1/2f$) calculated from the frequency, impedance experiments were conducted at 3.19 mHz, which corresponds to the discharge time (156.4 s) at 2.0 A, with different DC potentials and 10 mV amplitude. The real capacitances are plotted as a function of DC potential in Fig. 7.3. It can be seen that the real capacitances increased with increasing DC potential. For example, the capacitance increased from 107 F to 142 F with increasing DC potential from 0.0 V to 2.5 V. The average capacitance was 123 F for the potential window of 0.0 V to 2.5 V, so the predicted energy was 383 J by Eq. 7.10, which is slightly less than the energy from

constant current discharging (406 J) at 2.0 A. This difference can be attributed to the low amplitude (10 mV), leading to a lower measured capacitance.[7] The similar energies from the two methods indicated that the calculated discharge time is provides a good approximation.

7.3.3 CF supercapacitor

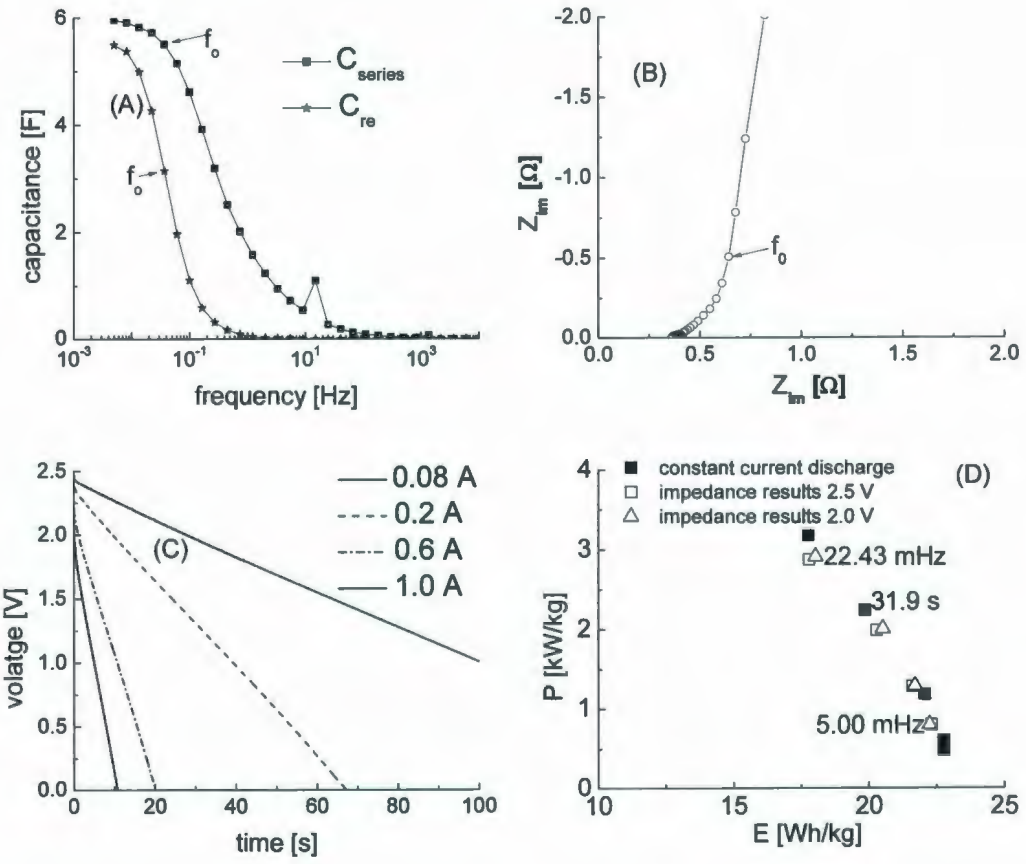

Fig. 7.4 Electrochemical data for a CF supercapacitor with 0.200 g (0.102 g + 0.098 g) CF and a NRE211 separator in an organic electrolyte (saturated tetraethylammonium tetrafluoroborate solution in acetonitrile). (A) Capacitance plots, (B) Nyquist plot, (C) constant current discharging curves and (D) Ragone plots.

A CF supercapacitor was characterized by impedance spectroscopy with a DC bias potential of 2.0 V and 10 mV amplitude. Fig. 7.4(A) shows capacitance plots. It can be seen that both C_{series} and C_{re} increased with decreasing frequency, and did not reach limiting values at 5 mHz. The Nyquist plot (see Fig. 7.4(B)) shows the expected characteristics for porous electrodes. Discharge curves (see Fig. 7. 4(C)) show that the voltage of the supercapacitor decreased linearly with time. The initial voltage quickly decreased over the first few milliseconds due to the ESR (ca. 0.4 Ω) of the cell.

Ragone plots (see Fig. 7.4(D)) for the CF supercapacitor show that the predicted energy and power at low frequencies ($< f_0$) matched those from constant current discharging very well.

7.3.4 Ru oxide supercapacitor

A Ru oxide supercapacitor was also characterized by constant current discharging and impedance spectroscopy as shown in Fig. 7.5. The capacitance plots in Fig. 7.5(A) show that both C_{series} and C_{re} reached a similar limiting value at 5 mHz. The Nyquist plot (see Fig. 7.5(B)) shows the expected characteristics for porous electrodes, including a ca. 45 degree region at high frequencies and a nearly vertical region at low frequencies. Discharge curves (see Fig. 7.4(C)) show that the voltage of the supercapacitor decreased nonlinearly with time, which was due to potential-dependent capacitance (see section 2.3.7).

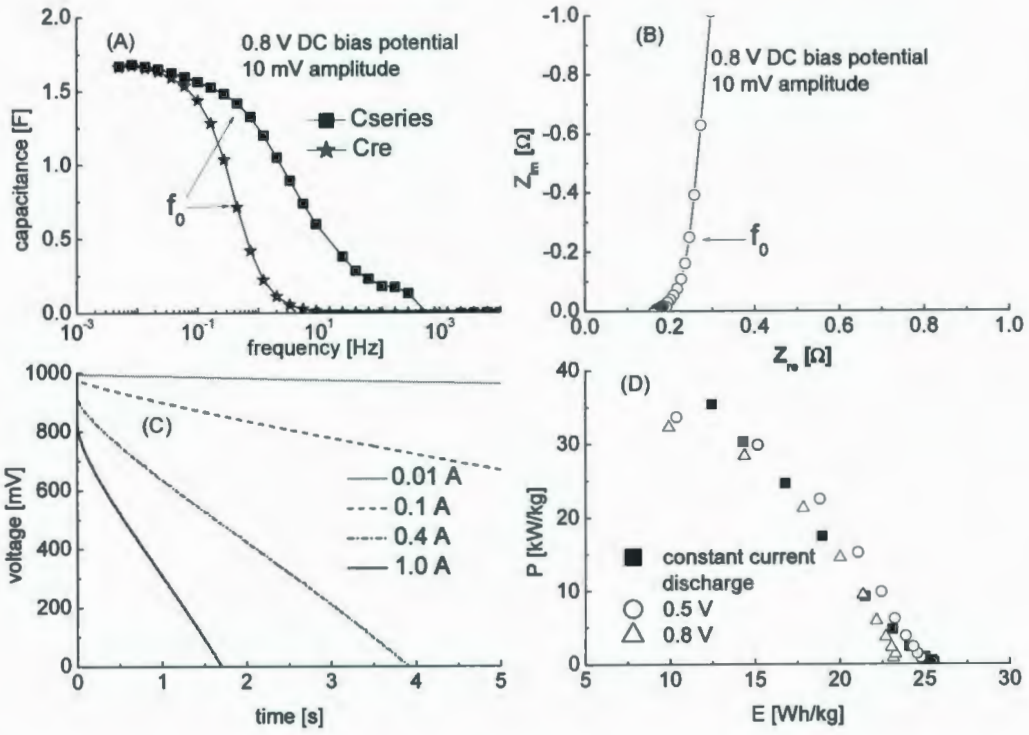

Fig. 7.5 Electrochemical data for a Ru oxide supercapacitor with 9.98 mg (5.03 mg + 4.95 mg) of hydrous Ru oxide annealed at 110 °C and a NRE211 separator in 1 M H_2SO_4. (A) Capacitance plots, (B) Nyquist plot, (C) constant current discharging curves and (D) Ragone plots. ■, results from constant current discharge; Δ, predicted results at a DC potential of 0.8 V; ○, predicted results at a DC potential of 0.5 V.

Fig. 7.5(D) shows Ragone plots for the Ru oxide supercapacitor. It can be seen that the predicted energy and power at low frequencies (less than the characteristic frequency) were close to the results from constant current discharging. The predicted results were similar for two different DC bias potentials employed (0.8 V vs. 0.5 V).

7.4 Conclusions

A new approach for predicting energy and power from impedance spectroscopy is proposed. The usable energy ($E=\frac{1}{2}C_{re}(f)V^2$) is proportional to the real capacitance ($C_{re}(f)$) and the operating voltage (V) of a supercapacitor, while power ($P=2fE$) depends on E and the frequency (f). Commercial, CF and Ru oxide supercapacitors were tested by impedance spectroscopy and constant current discharging. The predicted results for all of the supercapacitors generally agreed with the results from constant current discharging, when frequencies were lower than the characteristic frequency (the frequency at a phase angle of -45 degree. This proposed method can quickly give energy and power information, and is very useful for the development of new electrode materials and the design of circuits.

References

1. Kotz, R.; Carlen, M., *Electrochimica Acta* **2000,** *45* (15-16), 2483-2498.
2. Winter, M.; Brodd, R. J., *Chemical Reviews* **2004,** *104* (10), 4245-4269.
3. Pandolfo, A. G.; Hollenkamp, A. F., *Journal of Power Sources* **2006,** *157* (1), 11-27.
4. Burke, A., *Journal of Power Sources* **2000,** *91* (1), 37-50.
5. Conway, B. E., *Electrochemical supercapacitors: scientific fundamentals and technological applications*. Plenum Press: New York, 1999.
6. Hu, C. C.; Tsou, T. W., *Electrochemistry Communications* **2002,** *4* (2), 105-109.

7. Liu, X. R.; Pickup, P. G., *Journal of Power Sources* **2008,** *176* (1), 410-416.

8. Liu, X. R.; Pickup, P. G., *Energy & Environmental Science* **2008,** *1* (4), 494-500.

9. Barsoukov, E.; Macdonald, J. R., *Impedance spectroscopy : theory, experiment, and applications*. 2nd ed.; Wiley-Interscience: Hoboken, N.J., 2005; p xvii, 595 p.

10. Kotz, R.; Hahn, M.; Gallay, R., *Journal of Power Sources* **2006,** *154* (2), 550-555.

11. Chang, T. Y.; Wang, X.; Evans, D. A.; Roberson, S. L.; Zheng, J. P., *Ieee Transactions on Industrial Electronics* **2004,** *51* (6), 1313-1317.

12. Jang, J. H.; Kato, A.; Machida, K.; Naoi, K., *Journal of the Electrochemical Society* **2006,** *153* (2), A321-A328.

13. Miller, J. R., *8th International Seminar on Double Layer Capacitors and Similar Energy Storage Devices* **1998**.

14. Taberna, P. L.; Simon, P.; Fauvarque, J. F., *Journal of the Electrochemical Society* **2003,** *150* (3), A292-A300.

15. Kurzweil, P., *The 14th International Seminar On Double Layer Capacitors, Deerfield Beach, FL., U.S.A., December 6-8, 2004* **2004**.

16. Jang, J. H.; Machida, K.; Kim, Y.; Naoi, K., *Electrochimica Acta* **2006,** *52* (4), 1733-1741.

17. Sawai, K.; Ohzuku, T., *Journal of the Electrochemical Society* **1997,** *144* (3), 988-995.

Chapter 8 Summary and future work

8.1 Summary

Hydrous Ru oxide was synthesized by a modified sol-gel method using the reaction between ruthenium(III) chloride and sodium carbonate solutions. The properties of hydrous Ru oxide were characterized by SEM, TGA, XRD, CV, impedance spectroscopy and constant current discharging methods. The various factors influencing the performance of Ru oxide electrodes were investigated in detail. The specific capacitance of hydrous Ru oxide increased with increasing annealing temperature, reached a maximum value of 716 ± 24 F/g at 110 °C, then decreased.

Based on a proton insertion/extraction mechanism during charging/discharging, the capacitive behavior of hydrous Ru oxide should strongly depend on its proton conductivity. The experimental results showed that Nafion binder sharply improved the specific capacitances of Ru oxide electrodes with high loadings (up to 51 mg/cm^2), which level off at 700 F/g. This is much better than literature results, where specific capacitances are reported to sharply decrease with increasing electrode loading. In addition, Nafion membrane separators also improved the performances of Ru oxide supercapacitors due to the good proton conductivity pathways between the two electrodes. The use of a CFP support further improved the performance of Ru oxide supercapacitors because of its low contact resistance. Ru oxide supercapacitors (with a operating voltage of 1.0 V) assembled by an optimum method demonstrated a very high energy density of

ca. 30 W h/kg, a high power density of 59 kW/kg, and long lifetimes of over 120000 cycles.

The utilization of Ru in Ru oxide/CF composites prepared by an impregnation method was improved due to synergistic effects inolving interactions between quinone groups with different structures on the CF surface and the Ru oxide component. SEM experiments indicated that Ru oxide particles were evenly deposited on the CF surface for composites with low loading (< 20%), while most of the Ru oxide particles occupied the spaces between the fibers for composites with high loading (>20%). All of the composites showed high quality capacitive behaviors. However, the specific capacitances based on the Ru oxide components decreased with increasing loading. A 9.2% Ru oxide/CF composite showed an average specific capacitance of 1085 F/g based on the Ru oxide component, which is higher than that of pure Ru oxide.

A new method for preparing nanostructured and thin film Ru oxide/carbon composites was developed by using spontaneous reduction of Ru(VI) or Ru(VII). The sizes of Ru oxide particles for a nanostructured Ru oxide/MWCNT composite were less than 3 nm, while thin film Ru oxide layer structures were observed for Ru oxide/CF composites. The Ru oxide components for all composites exhibited high specific capacitances due to the thin film structures and nanostructured Ru oxide particles. For example, a 25.1% hydrous Ru oxide/MWCNT composite had an average specific capacitance of 704±62 F/g for the hydrous Ru oxide component, and a 7.4% Ru oxide/CF composite with film structure had an average specific capacitance of 824±152 F/g based on the Ru oxide component alone. The specific capacitances of hydrous Ru

oxide/MWCNT and Ru oxide/CF composites decreased with annealing, suggesting that ordered Ru oxide structures are formed by the spontaneous reduction method. Composite samples that had not been dried had lower R_i values than samples dried at room temperature. However, annealing sharply decreased R_i values.

The spontaneous reduction method was also be used to prepare Mn oxide/CF, and thin film Mn-Ru oxide/CF composites. The Mn oxide component of Mn oxide/CF composites showed very high specific capacitance in basic electrolytes for the first cycle, but it quickly decreased with cycling. The introduction of Ru oxide sharply enhanced the stability of Mn oxide/CF composites.

Ru oxide and Ru oxide/carbon composites are good candidates for the positive electrodes of hybrid supercapacitors. In 2 M KNO_3 electrolyte, the operating voltage for a hydrous Ru oxide/CF and CF hybrid supercapacitor reached to 2.0 V. Hybrid supercapacitors can provide high energy density due to integration of the advantages of different positive and negative electrodes. For example, the maximum energy density of a Ru oxide/CF//CF supercapacitor was ca. 18 W h/kg, and a maximum energy density of 41.3 W h/kg was obtained for a Ru oxide//Pd/C supercapacitor.

A new approach for predicting the energy and power from impedance spectroscopy is proposed. The usable energy ($E=\frac{1}{2}C_{re}(f)V^2$) and power ($P=2fE$) depend on the real capacitance ($C_{re}(f)$) and operating voltage (V). The predicted results at low frequencies agreed reasonably with those from constant current discharging.

8.2 Future work

Ru-based composites are excellent materials for supercapacitors. The Ru oxide and Ru oxide/carbon composites have been investigated in detail. These materials demonstrated high quality capacitive behavior and good performance. The following future work is proposed.

1) Optimization of the synthesis of binary Ru-Mn oxide films and full characterization;
2) Synthesis and characterization of composites of Ru oxide with other metal oxides, which include TiO_2, SnO_2, vanadium oxide and tungsten oxide. Further improve the utilization of Ru oxide;
3) Further optimize the preparation methods of Ru-based composites for obtaining electrode materials with high performance.